7 June 1991

Numerical Investigation of Some Aspects of Fourier Transform Ion Cyclotron Resonance Spectroscopy

Michael W. Deem

Jack L. Beauchamp

California Institute of Technology

Pasadena, CA 91125

Submitted to R. Flagen in
partial fulfillment of the
requirements of ChE 90ab.

TABLE OF CONTENTS

PREFACE.

CHAPTER I. Comparison of Quadrupole and Octopole Ion Guides for External Source FT-ICR Ion Injection.

CHAPTER II. A Fundamental Mass Resolution Limit of the Conventional FT-ICR Cubic Cell.

CHAPTER III. Numerical Evaluation of Space Charge Effects in Moderate Density, High m/z FT-ICR Studies.

CHAPTER IV. A Numerical Study of the Application of Magnetic Excitation to FT-ICR.

CHAPTER V. A Monte Carlo Study of Thermal Cross Sections and Collision Rates of Multiply-Charged, Linear, Gas-phase Proteins.

PREFACE

This senior thesis summarizes the research that I have done with Professor Jack L. Beauchamp during the last couple of years. Professor Beauchamp has provided me with an interesting sample of theoretical questions relevant to his FT-ICR research, the computational solution of which has given me many enjoyable hours of thought. I applaud his patience in putting up with the reams of computer output I delivered, mailed, or FAXed him!

I should also mention several other persons who I have worked for during my four years at Caltech. While the work I have done with them is not represented here, their impact upon my scientific outlook has been enormous. Professor Fred Shair first introduced me to engineering research as a freshman. One of Professor Shair's graduate students came to be one of my best friends: Robin Horrell is a man whose personal energy and engineering curiosity continue to amaze me. Through monte carlo simulations of surface reactions, Professor Henry Weinberg showed me that computer simulations can be of use in elucidating current scientific questions. He has continued to encourage me, and to inspire me with his boundless drive and intellect. Finally Dr. John Newsam of Exxon, now at BIOSYM, introduced me to some questions in the zeolite field, whose solution has given me a great deal of satisfaction. John is a first-rate scientist and I feel lucky to have been able to work with him.

My personal life has been kept sane by weekly conversations with my parents.

Without them, I might not have survived my stay at Caltech. Thanks Mom and Dad.

Last, but not least, I would like to thank ~~the~~ Jack for one last benefit. In his group I met the nicest person I have known. Thanks for giving me a chance, Ching-Hwa.

CHAPTER I

Comparison of Quadrupole and Octopole Ion Guides for External Source FT-ICR Ion Injection

M. W. Deem and J. L. Beauchamp

Contribution No. 8124 from the Arthur Amos Noyes Laboratory

California Institute of Technology, Pasadena, CA 91125

Submitted to Int. J. Mass. Spectrom. Ion Proc.

ABSTRACT

A detailed kinematic analysis is presented comparing the use of quadrupole and octopole ion guides in conjunction with external ion source Fourier transform ion cyclotron resonance spectrometers. Methods to determine simply the electric fields for ideal and real quadrupoles and octopoles are presented, with emphasis on the importance of the effective potential in analyzing the design of an ion guide. Trajectory calculations are presented for a wide range of ion guide operating parameters and initial ion energies, along with an evaluation of the range of injected masses. Radial and axial ion energies together with a projection of the off-axis excursions of the ion motion on the plane perpendicular to the axis of the ICR cell are graphically illustrated. The real octopole exhibits more nearly ideal behavior than does a real quadrupole. It does not suffer from the anti-magnetic mirror effect, has uniform mass cutoffs, and has a four times greater maximum mass cutoff for given operating parameters than does a quadrupole.

INTRODUCTION

The increasing popularity of high field Fourier transform ion cyclotron resonance (FT-ICR) spectrometers incorporating superconducting magnets is a result, in part, of the possibility of utilizing external ion sources in which the region of ion production is separated from the ICR cell. Usually the source is located outside the high field region and the ions are injected on axis into the ICR cell. This arrangement allows the use of techniques such as energetic particle bombardment [1], laser desorption [2], and electrospray ionization [3] to generate ions of interest. These techniques are often not directly compatible with the desired high vacuum conditions in which ICR cells are designed best to operate. This problem can be surmounted by incorporating several stages of differential pumping between the ion source and the ICR cell. To transport ions between the source and the ICR cell, ion lens systems [2] and rf-only quadrupole ion guides [4] have been employed, with design considerations being dictated by the need to overcome the magnetic mirror effect during ion injection. Relatively little study of the kinematics of the quadrupole ion guide loading process has been performed, and even less consideration has been given to the effects of nonhyperbolic rods or to the feasibility of ion injection with an octopole ion guide. We wish to report a detailed calculational study of the ion trajectories in quadrupole and octopole ion guides used to transfer ions from an external ion source into the high field region of a FT-ICR spectrometer.

INTENDED EXPERIMENTAL SETUP

Figure 1a illustrates the external-source FT-ICR instrument for which our calculations are appropriate. Airborne ions are produced externally to the ICR cell, directed by electrostatic lenses into an ion guide, transmitted by the ion guide though the region of increasing B-field, and captured by the ICR cell. Figures 1b and 1c depict the B-field generated by the 7 T superconducting magnet, vide infra. The ion guide is 100 cm long, with a bore radius of 0.275 cm.

THEORY

Electric Fields in Ion Guides. Since the B-field will in the end be a small perturbation on the time-varying electric fields present in an ion guide, we will discuss the electric field first. Friedman, et al., discuss the fundamental field equations of ion guides and remind us that Laplace's equation is a very good approximation to the true governing equation for the electric potential in ion guides as long as the resulting ion motion is nonrelativistic. [5] The common approximation of ignoring end effects of the guide will be made, thus restricting the partial differential equation (PDE) to two dimensions. With the further reminder that the real part of an analytic function is harmonic, then, an ideal quadrupole electric potential is represented by

$$\psi_q(x,y) = \text{Re } z^2 = x^2 - y^2, \tag{1}$$

and an ideal octopole electric potential is represented by

$$\psi_o(x,y) = \text{Re } z^4 = x^4 - 6x^2y^2 + y^4. \tag{2}$$

Customarily authors define a to be the rod radius for an ion guide with cylindrical rods and r_0 to be the distance from the symmetry axis to the nearest rod surface. The time-varying ideal electric potentials then become

$$\Psi_q(x,y,t) = (V_0/r_0^2)(x^2 - y^2)\cos(\omega t) \quad (3)$$

and

$$\Psi_o(x,y) = (V_0/r_0^4)(x^4 - 6x^2y^2 + y^4)\cos(\omega t), \quad (4)$$

where V_0 is the maximum voltage amplitude (not the rms value), and ω is the angular frequency.

The analysis of Landau and Lifshitz for a particle moving in a rapidly time-oscillating force field has often been used in the past, and it will be helpful here. [6] The analysis is basically a time-smoothing (as in fluid dynamics) of Newton's second equation and is valid for fields that cause motion that can be decoupled into a smooth component and a high-frequency additive oscillation to the smooth component. Their equations of motion involve a time-invariant potential $U(\mathbf{x})$ and a time varying force $\mathbf{F}(\mathbf{x})\cos(\omega t + \alpha)$. Given that $U(\mathbf{x})$ is well-behaved, $\mathbf{F}(\mathbf{x})$ is well-behaved, and the oscillation is high-frequency, their result is that the smooth motion is governed by the effective potential

$$U_{eff}(\mathbf{x}) = U(\mathbf{x}) + |\mathbf{F}(\mathbf{x})|^2/(4m\omega^2). \quad (5)$$

The effective potentials for the above ion-guide potentials are, then,

$$U_{eff,q}(x,y) = r^2q^2V_0^2/(m\omega^2r_0^4) \quad (6)$$

and

$$U_{eff,o}(x,y) = 4r^6q^2V_0^2/(m\omega^2r_0^8). \quad (7)$$

Figures 2a and 2b illustrate the ideal octopole potential along with its effective potential. Figures 4a and 4b show the same for the ideal quadrupole potential. Note that $U_{eff,o}(r = r_0) = 4U_{eff,q}(r = r_0)$, which will be shown later to imply that the

maximum mass cutoff for the octopole is four times that of the quadrupole.

It is clear from the Figures that the boundary conditions on the PDE are not satisfied. That is, the potential is defined by having the value V_0 on the entire circumference of the rods and by either decaying to zero far away from the origin or having another boundary condition at the edge of the region of interest. The standard literature approach to a useful, accurate, computational solution has been to fit a symmetry-adapted Legendre polynomial expansion to a numerical solution of the PDE with the correct boundary conditions. [7] Kent Ervin presents the results of such a fit for octopoles with various values of a/r_0; his fit for $a/r_0 = 0.4$ is illustrated in Figures 2c and 2d. [8] We chose, however, to represent the octopole electric potential by a collection of image charges. Charges of identical magnitude and alternating sign are placed at the center of the rods ($r = r_0 + a$) and at twice that radius, 2r, (with the factor of two somewhat arbitrary, but satisfactory). The potential is then the potential due to these charges, a sum of logarithms in two dimensions (see Figure 3). The potential is normalized by forcing the value at $r = r_0$ and $\theta = 0$ to be V_0. This enables us to examine simply the effect of rod size on the effective potential, with some results presented in Figure 3. We optimize a/r_0 by numerically minimizing the standard deviation of the effective potential from $\theta = 0$ to $\theta = \pi/8$ at $r = 0.8\ r_0$. We find that the effective potential becomes more nearly θ independent as the rods are made larger. Note, however, that for a/r_0 greater than about 0.45, our potential is not satisfying the boundary conditions very well. Thus we conclude that there is no basis for choosing $a/r_0 = 0.37$, as is suggested by the nonphysical desire to minimize the next higher

symmetry-adapted coefficient in the Legendre polynomial expansion. [7,8] Note that Laplace's equation is a very forgiving PDE, for despite the great differences in the potentials outside the guide bore, the interior bore potentials of Figures 2a, 2c, and 3a are nearly identical. Similarly, eight charges are used to fit better the electric potential generated in the quadrupole guide bore by the real, cylindrical rods. The image charges are placed at $\theta = -0.2\,\pi$ and $0.2\,\pi$, $r = 0.6(r_0 + a)$, and then replicated, alternating sign, three times. An example of this potential is shown in Figure 4c. The potential is normalized at the rod surface as above. Again these values are arbitrary, but satisfactory. In subsequent calculations we will always use $r_0 = 0.275$ and $a = 0.637$ for the "real" quadrupole potential, following McIver [9], $r_0 = 0.275$ for the ideal quadrupole potential, and $r_0 = 0.275$ and $a/r_0 = 0.4$ for the "real" octopole potential.

Magnetic Fields. The B-field of interest in our calculations will be an axially symmetric one due to the superconducting magnet. Our coordinate system will be right-handed, with the z axis the axis of symmetry of the magnet. McIver notes that since

$$\nabla \cdot \mathbf{B}(r,z) = 0 \tag{8}$$

and

$$\mathbf{B}(0,z) = \mathbf{0}, \tag{9}$$

the divergence in cylindrical coordinates can be integrated to yield

$$B_r(r) = -(r/2)\,[dB_z(z)/dz]_{r=0} \tag{10}$$

if dB_z/dz can be considered independent of r for the small range of r of interest. [9]

Typically measured $B_z(z)$ data are fit with cubic splines for use in computation. A function with a discontinuous third derivative can cause problems during high-order numerical integration, however. So we choose to fit the B-field of a radially-thin solenoid, [10]

$$B_z(z) = A(\cos \theta_1 - \cos \theta_2), \tag{11}$$

where θ_1 and θ_2 are the angles between the solenoid axis and the first and last solenoid coils with respect to the point at z, numerically to several data points read from McIver's graph. [9] McIver's data is actually for a 6 T magnet, so his data and Eq. (11) are scaled to 7 T. The result, illustrated in Figures 1b and 1c, is that the solenoid is centered at 88.66 cm, has a 11.66 cm radius, and is 42.40 cm long; B_z for z greater than 88.66 is set to 7 T. The curve does not have quite a sharp enough shoulder at 80 cm, but is otherwise accurate. The scaled curve compares satisfactorily with $B_z(z,r=0)$ data for a 7 T magnet supplied by the manufacturer, Oxford, indicating Eq. (11) is a transferable form.

As particles enter the region of increasing B_z, they begin to execute the classic magnetron motion. This motion is in such a direction that the radially inward B_r causes a Lorentz force in the -z direction. This is the magnetic mirror effect, which is also responsible for such phenomena as the van Allen radiation belt in the Earth's atmosphere. This force can be significant enough that it reverses the motion of ions injected into the high field region of a FT-ICR spectrometer. For ions to be successfully injected, they must be kept at small values of r, for there B_r is weak. This is accomplished by the ion guide.

CALCULATIONS

Trajectories. With current compute power, we are able to study carefully the injection trajectory of only a single ion. The equation of motion for the ion is

$$\mathbf{F} = m\,\mathbf{a} = q\,(\mathbf{E}_0 \cos \omega t + \mathbf{v} \times \mathbf{B}), \quad \mathbf{x}(0) = \mathbf{x}_0, \mathbf{v}(0) = \mathbf{v}_0, \tag{12}$$

where $\mathbf{E}_0$ is the maximum amplitude of the electric field, ω is the angular frequency, m is the ion's mass, and q is the ion's charge.

For an ideal quadrupole,

$$\mathbf{E}_0 = -2V_0\langle x,-y,0\rangle\cos(\omega t)/r_0^2, \tag{13}$$

so that if the B-field is ignored

$$d^2\langle x,y\rangle/d\tau^2 + 8qV_0\langle x,-y\rangle\cos(2\tau)/(m\omega^2 r_0^2) = 0, \qquad \tau = \omega t/2, \tag{14}$$

which as others have noticed [11] is the uncoupled, linear Mathieu equation, with the defining parameters

$$a_m = 0 \text{ and } q_m = \pm 4qV_0/(m\omega^2 r_0^2). \tag{15}$$

The ideal octopole potential leads to nonlinear, coupled ordinary differential equations (ODEs) that are not immediately recognizable, as do the image charge potentials.

The above equation of motion is integrated numerically by VODE, a variable order, variable step size ODE integration package designed to deal with difficult to integrate, nonlinear equations. [12,13,14,15,16,17] The stable, backward differentiation formula algorithm (MF = 20) is used in the eight-byte-real version of this code. For the trajectory calculations we specify rtol = 10^{-4} and atol = 10^{-6}, which

means essentially four significant figure accuracy for integration over a reasonable time range. As part of our validation of the code, we compute the turning point of an ion with $E_{r\,0}$ = 2 eV, $E_{z\,0}$ = 80 eV, and $\mathbf{x}_0 = \mathbf{0}$ in a 6 T magnet with no ion guide. We find it to be 37.6 cm, whereas McIver finds it to be 42 cm, which is reasonable agreement, vide infra. [9] While appropriate for code verification, this is an unrealistic computation, as the ion is at about r = 5 cm, where B_r given by Eq. (10) is probably inaccurate, when reflection occurs.

Our code calculates trajectories for three types of ion guides: ideal quadrupole (potential given by Eq. 3, see also Figure 4a), real quadrupole (Figure 4c), and real octopole (Figure 3a). Figures 5-9 illustrate representative runs for the ideal quadrupole, with the ion started on the axis, with prescribed initial energies $E_{r\,0}$ and $E_{z\,0}$. Comparisons of ten trajectories for a given set of guide parameters in these Figures, varying the initial θ, show all ideal quadrupole runs to be very similar. This is intuitively acceptable since the effective potential is θ independent. Similarly, Figures 10-13 illustrate runs for the real quadrupole. That the effective potential is no longer θ independent results in some unexpected trajectories. And finally Figures 14-18 illustrate again representative runs for the real octopole, which has a nearly θ independent effective potential. All Figures were produced with the GraphiC™ 5.01 program, Scientific Endeavors Corporation.

Several facts can be gleaned from these plots. A significant result is that the time-

averaged total energy is roughly constant, even though the potential is time-varying. Nevertheless the instantaneous radial energy does vary by a factor of two to three as the ion travels down the guide bore. This could result in a spread of radial energies in the final, collected ions. The octopole produces distinctive trajectories with compact bursts of off-axis energy as the ion reaches radial turning points, whereas the quadrupoles produce simply noisy energy traces. These different energy histories could have an effect in kinetically activated ion beam chemistry [8,18] The parameter dependence of $U_{eff,q}$ and $U_{eff,o}$ is quantitatively apparent in the variations of the maximum off-axis excursions. Of fundamental interest is that the path taken by ions of a given initial energy is not defined by m/q. Clearly the octopole, with an effective potential that is more nearly a square-well, is less sensitive to its parameters than are the quadrupoles. Of course the magnetic mirror effect is apparent. Interestingly, the change in E_z seems to be fairly constant. Also note that ions with $E_{z\,0}$ as low as 2 eV are injected, with the results for the real quadrupole not shown but very similar to those of the ideal case. The final energy of the ions in the octopole, however, is substantially lower than that of the ions in the quadrupoles. The real quadrupole runs provide the most dramatic effects, however. The θ dependent effective potential can cause the ions to start spinning even before they encounter a significant B_z. This results in the doughnut trajectories. It even produces an anti-magnetic mirror effect if the ion is spinning in the "wrong" direction, as can be seen in Figure 12. Only at low mass, however, are the velocities large enough to produce this odd effect.

Mass Injection Ranges. The range of masses injected by an ion guide is a very important design criterion. To compute such a range, we identify minimum and maximum masses that are not injected and then use a binary search to locate the actual minimum and maximum mass injected for given operating parameters. Failure to inject is defined as a trajectory that exceeds $r = r_0$. The minimum mass is forced to be at least 10 amu and is located to within 10 amu. The maximum mass is forced to be less than 100000 amu and is located to within 100 amu. Thus 100000 in the Tables means ≥100000, and the granularity of the search must be kept in mind. Three dashes indicate that no mass is found to inject. We find that stringent accuracy requirements are necessary to generate reliable results, so rtol = 10^{-6} and atol = 10^{-8} are specified in VODE. Another check on our code is to compute the masses injected through the ideal quadrupole in Figure 4a for $E_{z\,0}$ = 80eV and $E_{r\,0}$ = 5 eV in a 6 T magnet. For f = 1 MHz and V_0 = 200 V, we find min = 470 and max = 2160; McIver finds min = 475 and max = 2200. [9] For f = 1 MHz and V_0 = 400 V, we find min = 750 and max = 9680; McIver finds min = 750 and max = 9800. For f = 3 MHz and V_0 = 200 V, we find min = 90 and max = 240; McIver finds min = 90 and max = 650. We suspect either McIver uses $E_{r\,0}$ = 2 eV on this last run, or his integration is inaccurate, as the ideal effective potential analysis predicts a maximum mass of 287 amu in this case.

The data listed in the tables represents the outcomes of four runs for each parameter set, with the initial θ being varied. Typically the minimum mass injected is essentially the same for the four runs, but the maximum often varies. The range listed next to a

mass is one-half of the spread of four data. Table I lists the mass ranges injected for various ideal quadrupole operating parameters. Table II lists the mass ranges injected for various real quadrupole operating parameters. Table III lists the mass ranges injected for various real octopole operating parameters. Table IV lists the mass ranges of high-initial-energy ions injected through real quadrupole and octopoles. Tables V-VII list the predicted minimum mass value for the ideal quadrupole, and the maximum mass value for all the guides. Intuitively the minimum mass injected is determined by stability considerations, and the minimum values listed in Tables V-VII are determined from the stability boundary. Abramowitz and Stegun define the stability regions of the Mathieu equation by [19,20]

$$a_{m,n}(|q_m|) < a_m < b_{m,n+1}(|q_m|). \tag{16}$$

The relevant zero is $b_{m,1}(q_m) = 0$, since $a_m = 0$. Solving the polynomial approximation given by Abramowitz and Stegun, we find $q_{m,critical} = \pm 0.908048$. The definition of q_m by Eq. (15) then identifies the minimum possible mass. This analysis does accurately predict the masses injected when there is no B-field present, as Table I indicates. The B-field is an important parameter, however, and this analysis is worthless for predicting ICR minimum masses injected. Table I does not even have the parameter dependence predicted by the above analysis. It does indicate, however, that the minimum mass injected is independent of $E_{r\,0}$. By the basic structure of the equations of motion, then, q and m enter only as the ratio q/m. Similarly, the maximum mass injected is determined by the confinement ability of the guide. It is predicted by equating $E_{r\,0}$ with the effective potential numerically computed at $r = r_0$, with θ equal to the value that predicts the lowest maximum mass. This analysis is

rather accurate, especially for the heavier species. The real quadrupole seems not always to eject at the effective potential minimum, and thus has a higher than predicted maximum mass. In fact, the θ dependence of the effective potential is what causes the spread in maximum masses injected evident in Table II. Note that the ideal octopole effective potential predicts well the maximum mass injected for the real octopole. Occasionally the real octopole results indicate that there are dual stability regions, separated by a region of instability slightly higher than the minimum mass.

These tables are the result of two weeks of DEC 3100 CPU time, a machine well suited for numerical calculations, with the unvectorized code running about one-fifth as fast as on a Cray XMP/14se.

CONCLUSIONS

We conclude that a real octopole behaves more nearly ideally than does a real quadrupole. While it occasionally has dual regions of stability with a small unstable region near the minimum mass injected, the octopole does not suffer from the anti-magnetic mirror effect, and it has uniform mass cutoffs. In fact, the octopole has a four times greater maximum mass cutoff for given operating parameters than does a quadrupole, which is a decided advantage when dealing with biological molecules.

ACKNOWLEDGEMENTS

We would like to thank Paul Messina, the Director of Caltech Concurrent Computing Facilities, for generous grants of computer time.

Bibliography

(1) C. B. Lebrilla, D. T. S. Wang, T. J. Mizoguchi, and R. T. McIver, J. Am. Chem. Soc. 111 (1989) 8593.

(2) J. M. Alford, P. E. Williams, D. J. Trevor, and R. E. Smalley, Int. J. Mass. Spectrom. Ion Proc. 72 (1986) 33.

(3) C. K. Meng, M. Mann, and J. B. Fenn, Z. Phys. D. 10 (1988) 361.

(4) Carlito B. Lebrilla, I. J. Amster, and Robert T. McIver, Int. J. Mass Spectrom. Ion Proc. 87 (1989) R7.

(5) M. H. Friedman, A. L. Yergey, and J. E. Campana, J. Phys E 15 (1982) 53.

(6) L. D. Landau and E. M. Lifshitz, Mechanics, 3rd ed., Oxford, 1976, pp. 93-95.

(7) D. R. Denison, J. Vac. Sci 8 (1971) 266.

(8) Kent M. Ervin, Ph.D. Thesis, University of California, Berkeley, 1986. Also, K. M. Ervin and P. B. Armentrout, J. chem. Phys 83 (1985) 166.

(9) Robert T. McIver, submitted to Int. J. Mass Spectrom. Ion Proc. (1989).

(10) Edward M. Purcell, Electricity and Magnetism, 2nd ed., McGraw-Hill, 1985, p. 228.

(11) D. J. Wineland, Wayne M. Itano, and R. S. Van Dyck, Jr., Adv. At. Mol. Phys. 19 (1983) 135.

(12) P. N. Brown, G. D. Byrne, and A. C. Hindmarsh, "VODE, a Variable Coefficient ODE Solver," LLNL Report UCRL-98412, June 1988. Also, SIAM J. Sci. Stat. Comput., to appear.

(13) G. D. Byrne and A. C. Hindmarsh, ACM Trans. Math. Software 1 (1975) 71.

(14) A. C. Hindmarsh and G. D. Byrne, "EPISODE: An Effective Package for the Integration of Systems of Ordinary Differential Equations," LLNL Report UCID-30112, Rev. 1, April 1977.

(15) G. D. Byrne and A. C. Hindmarsh, "EPISODEB: An Experimental Package for the Integration of Systems of Ordinary Differential Equations with Banded Jacobians," LLNL Report UCID-30132, April 1976.

(16) A. C. Hindmarsh, Scientific Computing, R. S. Stepleman et al., eds., North-Holland, Amsterdam, 1983, pp. 55-64.

(17) K. R. Jackson and R. Sacks-Davis, ACM Trans. Math. Software 6 (1980) 295.

(18) Stephen C. Davis and Barry Wright, Rapid. Commun. Mass Spectrom. 4 (1990) 186.

(19) M. Abramowitz and I. E. Stegun, Handbook of Mathematical Functions, Dover, 1972, ch. 20.

(20) Carl M. Bender and Steven A. Orszag, Advanced Mathematical Methods for Scientists and Engineers, McGraw-Hill, 1978, ch. 11.4.

TABLES

Table I

Ideal quadrupole mass ranges, with B = 7 T, r_0 = 0.275 cm, $E_{z\,0}$ = 80 eV, and q = 1, 5, and 10 $|e^-|$ and for no magnetic field, with q = 1 $|e^-|$.

			z = 1		z = 5		z = 10		no magnetic field	
$E_{r\,0}$ (eV)	f (MHz)	V_0 (V)	min (amu)	max (amu)	min (amu)	max (amu)	min (amu)	max (amu)	min (amu)	max (amu)
2.0	1	100	350	1600 ± 80	1750	40280 ± 240	3490	100000	150	1640 ± 80
2.0	1	200	490	6320 ± 160	2430	100000	4870	100000	290	6400 ± 160
2.0	1	400	770	25800 ± 320	3830	100000	7670	100000	570	25720 ± 240
2.0	3	100	90	240	430	4520 ± 80	870	18000 ± 160	15	240
2.0	3	200	110	720	510	18000 ± 160	1010	71920 ± 160	30	720
2.0	3	400	130	2840 ± 80	650	71920 ± 160	1310	100000	70	2800
2.0	6	100	30	60	190	1160 ± 80	390	4520 ± 80	15	60
2.0	6	200	50	240	210	4520 ± 80	430	18000	15	240
2.0	6	400	50	720	250	18000	510	71920 ± 160	15	720
2.0	9	100	---	---	130	560	250	2000	---	---
2.0	9	200	30	75 ± 30	130	2000	270	8000 ± 80	15	60
2.0	9	400	30	280 ± 80	150	8000 ± 80	310	31960 ± 80	15	240
0.5	1	100	350	6440 ± 80	1750	100000	3490	100000	150	6440 ± 80
0.5	1	200	490	25840 ± 160	2430	100000	4870	100000	290	25800 ± 80
0.5	1	400	770	100000	3830	100000	7670	100000	570	100000
0.5	3	100	90	720	430	18000	870	71920 ± 160	15	720
0.5	3	200	110	2840 ± 80	510	71920 ± 160	1010	100000	30	2840 ± 80
0.5	3	400	130	11480 ± 80	650	100000	1310	100000	70	11480 ± 80
0.5	6	100	30	240	190	4560	390	18040 ± 80	15	240
0.5	6	200	50	720	210	18040 ± 80	430	71960 ± 240	15	720
0.5	6	400	50	2800	250	71960 ± 240	510	100000	15	2840 ± 80
0.5	9	100	30	75 ± 30	130	2000	250	8080	15	60
0.5	9	200	30	320 ± 80	130	7960 ± 80	270	31960 ± 80	15	240
0.5	9	400	30	1240 ± 80	150	31960 ± 80	310	100000	15	1240 ± 80

Table II

Real quadrupole mass ranges, with B = 7 T, r_0 = 0.275 cm, a = 0.637 cm, $E_{z\,0}$ = 80 eV, and q = 1, 5, and 10 |e|.

			z = 1		z = 5		z = 10	
$E_{z\,0}$ (eV)	f (MHz)	V_0 (V)	min (amu)	max (amu)	min (amu)	max (amu)	min (amu)	max (amu)
2.0	1	100	350	1720 ± 480	1770	42800 ± 13120	3550	100000
2.0	1	200	490	5120 ± 400	2470	100000	4970	100000
2.0	1	400	790	27720 ± 7600	3970	100000	7970	100000
2.0	3	100	90	240	430	4920 ± 1440	870	19560 ± 5840
2.0	3	200	110	760 ± 240	510	19160 ± 4960	1030	81520 ± 20680
2.0	3	400	130	3000 ± 960	670	80800 ± 20680	1330	100000
2.0	6	100	---	---	190	1200 ± 400	390	4800 ± 1440
2.0	6	200	50	210 ± 60	210	4920 ± 1440	430	19680 ± 5760
2.0	6	400	50	760 ± 240	250	19240 ± 4960	510	81680 ± 20600
2.0	9	100	---	---	130	520 ± 160	250	2080 ± 560
2.0	9	200	30	75 ±30	130	2160 ± 640	270	8520 ± 2480
2.0	9	400	30	320 ±80	150	8560 ± 2640	310	34880 ± 10400
0.5	1	100	350	6880 ± 1440	1770	100000	3550	100000
0.5	1	200	490	24600 ± 3840	2490	100000	4970	100000
0.5	1	400	790	100000	3950	100000	7930	100000
0.5	3	100	90	760 ± 240	430	19600 ± 5680	870	81960 ± 20680
0.5	3	200	110	3120 ± 880	510	81360 ± 20840	1030	100000
0.5	3	400	130	12560 ± 2640	670	100000	1350	100000
0.5	6	100	30	210 ± 60	190	4840 ± 1280	390	19440 ± 5280
0.5	6	200	50	800 ± 240	210	19720 ± 5680	430	81960 ± 20680
0.5	6	400	50	3120 ± 880	250	81480 ± 20680	510	100000
0.5	9	100	30	90 ± 30	130	2120 ± 560	250	8440 ± 2160
0.5	9	200	30	360 ± 80	130	8600 ± 2400	270	34480 ± 9680
0.5	9	400	30	1440 ± 400	150	35440 ± 10000	310	100000

Table III

Real octopole mass ranges, with B = 7 T, r_0 = 0.275 cm, a/r_0 = 0.4, $E_{z\,0}$ = 80 eV, and q = 1, 5, and 10 |e⁻| and for r_0 = 0.1375, a/r_0 = 0.4, and q = 1 |e⁻|.

			z = 1		z = 5		z = 10		r_0 = 0.1375	
$E_{r\,0}$ (eV)	f (MHz)	V_0 (V)	min (amu)	max (amu)	min (amu)	max (amu)	min (amu)	max (amu)	min (amu)	max (amu)
2.0	1	100	890	5640 ± 320	2550	100000	4730	100000	2730	22160 ± 960
2.0	1	200	990	22160 ± 1280	3110	100000	4910	100000	3470	100000
2.0	1	400	1430	100000	3510	100000	6330	100000	4930	100000
2.0	3	100	170	640 ± 80	270-400, 450-16720[1]		490	63960 ± 3520	350	2400 ± 80
2.0	3	200	170	2560 ± 80	750	63720 ± 4000	590-720, 1470-100000		490	9920 ± 640[1]
2.0	3	400	210	10200 ± 560	790	100000	1510	100000	570	40840 ± 2560
2.0	6	100	30	180 ± 60	70	4040 ± 240	170	16080 ± 880	110	600 ± 80
2.0	6	200	70	640 ± 80	130	16080 ± 880	210	64160 ± 3600	150	2480 ± 160
2.0	6	400	70	2560 ± 80	150-240, 370-62000[1]		270-400, 450-100000[1]		190	10000 ± 720
2.0	9	100	15	45 ± 15	50	1760 ± 80	70	7160 ± 480	70	240
2.0	9	200	30	240	50	7120 ± 400	110	28520 ± 1600	70	1120 ± 80
2.0	9	400	50	1160 ± 80	130	28840 ± 1760	150	100000	90	4520 ± 240
0.5	1	100	490	22600 ± 1120	2270	100000	4450	100000	1490	100000
0.5	1	200	650	100000	2350	100000	3830	100000	1810	100000
0.5	1	400	850	100000	2470	100000	4670	100000	2470	100000
0.5	3	100	90	2520 ± 160	130	63080 ± 4160	250	100000	210	10160 ± 560
0.5	3	200	70	10080 ± 560	210	100000	290	100000	290	40560 ± 2400
0.5	3	400	150	40040 ± 2000	310-560, 730-100000[1]		470-1200, -100000[1]		310	100000
0.5	6	100	15	640 ± 80	50	16000 ± 1120	70	63920 ± 4320	70	2520 ± 160
0.5	6	200	30	2520 ± 160	70	63240 ± 4080	90	100000	90	10240 ± 640
0.5	6	400	30	10080 ± 560	70	100000	70	100000	110	40840 ± 2480
0.5	9	100	15	240	15	7120 ± 480	30	28480 ± 2160	30	868 ± 585
0.5	9	200	15	1120 ± 80	30	28280 ± 1840	30	100000	50	4320 ± 80
0.5	9	400	15	4480 ± 240	30	100000	70	100000	50	17720 ± 1120

[1]These data indicate dual stability regions. See text.

Table IV

Real quadrupole and octopole mass ranges, with B = 7 T, r_0 = 0.275 cm, either a = 0.637 cm or a/r_0 = 0.4, $E_{z\,0}$ = 80 eV, and q = 1 |e⁻|.

			Real quadrupole		Real octopole	
$E_{r\,0}$ (eV)	f (MHz)	V_0 (V)	min (amu)	max (amu)	min (amu)	max (amu)
10.0	1	100		---		---
10.0	1	200	543 ± 70	933 ± 240	2257 ± 320	2960 ± 320
10.0	1	400	815 ± 30	5360 ± 1520	3045 ± 240	17440 ± 800
10.0	3	100		---		---
10.0	3	200		---		---
10.0	3	400	130	520 ± 160	385 ± 60	1880 ± 80
10.0	6	100		---		---
10.0	6	200		---		---
10.0	6	400	50	200 ± 60	115 ± 10	520 ± 80
10.0	9	100		---		---
10.0	9	200		---		---
10.0	9	400	30	75 ± 30	65 ± 10	240
5.0	1	100		---	1270	1520
5.0	1	200	505 ± 10	1760 ± 400	1590 ± 120	8720 ± 320
5.0	1	400	805 ± 10	10720 ± 3620	2090 ± 110	36280 ± 1840
5.0	3	100		---		---
5.0	3	200	110	280 ± 80	225 ± 10	960 ± 40
5.0	3	400	130	1080 ± 80	305 ± 30	3960 ± 160
5.0	6	100		---		---
5.0	6	200		---	85 ± 10	240
5.0	6	400	50	280 ± 80	105 ± 10	1000 ± 80
5.0	9	100		---	15	30
5.0	9	200		---	50	120
5.0	9	400	30	150 ± 60	50	400

Table V

Mass range predictions, ignoring magnetic effects, with r_0 = 0.275 cm for the quadrupoles and larger octopole, r_0 = 0.1375 cm for the smaller octopole, a = 0.637 cm for the real quadrupole, $E_{z\,0}$ = 80 eV, and q = 1 |e|.

$E_{r\,0}$	f	V_0	Ideal quadrupole		Real quad.	Ideal oct.	Ideal smaller oct.
			min	max	max	max	max
(eV)	(MHz)	(V)	(amu)	(amu)	(amu)	(amu)	(amu)
2.0	1	100	142	1616	1287	6463	25854
2.0	1	200	285	6463	5147	25854	100000
2.0	1	400	569	25854	20589	100000	100000
2.0	3	100	16	180	143	718	2873
2.0	3	200	32	718	572	2873	11491
2.0	3	400	63	2873	2288	11491	45962
2.0	6	100	4	45	36	180	718
2.0	6	200	8	180	143	718	2873
2.0	6	400	16	718	572	2873	11491
2.0	9	100	2	20	16	80	319
2.0	9	200	4	80	64	319	1277
2.0	9	400	7	319	254	1277	5107
0.5	1	100	142	6463	5147	25854	100000
0.5	1	200	285	25854	20589	100000	100000
0.5	1	400	569	100000	82356	100000	100000
0.5	3	100	16	718	572	2873	11491
0.5	3	200	32	2873	2288	11491	45962
0.5	3	400	63	11491	9151	45962	100000
0.5	6	100	4	180	143	718	2873
0.5	6	200	8	718	572	2873	11491
0.5	6	400	16	2873	2288	11491	45962
0.5	9	100	2	80	64	319	1277
0.5	9	200	4	319	254	1277	5107
0.5	9	400	7	1277	1017	5107	20428

Table VI

Mass range predictions, ignoring magnetic effects, with r_0 = 0.275 cm for the quadrupoles and larger octopole, r_0 = 0.1375 cm for the smaller octopole, a = 0.637 cm for the real quadrupole, $E_{z\,0}$ = 80 eV, and q = 5 |e|.

$E_{r\,0}$	f	V_0	Ideal quadrupole		Real quad.	Ideal oct.	Ideal smaller oct.
			min	max	max	max	max
(eV)	(MHz)	(V)	(amu)	(amu)	(amu)	(amu)	(amu)
2.0	1	100	712	40396	32170	100000	100000
2.0	1	200	1424	100000	100000	100000	100000
2.0	1	400	2847	100000	100000	100000	100000
2.0	3	100	79	4488	3574	17954	71816
2.0	3	200	158	17954	14298	71816	100000
2.0	3	400	316	71816	57192	100000	100000
2.0	6	100	20	1122	894	4488	17954
2.0	6	200	40	4488	3574	17954	71816
2.0	6	400	79	17954	14298	71816	100000
2.0	9	100	9	499	397	1995	7980
2.0	9	200	18	1995	1589	7980	31918
2.0	9	400	35	7980	6355	31918	100000
0.5	1	100	712	100000	100000	100000	100000
0.5	1	200	1424	100000	100000	100000	100000
0.5	1	400	2847	100000	100000	100000	100000
0.5	3	100	79	17954	14298	71816	100000
0.5	3	200	158	71816	57192	100000	100000
0.5	3	400	316	100000	100000	100000	100000
0.5	6	100	20	4488	3574	17954	71816
0.5	6	200	40	17954	14298	71816	100000
0.5	6	400	79	71816	57192	100000	100000
0.5	9	100	9	1995	1589	7980	31918
0.5	9	200	18	7980	6355	31918	100000
0.5	9	400	35	31918	25418	100000	100000

Table VII

Mass range predictions, ignoring magnetic effects, with r_0 = 0.275 cm for the quadrupoles and larger octopole, r_0 = 0.1375 cm for the smaller octopole, a = 0.637 cm for the real quadrupole, $E_{z\,0}$ = 80 eV, and q = 10 $|e^-|$.

$E_{r\,0}$ (eV)	f (MHz)	V_0 (V)	Ideal quadrupole min (amu)	Ideal quadrupole max (amu)	Real quad. max (amu)	Ideal oct. max (amu)	Ideal smaller oct. max (amu)
2.0	1	100	1424	100000	100000	100000	100000
2.0	1	200	2847	100000	100000	100000	100000
2.0	1	400	5694	100000	100000	100000	100000
2.0	3	100	158	17954	14298	71816	100000
2.0	3	200	316	71816	57192	100000	100000
2.0	3	400	633	100000	100000	100000	100000
2.0	6	100	40	4488	3574	17954	71816
2.0	6	200	79	17954	14298	71816	100000
2.0	6	400	158	71816	57192	100000	100000
2.0	9	100	18	1995	1589	7980	31918
2.0	9	200	35	7980	6355	31918	100000
2.0	9	400	70	31918	25418	100000	100000
0.5	1	100	1424	100000	100000	100000	100000
0.5	1	200	2847	100000	100000	100000	100000
0.5	1	400	5694	100000	100000	100000	100000
0.5	3	100	158	71816	57192	100000	100000
0.5	3	200	316	100000	100000	100000	100000
0.5	3	400	633	100000	100000	100000	100000
0.5	6	100	40	17954	14298	71816	100000
0.5	6	200	79	71816	57192	100000	100000
0.5	6	400	158	100000	100000	100000	100000
0.5	9	100	18	7980	6355	31918	100000

FIGURES

Figure 1. (a) Schematic view of experimental apparatus for which our calculations are intended. (b) Axial B-field, a solenoidal field fit to data, Eq. (11). (c) Radial B-field, Eq. (10). The radial field is plotted at r = 0.275 cm (dashed line) and r = 1.0 cm (solid line).

Figure 2. Illustrated are octopole electrostatic potentials and effective potentials, all for r_0 = 0.275. The contour lines range from -1.0 to 1.0 in steps of 0.1, with the long dashed lines indicating negative levels; the short dashed, zero; and the solid, positive. The effective potential is plotted from r = $-r_0$ to r_0 for values of θ between 0 and $\pi/8$. (a) Ideal octopole electrostatic potential, with the corresponding (b) axially symmetric effective potential. (c) Ervin's Legendre polynomial fit to a numerical solution of Laplace's equation for a/r_0 = 0.4, with the corresponding (d) effective potential. [8]

Figure 3. Image charge octopole electrostatic and effective potentials, r_0 = 0.275, are illustrated. (a) Real octopole electrostatic potential for a/r_0 = 0.4, with the corresponding (b) effective potential. (c) Real octopole electrostatic potential for a/r_0 = 0.1, with the corresponding (d) effective potential. Note that for the smaller rods, the real octopole effective potential is no longer θ independent. Note also that these octopoles are essentially in a cylindrical, grounded housing of radius $1.5(r_0 + a)$.

Figure 4. Illustrated are quadrupole electrostatic and effective potentials for

r_0 = 0.275. The effective potential is plotted from r = $-r_0$ to r_0 for values of θ between 0 and $\pi/4$. (a) Ideal electrostatic potential. (b) Effective potential. (c) Image charge electrostatic potential. (d) Effective potential for the a = 0.637 quadrupole used by McIver. [9]

Figure 5. A typical, low-mass injection trajectory though an ideal quadrupole.

Figure 6. An ideal quadrupole injection trajectory with the same m/z as Figure 5 but with a higher mass. Note that an ideal effective potential analysis correctly predicts the off-axis excursions will be reduced in this Figure even though m/z is kept constant. (Fundamentally, V_0 is different in Eq. (12).)

Figure 7. An ideal quadrupole injection trajectory with the same m/z as Figure 5 but with a four-times lower $E_{r\ 0}$. An ideal effective potential analysis correctly predicts the off-axis excursions will be a factor of two smaller than those in Figure 5.

Figure 8. An ion with $E_{z\ 0}$ just 2.0 eV is successfully injected through an ideal quadrupole.

Figure 9. An ideal quadrupole injection trajectory with the same parameters as Figure 6 except for a four-times greater mass. An ideal effective potential analysis correctly predicts the off-axis excursions will be a factor of two larger than those in Figure 6.

Figure 10. A low-mass injection trajectory though a real quadrupole. The θ dependent effective potential has caused the ion to start spinning even before B_z is significant.

Figure 11. An odd low-mass injection trajectory though a real quadrupole. The θ dependent effective potential has caused the ion to start spinning in the direction of the eventual magnetron motion even before it has encountered a significant B_z.

Figure 12. An odd low-mass injection trajectory though a real quadrupole. The θ dependent effective potential has caused the ion to start spinning in the opposite direction of the magnetron motion before it has encountered a significant B_z. The E_z trace shows this to be an example of the anti-magnetic mirror effect.

Figure 13. A real quadrupole injection trajectory with the same parameters as Figure 10 except for a four-times greater mass. An ideal effective potential analysis correctly predicts the off-axis excursions will be reduced from Figure 10. Note again the anti-magnetic mirror effect.

Figure 14. A typical, low-mass injection trajectory though a real octopole. Note that $E_r(z)$ experiences large oscillations only at the radial ion turning points.

Figure 15. A real octopole injection trajectory with the same m/z as Figure 14 but with a higher mass. Note that an ideal effective potential analysis correctly predicts the off-

axis excursions will be reduced in this Figure even though m/z is kept constant.

Figure 16. A real octopole injection trajectory with the same m/z as Figure 14 but with a higher octopole voltage. An ideal effective potential analysis correctly predicts the off-axis excursions will be reduced.

Figure 17. A real octopole injection trajectory with the same m/z as Figure 14 but with a four-times lower $E_{r\ 0}$. An ideal effective potential analysis correctly predicts the off-axis excursions will be a factor of $2^{1/3}$ smaller than those in Figure 14.

Figure 18. An ion with $E_{z\ 0}$ just 2.0 eV is successfully injected through a real octopole. The finial axial energy is lower that that of the ion in the ideal quadrupole in Figure 8, which is similar to that in a real quadrupole.

(a)

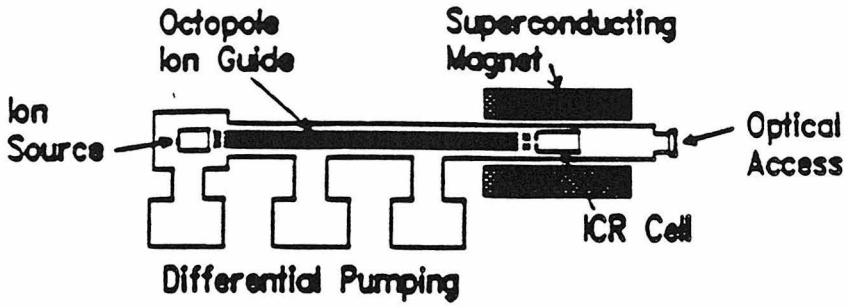
Octopole
Ion Guide
Superconducting
Magnet
Ion
Source
Optical
Access
ICR Cell
Differential Pumping

(b)

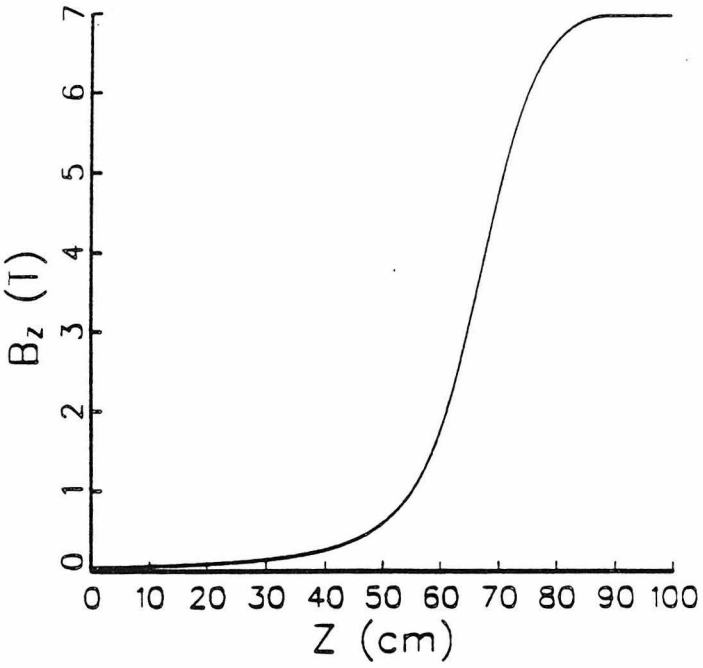
B_z (T)
0
1
2
3
4
5
6
7
0 10 20 30 40 50 60 70 80 90 100
Z (cm)

(c)

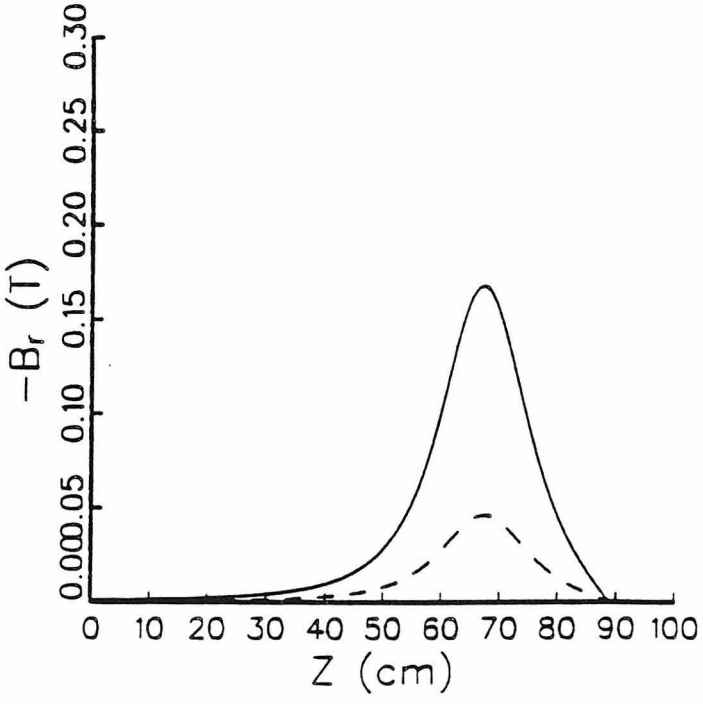
$-B_r$ (T)
0.00
0.05
0.10
0.15
0.20
0.25
0.30
0 10 20 30 40 50 60 70 80 90 100
Z (cm)

Figure 1

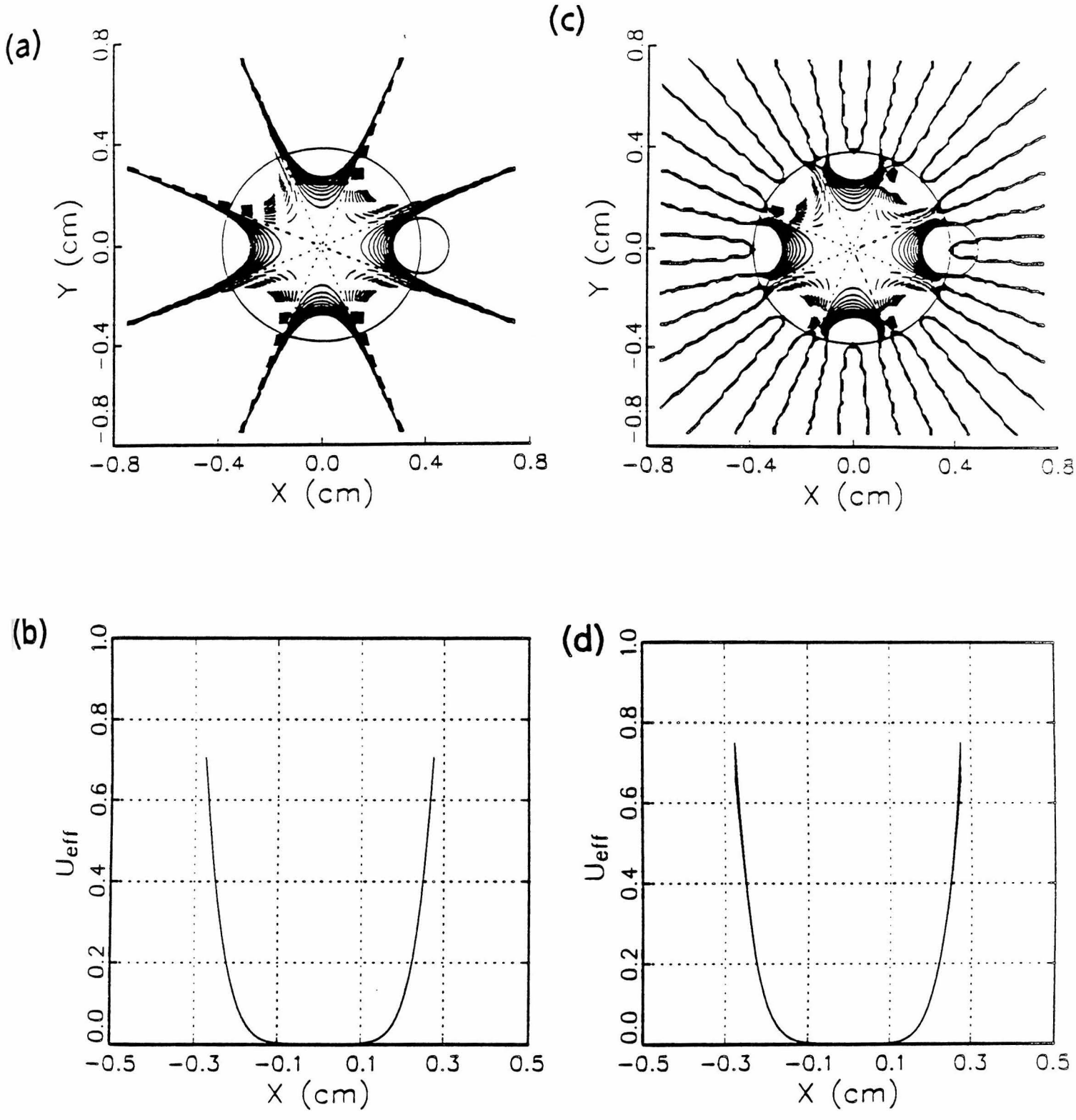

Figure 2

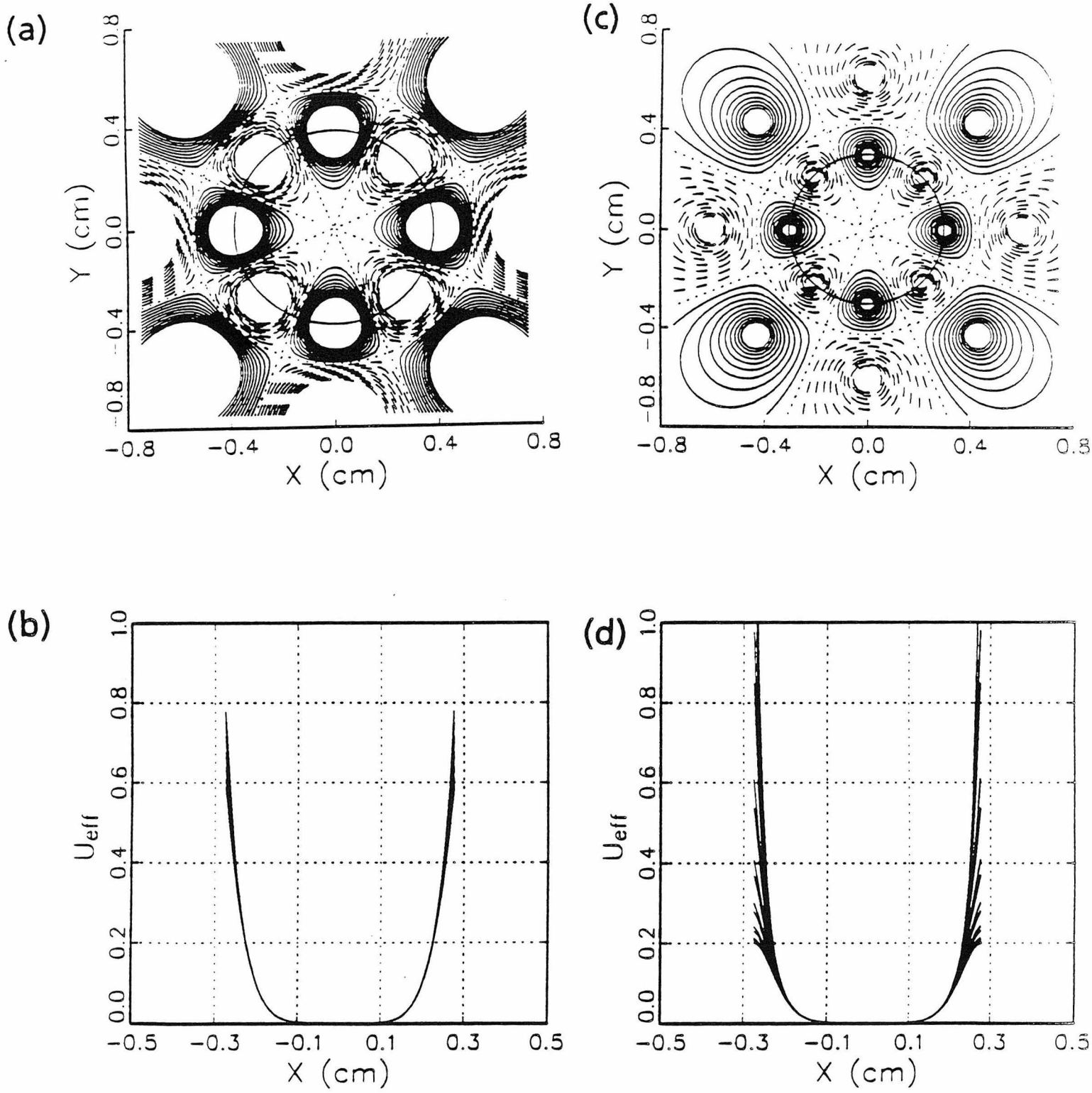

Figure 3

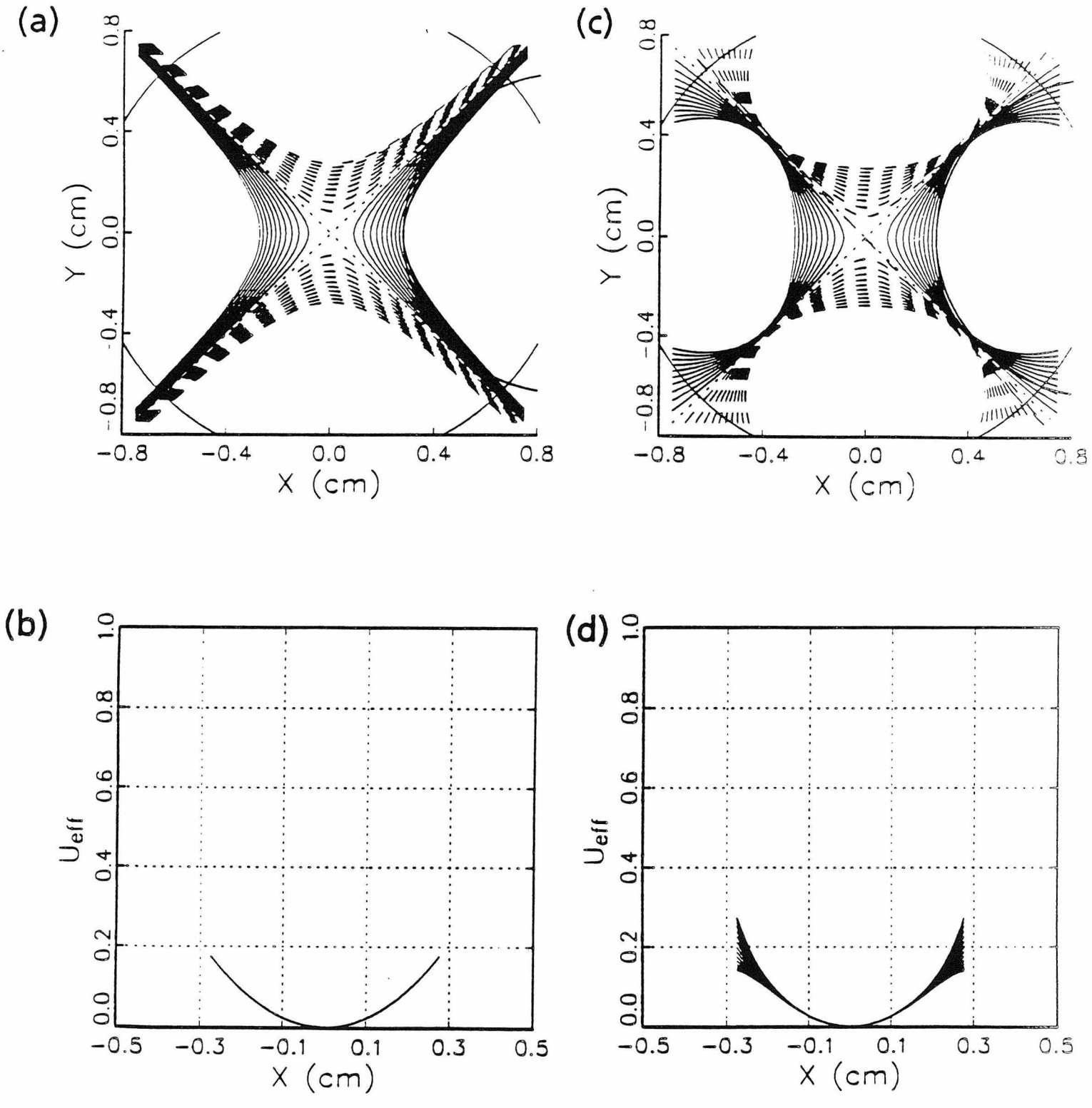

Figure 4

Ideal Quadrupole
z = 1 e
m = 1000 amu
f = 1 MHz
V_0 = 100 V
r_0 = 0.275 cm
$E_{r\,0}$ = 2 eV
$E_{z\,0}$ = 80 eV

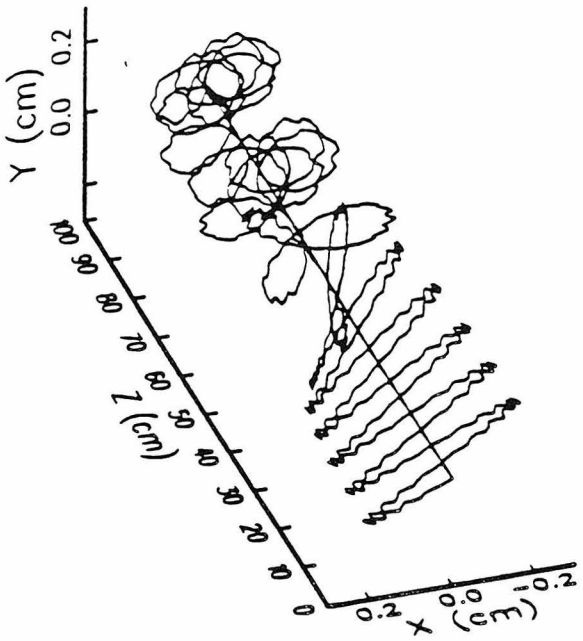

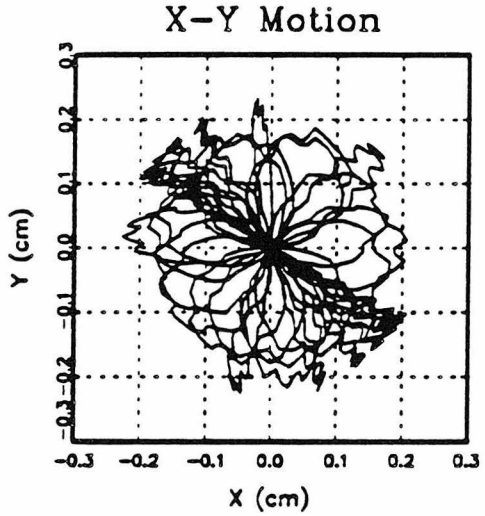

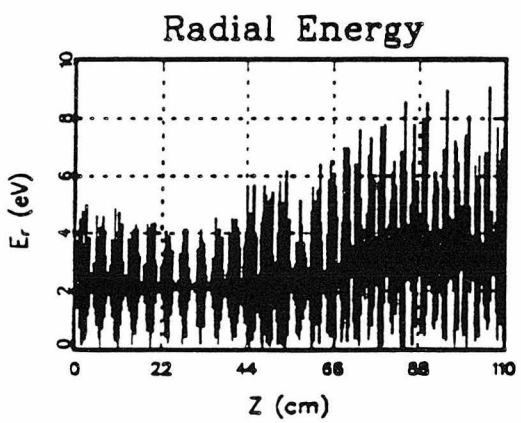

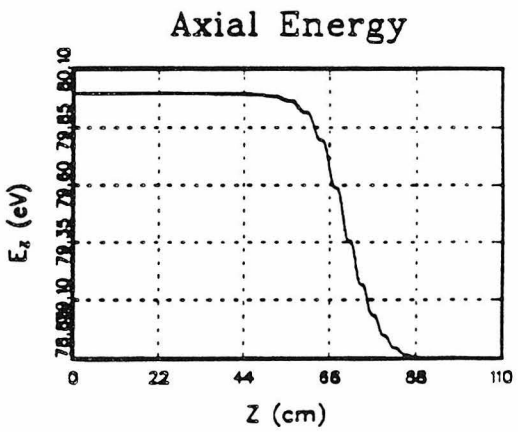

Figure 5

Ideal Quadrupole
z = 10 e
m = 10000 amu
f = 1 MHz
V_0 = 100 V
r_0 = 0.275 cm
$E_{r\,0}$ = 2 eV
$E_{z\,0}$ = 80 eV

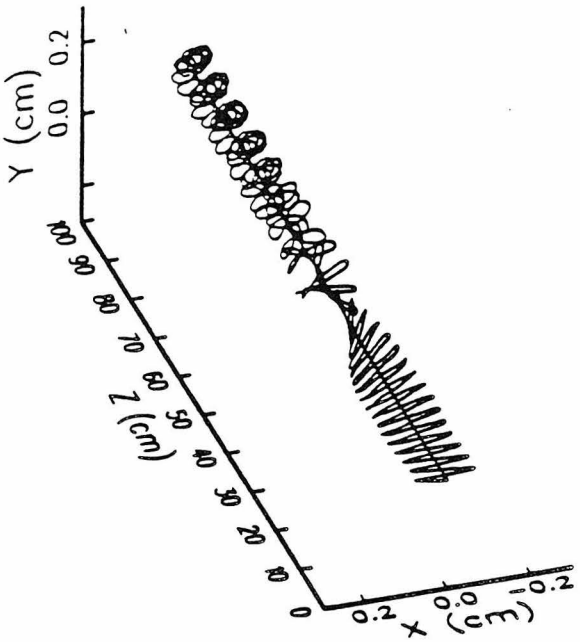

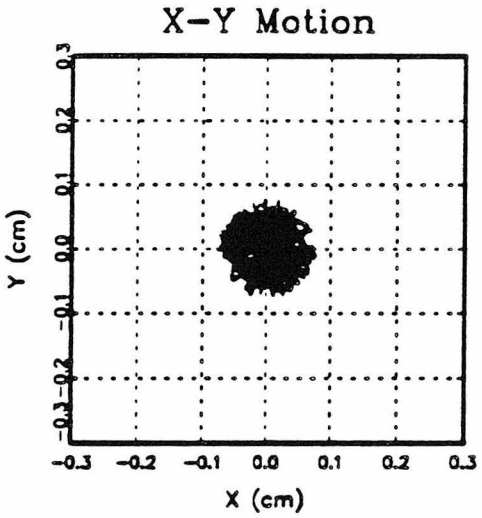

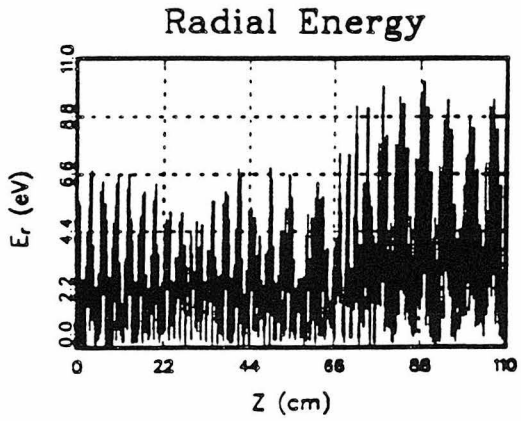

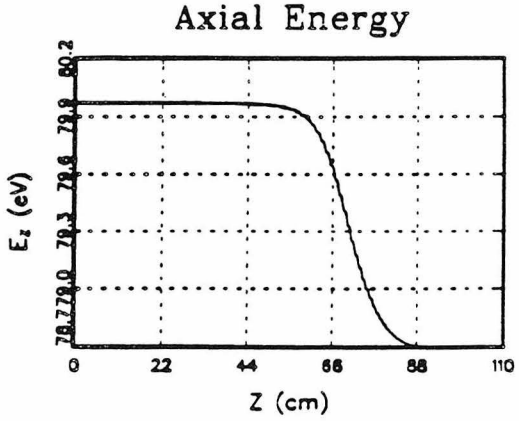

Figure 6

Ideal Quadrupole
z = 1 e
m = 1000 amu
f = 1 MHz
V_0 = 100 V
r_0 = 0.275 cm
$E_{r\,0}$ = 0.5 eV
$E_{z\,0}$ = 80 eV

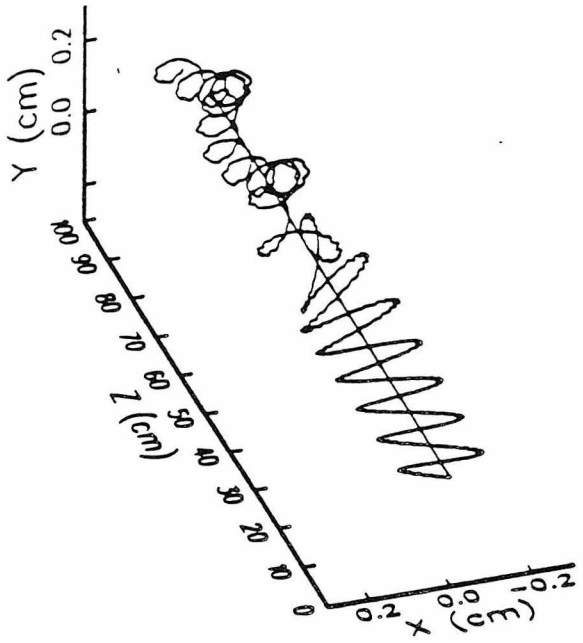

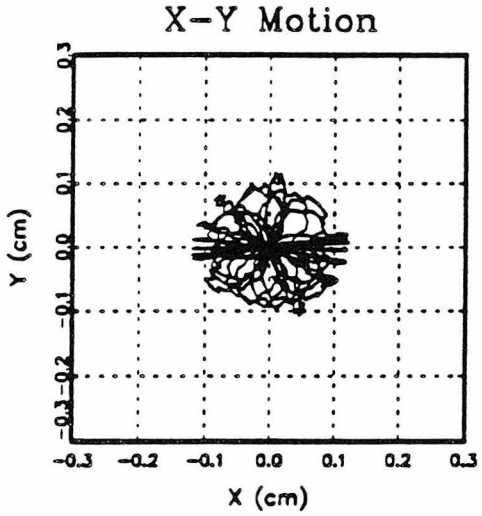

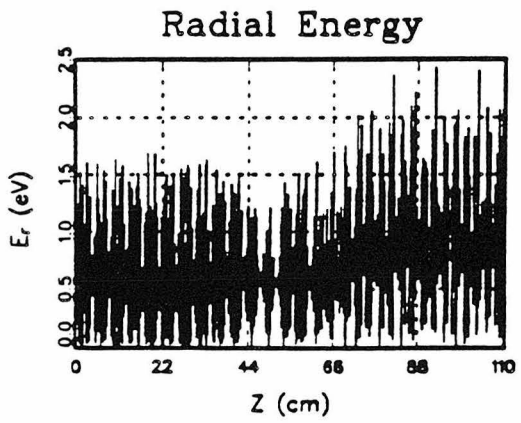

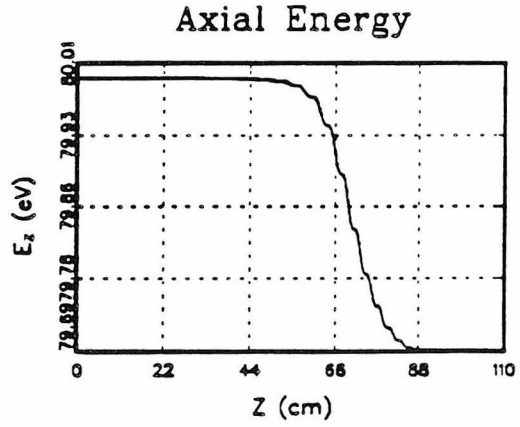

Figure ~~8~~ 7

Ideal Quadrupole
z = 1 e
m = 100 amu
f = 9 MHz
V_0 = 200 V
r_0 = 0.275 cm
$E_{r\,0}$ = 0.25 eV
$E_{z\,0}$ = 2 eV

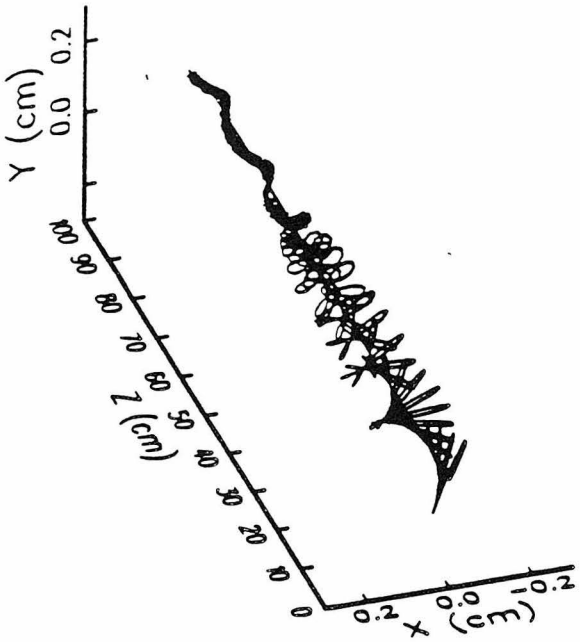

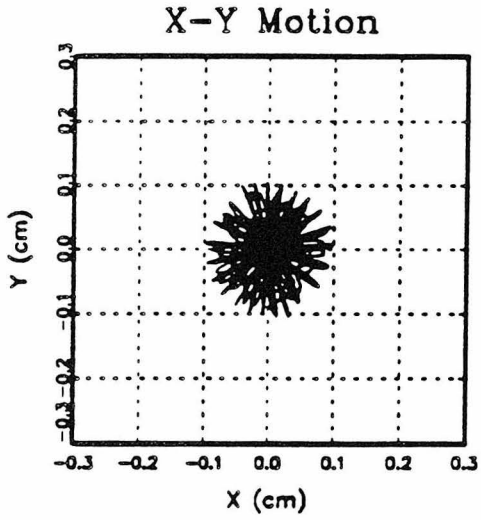

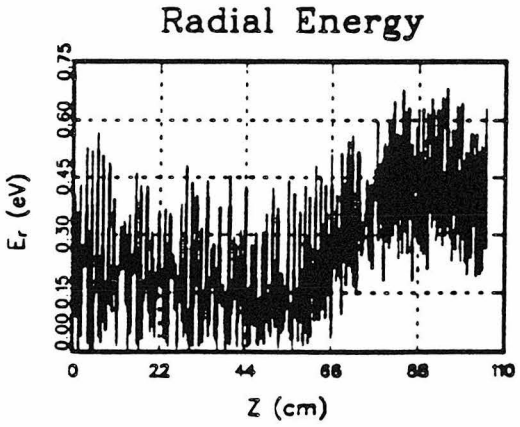

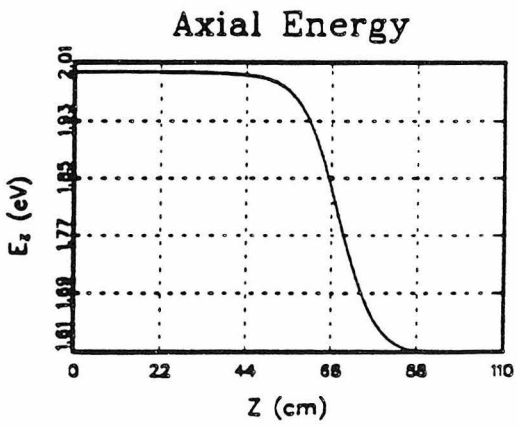

Figure ~~9~~ 8

Ideal Quadrupole
z = 10 e
m = 40000 amu
f = 1 MHz
v_0 = 100 V
r_0 = 0.275 cm
$E_{r\,0}$ = 2 eV
$E_{z\,0}$ = 80 eV

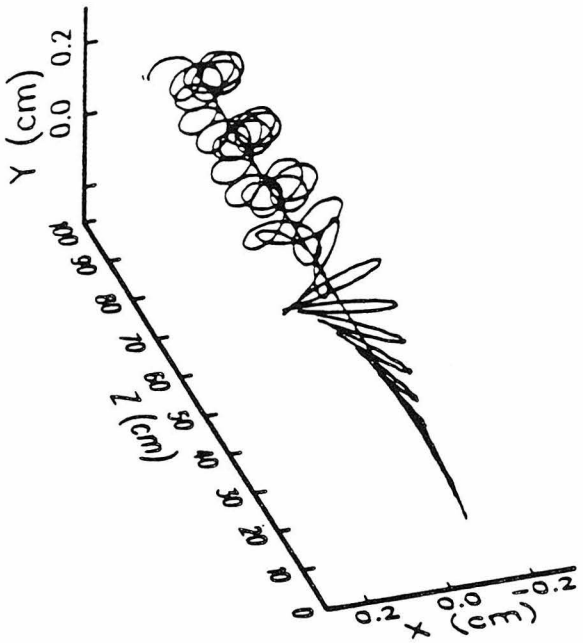

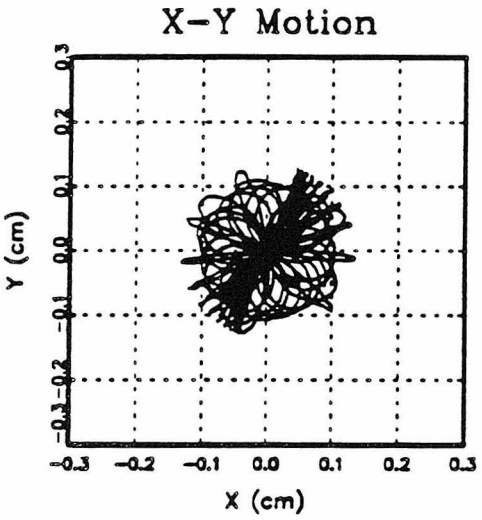

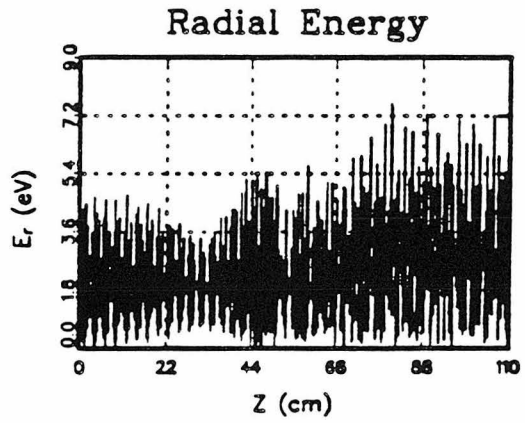

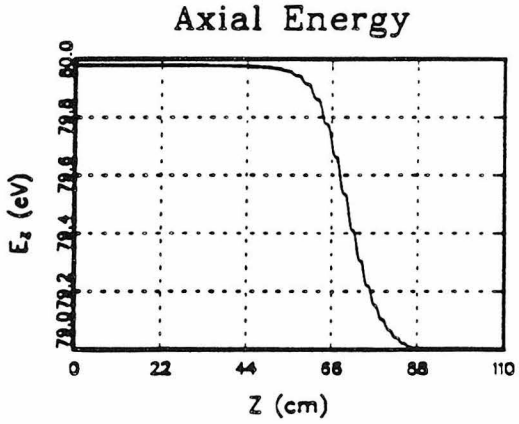

Figure ~~10~~ 9

Real Quadrupole
z = 1 e
m = 1000 amu
f = 1 MHz
V_0 = 100 V
r_0 = 0.275 cm
a_0 = 0.637 cm
$E_{r\,0}$ = 2 eV
$E_{z\,0}$ = 80 eV

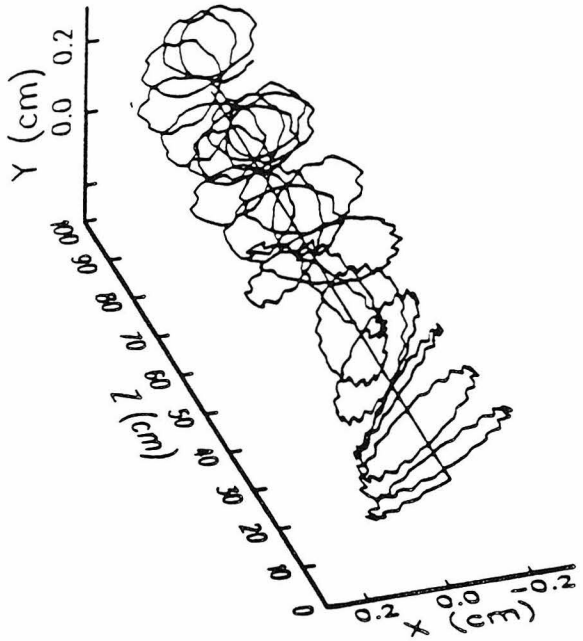

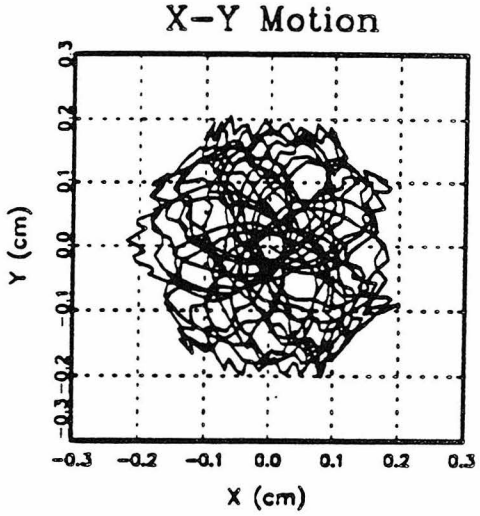

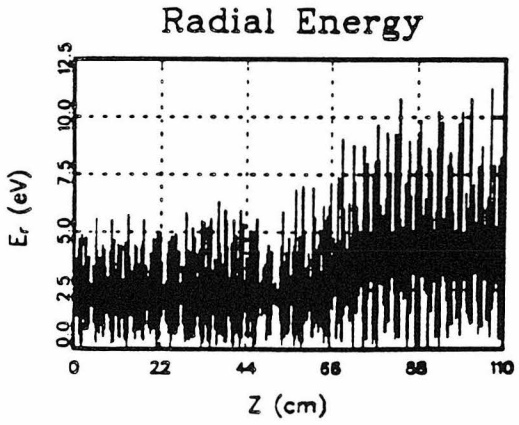

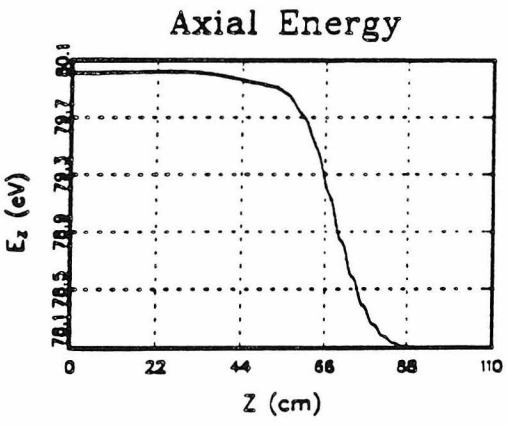

Figure ~~11~~ 10

Real Quadrupole
$z = 1\ e$
$m = 1000$ amu
$f = 1$ MHz
$v_0 = 100$ V
$r_0 = 0.275$ cm
$a_0 = 0.637$ cm
$E_{r\,0} = 2$ eV
$E_{z\,0} = 80$ eV

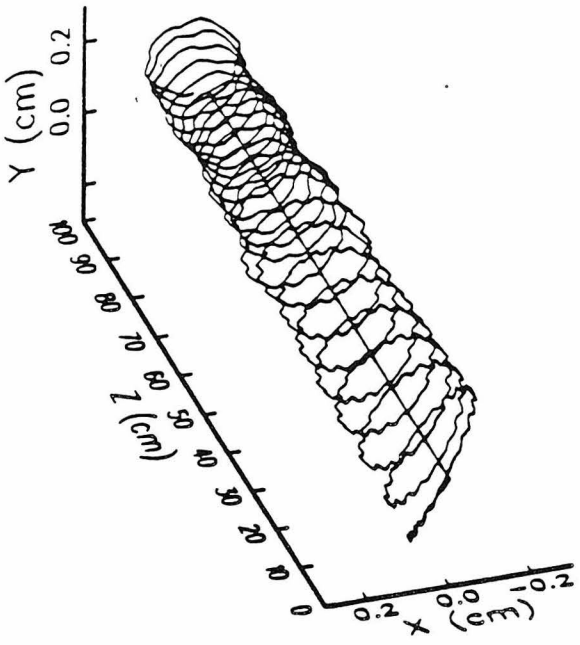

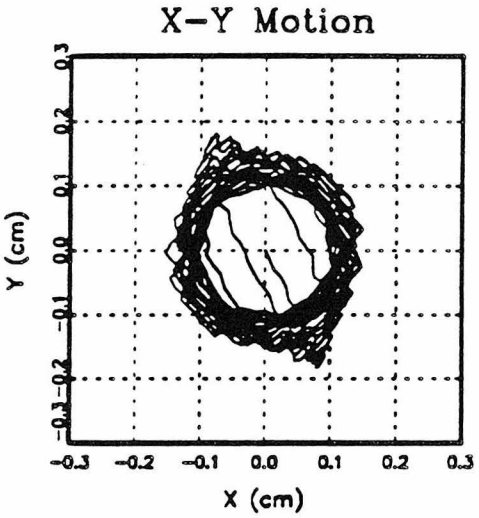

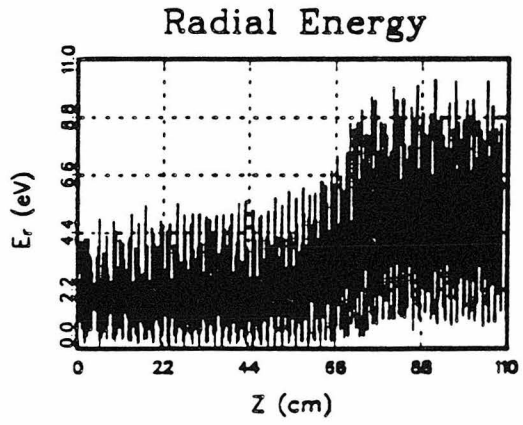

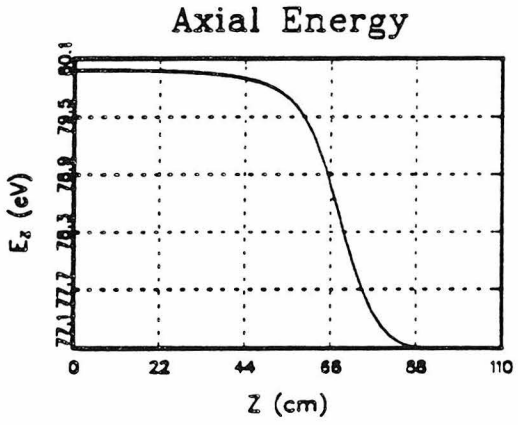

Figure ~~12~~ 11

Real Quadrupole
z = 1 e
m = 1000 amu
f = 1 MHz
v_0 = 100 V
r_0 = 0.275 cm
a_0 = 0.637 cm
$E_{r\,0}$ = 2 eV
$E_{z\,0}$ = 80 eV

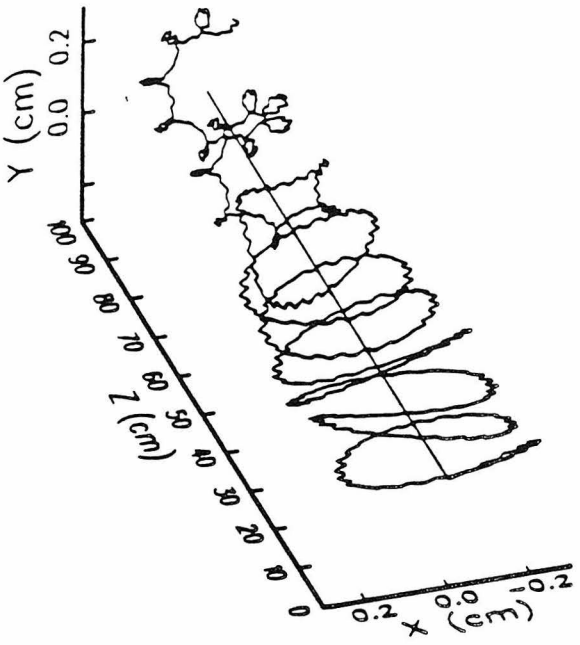

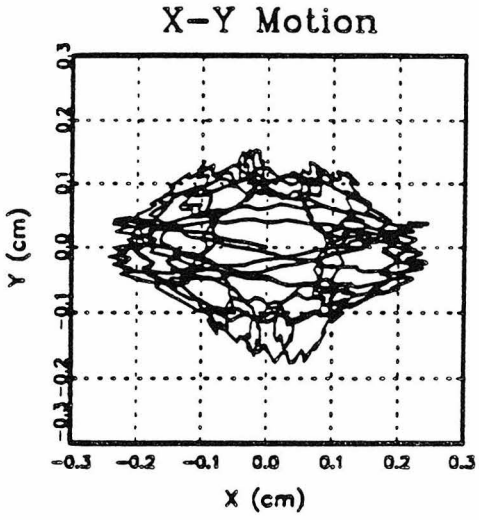

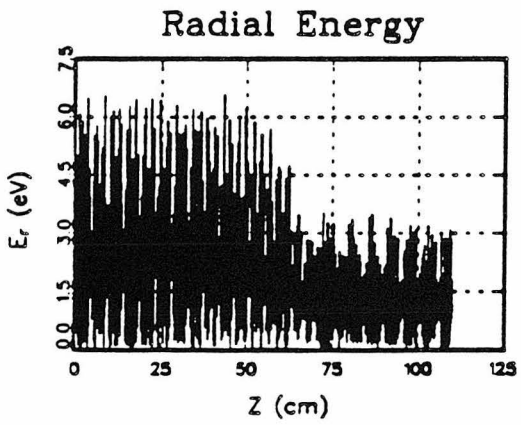

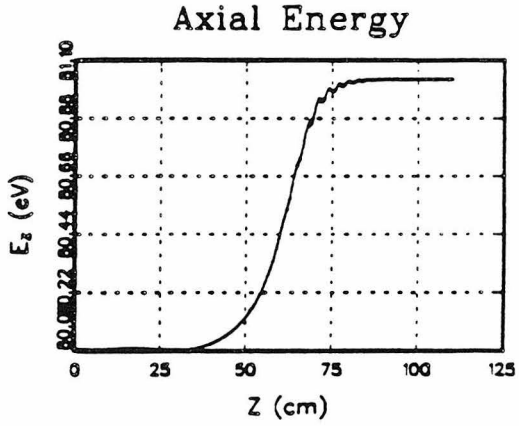

Figure ~~13~~ 12

Real Quadrupole
z = 10 e
m = 40000 amu
f = 1 MHz
v_0 = 100 V
r_0 = 0.275 cm
a_0 = 0.637 cm
$E_{r\,0}$ = 2 eV
$E_{z\,0}$ = 80 eV

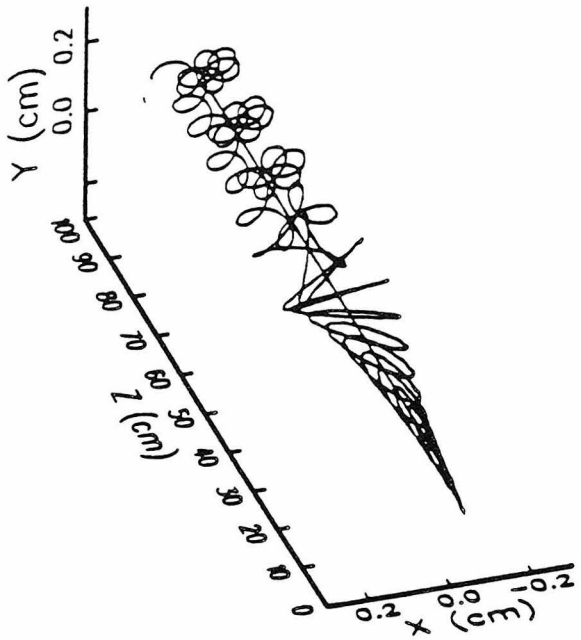

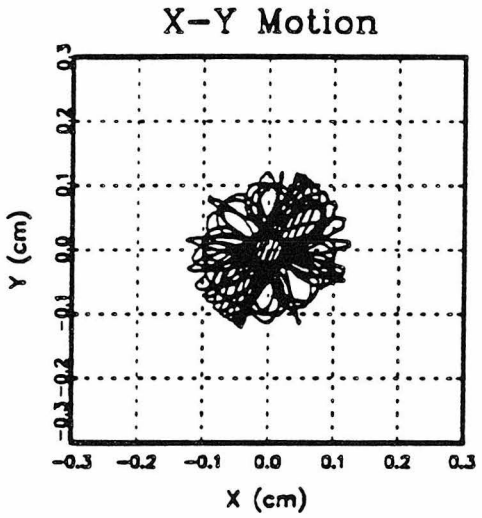

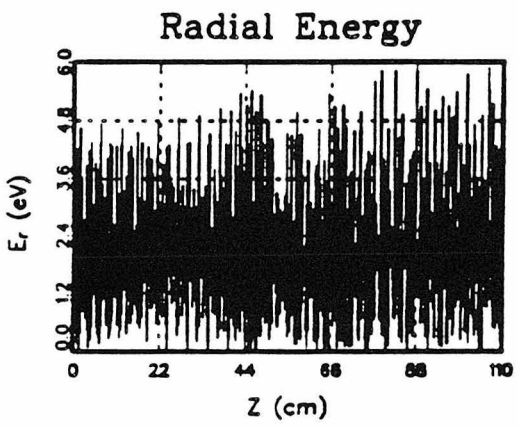

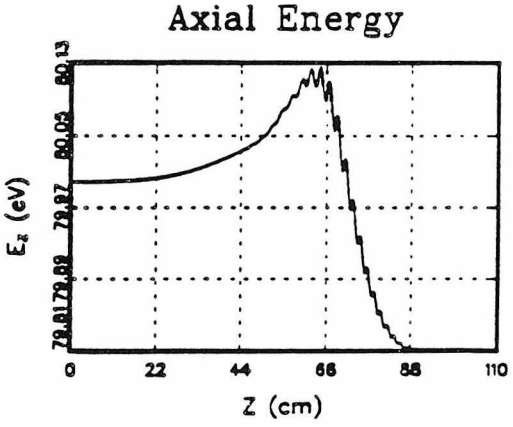

Figure ~~18~~ 13

Real Octopole
z = 1 e
m = 1000 amu
f = 1 MHz
v_0 = 100 V
r_0 = 0.275 cm
a_0 = 0.110 cm
$E_{r\,0}$ = 2 eV
$E_{z\,0}$ = 80 eV

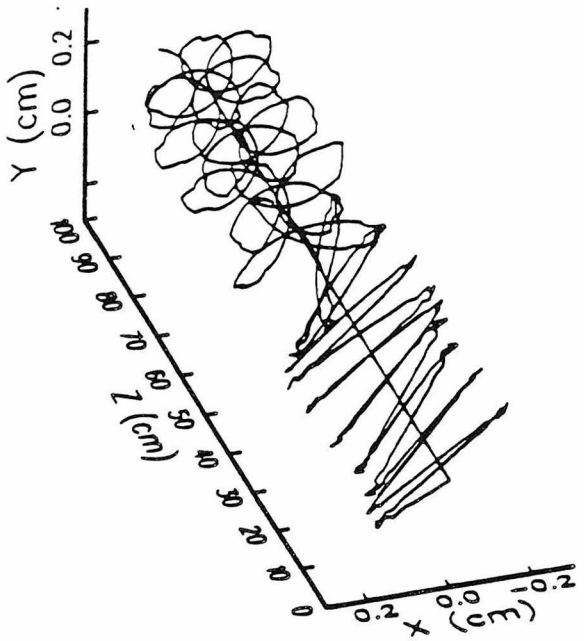

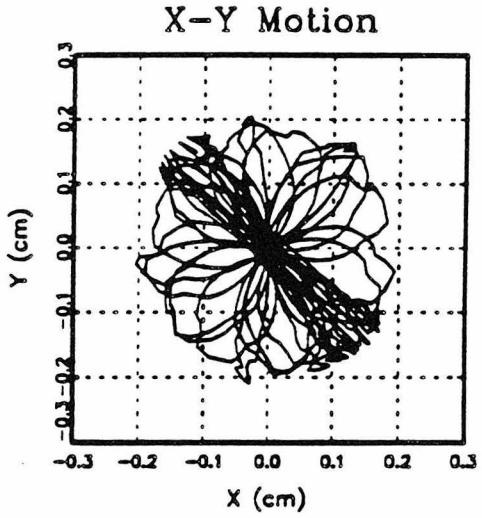

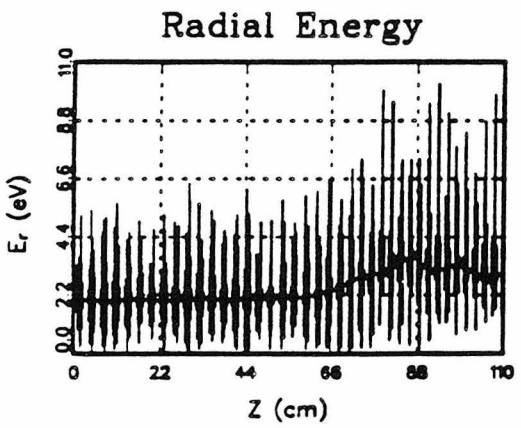

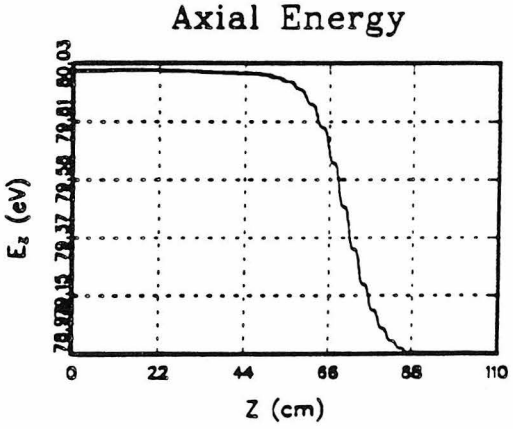

Figure ~~13~~ 14

Real Octopole
z = 10 e
m = 10000 amu
f = 1 MHz
v_0 = 100 V
r_0 = 0.275 cm
a_0 = 0.110 cm
$E_{r\,0}$ = 2 eV
$E_{z\,0}$ = 80 eV

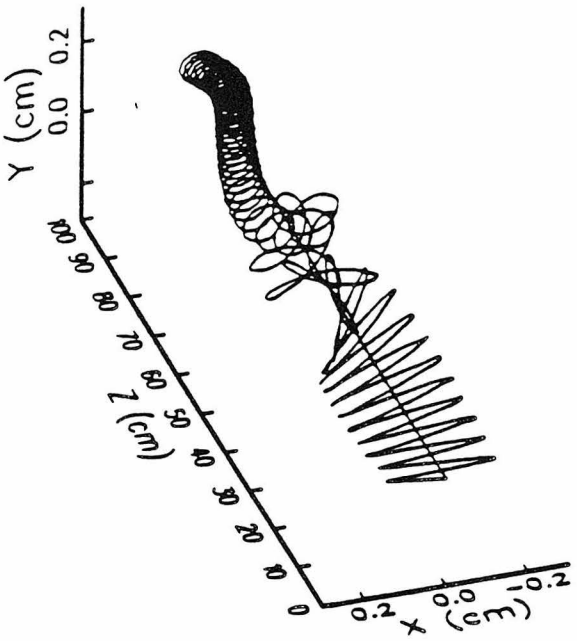

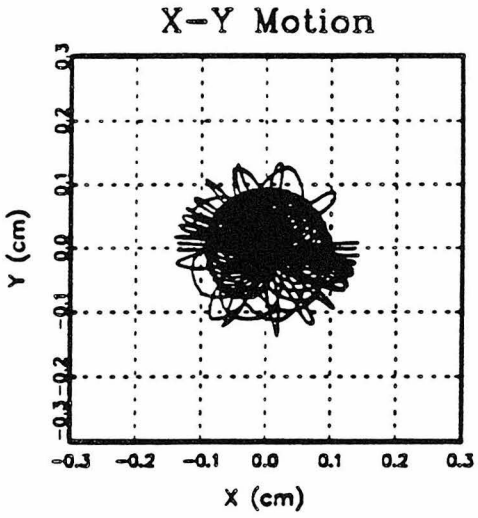

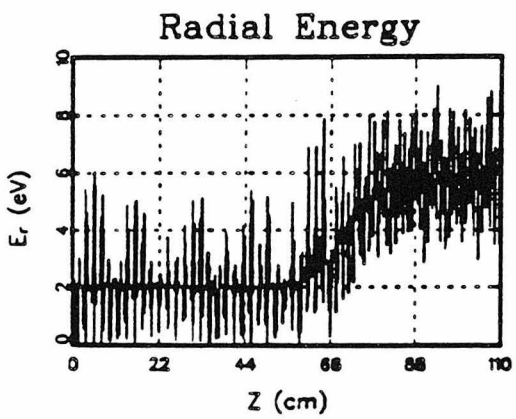

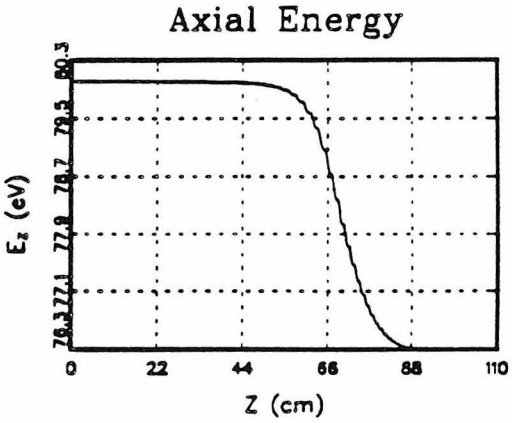

Figure ~~20~~ 15

Real Octopole
z = 10 e
m = 10000 amu
f = 1 MHz
v_0 = 300 V
r_0 = 0.275 cm
a_0 = 0.110 cm
$E_{r\,0}$ = 2 eV
$E_{z\,0}$ = 80 eV

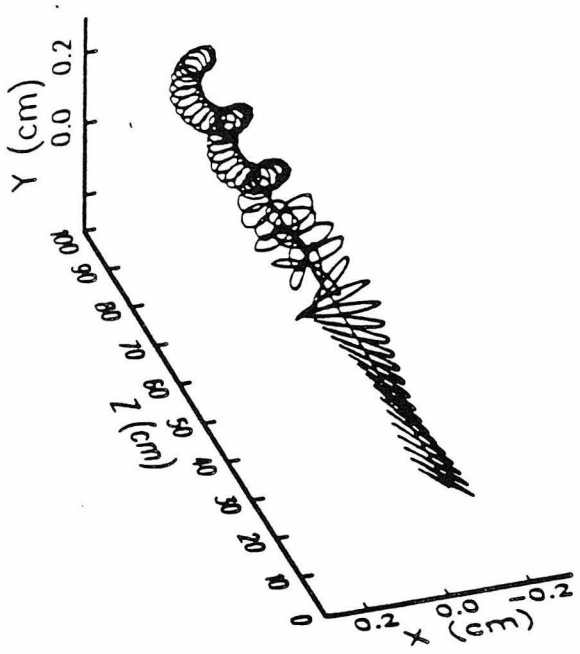

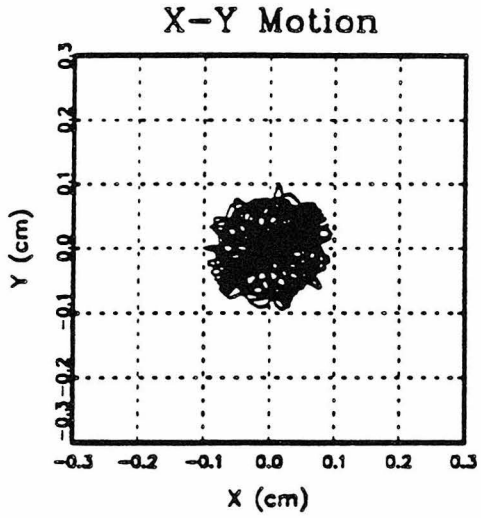

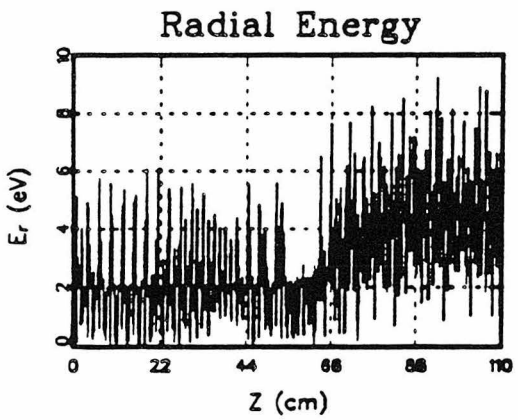

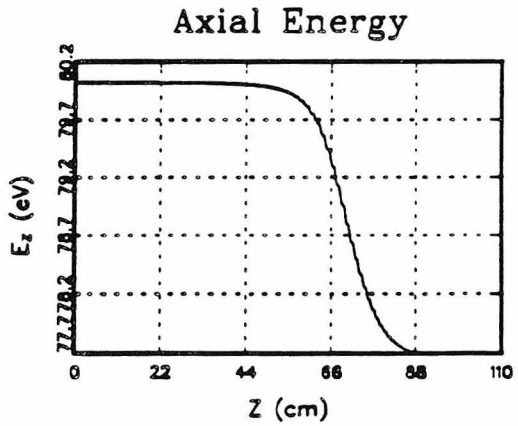

Figure ~~21~~ 16

Real Octopole
z = 1 e
m = 1000 amu
f = 1 MHz
v_0 = 100 V
r_0 = 0.275 cm
a_0 = 0.110 cm
$E_{r\,0}$ = 0.5 eV
$E_{z\,0}$ = 80 eV

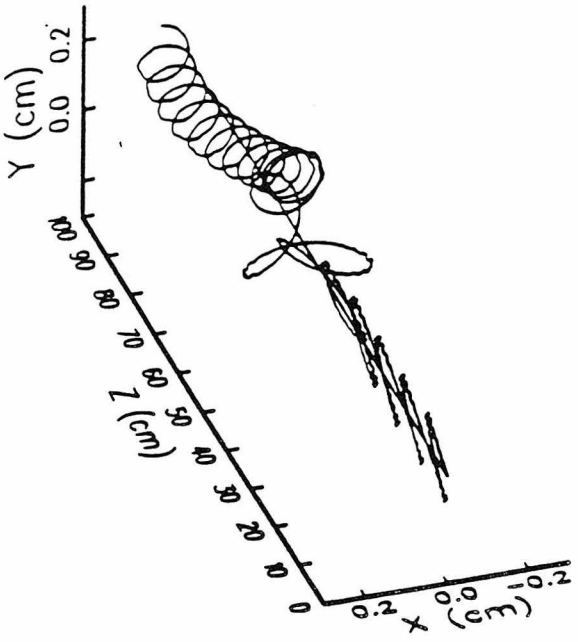

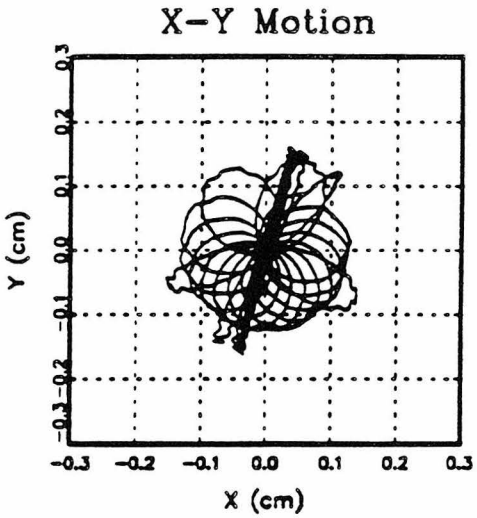

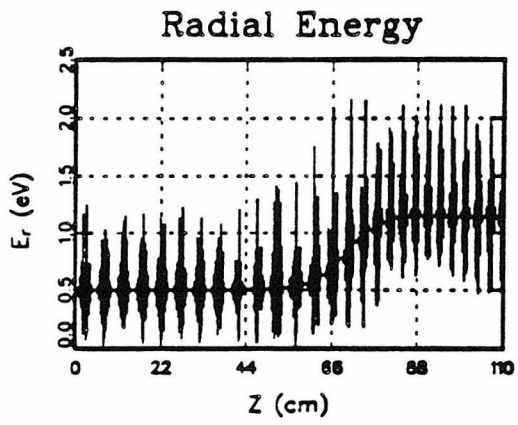

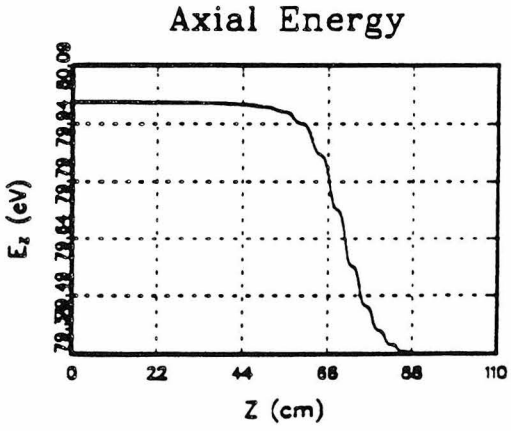

Figure ~~22~~ 17

Real Octopole
z = 1 e
m = 100 amu
f = 9 MHz
v_0 = 200 V
r_0 = 0.275 cm
a_0 = 0.110 cm
$E_{r\,0}$ = 0.25 eV
$E_{z\,0}$ = 2 eV

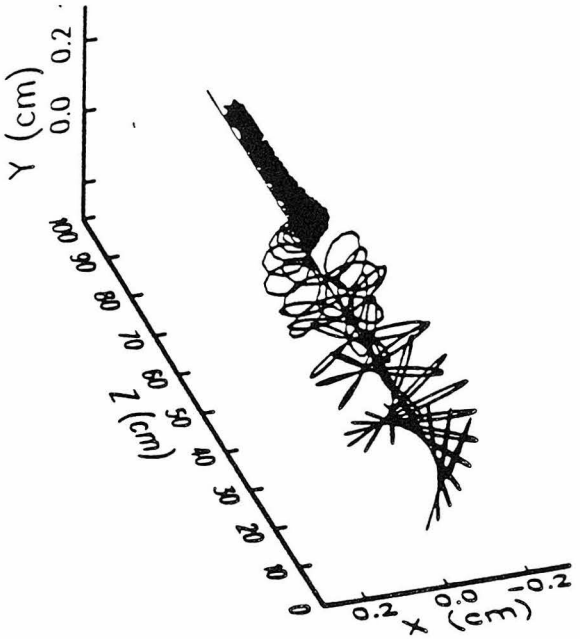

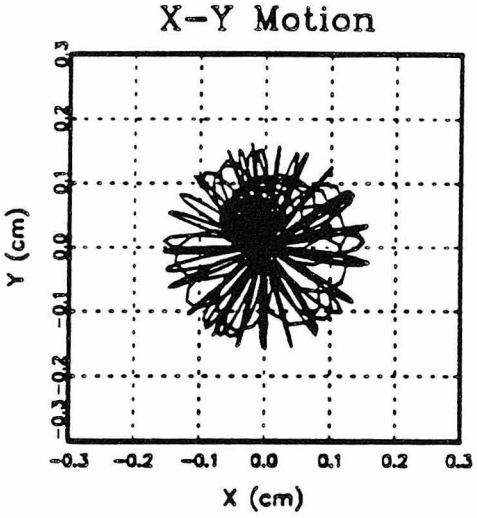

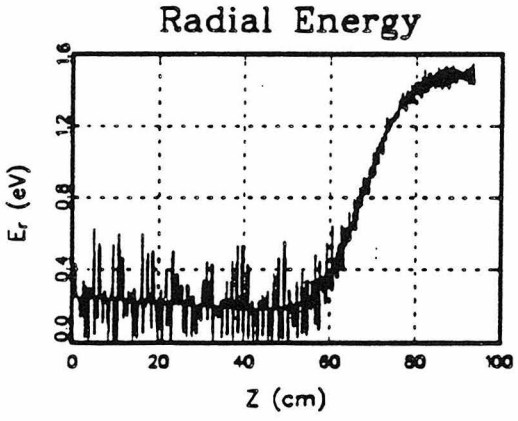

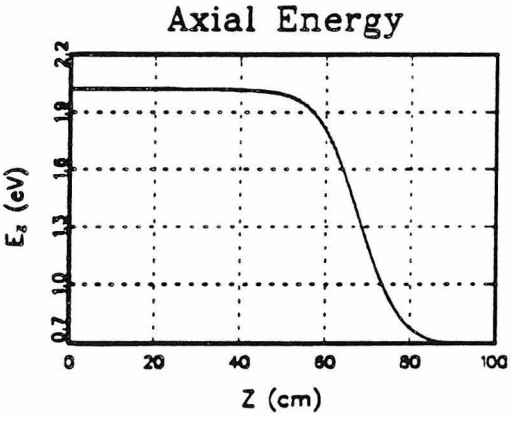

Figure ~~23~~ 18

CHAPTER II

A Fundamental Mass Resolution Limit of The Conventional FT-ICR Cubic Cell

M. W. Deem and J. L. Beauchamp

Contribution No. 8193 from the Arthur Amos Noyes Laboratory

California Institute of Technology, Pasadena, CA 91125

To appear in Int. J. Mass Spectrom. Ion Proc. (1991)

ABSTRACT

A detailed analysis of ion motion in a cubic FT-ICR cell reveals dephasing effects of the z-axis (magnetic field direction) oscillations that limit the maximum resolution that can be achieved. With typical ranges of operating conditions using a 1 inch cubic cell in a 7 Tesla field, unit mass resolution is lost in the range between 10^3 and 10^4 amu, and peaks may be up to 20 amu in width at the upper end of this range. The finite transient length is due to the coupling between the effective radial force on the ion and the z-axis motion and to a lesser extent, on the instantaneous center of the cyclotron orbit. Operating conditions that minimize the amplitude of the z-axis oscillations and cell designs that incorporate more homogeneous electric fields serve to increase the coherence time and provide higher ultimate resolution.

INTRODUCTION

Fourier transform ion cyclotron resonance (FT-ICR) spectroscopy is a widely used experimental technique for ion detection and precise mass measurement. It has recently become apparent, however, that the mass resolution achieved with conventional FT-ICR cell designs for singly-charged, high mass species can be disappointing. The utility of the technique becomes severely limited when the resolution ($m/\Delta m$) decreases below 10^{-3}, which usually occurs in the mass range 10^3 - 10^4 amu.[1] Analysis of degradation resulting from effects of a finite observation period and the use of a discrete rather than continuous Fourier transform is straightforward. A detection scheme that samples at a constant fraction of the maximum cyclotron period of interest, for example, results in peak broadening at high mass, for the total number of data points collected in a given time decrease with decreased sampling rate.

Although there have been many studies of ion motion in FT-ICR experiments, relatively little attention has been given to the effects of nonuniform fields, i.e. the proper solution to the field equations, during observation. We show here that the nonuniform static fields in a conventional cubic FT-ICR cell cause ion dephasing that limits the maximum signal transient duration. We argue that the mass enters as the ratio of mass to charge and that the maximum coherence time is approximately inversely proportional to the trapping voltage.

THEORY

Electric fields. A typical FT-ICR trap, upon which our calculations will be based, is illustrated in Figure 1. This ion trap is of the differential excitation/detection type.[2] Both excitation and trapping electric fields occur within the trap. The electrostatic trapping field must satisfy Laplace's equation. The excitation field can be found by multiplying an electrostatic solution of Laplace's equation by the desired oscillating factor if the resulting ion motion is nonrelativistic.[3] The geometry of a cubic trap is a separable one, and the solutions to Laplace's equation can, therefore, be directly and exactly found. The linearity of Laplace's equation and the partial homogeneity of the boundary conditions allow the field due to the trapping to be found and then superimposed on the field due to the excitation. The solution to the equation for a general, two-active-plates field

$$\nabla^2 \phi(x,y,z) = 0, \qquad \begin{aligned} \phi(x=0,y,z) &= \phi(x=L_x,y,z) = 0 \\ \phi(x,y=0,z) &= \phi(x,y=L_y,z) = 0 \\ \phi(x,y,z=0) &= \phi_0, \quad \phi(x,y,z=L_z) = \phi_1 \end{aligned} \tag{1}$$

in terms of the spectral representation of a Fourier series[4]

$$\phi(x,y,z) = \sum_{m=1}^{\infty} \sum_{n=1}^{\infty} \sin\left(\frac{m\pi x}{L_x}\right) \sin\left(\frac{n\pi y}{L_y}\right) f_{mn}(z) \tag{2}$$

is found by transforming Eq. (1) and solving the resulting ordinary differential equation to be

$$\phi(x,y,z) = \frac{16}{\pi^2} \sum_{\substack{m=1 \\ m\ odd}}^{\infty} \sum_{\substack{n=1 \\ n\ odd}}^{\infty} \frac{1}{mn} \sin\left(\frac{m\pi x}{L_x}\right) \sin\left(\frac{n\pi y}{L_y}\right) C_{mn}(z)$$

$$C_{mn}(z) = \left[\frac{\phi_0 e^{-\lambda(L_z - z)} - \phi_1 e^{\lambda z}}{e^{-\lambda L_z} - e^{\lambda L_z}} + \frac{\phi_1 e^{-\lambda z} - \phi_0 e^{\lambda(L_z - z)}}{e^{-\lambda L_z} - e^{\lambda L_z}} \right]$$

$$\lambda^2 = \frac{m^2\pi^2}{L_x^2} + \frac{n^2\pi^2}{L_y^2} \tag{3}$$

For the trapping field

$$\phi_0 = \phi_1 = V_{trap}$$

and

$$U_{trap}(x,y,z,t) = \phi(x,y,z) \tag{4}$$

While for the single-frequency excitation field

$$\phi_0 = -\phi_1 = V_{excite}$$

and

$$U_{excite}(x,y,z,t) = \phi(x,z,y) \sin(\omega t) \tag{5}$$

Both of these series are exponentially converging in m and n, but they are nonuniformly converging at the walls with nonzero boundary conditions.

The remaining task necessary to model fully a FT-ICR experiment is a description of

the measured signal. We assume the measured signal is proportional to the charge induced on the cell walls. Whether this is rigorously true or whether a voltage or current is measured is of little consequence, as the Fourier-transformed signals for these cases will look similar over a small mass range. The total charge induced on a conducting plate, i.e. a plate for which the time constant is smaller than the time over which the ion positions change substantially, is given by[5]

$$Q_{ind}(x) = -\int_0^{L_y}\int_0^{L_z} \nabla\cdot G(x,y,z)\; dy\,dz \tag{6}$$

Where the Green's function (i.e. the field produced at **x** by a unit charge at **x'**) solves

$$\begin{aligned} \nabla^2 G(x,y,z|x',y',z') &= \delta(x-x')\;\delta(y-y')\;\delta(z-z') \\ G(x=0,y,z) &= G(x=L_x,y,z) = 0 \\ G(x,y=0,z) &= G(x,y=L_y,z) = 0 \\ G(x,y,z=0) &= G(x,y,z=L_z) = 0 \end{aligned} \tag{7}$$

and is given in the spectral representation of Eq. (2) by

$$\begin{aligned} &G(x,y,z|x',y',z') = \\ &-\frac{4}{L_y L_z}\sum_{m=1}^{\infty}\sum_{n=1}^{\infty} \sin\left(\frac{m\pi y'}{L_y}\right)\sin\left(\frac{m\pi y}{L_y}\right)\sin\left(\frac{n\pi z'}{L_z}\right)\sin\left(\frac{n\pi z}{L_z}\right)\times \\ &\frac{\sinh[\lambda(L_x-x_>)]\sinh[\lambda x_<]}{\lambda\sinh[\lambda L_x]}, \\ &x_< = \min(x,x'), \qquad x_> = \max(x,x') \end{aligned} \tag{8}$$

The measured induced charge is, therefore,

$$Q_{obs} = Q_{ind}(0) - Q_{ind}(L_x) =$$

$$\frac{16}{\pi^2} \sum_{\substack{m=1 \\ m\ odd}}^{\infty} \sum_{\substack{n=1 \\ n\ odd}}^{\infty} \frac{1}{mn} \sin\left(\frac{m\pi y'}{L_y}\right) \sin\left(\frac{n\pi z'}{L_z}\right) \times$$

$$\frac{\sinh[\lambda x'] - \sinh[\lambda (L_x - x')]}{\sinh[\lambda L_x]} \tag{9}$$

For the purpose of dealing with a familiar form, Eq. (4) is fit to a polynomial about the center of the 2.54 cm cubic trap that will be used in the simulations. Appendix I lists the result of an ordinary least squares fit of coefficients though the sixth power in all variables, with the fit done on a 20×20×20 grid of points inside the cell. This trapping polynomial has a relative error of 1.2% on the fit data. Appendix II contains the result of a similar fit to Eq. (5). This excitation polynomial has a relative error of 1.4% on the fit data. Given that the gradient is not a bounded operator, it is not surprising that the relative error of the force due to these polynomials is an order of magnitude larger than that of the potential. The degree of asymmetry in these polynomials is an indication of the accuracy of the coefficients. Many coefficients are zero in the polynomials because of the requirements of symmetry. Note that although it is an optimal polynomial, the trapping field in Appendix I agrees well with the exact, quadrupolar truncation of the Taylor series of Eq. (4):[6]

$$U_{trap,quad} = V_{trap}\left[\frac{1}{3} - \frac{\alpha}{L^2}(x^2 + y^2 - 2z^2)\right], \qquad \alpha = 1.386$$

(10)

Equation of motion. An ion inside the cell is acted upon by the imposed magnetic field, by the imposed trapping and excitation fields, and by other ions inside the cell. We take into account exactly all of the nonrelativistic forces except for the ion-ion Coulomb forces. While they can be of interest at the maximum ion densities used in FT-ICR experiments, ion-ion forces are very small, and a large number of ions is required for a significant effect compared to, for example, the trapping field. The equation of motion for an ion excited at the expected (nonshifted) cyclotron frequency for a time τ is, then,

$$m\ddot{\boldsymbol{x}} = -q\nabla U_{trap}(\boldsymbol{x}) - q\nabla U_{excite}(\boldsymbol{x}, t)\,H(t) + q\dot{\boldsymbol{x}}\times\boldsymbol{B}$$
$$\boldsymbol{x}(0) = \boldsymbol{x}_0, \qquad \dot{\boldsymbol{x}}(0) = \boldsymbol{v}_0$$
$$H(t) = \begin{cases} 1, & t \le \tau \\ 0, & t > \tau \end{cases}$$

(11)

The magnetic field **B** will be assumed a constant value, B_0 = 7 T, along the z-axis. This approximation becomes more accurate the lower the magnetic susceptibility of the metal FT-ICR cell, and it would be better, for example, for an oxygen-free copper cell than for a stainless steel cell. Even for 316 stainless steel, however, calculations show B to be fairly constant in a typical FT-ICR cell.[7]

CALCULATIONS

Initial conditions and numerical integration. Our calculations are intended to be appropriate for FT-ICR applications in which the z oscillation is large and is not allowed to relax. This can be the case, for example, in electron impact ionization, where ions are formed uniformly along the z-axis between the trapping plates. In addition, ion injection in an external ion source instrument can result in large z oscillation. A large cyclotron radius will be produced in the simulations, satisfying an experimental desire for a high signal to noise ratio. The initial phase space distribution placed upon Eq. (11) is, accordingly, Maxwellian velocities and positions uniformly distributed in a cylinder centered at the middle of the cell with radius 0.05 cm, the axis of rotation the z-axis, and a length that is 80% of the trapping electrode spacing. The initial velocities, which actually cannot be three-dimensional Maxwellian in a constant magnetic field, are relatively unimportant, as excitation supplies a large amount of radial energy, and the initial z dispersion implies a moderate amount of z energy. The equation of motion, Eq. (11), is integrated numerically by VODE, a variable order, variable step size ODE integration package designed to deal with difficult to integrate, nonlinear equations. [8,9,10,11,12,13] The stable, backward differentiation formula algorithm (MF = 20) is used. For the trajectory calculations we specify a relative error (rtol) of 10^{-6} and an absolute error (atol) of 10^{-8}, which denotes six significant figure accuracy for integration over a reasonable time range. For consistency, Eqs. (4) and (5) are evaluated to a relative accuracy of six significant figures, with the series optimized to allow for precomputation of most of the constant terms. While the approximate field equations of Appendices I and II could be used, we chose to use the exact representation so that there will be no ambiguity about the

accuracy of our equation of motion. Several simulations were done at one-hundred times the above accuracy, with essentially no difference in the overall results.

Base case and code verification. To establish a base case, let us first present results for five ions in a quadratic and a quadrupolar, Eq. (10), trapping field. Eq. (5) is used for the excitation, however. Figure 2 illustrates the result of a trapping field that only depends quadratically on z.[14] Figure 2c shows that the envelope of the signal defined by Eq. (9) is constant, which is also implied by no radial field. The mass spectrum in Figure 2d is a discrete fast Fourier transform of the signal data.[15] In conformance with standard experimental practice, the DC component of the signal is removed, a Hanning window is applied, and zero filling is done to the integer 2^n that is at least twice as large as the original data set.[16] Applying the window before zero filling has the effect of reducing the width of the bases of the peaks while creating small sidelobes. The peak width in Figure 2 is due to leakage associated with a finite sampling time and to the discreteness of the basis of the transform. (To understand the importance of the discrete basis, consider the discrete Fourier transform of a sinusoid at exactly one of the discrete frequencies and of a sinusoid at an interpolated frequency. By orthogonality, the first transform will have only one component, the other will have several.[15]) Figure 3 illustrates the result of using the quadrupolar trapping field, Eq. (10), which has come to be widely accepted by FT-ICR spectroscopists.[6] The resulting linear, constant coefficient equation of motion is easily solved for motion after excitation, with the result that an ion undergoes

cyclotron and magnetron motion at the angular frequencies of

$$\omega_c = \frac{qB_0}{m} - \omega_m$$

$$\omega_m = \frac{2\alpha V_{trap}}{L^2 B_0} \qquad (12)$$

Figure 3c shows the magnetron motion, and Figure 3d shows the signal transient envelope, which is again not dephased because there is only one high-frequency component to the signal. The mass shift agrees with the predicted value of 7.3 amu.

Rapid excitation. Having gained confidence in the operation of the code, we now solve the true equation of motion, using the trapping field given by Eq. (4). Since impulse excitation promises to offer increased applicability of FT-ICR in kinetic studies,[17] calculations for rapid excitation, e.g. 20 μs excitation duration, will be presented first. Note that this is not exactly an impulse excitation scheme, since it is an AC excitation. Also note that there is no switching delay. Figure 4 depicts the results for a representative m/q = 100 amu/$|e^-|$ run. A very notable feature is the existence of multiple magnetron periods. A second important feature is the dephasing that is observed. Yet another general conclusion is that the magnetron motion is centered exactly at x = 0, y = 0. Figure 5 depicts the results for m/q = 1000 amu/$|e^-|$. A feature to be noted here is the increased z-axis oscillation amplitude caused by the excitation. Since the excitation is at a frequency slightly higher than the observed, shifted frequency, this z-axis ejection is consistent with previous

observations.[18] The dependence of this ejection on mass can be reasoned intuitively by considering a particle surfing on a potential wave, with the cyclotron frequency playing the role of an effective gravity. The mass to charge ratio of the particle defines the phase relative to excitation and so defines the degree of z-axis excitation. For low mass to charge ratios, increasing m/q intuitively implies a phase that favors z-axis excitation. The greater radial inertia of the particle after the fixed excitation time has caused the magnetron motion at the end of the excitation to be more pronounced in Figure 5 than it is in Figure 4.

Figure 6 depicts the exaggerated z-axis amplitude that occurs for $m/q = 2000$ amu/$|e^-|$. The phase relative to excitation is such that z-axis excitation is maximal at $m/q = 2000$ amu/$|e^-|$. Figures 4-6 show decreased excitation below this value, and in fact, ion ejection occurs above this value. Thus, conclusions[19] based upon calculations[20] performed for chirp excitation that show greater z-axis excitation for nitrogen molecular ions than for benzene molecular ions cannot be extrapolated to higher mass to charge ratios, at least not for the single frequency excitation case displayed in Figures 4-6. The signal transient suggests complete dephasing occurs at a time somewhat longer than 40 ms. Figure 6d assures us that the dephasing is a collective phenomenon, as an individual ion's transient does not decay. Figure 6d also indicates that despite the formidable appearance of Eq. (9), the observed mass spectrum is indistinguishable from one derived from a signal defined by the x-displacement of the particle from the center of the cell until significant dephasing has taken place. The only significant effect of using Eq. (9) seems to be

an occasional sidelobe; this effect is evident in Figure 6d. As noted above, the initial velocity is of relatively minor importance, as a large amount of radial energy is supplied by the excitation, and the particles start off with a moderate amount of z potential energy. The dependence of a final ion trajectory on mass and charge should enter only as the ratio mass to charge, for the equation of motion itself depends only on this ratio. Figure 7 shows that, indeed, a system with q = 2 $|e^-|$ and m = 2000 amu has similar z-axis and magnetron amplitudes as does the system with q = 1 $|e^-|$ and m = 1000 amu in Figure 5.

Slow excitation. While more moderate excitation voltages do reduce the z-axis heating and the magnetron amplitude, the dephasing persists, as Figure 8 shows. Simulations for q = 1 $|e^-|$ and m = 1000 to 10 000 amu with a statistically significant fifty ions show the coherence time decreases from roughly 50 ms to 40 ms for a 1 V trapping field. Such a coherence time implies a range of about 15 Hz in the cyclotron frequencies. Figures 9 and 10 show two endpoint spectra. Decreasing the amplitude of the z-axis oscillation should reduce the dephasing, since this eliminates one of the variables determining the effective radial force on the ion. Indeed, the relevant endpoint spectra of Figures 9 and 10 indicate substantially reduced dephasing and suggest a coherence time of greater than 150 ms. These Figures also prove the z-oscillation to be a more significant cause of dephasing than are variations in magnetron radius.

Increased trapping voltage. Assuming the trapping field does not affect the ion

during excitation, the transient length should depend inversely on V_{trap}, as this defines the range of frequency shifts seen by the ion. Simulations for V_{trap} = 5 V, V_{excite} = 1 V, and τ = 2 ms showed deceleration of the ion after an initial acceleration. This is intuitively acceptable, as field lines originate on the trapping plates in this case. To reduce the effect of the trapping field during excitation, rapid excitation is again used. Figure 11 shows that, indeed, the coherence time has reduced to roughly 8 ms. The sharp excitation field cutoff has caused substantial magnetron motion that is evident. Also note the split peaks. This splitting is due in this case to individual ions orbiting at only one of these two frequencies, not to individual ions assuming multiple frequencies. Such doublets have been observed experimentally at high trapping voltages.[21] Despite Figure 6 and the suggestion[18] that excitation at frequencies lower than the observed resonance would cool z-axis oscillations, we are unable to excite the system of V_{trap} = 1 V, V_{excite} = 100 V, and τ = 20 μs so as to prevent any of our 50 initial ions from escaping.

DISCUSSION

The dephasing effect of the z-axis oscillations is significant even in the 60 ms observation period used here. Figure 12a displays the relative mass precision obtained from the response function (i.e. the discrete Fourier transform of a sine function lasting 60 ms), the signal for 20% z-axis occupation, and the signal for 80% z-axis occupation. The reduced mass discrimination resulting from larger-amplitude z-axis excursion is obvious. While the reduction in resolution for the 80% peaks may appear small with the 60 ms observation period used, note that dephasing is

irreversible for a macroscopic number of ions. FT-ICR precision in mass determination of ions with large z-axis motion is fundamentally limited by this dephasing. That is, the 80% peaks would not become much narrower with a longer observation time (although they would become a bit narrower with an increased sampling rate), whereas the 20% peaks would narrow until the observation time exceeded 150 ms. The maximum resolution for a exponentially damped signal with a transient length similar to those of the 80% signals is indicated in Figure 12; such resolution would be observed only at an infinite sampling rate.[6] Also indicated in Figure 12 is the shift in mass from the true value. It would appear that in some cases, the magnitude of the z-axis oscillation can affect the apparent, observed mass.

The z-axis oscillations have been cited as being responsible for decreased ion signal.[22] That is, the signal of an individual ion was felt to decrease as it deviated from the equilibrium $\frac{1}{2}L_z$ plane. The difference in peak heights between the mass spectra of the five individual ions of Figure 6, which have quite a range of z-axis amplitudes, is only 1.6%. It is the change in <u>phase</u>, rather than amplitude, with z-axis motion that causes decreased total ion signals. Detailed examination of the trajectories of the ions of Figure 6 reveals that both the radius of the cyclotron motion and the tangential velocity of an ion vary dynamically with z. The Fourier transform then averages the deviations from pure uniform circular motion to produce broadened frequency peaks responsible for the decreased resolution seen in Figure 12. We note that defining a density of states by using the instantaneous tangential velocity and instantaneous cyclotron radius to define a frequency, i.e.

$$\omega = \frac{v_\theta(t)}{r_c(t)} \tag{13}$$

and then histogramming the frequencies to produce $g(\omega)$ reveals the variation of frequency with z. Such a $g(\omega)$ is not, however, the discrete Fourier transform of, say, x(t). For example, small oscillations in v(t) drastically affect Eq. (13), but they are averaged out by a discrete Fourier transform of x(t).

Since the finite transient length is due to the coupling between the effective radial force on the ion and the z-axis motion, and to a lesser extent the instantaneous center of the cyclotron orbit, more homogeneous electric fields should increase the coherence time. Figures 2 and 3 provide the extreme example of this. Of course, one solution to the inhomogeneous field problem is to use the Penning trap, which has a purely parabolic trapping field.[23] The Penning trap does not have any means of ion excitation or detection, however. Marshall[24,19]; Russell[21]; and Rempel, Grese, and Gross[25] have recently described methods for creating a more homogeneous field in an FT-ICR cell. Rempel, Grese, and Gross used a cell that allowed two distinct voltages to be placed on the trapping plates. The voltage beyond a certain radius was approximately twice that near the cell axis, which compensated for the required decay of the electric field at the remaining four cell sides. Russell employed guard rings within the cell to homogenize both the rf excitation field and the dc trapping field. Marshall's screened trap extends this concept. It incorporates a grounded screen of 1/16" spacing just inside the trapping plates and appears to be

particularly effective at reducing the entire trapping field to negligible levels over most of the cell. Only within a few aperture diameters from the screen or the walls is the field significant. If ions are not adsorbed by the grounded screen and are sufficiently stabilized by the orbit-creating magnetic field that they are not deflected at their turning points by the fine-scale structure of the screen, the mass spectra resulting from such a cell should be much like those of Figure 2. No magnetron motion, and hence no peak shifting, would occur. Additionally there would be no spatially varying trapping field to cause dephasing, so that, in principle, infinitely high mass resolution could be obtained.

CONCLUSIONS

Collisions are not necessary for dephasing in a conventional cubic FT-ICR cell. Nor are space charge effects. The fundamental relative precision of a mass peak is proportional to the cyclotron frequency multiplied by a coherence time.[6] This coherence time is finite, approximately inversely related to the trapping voltage, and only slightly dependent on mass. This dephasing is particularly significant for high ratios of mass to charge, as might occur, for example, in studies of clusters, polymers, or biomolecules. If experimentally feasible, this dephasing can be reduced by allowing the z-oscillation to relax, by, for example, allowing collisional cooling or adiabatically raising the trapping voltage. If not, it would appear fruitful to investigate experimentally alterations to the basic cell that reduce the inherent coupling of the degrees of freedom, perhaps by reducing the electric field itself over most of the trap.[19,21,22,25]

Acknowledgements

We would like to thank Paul Messina, the Director of the Caltech Concurrent Supercomputing Facilities, for generous grants of computer time.

Bibliography

(1) D. F. Hunt, J. Shahanowitz, J. R. Yates III, N. -Z, Zhu, D. H. Russell, and M. Castro, Proc. Natl. Acad. Sci. U.S.A 84 (1987) 620-623. See also C. F. Ijames and C. L. Wilkins, J. Am. Chem. Soc. 110 (1988) 2687-2688.

(2) Melvin B. Comisarow, Int. J. Mass Spec. Ion Phys. 37 (1981) 251-257.

(3) M. H. Friedman, A. L. Yergey, and J. E. Campana, J Phys. E. 15 (1982) 53-72.

(4) Bernard Friedman, Principles and Techniques of Applied Mathematics, John Wiley & Sons, 1956, ch. 5.

(5) J. D. Jackson, Classical Electrodynamics, John Wiley & Sons, 1975.

(6) Alan G. Marshall and Francis R. Verdun, Fourier Transforms in NMR, Optical, and Mass Spectrometry: A User's Handbook, Elsevier, 1990, p. 235.

(7) C. D. Hanson, E. L. Kerley, and D. H. Russell, "Recent Developments in Experimental Fourier Transform Ion Cyclotron Resonance," in Treatise on Analytical Chemistry, Part I, Volume 11, J. D. Winefordner and M. M. Bursey, eds., John Wiley & Sons, 1978, p. 139.

(8) P. N. Brown, G. D. Byrne, and A. C. Hindmarsh, "VODE, a Variable Coefficient ODE Solver," LLNL Report UCRL-98412, June 1988. Also, SIAM J. Sci. Stat. Comput., to appear.

(9) G. D. Byrne and A. C. Hindmarsh, ACM Trans. Math. Software 1 (1975) 71.

(10) A. C. Hindmarsh and G. D. Byrne, "EPISODE: An Effective Package for the Integration of Systems of Ordinary Differential Equations," LLNL Report UCID-30112, Rev. 1, April 1977.

(11) G. D. Byrne and A. C. Hindmarsh, "EPISODEB: An Experimental Package for the Integration of Systems of Ordinary Differential Equations with Banded Jacobians," LLNL Report UCID-30132, April 1976.

(12) A. C. Hindmarsh, Scientific Computing, R. S. Stepleman et al., eds., North-Holland, Amsterdam, 1983, pp. 55-64.

(13) K. R. Jackson and R. Sacks-Davis, ACM Trans. Math. Software 6 (1980) 295.

(14) This and all subsequent Figures were produced with the GraphiC 5.01 graphics program, Scientific Endeavors Corporation.

(15) William H. Press, Brian P. Flannery, Saul A. Teukolsky, and William T. Vetterling, Numerical Recipes: The Art of Scientific Computing, Cambridge University Press, 1987, ch. 12.

(16) For a discussion of windowing see reference 5, p. 47, and reference 14, ch. 12.7.

(17) For the specific case of impulse excitation with a pulsed (static) electric field, see R. T. McIver, G. Baykut, and R. L. Hunter, Int. J. Mass Spectrom. Ion Proc. 89 (1989) 343-358.

(18) P. Kofel, M. Allemann, HP. Kellerhals, and K. P. Wanczek, Int. J. Mass. Spectrom. Ion Proc. 74 (1986) 1-12.

(19) M. Wang and A. G. Marshal, Anal. Chem. 62 (1990) 515-520.

(20) S. K. Huang, D. L. Rempel, and M. L. Gross, Int. J. Mass Spectrom. Ion Proc. 72 (1986) 15-31.

(21) C. D. Hanson, M. E. Castro, E. L. Kerley, and D. H. Russell, Anal. Chem. 62 (1990) 520-526.

(22) D. L. Rempel, S. K. Huang, and M. L. Gross, Int. J. Mass Spectrom. Ion Proc. 70 (1986) 163-184.

(23) H. G. Dehmelt, Adv. At. Mol. Phys. 3 (1967) 53-72.

(24) M. Wang and A. G. Marshal, Anal. Chem. 61 (1989) 1288-1293.

(25) D. L. Rempel, R. P. Grese, and M. L.Gross, "A Scaling Technique for Studying the Dynamics of High Mass Ions in FTMS: A Preliminary Report," to appear in Int. J. Mass Spectrom. Ion Proc. 100 (1990).

FIGURES

Figure 1. Depicted is the FT-ICR cell and coordinate system for which our calculations are appropriate. The direction of **B** is along the z-axis as indicated. Also indicated are the trapping, excitation, and detection plates.

Figure 2. 2a and b show the motion of five ions during the last 100 μs of their 40 ms trajectory. The trapping potential is simply $U_{trap} = \alpha V_{trap} z^2$. V_{trap} = 2 V, V_{excite} = 1 V, τ = 2 ms, m = 2000 amu, and z = 1 $|e^-|$. Recall that B = 7 T in all these calculations. 2c reports the signal envelope defined by Eq. (9) for the trajectory, and 2d reports the discrete Fourier transform of the signal, with the small vertical line indicating the actual mass. Only data after the excitation are transformed. Note that no mass shifting or dephasing is expected in this Figure, and none is observed.

Figure 3. 3a and b show the motion of five ions in the trapping potential of Eq. (10), with the other parameters taken from Figure 2. 3c attempts to represent the magnetron motion by plotting the ion positions averaged over 400 μs intervals. 3d reports the signal envelope, and 3e, the Fourier transformed signal. Note the magnetron motion evident in 3c and 3d; the oscillations in the signal transient are due to the magnetron motion. Also note the mass shift is 7.3 amu, as expected.

Figure 4. 4a and b show the motion of five ions in the correct trapping potential of Eq. (4). V_{trap} = 1 V, V_{excite} = 100 V, τ = 20 μs, m = 100 amu, and z = 1 $|e^-|$. For this

Figure (only), the motion is displayed by undersampling the actual motion at a rate of 1 MHz, which is slightly less than the cyclotron frequency of 1.075 MHz, to produce 4a and b. 4c represents the magnetron motion; it explicitly demonstrates the existence of multiple magnetron periods. 4d and e exhibit both mass shifting and, now, dephasing.

Figure 5. 5a and b show the motion of five ions with a mass of 1000 amu, with other parameters taken from Figure 4. The sharp cutoff of the excitation has caused the greater magnetron radius shown in 5c compared to 4c. Note that the magnetron motion continues to be centered about the origin in the x-y plane, however. 5d and e are the signal and its transform, with 5d again showing the effect of dephasing.

Figure 6. 6a and b show the motion of 5 ions with a mass of 2000 amu, with other parameters taken from Figure 4. Note the exaggerated z-axis oscillations caused by the excitation field. 6c depicts the large magnetron motion, which is responsible for the off-centered cyclotron motion of 6a. 6d and e show the signal and its transient for (solid line) the five ions, (short dashed line) a single ion, and (long dashed line) the signal defined by $\Sigma(x - \frac{1}{2}L_x)$. No dephasing can occur in the single-ion trajectory, and none does.

Figure 7. 7a and b show the motion of five ions with a mass of 2000 amu and a charge of 2 $|e^-|$, with other parameters taken from Figure 5. Since the initial velocity

is relatively unimportant, the trajectories for this case are very similar to those of Figure 5. The magnetron motion in 7c and the dephasing in 7d are also very similar to those of 5c and 5d.

Figure 8. 8a and b show the motion of five ions with a mass of 2000 amu excited for τ = 2 ms, with V_{excite} = 1 V, and other parameters taken from Figure 4. Note the reduced z-axis oscillations in 8b. The magnetron motion in 8c is similarly reduced from that in 5c. Although the transient in 8d lacks the low-frequency oscillation of 5d, the dephasing is still evident, as is the mass shifting in 8e.

Figure 9. 9a shows the signal resulting from the motion of 50 ions with V_{trap} = 1 V, V_{excite} = 1 V, τ = 2 ms, m = 1000 amu, and z = 1 $|e^-|$. The solid line represents the solution of Eq. (11) with the usual 80% initial z-axis occupation, while the dashed line represents the solution with just 20% initial z-axis occupation. 9b shows the mass spectra of the signals.

Figure 10. 10a shows the signal resulting from the motion of 50 ions with a mass of 10 000 amu, with other parameters taken from Figure 9. Again, the solid line represents 80% initial z-axis occupation, while the dashed line represents just 20% initial z-axis occupation. 10b shows the mass spectra of the signals.

Figure 11. 11 shows the spectra resulting from rapid excitation of 50 ions, with

V_{trap} = 5 V, V_{excite} = 100 V, τ = 20 μs, m = 2000 amu, and z = 1 $|e^-|$. The initial z-dimension is 80% populated.

Figure 12. Illustrated are the mass precision and mass shift for the 80% occupancy (◇) and 20% occupancy (○) signals shown in Figures 9 and 10. The mass shift plotted is the difference between the observed shift and the shift predicted (to second order in mass) by Eq. (12). Also shown is the mass precision for the response function (□). Only the 80% peaks are broadened by dephasing during the 60 ms observation period used; the fundamental mass precision of a exponentially damped signal with a characteristic time of 25 ms is indicated (+).

Appendix I

The optimal polynomial fit to the trapping field. The variables here represent deviations from the center of the trap. Symmetry on the variables, for example between x and y, is not enforced, nor is solution of Laplace's equation.

$U_{trap}(x,y,z) / V_{trap} =$

$$
\begin{aligned}
&0.33334 + 0.43156\,z^2 + 0.00999\,z^4 - 0.00916\,z^6 - \\
&0.21587\,y^2 - 0.07320\,y^2z^2 + 0.30226\,y^2z^4 - 0.15794\,y^2z^6 - \\
&0.00482\,y^4 - 0.30310\,y^4z^2 - 0.00099\,y^4z^4 + 0.28257\,y^4z^6 + \\
&0.00449\,y^6 + 0.16348\,y^6z^2 - 0.28207\,y^6z^4 - 0.00082\,y^6z^6 - \\
&0.21583\,x^2 - 0.07383\,x^2z^2 + 0.30364\,x^2z^4 - 0.15866\,x^2z^6 + \\
&0.14814\,x^2y^2 - 0.00136\,x^2y^2z^2 - 0.10523\,x^2y^2z^4 + 0.04021\,x^2y^2z^6 - \\
&0.00280\,x^2y^4 + 0.05677\,x^2y^4z^2 - 0.05516\,x^2y^4z^4 - 0.01645\,x^2y^4z^6 - \\
&0.00367\,x^2y^6 - 0.02227\,x^2y^6z^2 + 0.01703\,x^2y^6z^4 + 0.02198\,x^2y^6z^6 - \\
&0.00491\,x^4 - 0.30157\,x^4z^2 - 0.00434\,x^4z^4 + 0.28431\,x^4z^6 - \\
&0.00264\,x^4y^2 + 0.05389\,x^4y^2z^2 - 0.04875\,x^4y^2z^4 - 0.01981\,x^4y^2z^6 + \\
&0.00929\,x^4y^4 + 0.09881\,x^4y^4z^2 - 0.00067\,x^4y^4z^4 + 0.04878\,x^4y^4z^6 - \\
&0.00426\,x^4y^6 + 0.00566\,x^4y^6z^2 - 0.02439\,x^4y^6z^4 - 0.05871\,x^4y^6z^6 + \\
&0.00454\,x^6 + 0.16266\,x^6z^2 - 0.28028\,x^6z^4 - 0.00175\,x^6z^6 - \\
&0.00379\,x^6y^2 - 0.02030\,x^6y^2z^2 + 0.01262\,x^6y^2z^4 + 0.02430\,x^6y^2z^6 - \\
&0.00420\,x^6y^4 + 0.00461\,x^6y^4z^2 - 0.02202\,x^6y^4z^4 - 0.05996\,x^6y^4z^6 + \\
&0.00354\,x^6y^6 - 0.04688\,x^6y^6z^2 + 0.11693\,x^6y^6z^4 + 0.00036\,x^6y^6z^6
\end{aligned}
$$

Appendix II

The optimal polynomial fit to the excitation field. The variables here represent deviations from the center of the trap. Symmetry on the variables, for example between x and z, is not enforced, nor is solution of Laplace's equation.

$U_{excite}(x,y,z,t=0) / V_{excite} =$

$$
\begin{aligned}
&-0.56824\, y^1 + 0.29547\, y^1 z^2 + 0.06052\, y^1 z^4 - 0.00654\, y^1 z^6 - \\
&0.19108\, y^3 - 0.21486\, y^3 z^2 + 0.57308\, y^3 z^4 - 0.31641\, y^3 z^6 + \\
&0.03424\, y^5 - 0.04114\, y^5 z^2 - 0.67671\, y^5 z^4 + 0.64654\, y^5 z^6 - \\
&0.00344\, y^7 + 0.07779\, y^7 z^2 + 0.06691\, y^7 z^4 - 0.20307\, y^7 z^6 + \\
&0.29496\, x^2 y - 0.15765\, y^2 y^1 z^2 - 0.04520\, x^2 y^1 z^4 + 0.01905\, x^2 y^1 z^6 - \\
&0.21022\, x^2 y^3 + 0.04864\, x^2 y^3 z^2 + 0.06174\, x^2 y^3 z^4 - 0.00281\, x^2 y^3 z^6 - \\
&0.04936\, x^2 y^5 + 0.10669\, x^2 y^5 z^2 - 0.03125\, x^2 y^5 z^4 - 0.02484\, x^2 y^5 z^6 + \\
&0.08164\, x^2 y - 0.05767\, x^2 y^7 z^2 + 0.03027\, x^2 y^7 z^4 - 0.00525\, x^2 y^7 z^6 + \\
&0.06168\, x^4 y^1 - 0.04748\, x^4 y^1 z^2 - 0.01441\, x^4 y^1 z^4 + 0.01347\, x^4 y^1 z^6 + \\
&0.56199\, x^4 y^3 + 0.08641\, x^4 y^3 z^2 - 0.20159\, x^4 y^3 z^4 - 0.06570\, x^4 y^3 z^6 - \\
&0.65672\, x^4 y^5 - 0.07725\, x^4 y^5 z^2 + 0.12662\, x^4 y^5 z^4 + 0.16608\, x^4 y^5 z^6 + \\
&0.05746\, x^4 y^7 + 0.05238\, x^4 y^7 z^2 - 0.06756\, x^4 y^7 z^4 - 0.02910\, x^4 y^7 z^6 - \\
&0.00707\, x^6 y^1 + 0.02020\, x^6 y^1 z^2 + 0.01323\, x^6 y^1 z^4 - 0.01572\, x^6 y^1 z^6 - \\
&0.31091\, x^6 y^3 - 0.01782\, x^6 y^3 z^2 - 0.05907\, x^6 y^3 z^4 + 0.13752\, x^6 y^3 z^6 + \\
&0.63641\, x^6 y^5 + 0.00438\, x^6 y^5 z^2 + 0.15182\, x^6 y^5 z^4 - 0.30014\, x^6 y^5 z^6 - \\
&0.19823\, x^6 y^7 - 0.01956\, x^6 y^7 z^2 - 0.02184\, x^6 y^7 z^4 + 0.10084\, x^6 y^7 z^6
\end{aligned}
$$

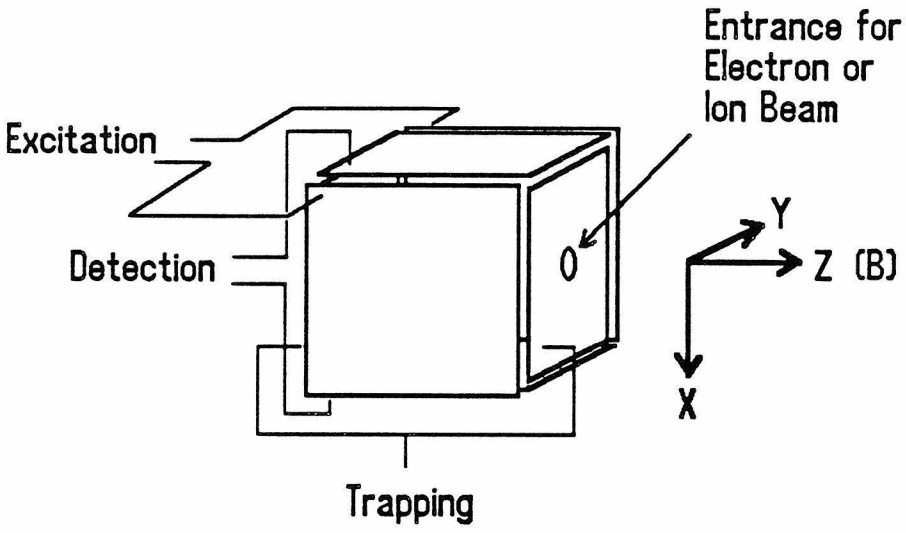
Entrance for
Electron or
Ion Beam
Excitation
Detection
O
Y
Z (B)
X
Trapping

Figure 1

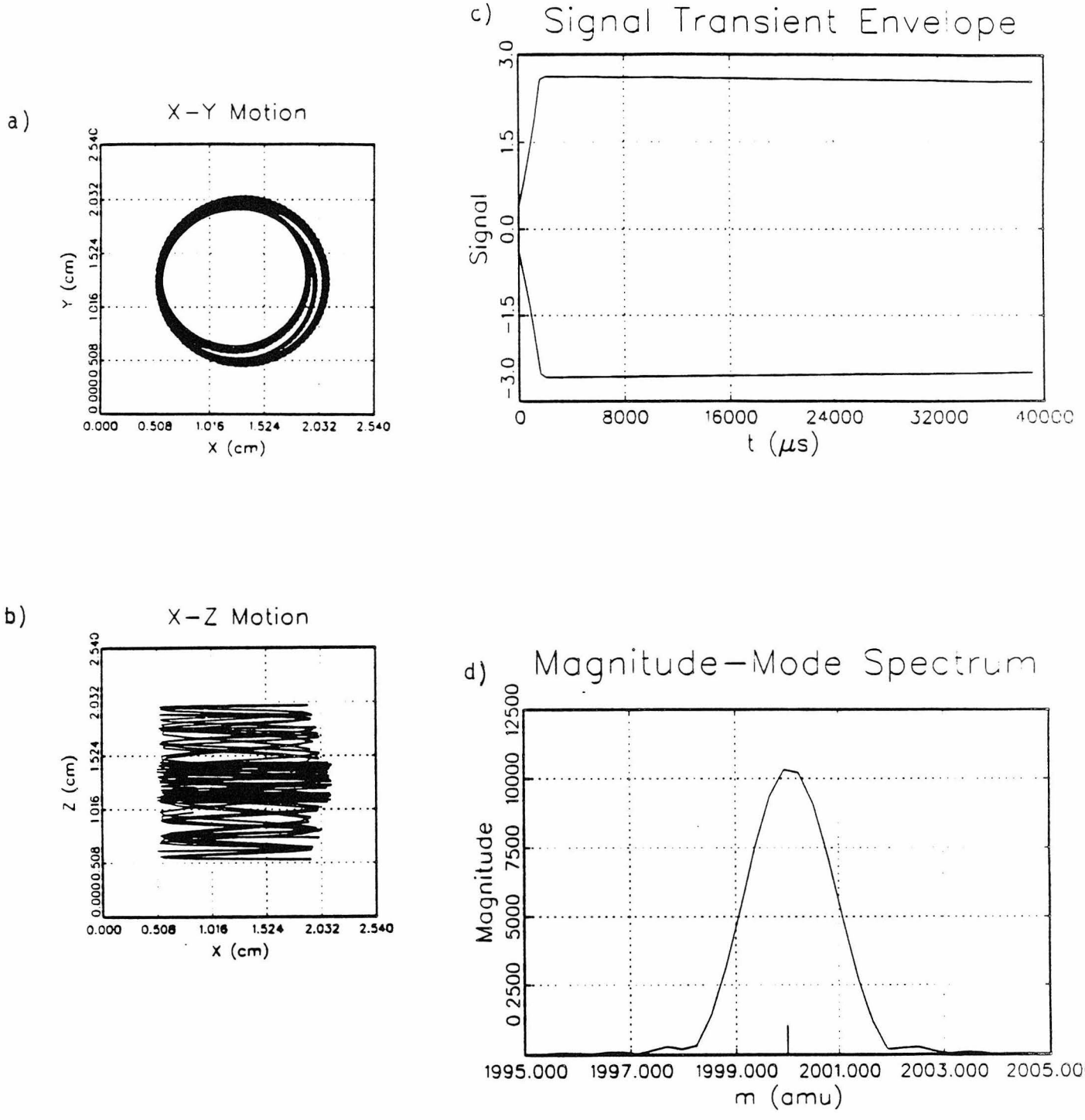
a)
X-Y Motion
Y (cm)
X (cm)
0.000
0.508
1.016
1.524
2.032
2.540
b)
X-Z Motion
Z (cm)
X (cm)
c)
Signal Transient Envelope
Signal
t (μs)
3.0
1.5
0.0
-1.5
-3.0
0
8000
16000
24000
32000
40000
d)
Magnitude-Mode Spectrum
Magnitude
m (amu)
0
2500
5000
7500
10000
12500
1995.000
1997.000
1999.000
2001.000
2003.000
2005.000

Figure 2

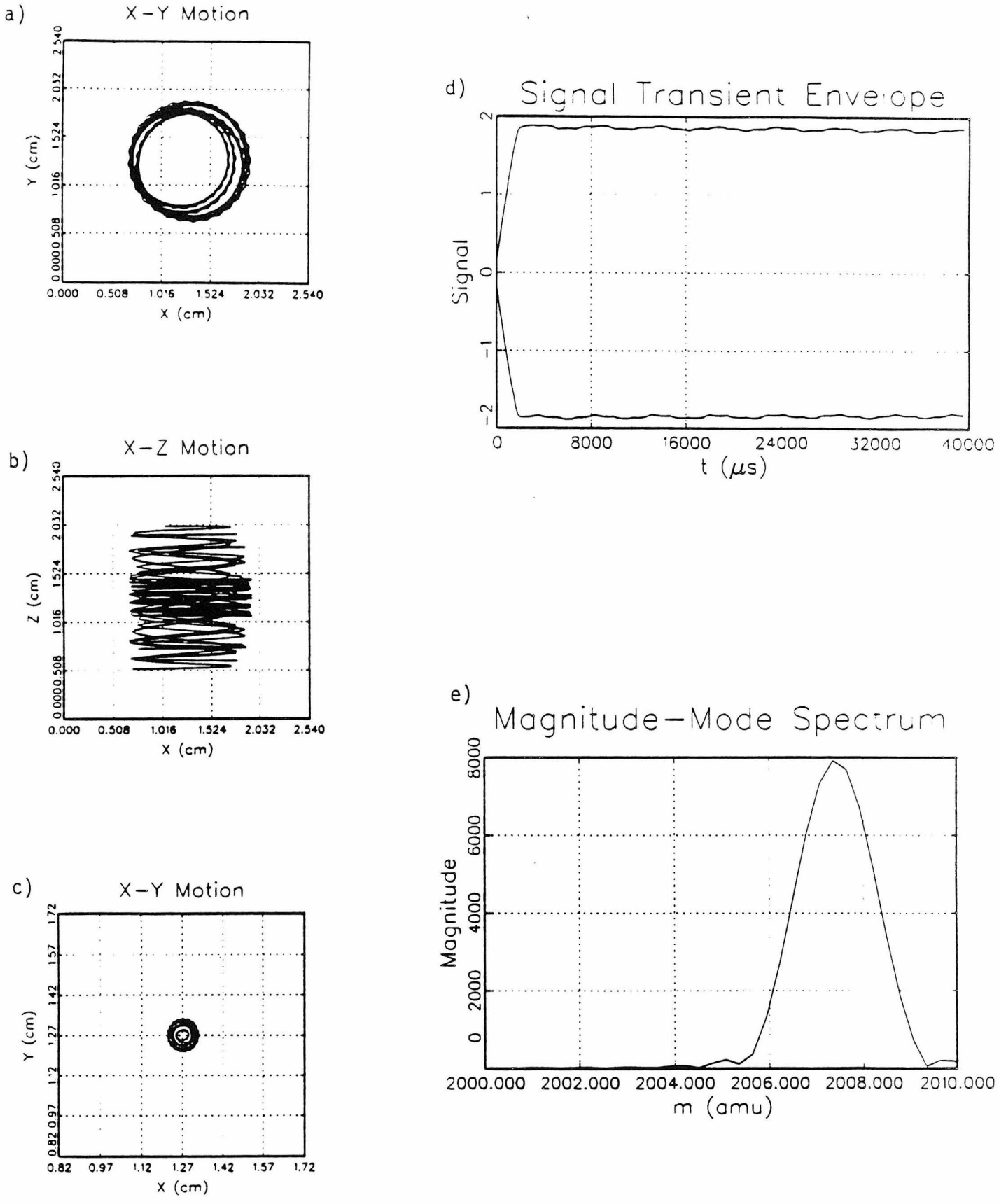
a)
X-Y Motion
Y (cm)
X (cm)
0.000
0.508
1.016
1.524
2.032
2.540
b)
X-Z Motion
Z (cm)
X (cm)
c)
X-Y Motion
Y (cm)
X (cm)
0.82
0.97
1.12
1.27
1.42
1.57
1.72
d)
Signal Transient Envelope
Signal
t (μs)
-2
-1
0
1
2
8000
16000
24000
32000
40000
e)
Magnitude-Mode Spectrum
Magnitude
m (amu)
0
2000
4000
6000
8000
2000.000
2002.000
2004.000
2006.000
2008.000
2010.000

Figure 3

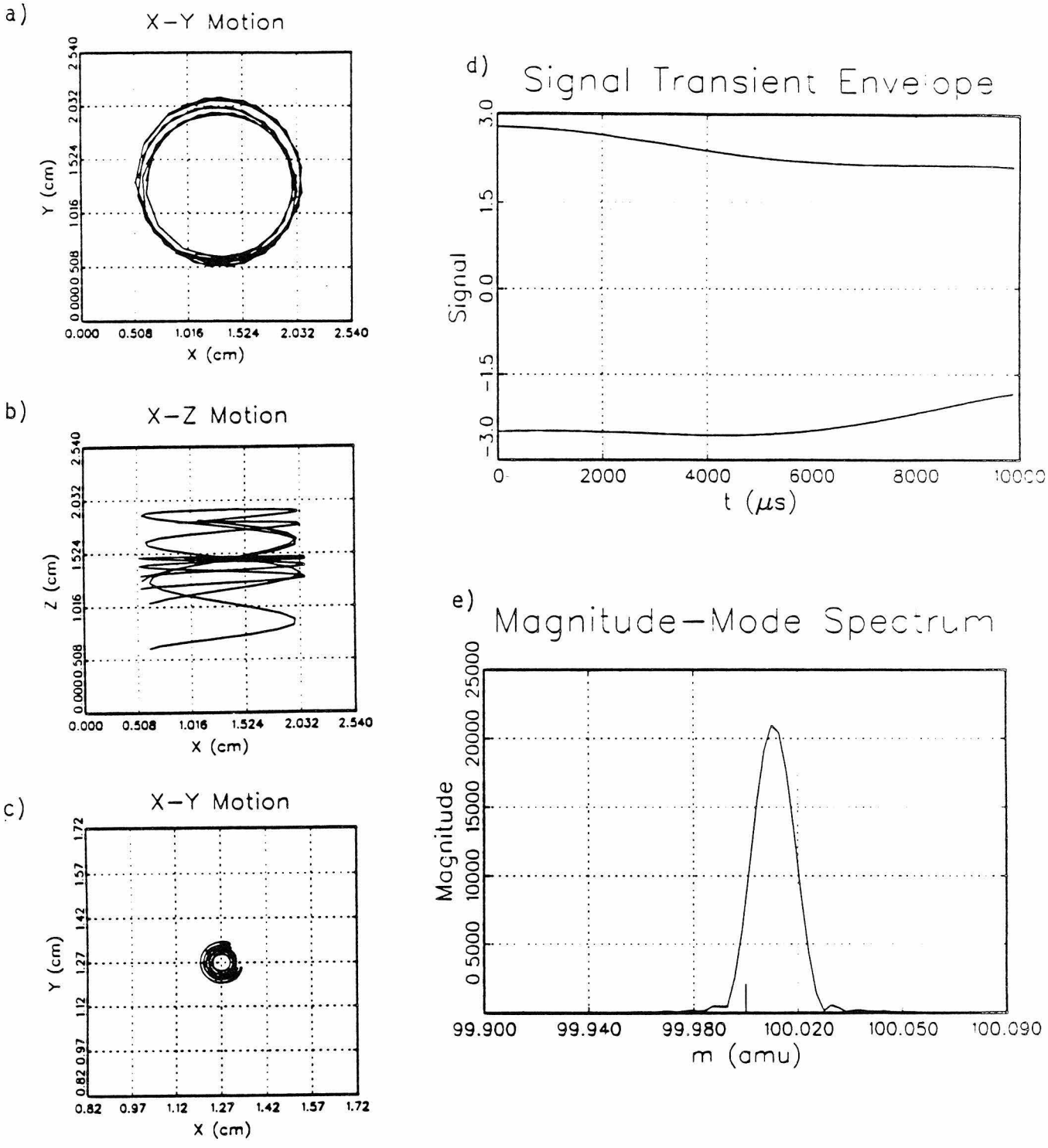
a)
X–Y Motion
Y (cm)
X (cm)
0.000 0.508 1.016 1.524 2.032 2.540
b)
X–Z Motion
Z (cm)
X (cm)
0.000 0.508 1.016 1.524 2.032 2.540
c)
X–Y Motion
Y (cm)
X (cm)
0.82 0.97 1.12 1.27 1.42 1.57 1.72
d)
Signal Transient Envelope
Signal
t (μs)
3.0 1.5 0.0 -1.5 -3.0
0 2000 4000 6000 8000 10000
e)
Magnitude–Mode Spectrum
Magnitude
m (amu)
0 5000 10000 15000 20000 25000
99.900 99.940 99.980 100.020 100.050 100.090

Figure 4

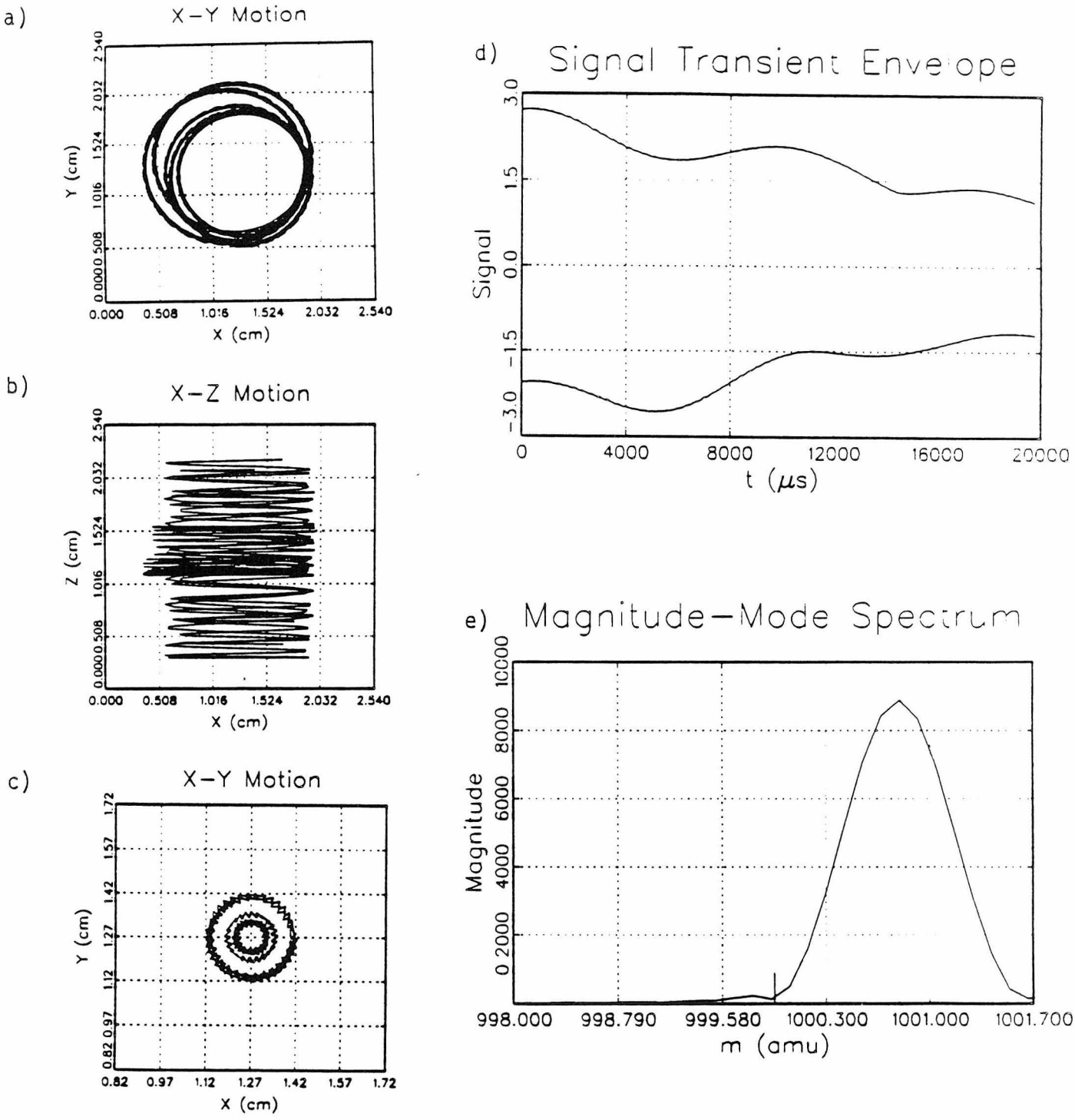
a)
X–Y Motion
Y (cm)
X (cm)
0.000
0.508
1.016
1.524
2.032
2.540
b)
X–Z Motion
Z (cm)
X (cm)
c)
X–Y Motion
Y (cm)
X (cm)
0.82
0.97
1.12
1.27
1.42
1.57
1.72
d)
Signal Transient Envelope
Signal
t (μs)
3.0
1.5
0.0
-1.5
-3.0
0
4000
8000
12000
16000
20000
e)
Magnitude–Mode Spectrum
Magnitude
m (amu)
0
2000
4000
6000
8000
10000
998.000
998.790
999.580
1000.300
1001.000
1001.700

Figure 5

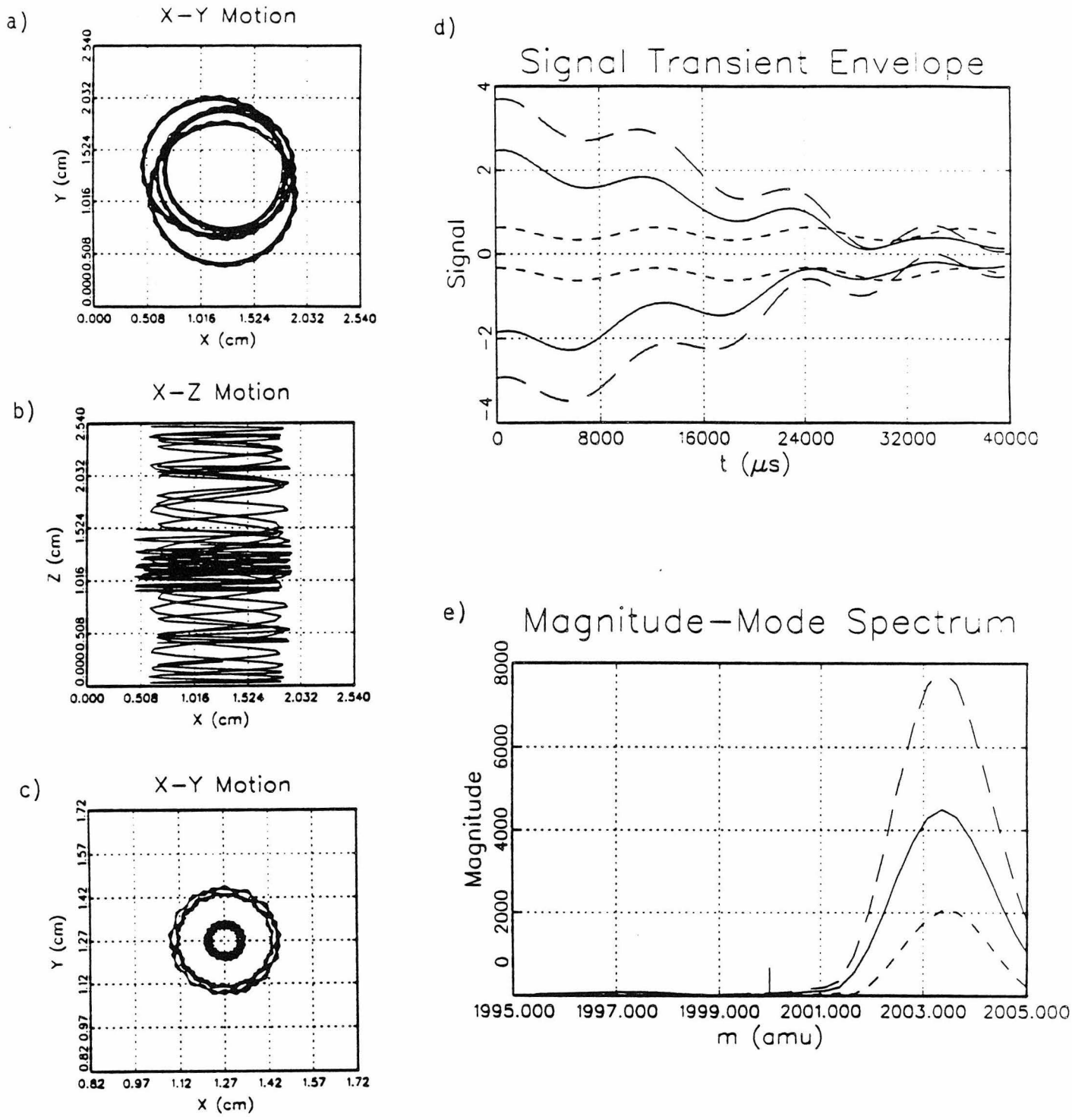
a)
X−Y Motion
Y (cm)
X (cm)
0.000
0.508
1.016
1.524
2.032
2.540
b)
X−Z Motion
Z (cm)
X (cm)
c)
X−Y Motion
Y (cm)
X (cm)
0.82
0.97
1.12
1.27
1.42
1.57
1.72
d)
Signal Transient Envelope
Signal
t (μs)
−4
−2
0
2
4
0
8000
16000
24000
32000
40000
e)
Magnitude−Mode Spectrum
Magnitude
m (amu)
0
2000
4000
6000
8000
1995.000
1997.000
1999.000
2001.000
2003.000
2005.000

Figure 6

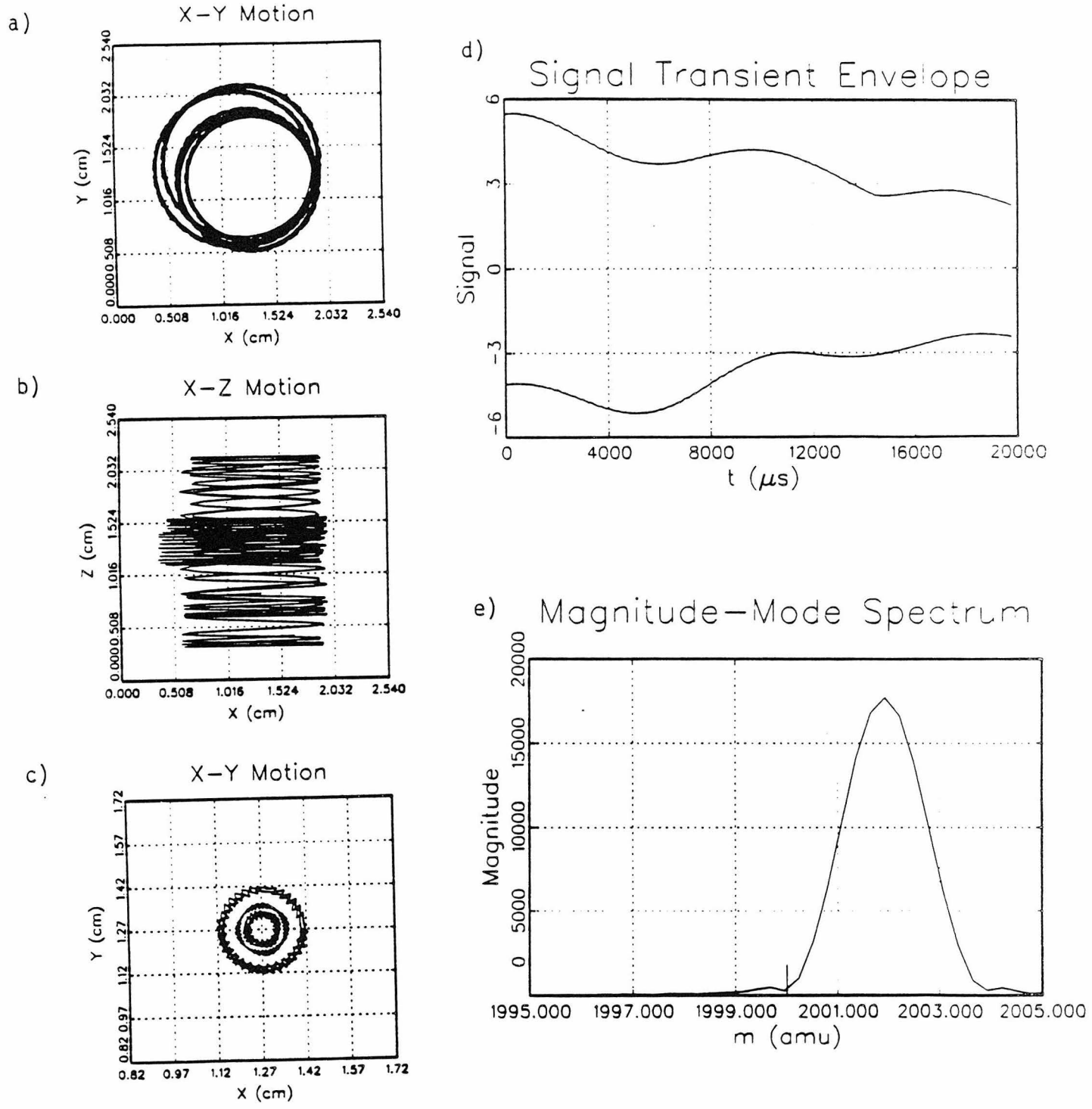
a)
X−Y Motion
Y (cm)
X (cm)
b)
X−Z Motion
Z (cm)
X (cm)
c)
X−Y Motion
Y (cm)
X (cm)
d)
Signal Transient Envelope
Signal
t (μs)
e)
Magnitude−Mode Spectrum
Magnitude
m (amu)

Figure 7

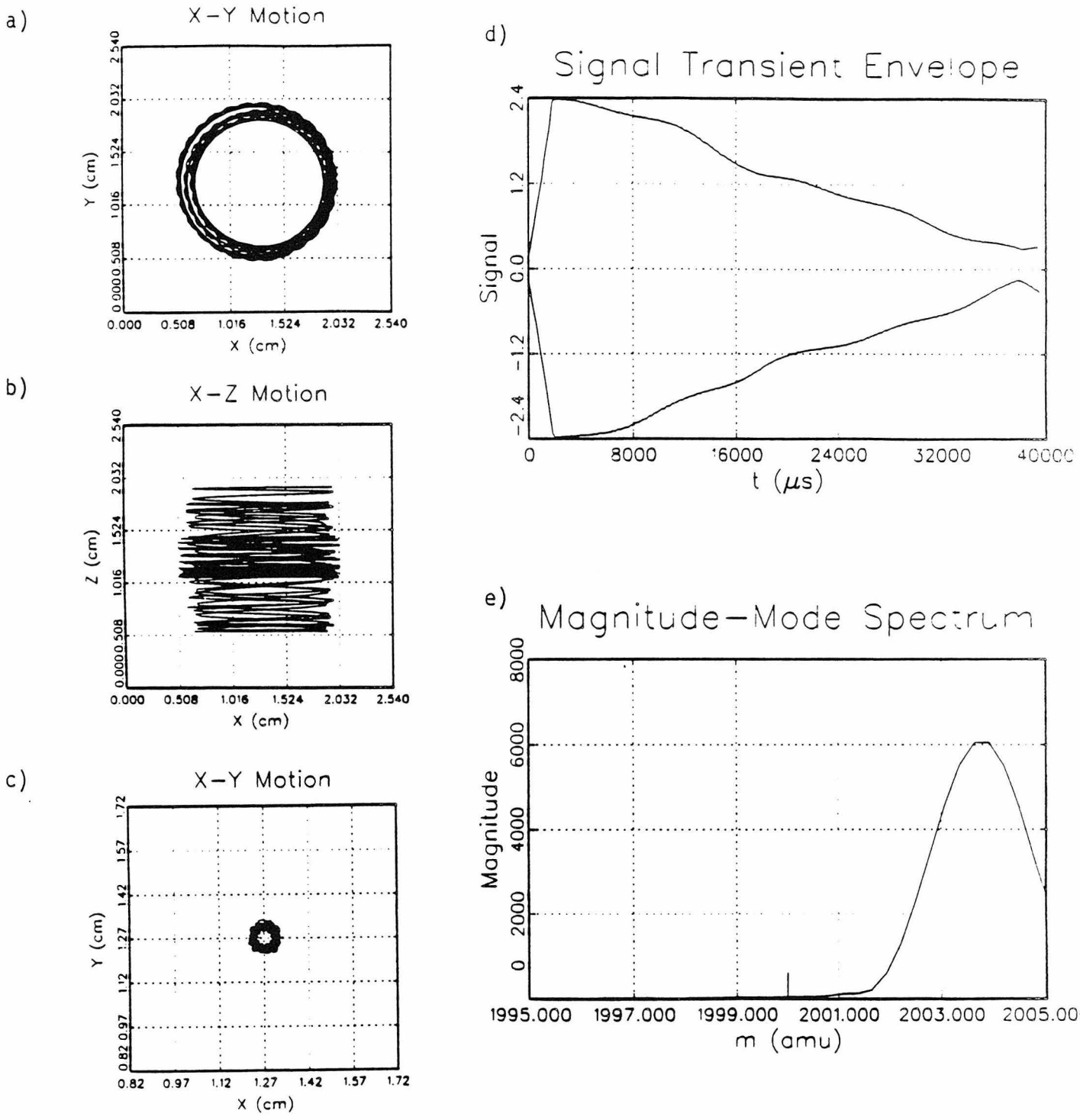
a)
X-Y Motion
Y (cm)
X (cm)
0.000 0.508 1.016 1.524 2.032 2.540
b)
X-Z Motion
Z (cm)
X (cm)
0.000 0.508 1.016 1.524 2.032 2.540
c)
X-Y Motion
Y (cm)
X (cm)
0.82 0.97 1.12 1.27 1.42 1.57 1.72
d)
Signal Transient Envelope
Signal
t (μs)
-2.4 -1.2 0.0 1.2 2.4
0 8000 16000 24000 32000 40000
e)
Magnitude-Mode Spectrum
Magnitude
m (amu)
0 2000 4000 6000 8000
1995.000 1997.000 1999.000 2001.000 2003.000 2005.000

Figure 8

a)

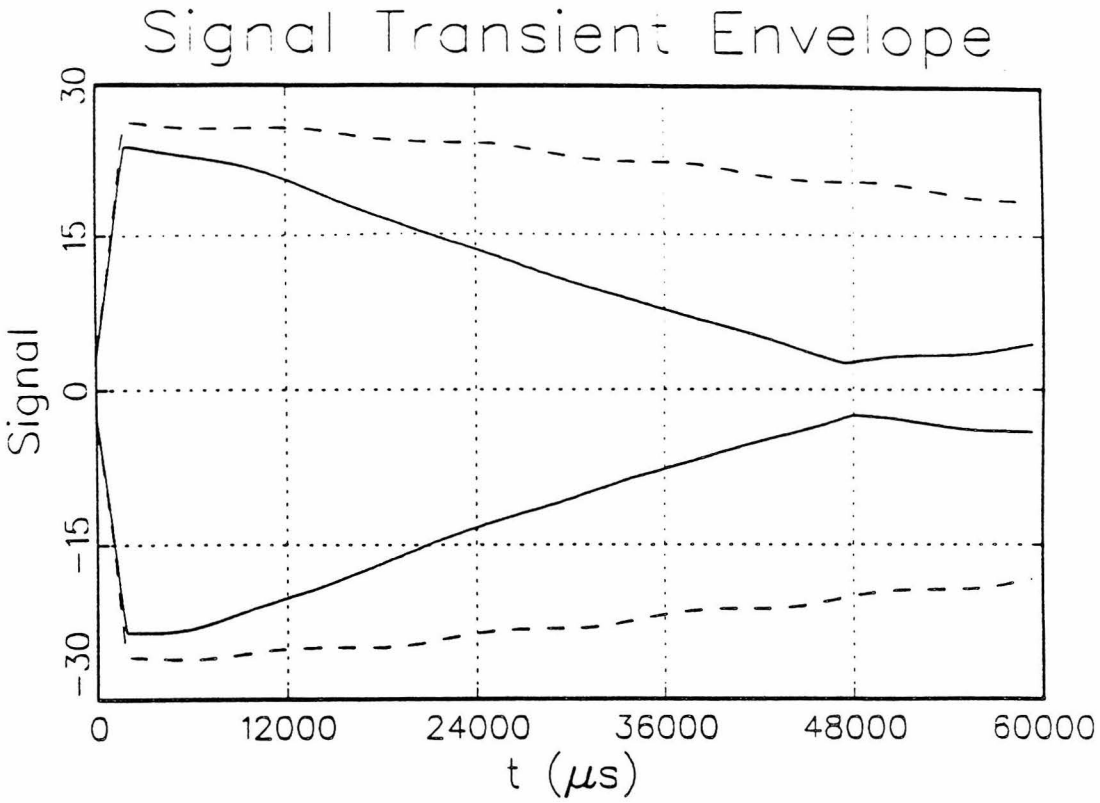
Signal Transient Envelope
Signal
30
15
0
−15
−30
0
12000
24000
36000
48000
60000
t (μs)

b)

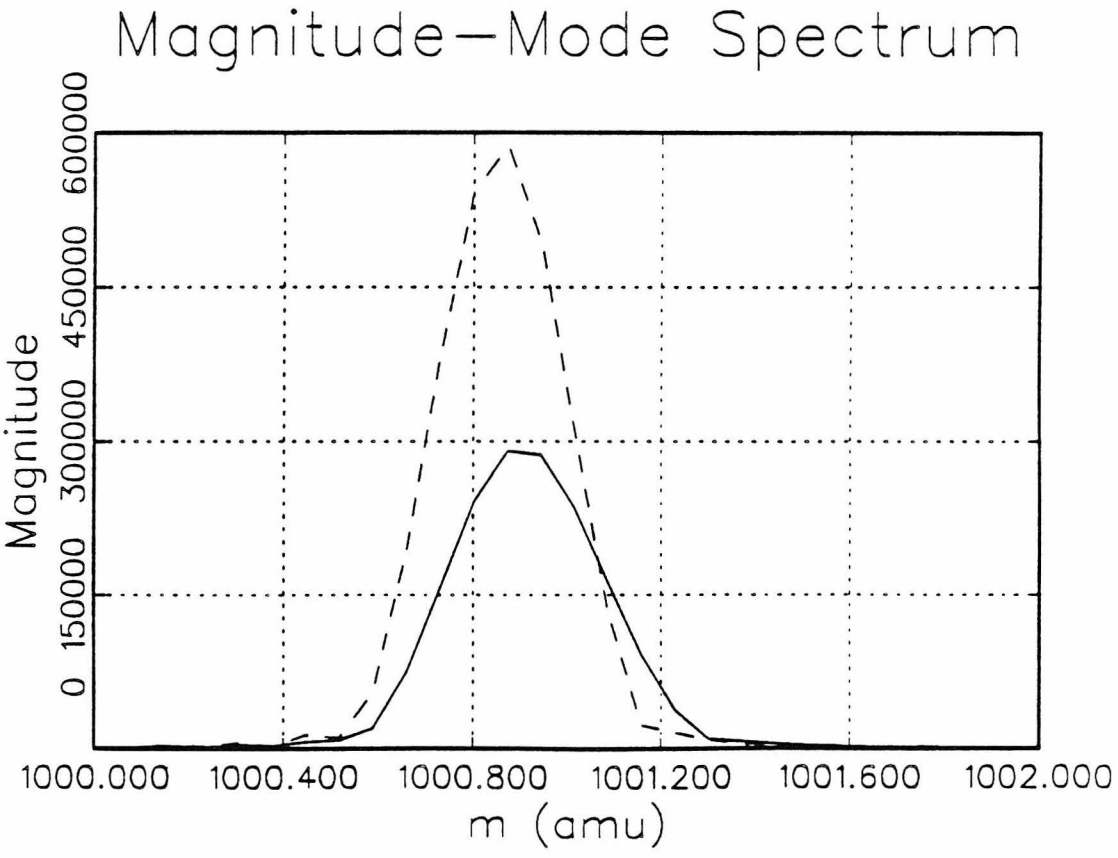
Magnitude−Mode Spectrum
Magnitude
0
150000
300000
450000
600000
1000.000
1000.400
1000.800
1001.200
1001.600
1002.000
m (amu)

Figure 9

a)

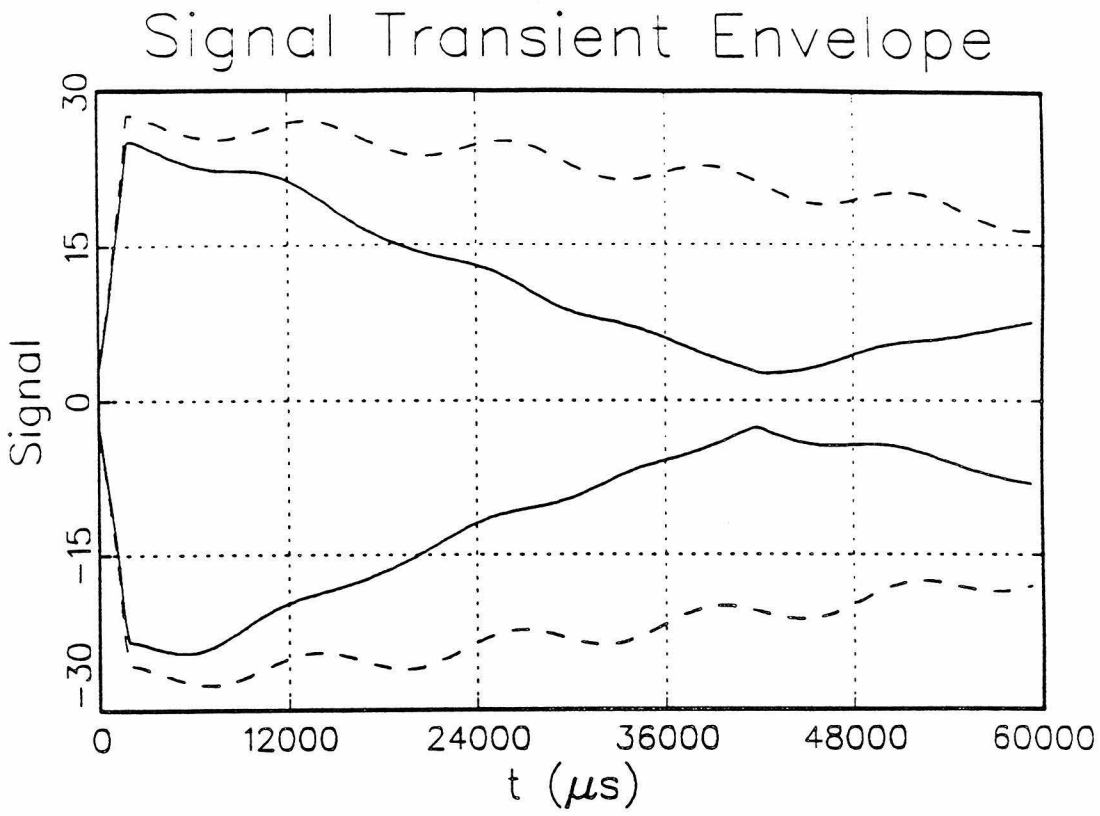
Signal Transient Envelope
Signal
30
15
0
-15
-30
0
12000
24000
36000
48000
60000
t (μs)

b)

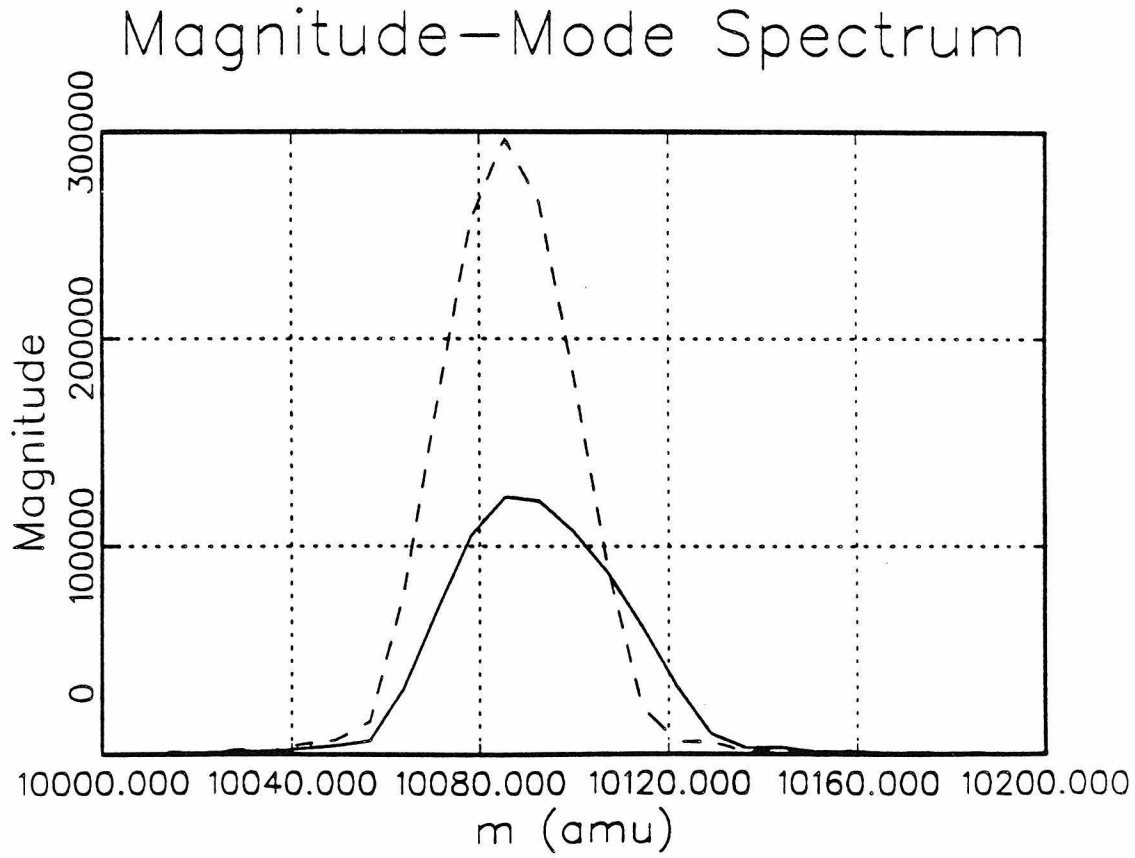
Magnitude-Mode Spectrum
Magnitude
300000
200000
100000
0
10000.000
10040.000
10080.000
10120.000
10160.000
10200.000
m (amu)

Figure 10

a)

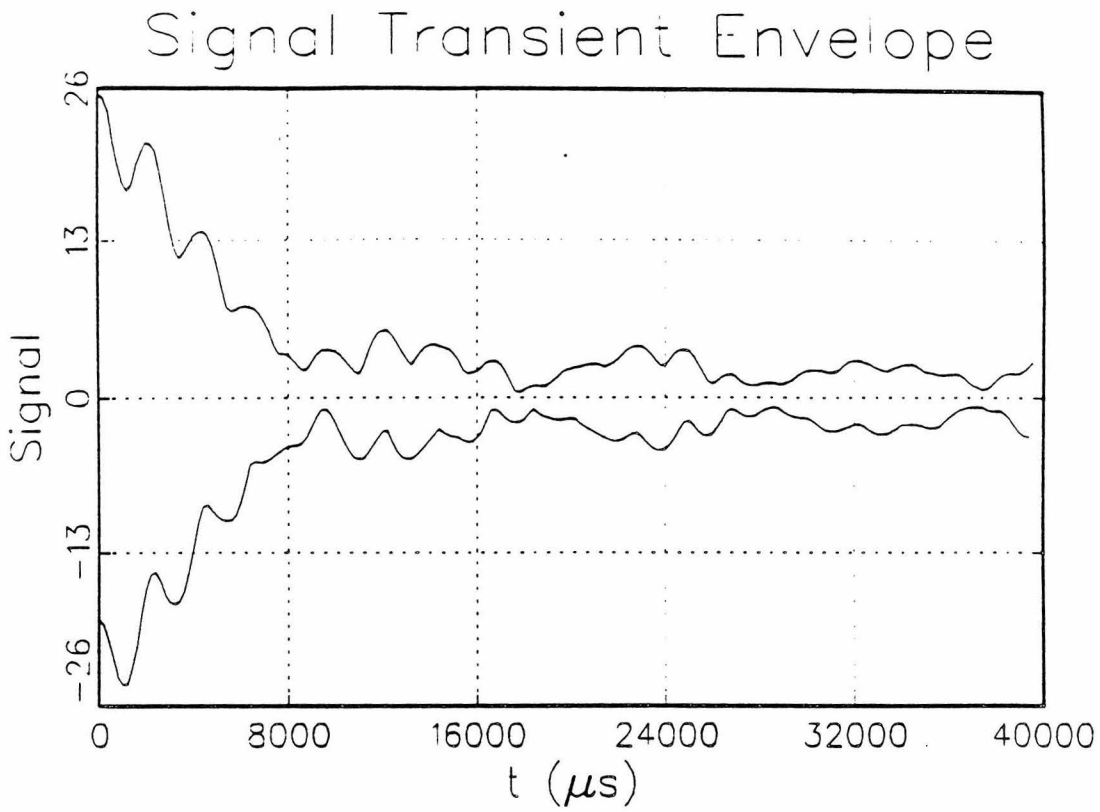
Signal Transient Envelope
Signal
26
13
0
-13
-26
0
8000
16000
24000
32000
40000
t (μs)

b)

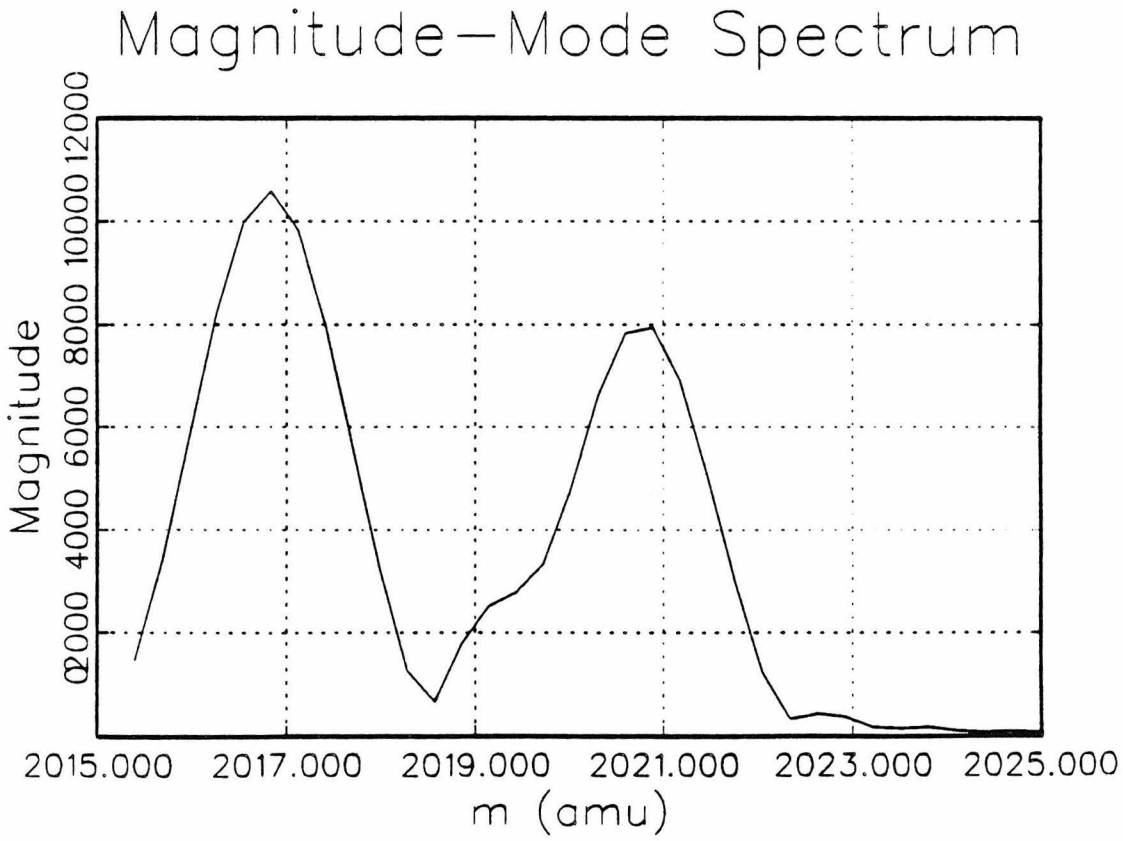
Magnitude-Mode Spectrum
Magnitude
12000
10000
8000
6000
4000
2000
2015.000
2017.000
2019.000
2021.000
2023.000
2025.000
m (amu)

Figure 11

a)

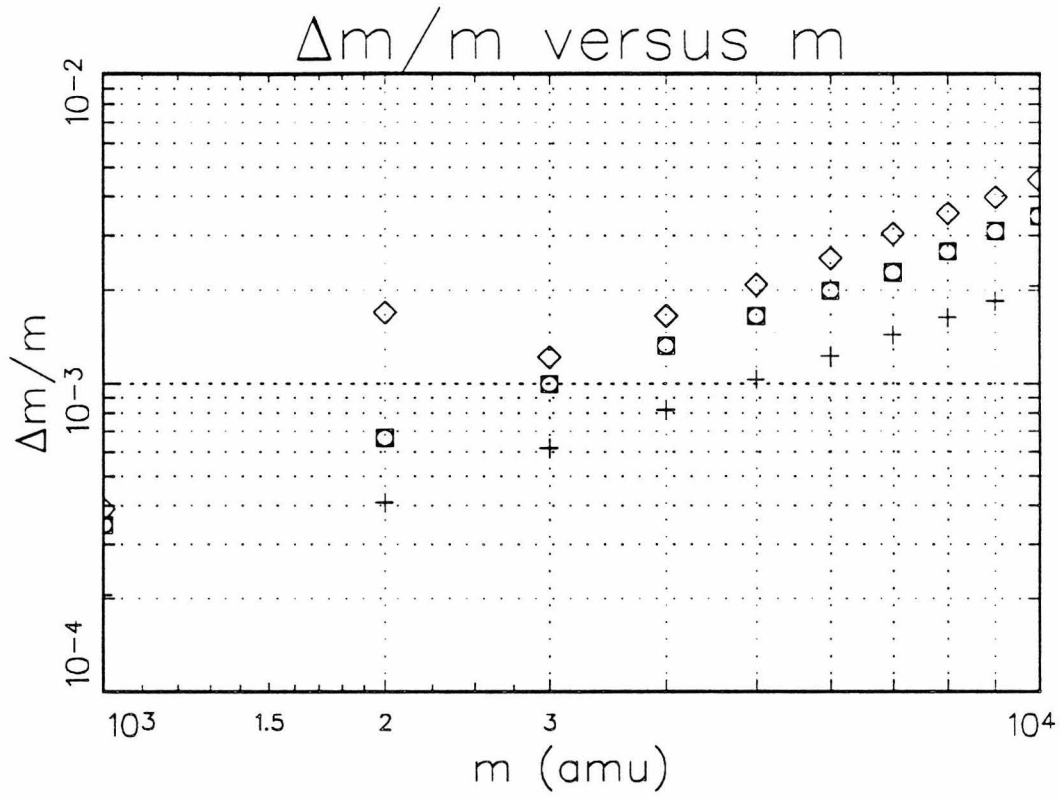
Δm/m versus m
Δm/m
10-2
10-3
10-4
10³
1.5
2
3
10⁴
m (amu)

b)

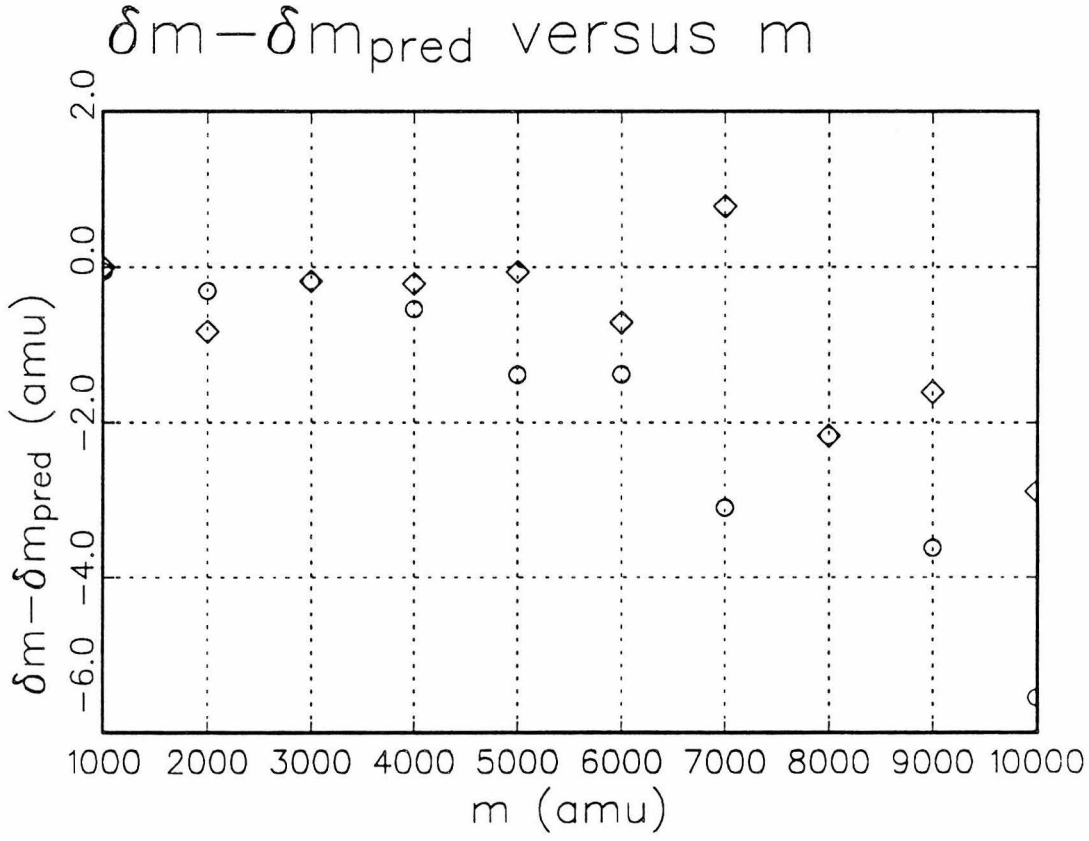
δm−δmpred versus m
δm−δmpred (amu)
2.0
0.0
-2.0
-4.0
-6.0
1000 2000 3000 4000 5000 6000 7000 8000 9000 10000
m (amu)

Figure 12

CHAPTER III

Numerical Evaluation of Space Charge Effects In Moderate Density, High m/z FT-ICR Studies

M. W. Deem and J. L. Beauchamp

California Institute of Technology, Pasadena, CA 91125

ABSTRACT

We report here a detailed numerical study of space charge effects on ion trajectories in a typical FT-ICR experiment. In particular, we focus on ions with high mass to charge ratios, 3000 amu/$|e^-|$ $\leq$ m/z $\leq$ 10000 amu/$|e^-|$, which are particularly relevant to experimental studies of clusters, polymers, or biomolecules. We assume excitation and trapping voltages of 1 V in the one inch cubic cell and a magnetic field of 7 T. We find essentially no discernable effect on the dephasing time, mass resolution, or mass shifts for ion densities below about 7×10^4 $|e^-|/cm^3$. That is, the natural inhomogeneous broadening due to the excitation fields[1] is far more deleterious to FT-ICR performance than are space charge effects.

INTRODUCTION

Ion-ion forces have long been thought to play a role in the performance of ion cyclotron resonance (ICR) spectrometers. Even the very first theoretical approaches to collision-broadening in ICR mention ion-ion effects.[2] Despite the long recognition of the issue, however, there has been no convincing analysis, either numerical or analytical, of the effects of Coulomb repulsion in ICR. Recently several approximate techniques, from 2-dimensional models[3,4] to a fixed, uniform charge cloud model[5], have been employed to study the problem. No exact calculations seem to have been done. We report here a numerical study of the effect of ion-ion repulsion on dephasing, mass resolution, and mass shifting in a typical FT-ICR cell. While our calculations are for fairly low ion densities, it should be noted that the trend among state of the art FT-ICR techniques is also towards low ion densities.

FT-ICR FIELD EQUATIONS

The electromagnetic fields within an ICR cell can be calculated from first principles. Figure 1 depicts the differential excitation/detection cell to which we refer.[6] The geometry of this cubic ICR cell allows Laplace's equation to be separated, and an analytical form for the trapping field can be obtained. If the ion velocities and accelerations due to the fields are nonrelativistic[7], the excitation field is time-separable and is obtained by multiplying a time-independent solution to Laplace's equation by the desired modulation factor. Furthermore, the Green function for the cube can be used to derive the difference between the total charges induced on opposite, parallel cube faces, which will be assumed proportional to the experimentally

measured signal. Given the fundamental solution[1]

$$\phi(x,y,z) = \frac{16}{\pi^2} \sum_{\substack{m=1 \\ m\ odd}}^{\infty} \sum_{\substack{n=1 \\ n\ odd}}^{\infty} \frac{1}{mn} \sin\left(\frac{m\pi x}{L_x}\right) \sin\left(\frac{n\pi y}{L_y}\right) c_{mn}(z)$$

$$c_{mn}(z) = \left[\frac{\phi_0 e^{-\lambda(L_z - z)} - \phi_1 e^{\lambda z}}{e^{-\lambda L_z} - e^{\lambda L_z}} + \frac{\phi_1 e^{-\lambda z} - \phi_0 e^{\lambda(L_z - z)}}{e^{-\lambda L_z} - e^{\lambda L_z}} \right]$$

$$\lambda^2 = \frac{m^2\pi^2}{L_x^2} + \frac{n^2\pi^2}{L_y^2} \tag{1}$$

the trapping field is defined by

$$\phi_0 = \phi_1 = V_{trap}$$

$$and$$

$$U_{trap}(x,y,z,t) = \phi(x,y,z) \tag{2}$$

and the single-frequency excitation field is defined by

$$\phi_0 = -\phi_1 = V_{excite}$$

$$and$$

$$U_{excite}(x,y,z,t) = \phi(x,z,y) \sin(\omega t) \tag{3}$$

While the total induced charge difference is given by

$$Q_{obs} = Q_{ind}(0) - Q_{ind}(L_x) =$$

$$\frac{16}{\pi^2} \sum_{\substack{m=1 \\ m\ odd}}^{\infty} \sum_{\substack{n=1 \\ n\ odd}}^{\infty} \frac{1}{mn} \sin\left(\frac{m\pi y'}{L_y}\right) \sin\left(\frac{n\pi z'}{L_z}\right) \times$$

$$\frac{\sinh[\lambda x'] - \sinh[\lambda(L_x - x')]}{\sinh[\lambda L_x]} \tag{4}$$

These series, which are exponentially converging in m and n but nonuniformly converging at the walls with nonzero boundary conditions, will be used in the numerical integration of the equation of motion.

ION-ION EFFECTS

The above equations do not take into account the force experienced by an ion due to its own induced charges on the cell walls or due to the ions within the cell and their induced charges. The Green function[1] could be used to calculate both the self-self and self-other ion-ion interactions. Such a calculation, however, would take $O(N^2M^2)$, where N is the number of ions, and M is the order to which the Fourier expansion is taken. This approach requires a prohibitive amount of computer resources and has not been pursued here.

Instead, an approach based on image charges has been formulated. The requirements on the solution to Laplace's equation for a point source, the Green function, are that it possess the proper singularity at the source and that it vanish on the cube faces. Recall that if the boundary conditions were that the potential vanish on a plane, rather than on the six faces of the cube, the solution is the original source plus a source of the same magnitude but opposite sign at the mirror image position. Attempting to construct an image charge solution for the boundary conditions of the cube leads to an infinite number of sources external to the cube. Explicitly, the solution for a cube of length L is

$$\frac{q^2}{L}\sum_{i=-\infty}^{\infty}{}'\sum_{j=-\infty}^{\infty}{}'\sum_{k=-\infty}^{\infty}{}'\frac{(-1)^{i+j+k}}{\left[(i+x(i)-x_0)^2+(j+y(j)-y_0)^2+(k+z(k)-z_0)^2\right]^{\frac{1}{2}}} \tag{5}$$

where the prime indicates the infinite self-self i=j=k=0 term is skipped, and

$$x(i)=\begin{cases} x_0, & i \text{ even} \\ 1-x_0, & i \text{ odd} \end{cases} \tag{6}$$

where x_0 is normalized to be in [0,1], and with y(j) and z(k) defined similarly. Figure 2 depicts a k=0 slice of this potential. The significant feature of Eq. (5) is that it is a crystal summation. The unit cell of the crystal is made up of the (000), (001), (010), (011), (100), (101), (110), and (111) terms in the sum. The crystal is created replicating this unit cell, which has eight times the volume of the original ICR cell, in all directions.

Eq. (5) captures just the self-self image charges of the ICR problem. Incorporation of the additional ion-ion interactions is simple, however, requiring just a summation over all the image charges due to each of the N-1 additional ions. That is

$$\Phi_{ion\text{-}ion} =$$

$$\frac{q^2}{L}\sum_{m=1}^{N}\sum_{n=m}^{N}\sum_{i=-\infty}^{\infty}{}'\sum_{j=-\infty}^{\infty}{}'\sum_{k=-\infty}^{\infty}{}'\frac{(-1)^{i+j+k}}{\left[(i+x_n(i)-x_{m,0})^2+(j+y_n(j)-y_{m,0})^2+(k+z_n(k)-z_{m,0})^2\right]^{\frac{1}{2}}} \tag{7}$$

Where now the prime on the summation indicates the infinite i=j=k=0, m=n self-self term is neglected. The complete sum (7) is still a crystal lattice summation. That the

ion-ion interaction term can be formulated as a crystal summation is significant because efficient methods exist for the calculation of such sums ("Madelung sums"). The Ewald transformation is, perhaps, the most efficient technique for the evaluation of general crystal summations.[8] Since the crystal defined by Eq. (7) has zero dipole moment, the subtleties of nonuniform convergence and nonuniqueness associated with the $\mathbf{h}=\mathbf{0}$ term do not appear in this problem.[9] Because of the symmetry imposed by definition (6), the reciprocal space component of the Ewald transformation need be evaluated over only one octant of reciprocal space. That the crystal under consideration is cubic, however, permits the use of a recently derived approximation to the Ewald technique.[10] This technique expands summations such as Eq. (7) as the singular 1/r term plus corrections expanded in terms of Kubic Harmonics. The originators of this technique offer a variety of orders of approximations, we go up to KH_8, which they claim and we find gives a relative root mean square error in the potential of randomly placed charges of 2.4×10^{-3}. The relative error in the gradient (used to find the force) is about one order of magnitude greater. Since the ion-ion electric fields are about 10^{-5} smaller than the trapping fields, this level of approximation should be adequate. We will use either Eq. (7) or the further approximation of using just the singular 1/r term in Eq. (7) in our numerical calculations. That is

$$\Phi_{ion\text{-}ion}^{approx} = \frac{q^2}{L} \sum_{m=1}^{N} \sum_{n=m+1}^{N} \frac{1}{\left[(x_{n,0}-x_{m,0})^2 + (y_{n,0}-y_{m,0})^2 + (z_{n,0}-z_{m,0})^2 \right]^{\frac{1}{2}}} \tag{8}$$

Note that the force is not the negative gradient of Eq. (7) with the definition of Eq. (6). That is, the image charges must be kept fixed when applying the principle of virtual work to get the force.[11] Alternatively, view the image charges as actual charges, and apply Coulomb's law to get the force. Specifically, the coupling between a ion and its image charges implied by Eq. (6) should not be taken into account in the force calculation.

ROLE OF ION-ION FORCES IN DEPHASING

Before presenting calculations of the effects of ion-ion forces, we should mention the role that these effects have played in previous discussions of the motions of ICR ions. It is important to first note that neither ion-ion forces nor collisions are necessary to produce dephasing of ICR ions.[1] The inhomogeneous excitation and trapping fields produce a dephasing that depends on the magnetron radius and the amplitude of z-axis oscillation. This dephasing is not the nonsecular, T_1 energy loss[12] that is usually postulated in phenomenological equations of motion (appearing as a $-\xi\mathbf{v}$ term in the force).[13,14] It is a secular relaxation caused by a loss of phase coherence. In fact, such dephasing is usually ignored. A commonly referenced treatment of space charge effects is that of Jeffries.[5] This analysis assumes the ion cloud does not change its shape as it undergoes excitation and further cyclotron motion. Such an assumption, of course, precludes dephasing.

Note that the center of mass motion of an ion cloud under the influence of a spatial

varying external force depends on whether or not there are ion-ion interactions. Even under the approximation of the central Coulomb (1/r) force, the total force depends on the location of all the charges in the cloud, even if it does act on a center of mass pseudo-particle. Only if the external forces were constant (or linear[15]), would the spreading out of the ions caused by the repulsive ion-ion forces not affect the center of mass motion. We previously found that defining the observed signal as $Q_{obs} = \Sigma(x - \frac{1}{2}L_x)$ is not greatly in variance with the exact result of Eq. (4). This definition is the same os $Q_{obs} = N\, x_{cm}$. Even in this approximation, then, the observed signal is affected by a Coulomb ion-ion interaction.

EQUATION OF MOTION

The equation of motion for an ion excited at the expected (nonshifted) cyclotron frequency for a time τ is, then,

$$m\,\ddot{\boldsymbol{x}} = -q\nabla U_{trap}(\boldsymbol{x}) - q\nabla U_{excite}(\boldsymbol{x}, t)\,H(t) + q\dot{\boldsymbol{x}}\times\boldsymbol{B} + F_{ion\text{-}ion}$$
$$\boldsymbol{x}(0) = \boldsymbol{x}_0, \qquad \dot{\boldsymbol{x}}(0) = \boldsymbol{v}_0$$
$$H(t) = \begin{cases} 1, & t \le \tau \\ 0, & t > \tau \end{cases} \tag{9}$$

where $\mathbf{F}_{ion\text{-}ion}$ is $(1/4\pi\epsilon_0)$ times the force generated by either Eq. (7) or Eq. (8) The magnetic field **B** will be assumed a constant value, $B_0 = 7$ T, along the z-axis. For all our simulations, the trapping and excitation parameters are $V_{trap} = 1$ V, $V_{excite} = 1$ V, and $\tau = 2$ ms. Our calculations are intended to be appropriate for FT-ICR applications in which the z oscillation is large and is not allowed to relax. The intended applications for these calculations are the same as those in [1], and

motivation is provided therein for our initial conditions. The initial phase space distribution placed upon Eq. (9) is, accordingly, Maxwellian velocities and positions uniformly distributed in a cylinder centered at the middle of the cell with radius 0.05 cm, the axis of rotation the z-axis, and a length that is 80% of the trapping electrode spacing. The equation of motion, Eq. (9), is integrated numerically by VODE, a variable order, variable step size ODE integration package designed to deal with difficult to integrate, nonlinear equations. [16,17,18,19,20,21] The stable, backward differentiation formula algorithm (MF = 20) is used. For the trajectory calculations we specify a relative error (rtol) of 10^{-5} and an absolute error (atol) of 10^{-7}, which denotes five significant figure accuracy for integration over a reasonable time range. For consistency, Eqs. (2) and (3) are evaluated to a relative accuracy of five significant figures, with the series optimized to allow for precomputation of most of the constant terms. The calculations were carried out on the Connection Machine 2 at the Advanced Computing Research Facility, Mathematics and Computer Science Division, Argonne National Laboratory. This massively parallel machine has 16K processors, which allows computation of the $O(N^2)$ terms in Eqs. (7) or (8) in a reasonable amount of time. This machine does not, unfortunately, have hardware capability of double precision arithmetic, and our single precision calculations do suffer from a small bit of numerical error. The essential effect is a small bit of energy loss, resulting in slightly decreasing signal with time.

The mass spectra are derived from a discrete fast Fourier transform of the signal defined by Eq. (4).[1] In distinction with our previous work, we now sample Eq. (4)

only every 20 ms, so heterodyning is needed to get precise spectra.[12] That is, the sampled signal is multiplied by $\sin(\omega_c t)$, then Fourier transformed. The resulting frequency spectra will have a peak at +f which represents a peak at ω_c-f in the spectrum of the true signal. (Magnetron motion decreases the signal frequency.) It turns out that spurious peaks do not appear, so that we are able to neglect filtering of the signal, which would not be possible given our sampling rate.

SIMULATIONS

We performed simulations for m/z = 3000 to 10000 amu/$|e^-|$ with z=1 and 10. Table I lists the results of the computations. Figures 3-5 show the signal envelopes, x-y and x-y-z radii of gyration, and mass spectra obtained for selected masses with z=1. Any effect of ion-ion forces should be most significant at low mass values, for the force is independent of mass, and the acceleration, given by F/m, varies inversely with mass. From these Figures and from Table I, it can be concluded that ion-ion forces at this density, approximated by Eq. (8), have relatively little effect. An interesting phenomenon related to excitation is to be noted in the x-y-z radii of gyration. During the initial excitation, the amount of z-axis dispersion varies in a systematic way. This variation decays away approximately exponentially after excitation. This motion shows that there is a z-component to the excitation field that very definitely affects the ion trajectories.

Figures 6-8 report results for calculations with z=10. The effect of increasing z while

keeping m/z constant can be approximately understood as an increase in charge density. This is because an ion with $m=10\ m_0$, and $z=10\ z_0$ can be considered to be a cloud of 10 ions with $m=m_0$ and $z=z_0$. (This is an approximation because such a cloud would disperse.) Note that the mass spectra seem to be a bit more Lorentzian compared to those of Figures 3-5. This can be rationalized by noting that the ion signal has more of an exponential decay that do the signals of Figures 3-5. In the case of the ion-ion interaction calculations, the decay could be from dephasing. But in the case of no interaction, the decay can only be from numerical integration error.

Figure 9 illustrates a calculation with the accurate ion-ion interaction of Eq. (7) with $z=10$. The charges induced on the cell plates, which are opposite in sign to the ions, should exert an outward force on the ions, causing mass shifting to higher masses and, perhaps, dephasing. From the induced charge differences of Figures 3-9, it can be concluded that there is a substantial amount of charge on the plates, comparable in magnitude to the total charge of the ion cloud. It is apparent, however, that at this density there is so discernable space charge effect.

One way of observing an effect due to space charge is to increase the density. Figures 10-12 illustrate the result of placing a much more compacted initial ion distribution on Eq. (9). That is, the ions are started off in an cylinder of radius .05 cm, occupying 2% of the 1" z-axis. Thus the initial ion density is $3 \times 10^6\ |e^-|/cm^3$ for these $z=10\ |e^-|$ ions. For calculations under Eq. (8), (Figures 10-12), there is a

noticeable dispersion of the ions along the z-axis. This can be deduced by comparison of r_{xyz} for no interaction with that for Coulomb interaction. Also note that the ion-ion interaction seems to allow better randomization of the z-axis positions after excitation, for the maximum and minimum r_{xyz} are closer when such interactions are present. Figure 13 illustrates a similar calculation for the interaction of Eq. (7). The differences between Figure 12 and 13 are small, suggesting there is very little effect of the image charges.

FURTHER WORK

This research could be extended in several directions. First it is important to perform calculations for the accurate ion-ion potential, Eq. (7), since there is a substantial amount of charge induce on the cell plates, and we intuitively expect this to affect the ion motion. Higher ion densities could be approximated by performing simulations for z=100. The lower mass to charge values in the range 1000 to 10000 amu/$|e^-|$ should be examined. Finally, and most distinct from the results presented here, the effects of ion-ion forces when there are two species with distinct m/z values present in the ion cell could be explored. It has long been speculated that the ion-ion repulsion results in different excitation amplitudes in this case, but the issue has yet to be quantitatively examined.

CONCLUSIONS

Ion-ion forces, when approximated by a Columbic (1/r) interaction, have almost no effect on dephasing, mass resolution, or mass shifts in FT-ICR spectra of low density

($\rho \leq 7 \times 10^4$ $|e^-|/cm^3$) ion clouds. For the case of m/z=10000 amu/$|e^-|$, our simulations with exact ion-ion interactions given the cubic boundary conditions appropriate for an ICR cell again show relatively little effect. We cannot say whether image forces or even simply Coulomb forces will play an important role at higher ion densities or lower masses.

ACKNOWLEDGEMENTS

The Connection Machine time required for this research was obtained from the Caltech Concurrent Supercomputer Facility and is supported by the NSF under Cooperative Agreement No. CCR-8809615. The government has certain rights in this material.

REFERENCES

(1) M. W. Deem and J. L. Beauchamp, A Fundamental Mass Resolution Limit of the Conventional FT-ICR Cubic Cell, to appear in Int. J. Mass Spectrom. Ion Proc. 1991.

(2) J. L. Beauchamp, J. Chem. Phys., 46, (1967) 1231.

(3) Tao-Chin Lin Wang and Alan G. Marshall, Int. J. Mass Spectrom. Ion Proc. 68 (1986) 287.

(4) Guy T. Euchi and Robert C. Dunbar, personal communication, 1991.

(5) J. B. Jeffries, S. E. Barlow, and G. H. Dunn, Int. J. Mass Spectrom. Ion Proc. 54 (1983) 169.

(6) Melvin B. Comisarow, Int. J. Mass Spec. Ion Phys. 37 (1981) 251-257.

(7) M. H. Friedman, A. L. Yergey, and J. E. Campana, J Phys. E. 15 (1982) 53-72.

(8) B. R. A. Nijboer and F. W. de Wette, Physica, XXIII, (1957) 309.

(9) M. W. Deem, J. M. Newsam, and S. K. Sinha, J. Phys. Chem. 94 (1990) 8356.

(10) D. J. Adams and G. S. Dubey, J. Compt. Phys. 72 (1987) 156.

(11) J. D. Jackson, Classical Electrodynamics, 2nd ed., John Wiley & Sons: New York, 1975.

(12) Alan G. Marshall and Francis R. Verdun, Fourier Transforms in NMR, Optical, and Mass Spectrometry, Elsevier: Amsterdam, 1990.

(13) D. L. Rempel, R. P. Grese, and M. L. Gross, Int. J. Mass Spectrom. Ion Proc. 100, (1990).

(14) Edward B. Ledford, Jr., Don L. Rempel, and M. L. Gross, Anal. Chem. 56 (1984) 2744.

(15) H. Dehmelt and D. J. Wineland, Bull. Am. Phys. Soc. 18 (1973) 1571.

(16) P. N. Brown, G. D. Byrne, and A. C. Hindmarsh, "VODE, a Variable Coefficient ODE Solver," LLNL Report UCRL-98412, June 1988. Also, SIAM J. Sci. Stat. Comput., to appear.

(17) G. D. Byrne and A. C. Hindmarsh, ACM Trans. Math. Software 1 (1975) 71.

(18) A. C. Hindmarsh and G. D. Byrne, "EPISODE: An Effective Package for the Integration of Systems of Ordinary Differential Equations," LLNL Report UCID-30112, Rev. 1, April 1977.

(19) G. D. Byrne and A. C. Hindmarsh, "EPISODEB: An Experimental Package for the Integration of Systems of Ordinary Differential Equations with Banded Jacobians," LLNL Report UCID-30132, April 1976.

(20) A. C. Hindmarsh, Scientific Computing, R. S. Stepleman et al., eds., North-Holland, Amsterdam, 1983, pp. 55-64.

(21) K. R. Jackson and R. Sacks-Davis, ACM Trans. Math. Software 6 (1980) 295.

TABLE I

m/z amu/|e⁻|	z |e⁻|	Interaction (Eq)	N	$\tau_{dephase}$ (ms)	Δm/m	δm (amu)
3000	1	none	120	50	0.0012	5.06
3000	1	8	120	52	0.0012	7.13
3000	10	none	120	54	0.0012	52.5
3000	10	8	120	45	0.0013	75.0
4000	1	none	120	54	0.0015	13.2
4000	1	8	120	51	0.0016	14.5
4000	10	none	120	53	0.0018	139
4000	10	8	120	44	0.0018	139
5000	1	none	120	48	0.0021	21.9
5000	1	8	120	50	0.0019	21.4
5000	10	none	120	45	0.0022	214
5000	10	8	120	43	0.0022	214
6000	1	none	120	55	0.0023	30.8
6000	1	8	120	49	0.0024	30.6
6000	10	none	120	46	0.0024	287
6000	10	8	120	43	0.0026	310
7000	1	none	120	48	0.0028	43.4
7000	1	8	120	48	0.0028	43.8
7000	10	none	120	46	0.0027	420
7000	10	8	120	42	0.0032	397
8000	1	none	120	46	0.0033	54.8
8000	1	8	120	46	0.0032	54.8
8000	10	none	120	46	0.0034	548
8000	10	8	120	43	0.0037	548
9000	1	none	120	45	0.0037	69.4
9000	1	8	120	46	0.0036	69.3
9000	10	none	120	43	0.0041	653
9000	10	8	120	41	0.0043	693
10000	1	none	120	51	0.0032	90.0
10000	1	8	120	45	0.0041	86.1
10000	1	7	120	45	0.0042	86.1
10000	1	none	500	46	0.0041	90.0
10000	1	8	500	44	0.0045	86.1
10000	10	none	120	42	0.0047	822
10000	10	8	120	41	0.0048	822
10000	10	7	120	41	0.0047	813

FIGURES

Figure 1. Depicted is the FT-ICR cell and coordinate system for which our calculations are appropriate. The direction of **B** is along the z-axis as indicated. Also indicated are the trapping, excitation, and detection plates.

Figure 2. Depicted is a k=0 slice of the potential given by Eq. (5). In this case, $x_0 = 0.2$ and $y_0 = 0.6$. The dotted lines delineate the crystal in units of ICR cell size. The solid lines delineate the unit cells of the crystal. The dashed box indicates the single, original ICR cell.

Figure 3. Depicted are the signal (a,b), x-y and x-y-z radii of gyration (c,d), and mass spectra (e,f) for a calculation with 120 ions with m=3000 amu and z=1 $|e^-|$. In each pair, the first figure is for no interaction, and the second is for the ion-ion interaction specified by Eq. (8). The radii of gyration are defined as
$r_{xy} = \{ \Sigma [(x-x_{cm})^2 + (y-y_{cm})^2]/N \}^{1/2}$ and
$r_{xyz} = \{ \Sigma [(x-x_{cm})^2 + (y-y_{cm})^2 + (z-z_{cm})^2]/N \}^{1/2}$. The trapping and excitation parameters are $V_{trap} = 1$ V, $V_{excite} = 1$ V, and $\tau = 2$ ms.

Figure 4. Depicted are the signal (a,b), x-y and x-y-z radii of gyration (c,d), and mass spectra (e,f) for m=7000 amu and z=1 $|e^-|$. The calculation is for 120 ions with no interaction and with the interaction of Eq. (8).

Figure 5. Depicted are the signal (a,b), x-y and x-y-z radii of gyration (c,d), and mass spectra (e,f) for m=10000 amu and z=1 $|e^-|$. The calculation is for 120 ions with no interaction and with the interaction of Eq. (8).

Figure 6. Depicted are the signal (a,b), x-y and x-y-z radii of gyration (c,d), and mass spectra (e,f) for m=30000 amu and z=10 $|e^-|$. The calculation is for 120 ions with no interaction and with the interaction of Eq. (8).

Figure 7. Depicted are the signal (a,b), x-y and x-y-z radii of gyration (c,d), and mass spectra (e,f) for m=70000 amu and z=10 $|e^-|$. The calculation is for 120 ions with no interaction and with the interaction of Eq. (8).

Figure 8. Depicted are the signal (a,b), x-y and x-y-z radii of gyration (c,d), and mass spectra (e,f) for m=100000 amu and z=10 $|e^-|$. The calculation is for 120 ions with no interaction and with the interaction of Eq. (8).

Figure 9. Depicted are the signal (a,b), x-y and x-y-z radii of gyration (c,d), and mass spectra (e,f) for m=100000 amu and z=10 $|e^-|$ for the exact ion-ion interaction of Eq. (7). The calculation is for 120 ions.

Figure 10. Depicted are the signal (a,b), x-y and x-y-z radii of gyration (c,d), and mass spectra (e,f) for a calculation with 120 ions with m=40000 amu and z=10 $|e^-|$, with the compacted initial distribution placed on Eq. (9). The interaction is Eq. (8).

Figure 11. Depicted are the signal (a,b), x-y and x-y-z radii of gyration (c,d), and mass spectra (e,f) for a calculation with 120 ions with m=70000 amu and z=10 $|e^-|$, with the compacted initial distribution placed on Eq. (9). The interaction is Eq. (8).

Figure 12. Depicted are the signal (a,b), x-y and x-y-z radii of gyration (c,d), and mass spectra (e,f) for a calculation with 120 ions with m=100000 amu and z=10 $|e^-|$, with the compacted initial distribution placed on Eq. (9). The interaction is Eq. (8).

Figure 13. Depicted are the signal (a,b), x-y and x-y-z radii of gyration (c,d), and mass spectra (e,f) for a calculation with 120 ions with m=10000 amu and z=10 $|e^-|$, with the compacted initial distribution placed on Eq. (9). The interaction is the exact Eq. (7).

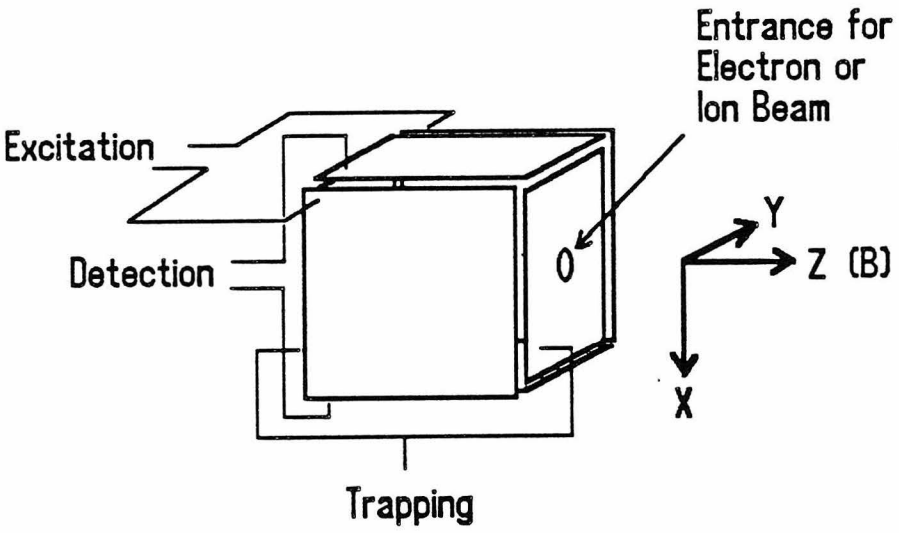
Entrance for
Electron or
Ion Beam
Excitation
Detection
O
Y
Z (B)
X
Trapping

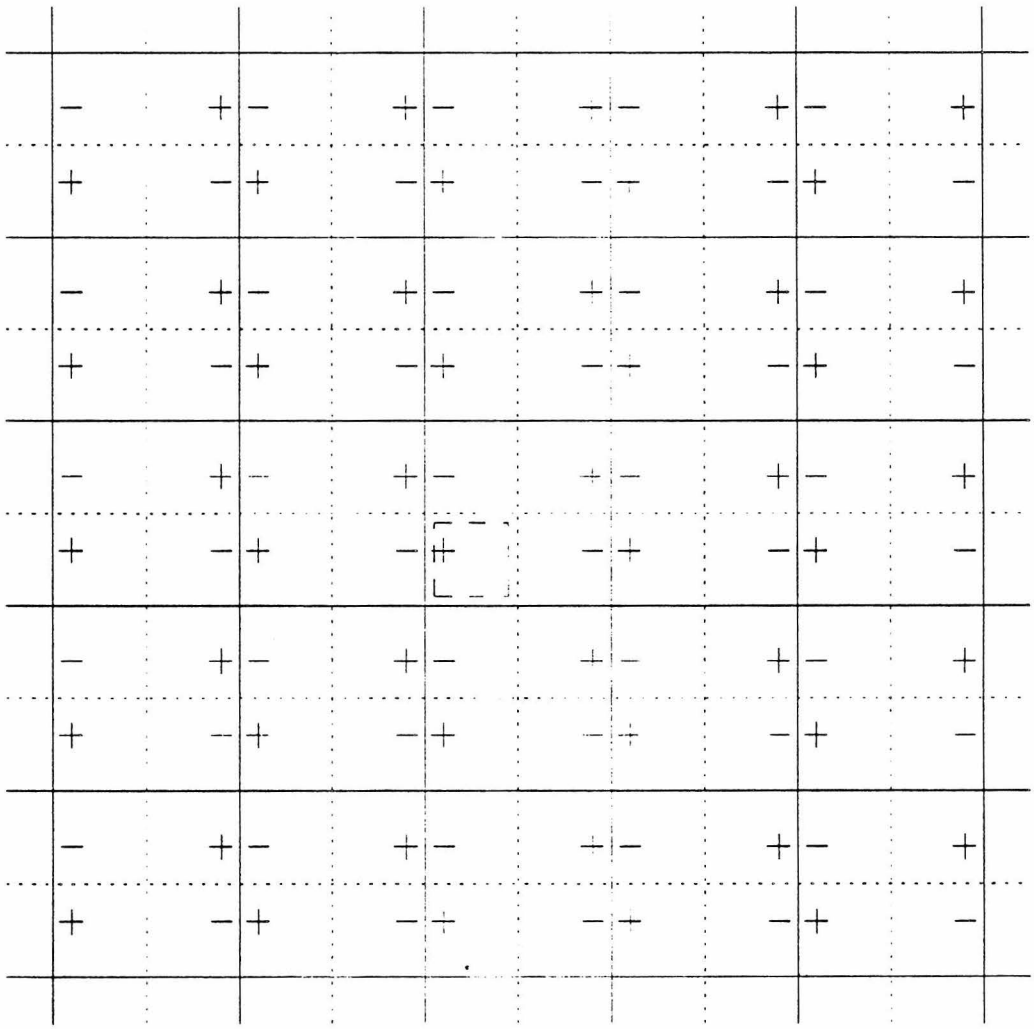

3a

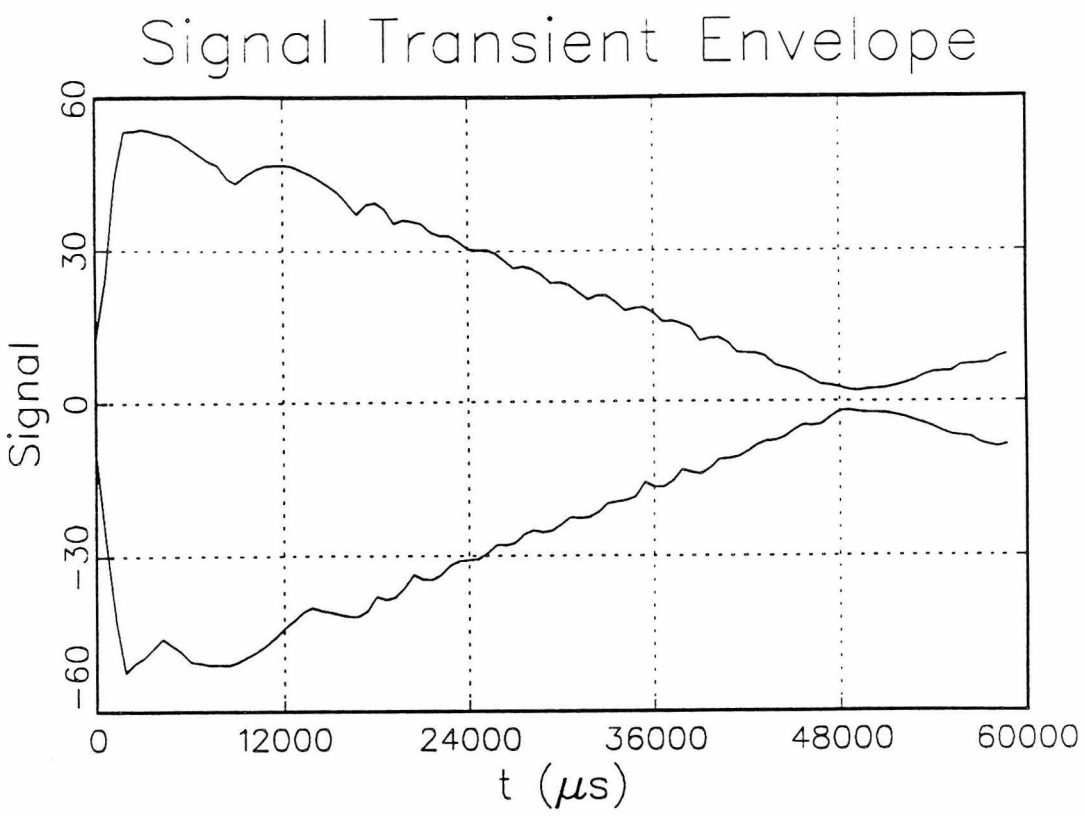
Signal Transient Envelope
Signal
60
30
0
−30
−60
0
12000
24000
36000
48000
60000
t (μs)

3b

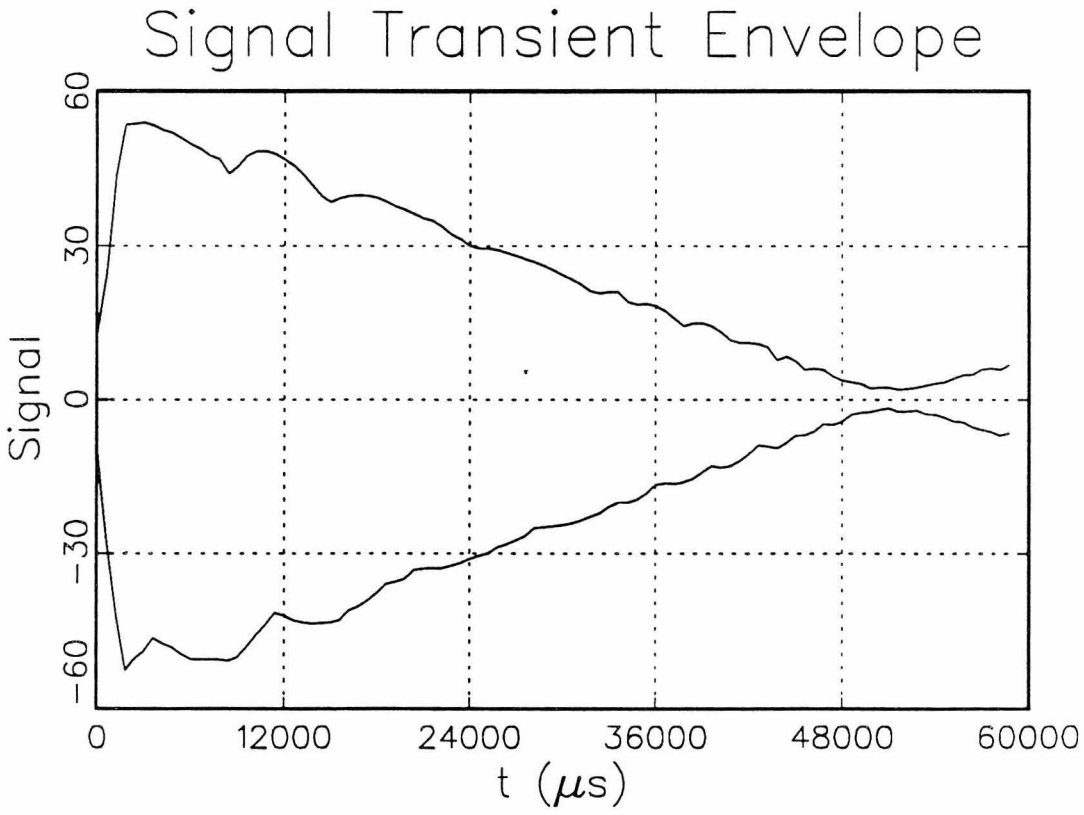
Signal Transient Envelope
Signal
60
30
0
−30
−60
0
12000
24000
36000
48000
60000
t (μs)

3c

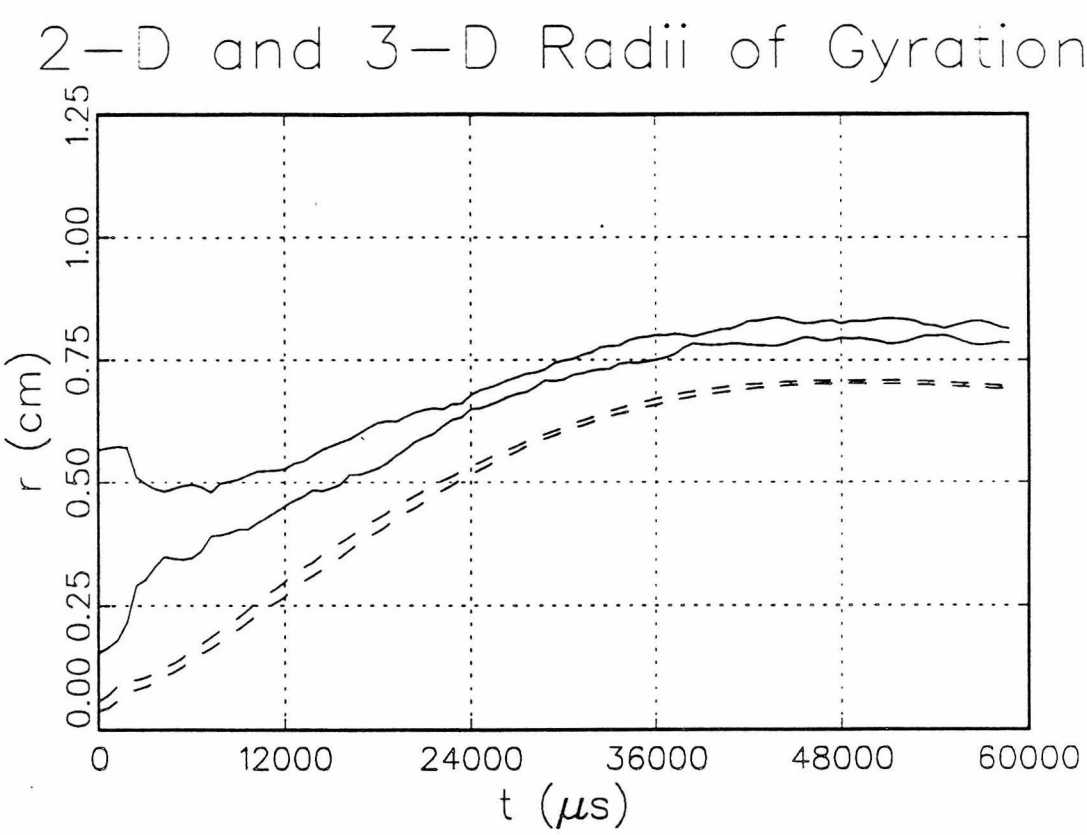
2−D and 3−D Radii of Gyration
r (cm)
0.00
0.25
0.50
0.75
1.00
1.25
0
12000
24000
36000
48000
60000
t (μs)

3d

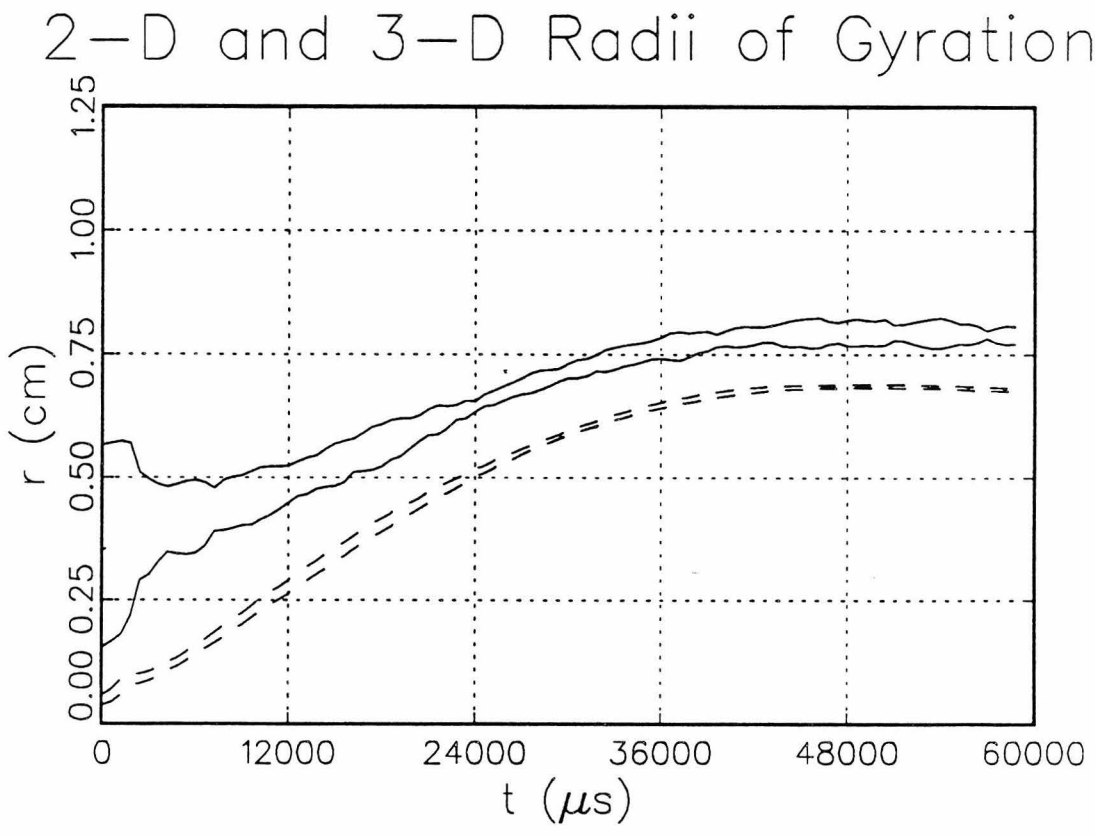
2−D and 3−D Radii of Gyration
r (cm)
0.00
0.25
0.50
0.75
1.00
1.25
0
12000
24000
36000
48000
60000
t (μs)

3e

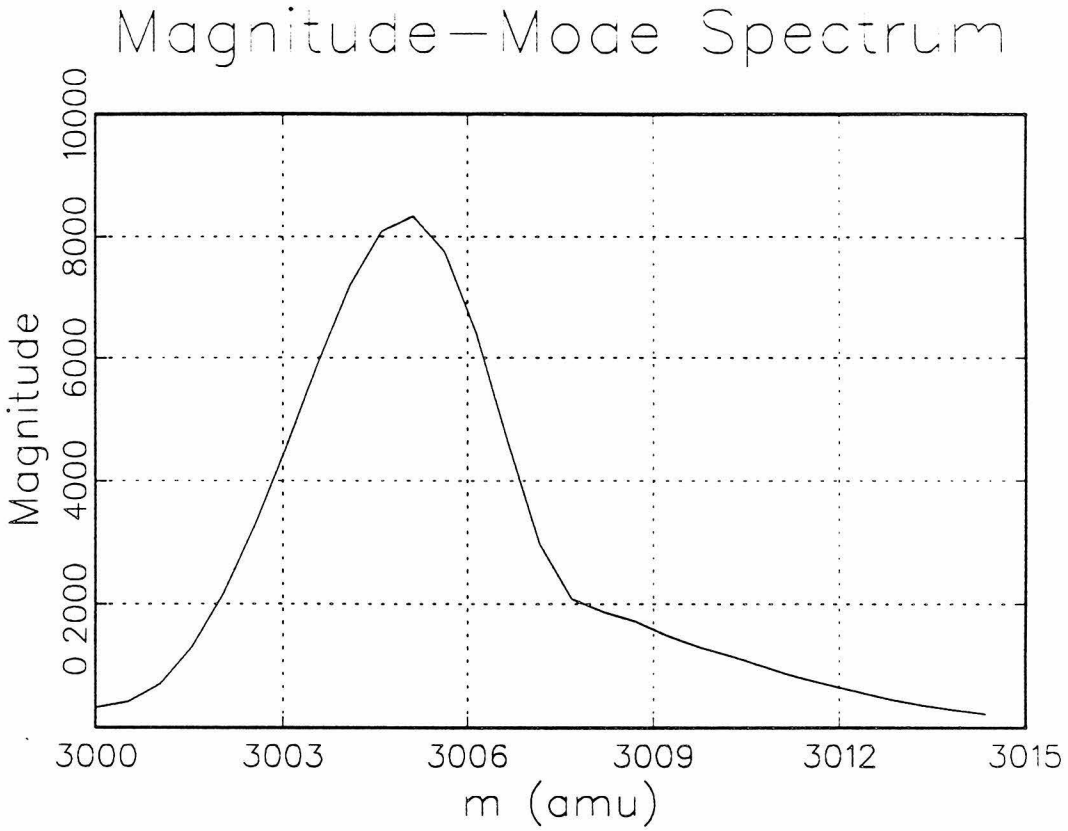
Magnitude–Mode Spectrum
Magnitude
0 2000 4000 6000 8000 10000
3000 3003 3006 3009 3012 3015
m (amu)

3f

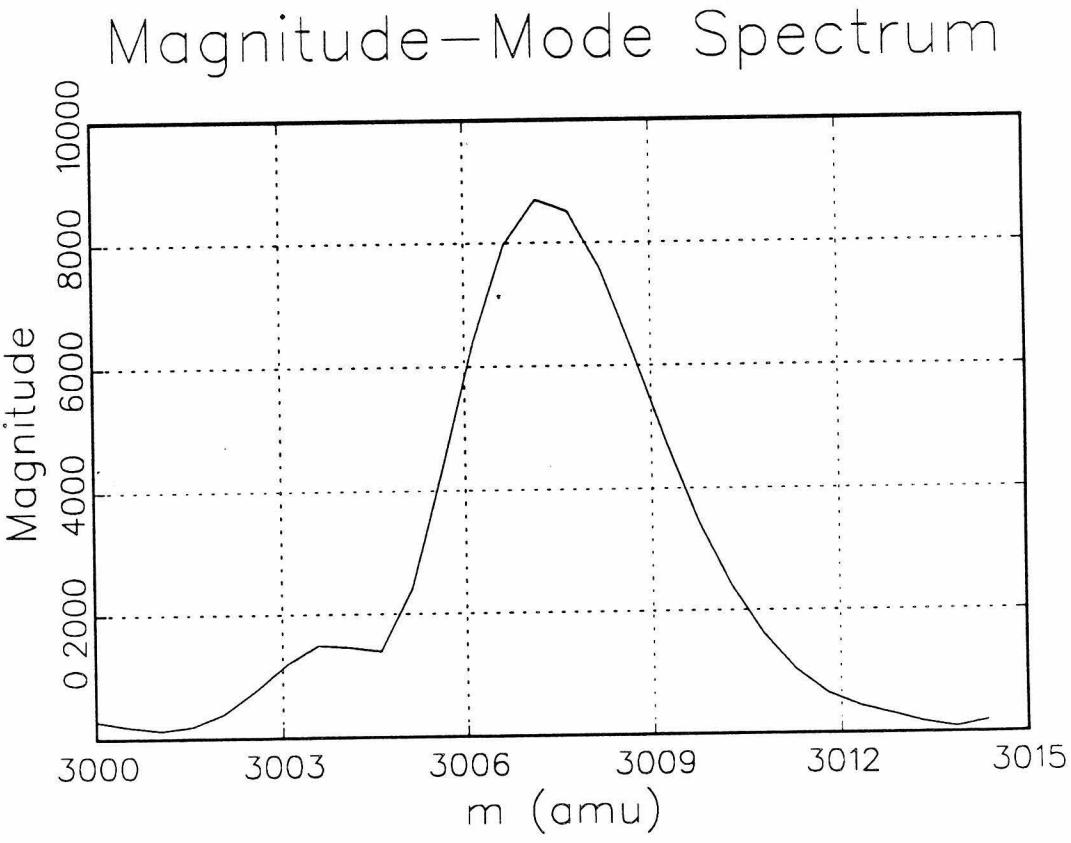
Magnitude–Mode Spectrum
Magnitude
0 2000 4000 6000 8000 10000
3000 3003 3006 3009 3012 3015
m (amu)

4 a

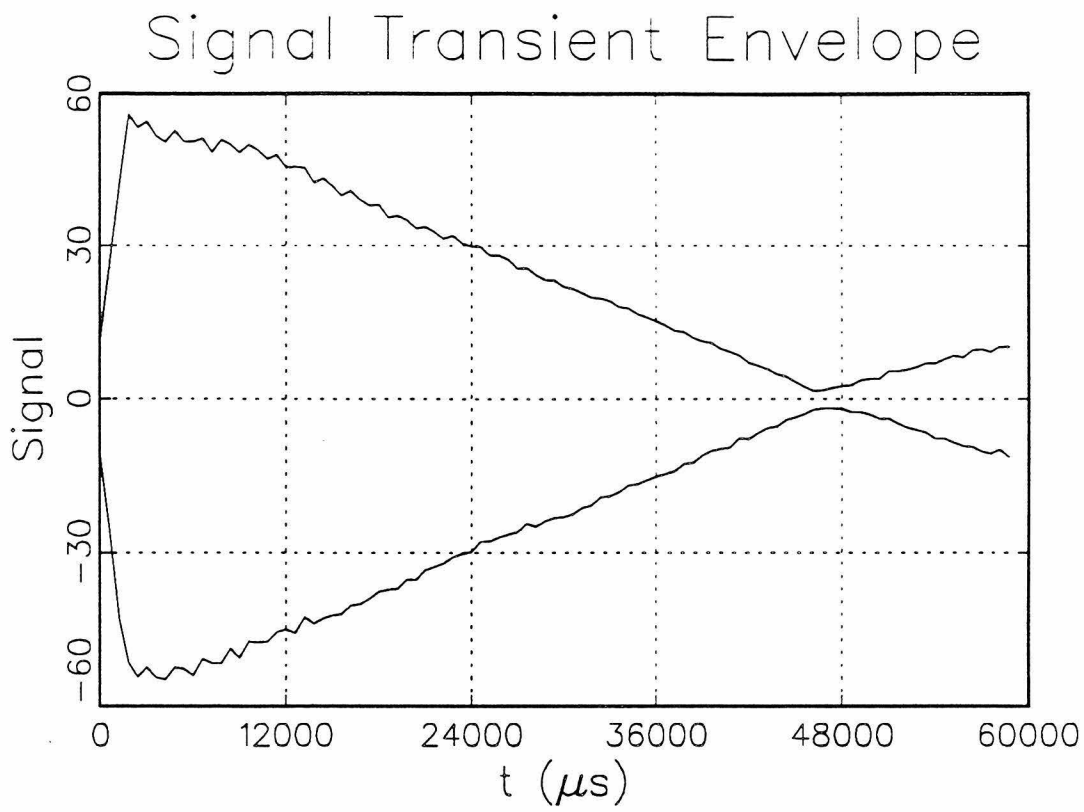
Signal Transient Envelope
Signal
60
30
0
−30
−60
0
12000
24000
36000
48000
60000
t (μs)

4 b

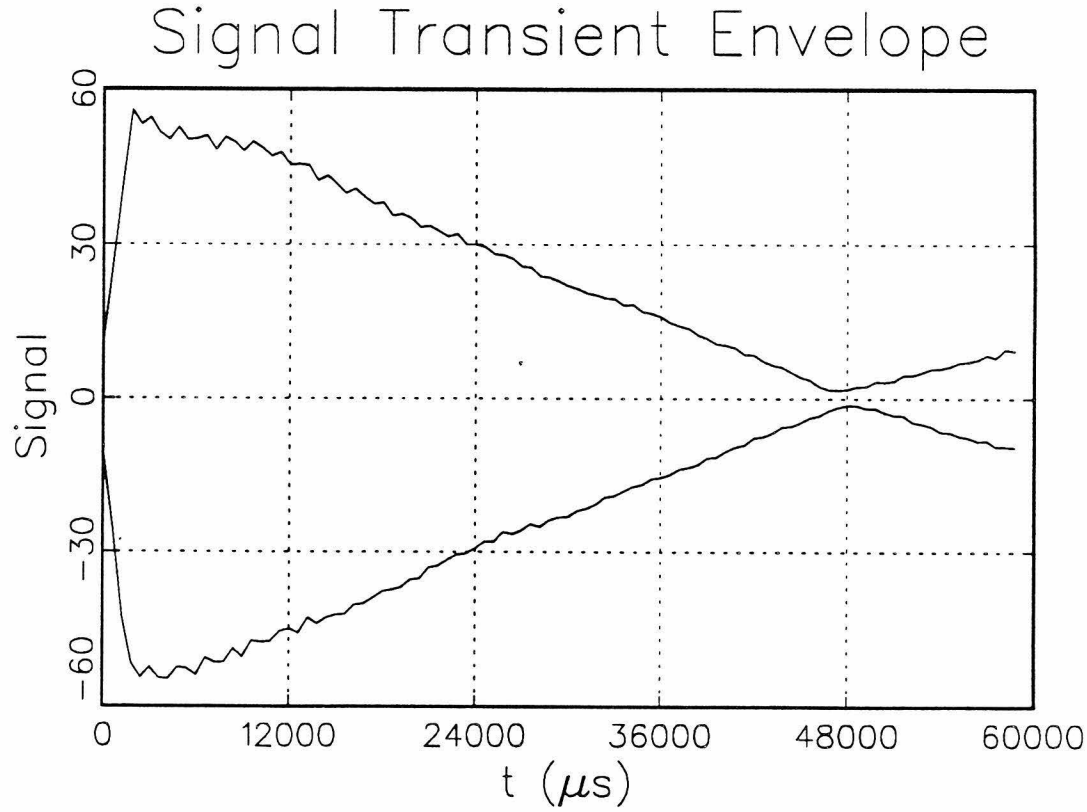
Signal Transient Envelope
Signal
60
30
0
−30
−60
0
12000
24000
36000
48000
60000
t (μs)

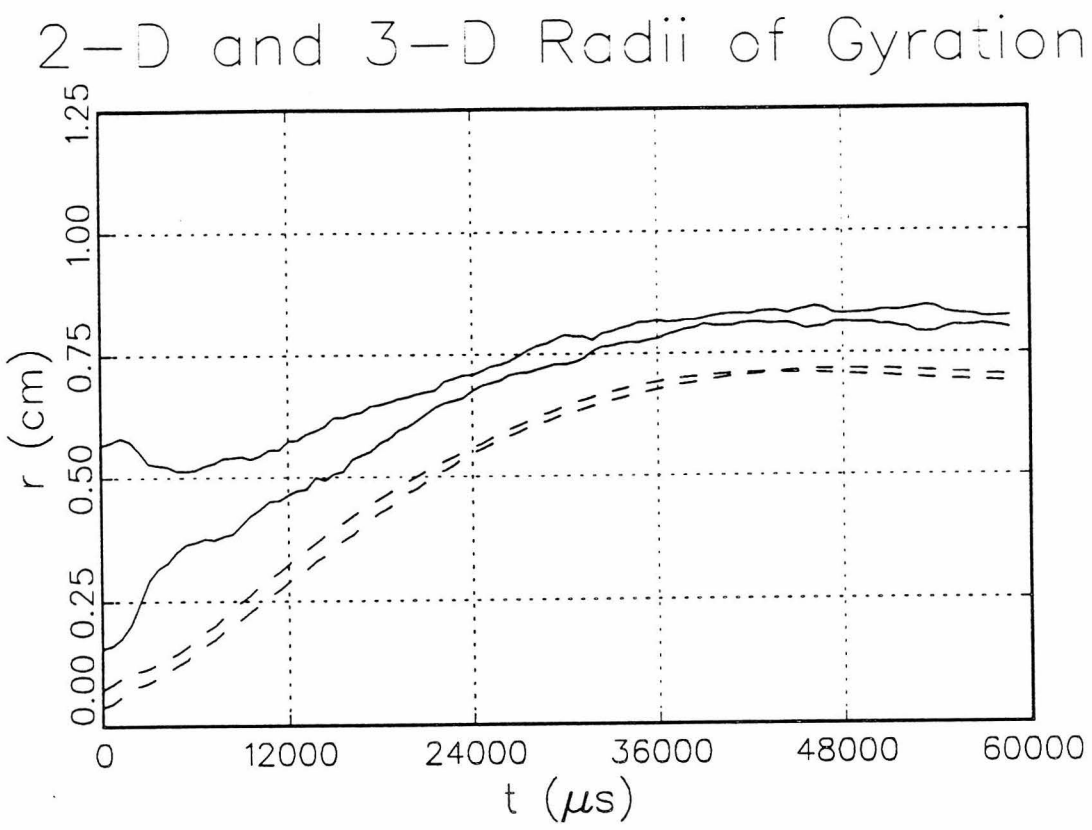
2−D and 3−D Radii of Gyration
r (cm)
0.00
0.25
0.50
0.75
1.00
1.25
0
12000
24000
36000
48000
60000
t (μs)

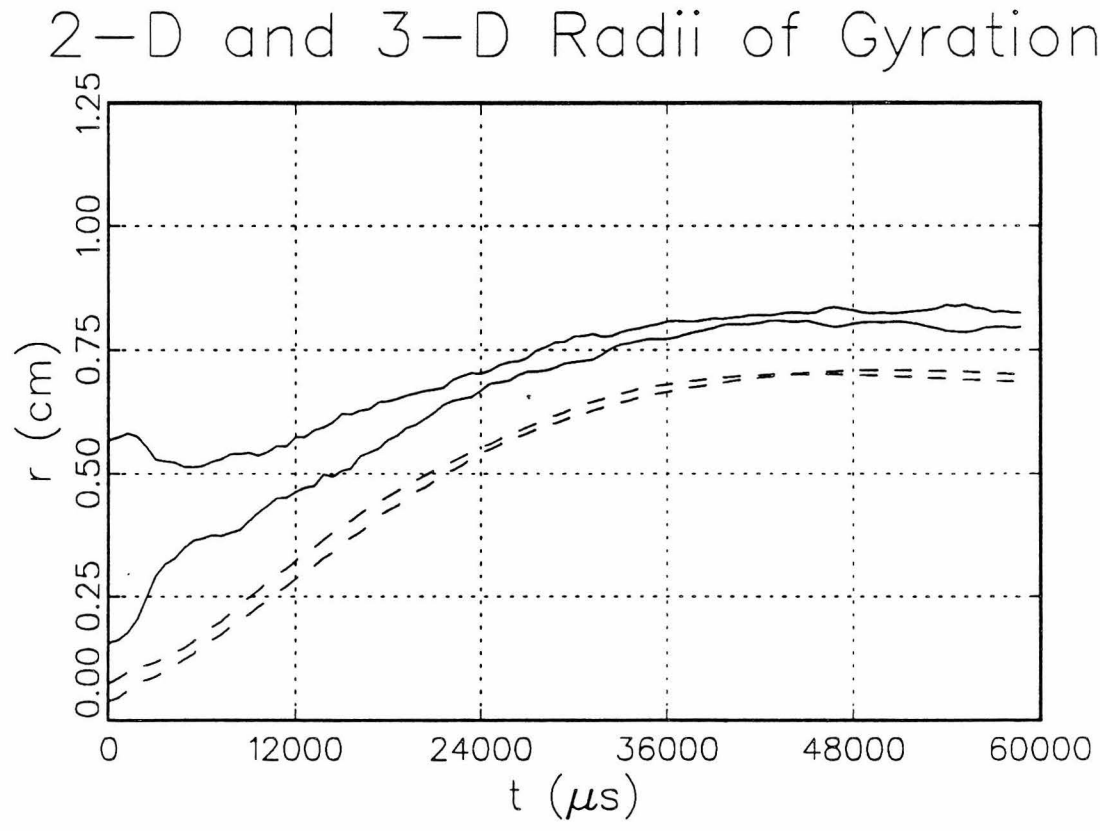
2−D and 3−D Radii of Gyration
r (cm)
0.00
0.25
0.50
0.75
1.00
1.25
0
12000
24000
36000
48000
60000
t (μs)

4 . e

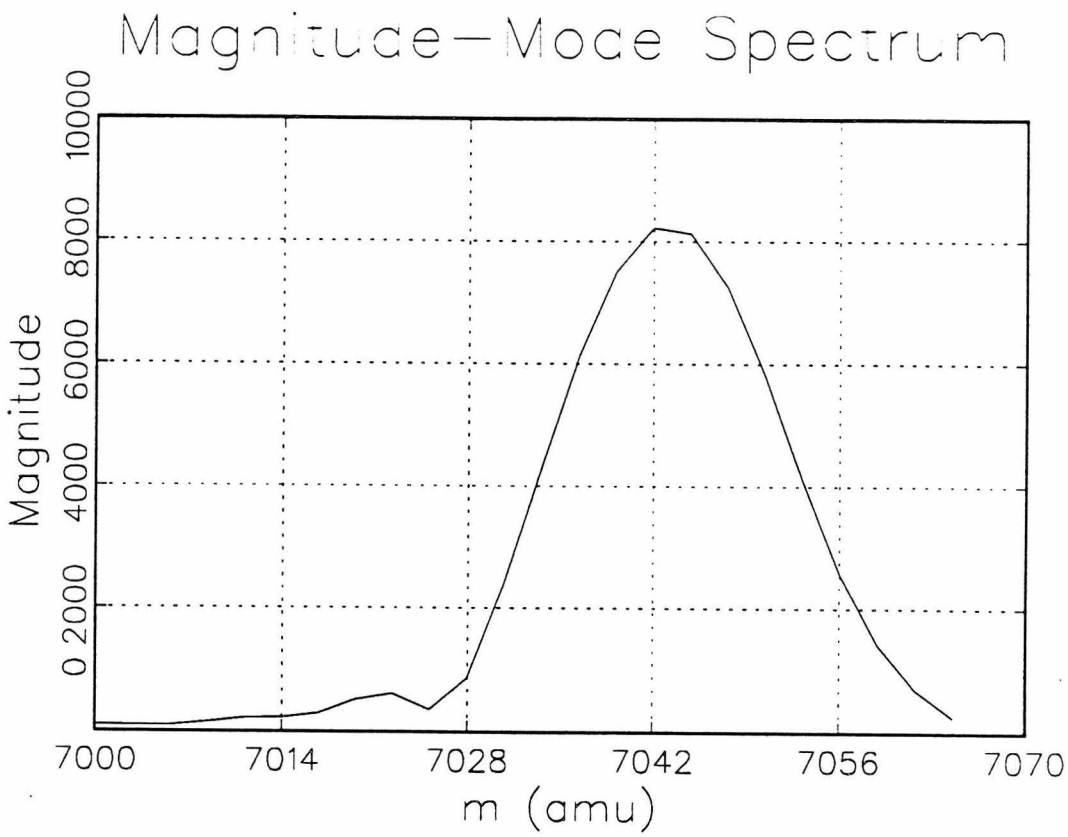
Magnitude—Mode Spectrum
Magnitude
0 2000 4000 6000 8000 10000
7000 7014 7028 7042 7056 7070
m (amu)

4 . f

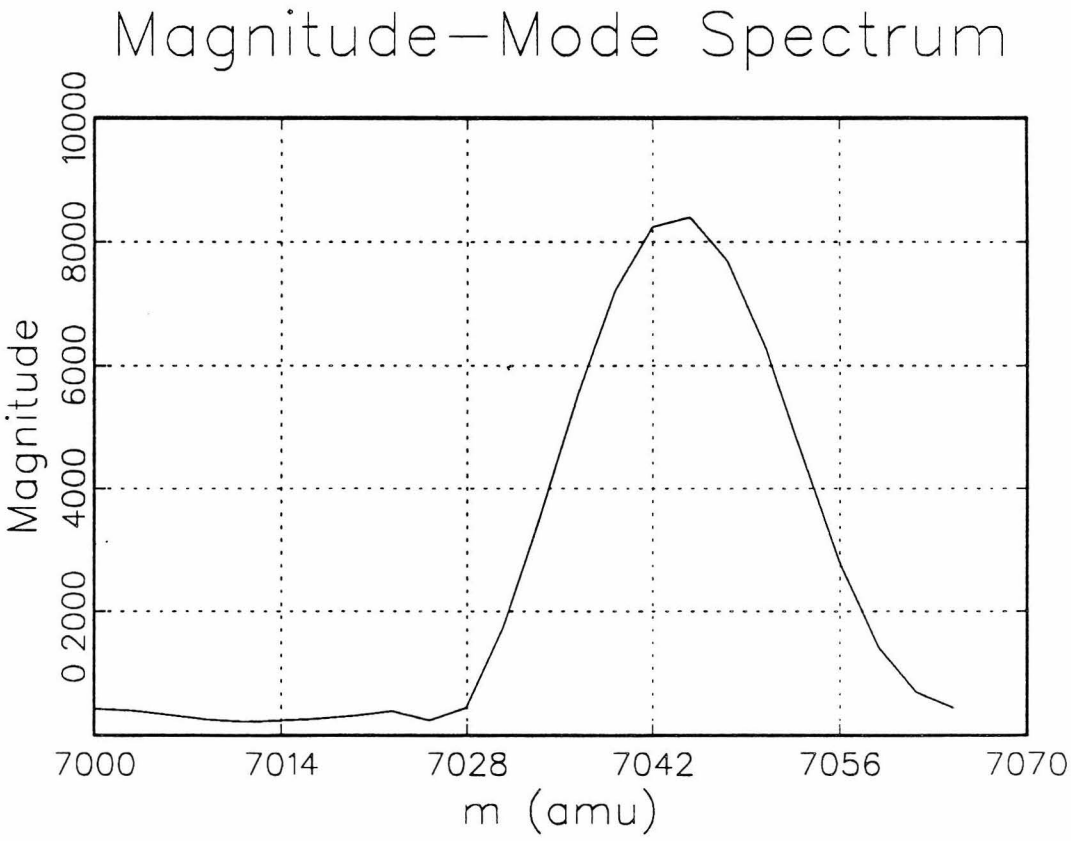
Magnitude—Mode Spectrum
Magnitude
0 2000 4000 6000 8000 10000
7000 7014 7028 7042 7056 7070
m (amu)

5a

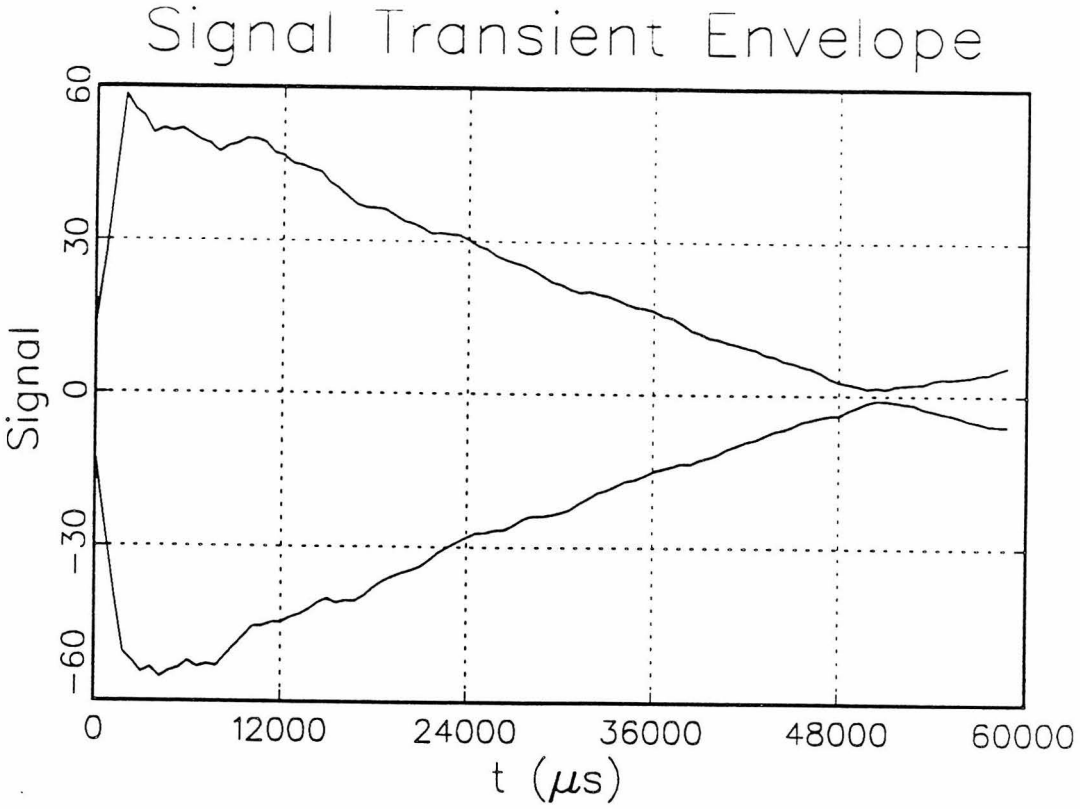
Signal Transient Envelope
Signal
60
30
0
−30
−60
0
12000
24000
36000
48000
60000
t (μs)

5b

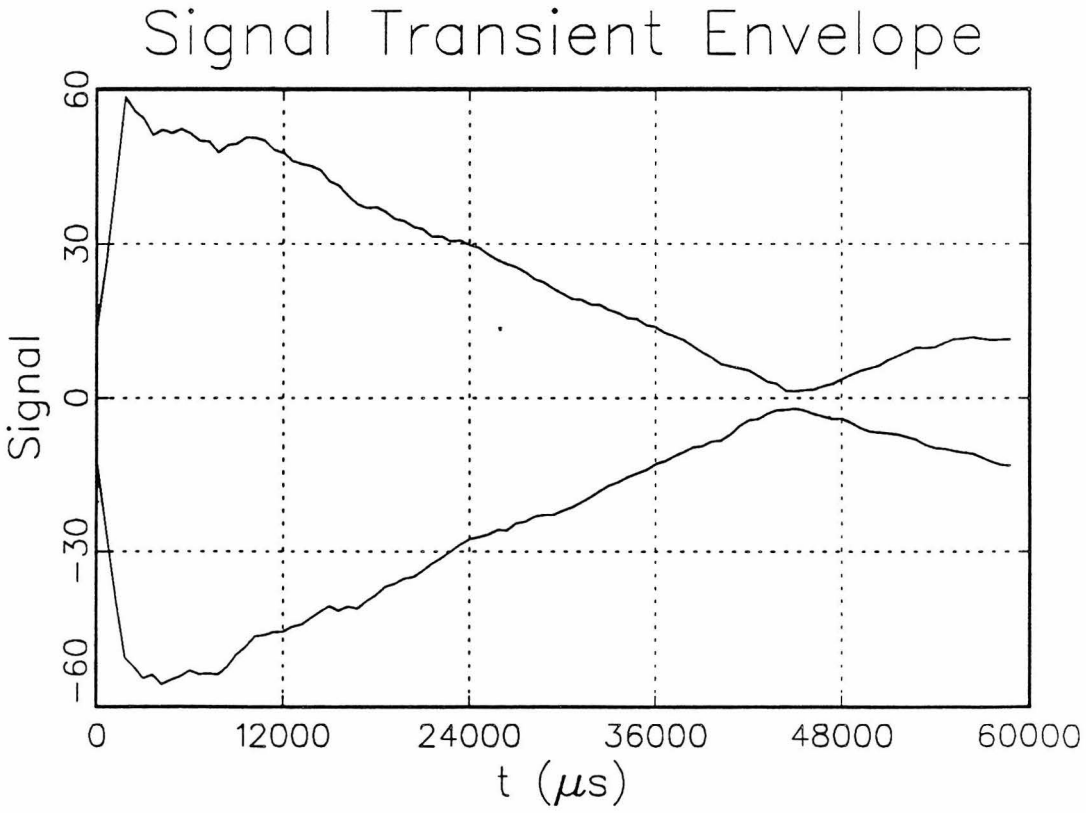
Signal Transient Envelope
Signal
60
30
0
−30
−60
0
12000
24000
36000
48000
60000
t (μs)

5c

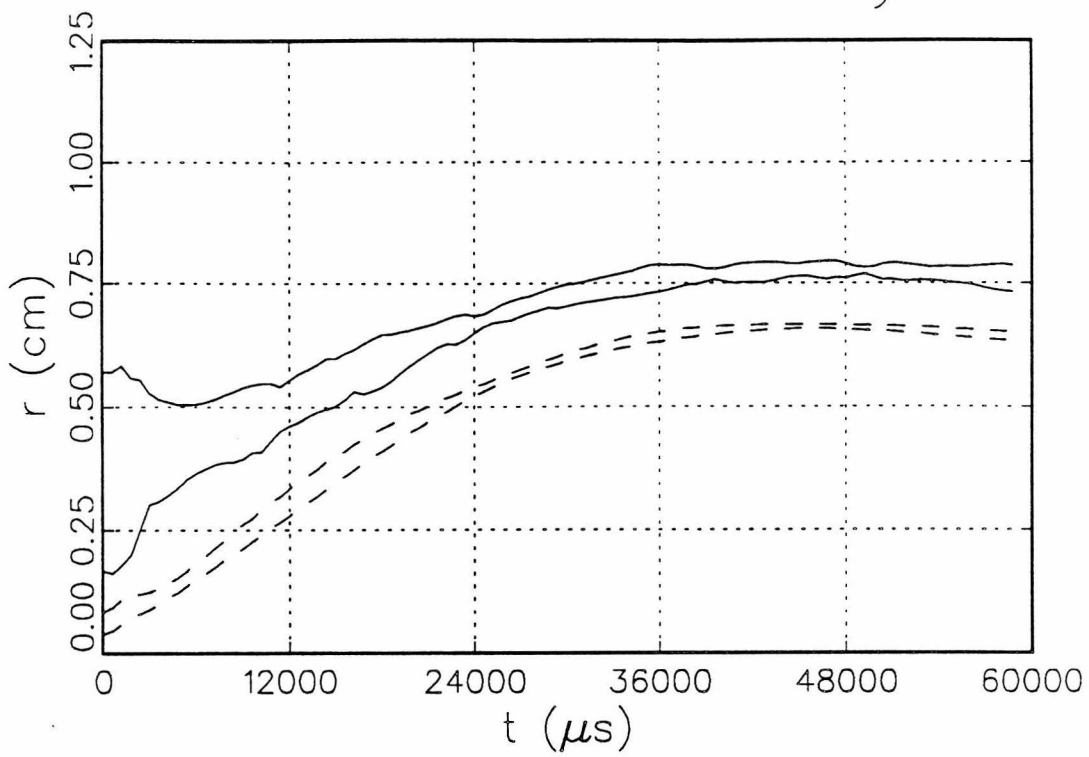
2−D and 3−D Radii of Gyration
r (cm)
0.00
0.25
0.50
0.75
1.00
1.25
0
12000
24000
36000
48000
60000
t (μs)

5d

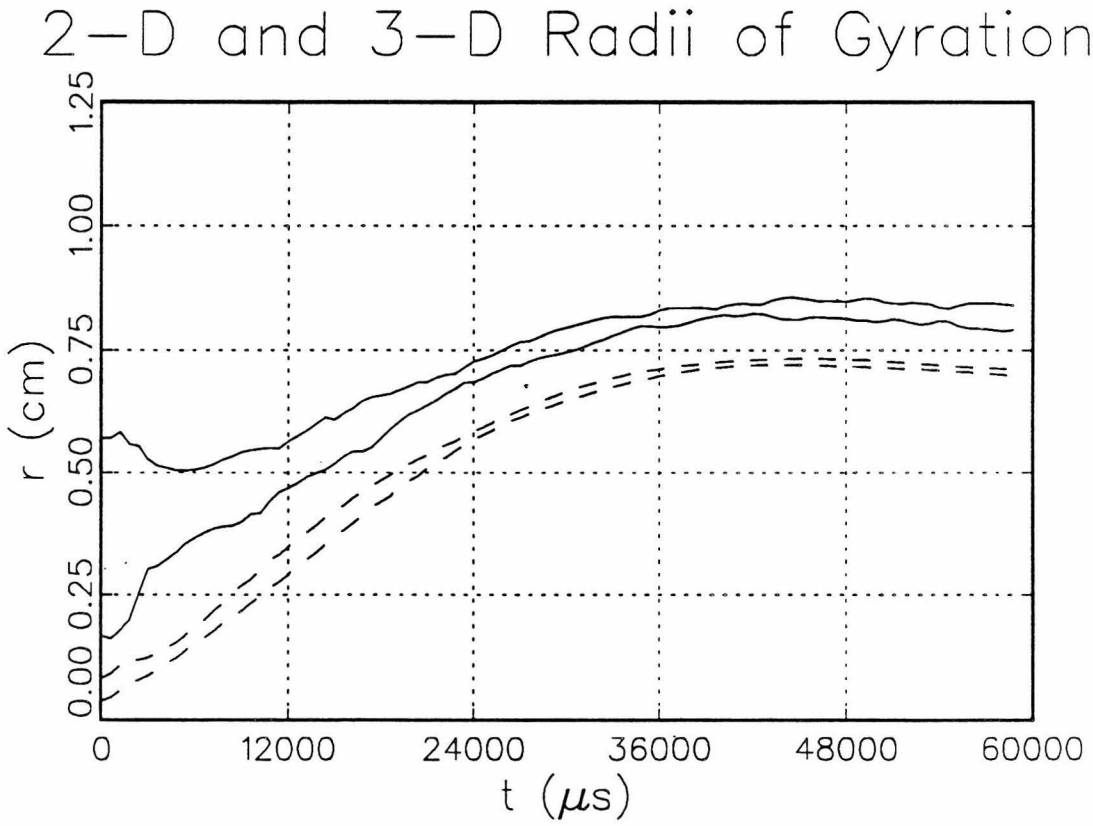
2−D and 3−D Radii of Gyration
r (cm)
0.00
0.25
0.50
0.75
1.00
1.25
0
12000
24000
36000
48000
60000
t (μs)

5e

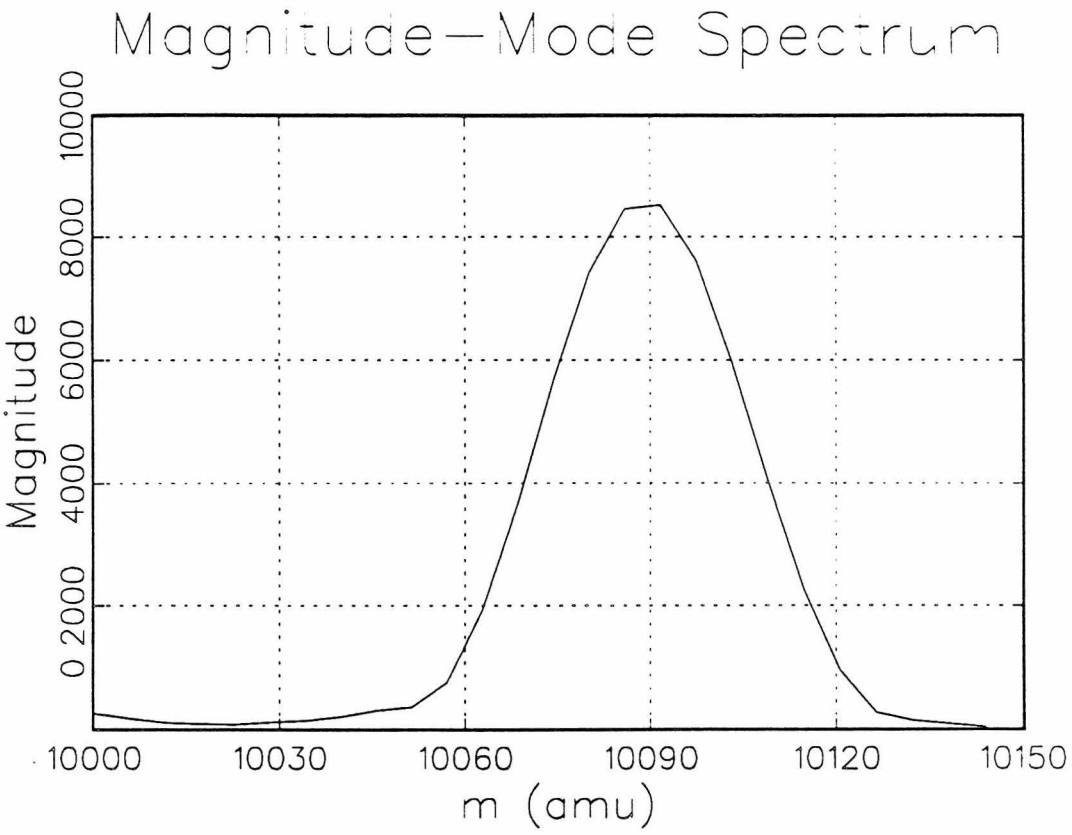
Magnitude–Mode Spectrum
Magnitude
0 2000 4000 6000 8000 10000
10000 10030 10060 10090 10120 10150
m (amu)

5f

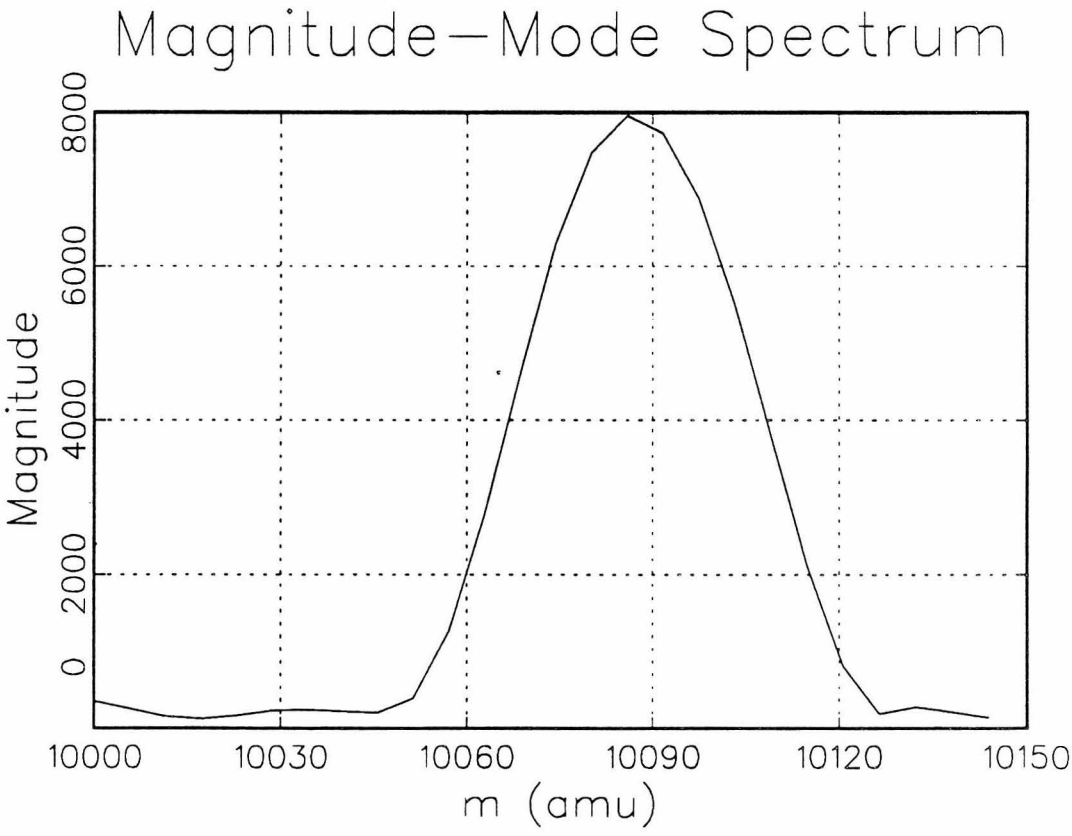
Magnitude–Mode Spectrum
Magnitude
0 2000 4000 6000 8000
10000 10030 10060 10090 10120 10150
m (amu)

6 a

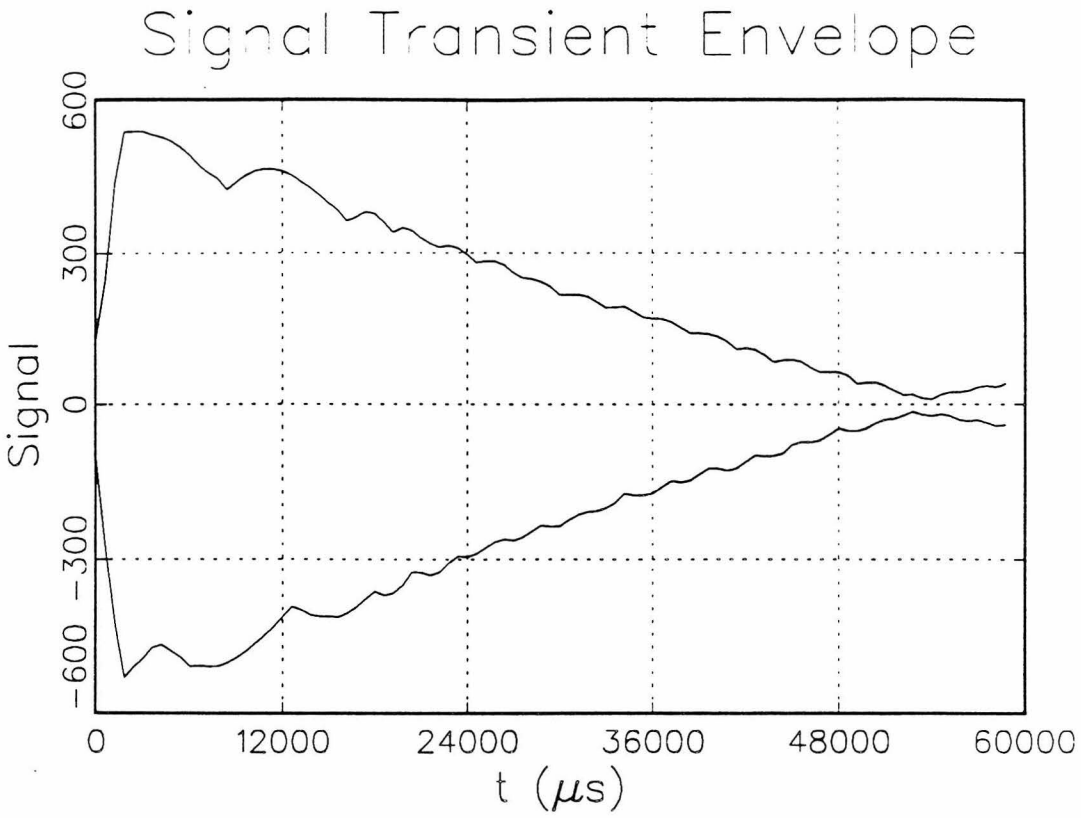
Signal Transient Envelope
Signal
600
300
0
−300
−600
0
12000
24000
36000
48000
60000
t (μs)

6 b

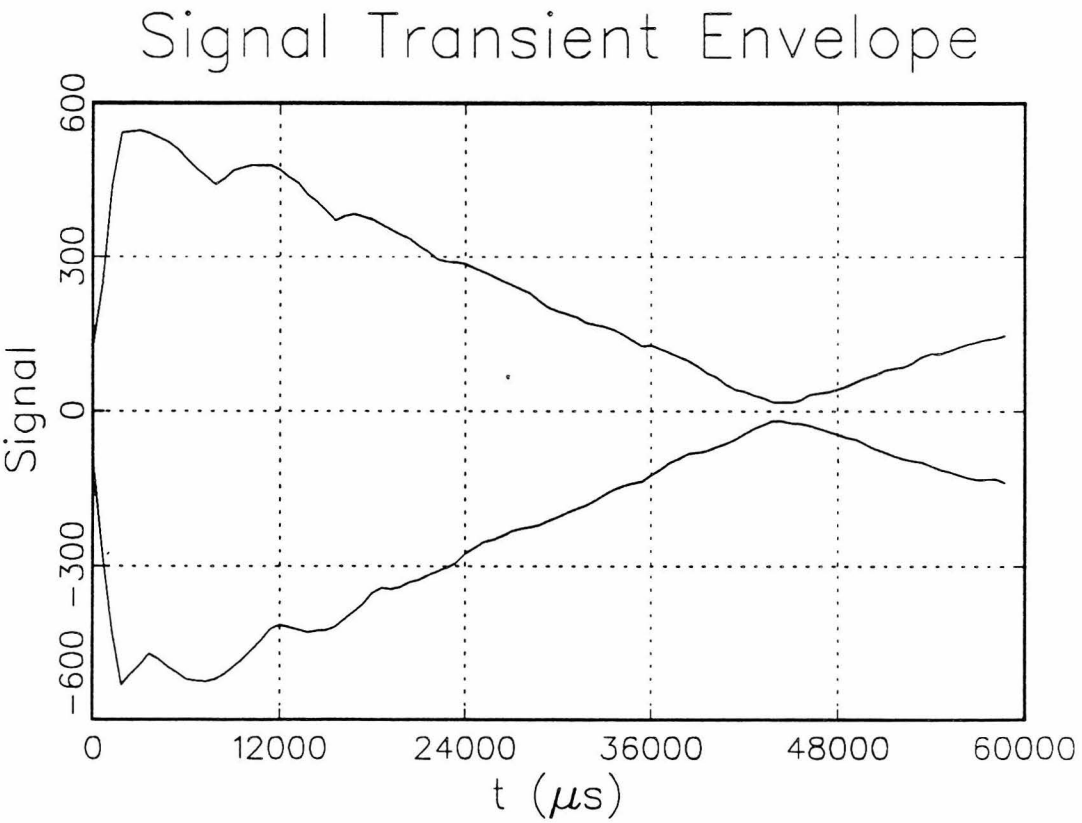
Signal Transient Envelope
Signal
600
300
0
−300
−600
0
12000
24000
36000
48000
60000
t (μs)

6 c

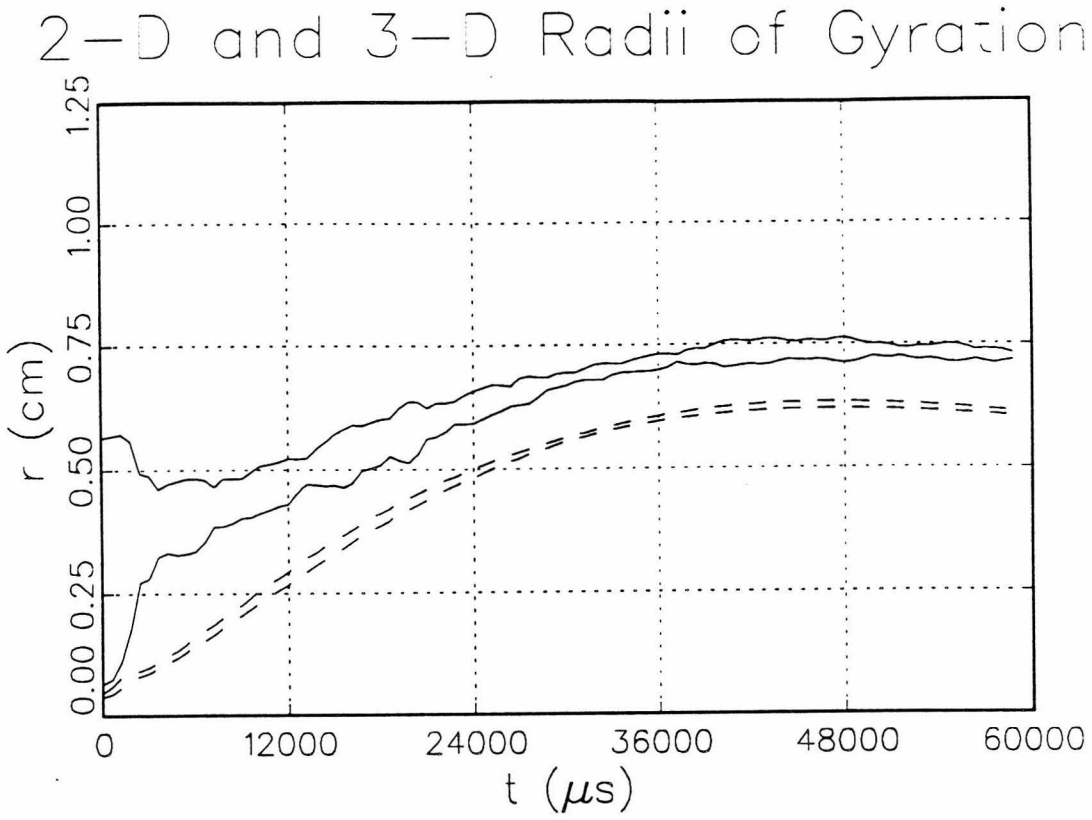
2−D and 3−D Radii of Gyration
r (cm)
0.00
0.25
0.50
0.75
1.00
1.25
0
12000
24000
36000
48000
60000
t (μs)

6 d

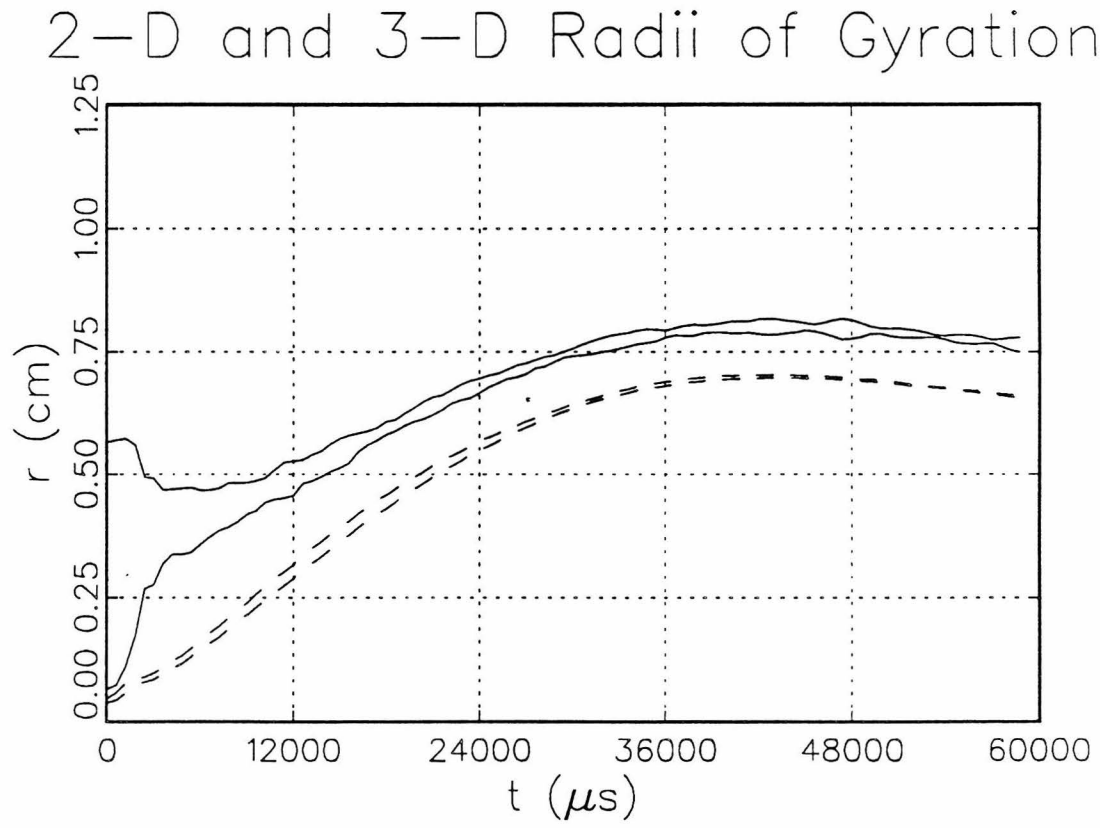
2−D and 3−D Radii of Gyration
r (cm)
0.00
0.25
0.50
0.75
1.00
1.25
0
12000
24000
36000
48000
60000
t (μs)

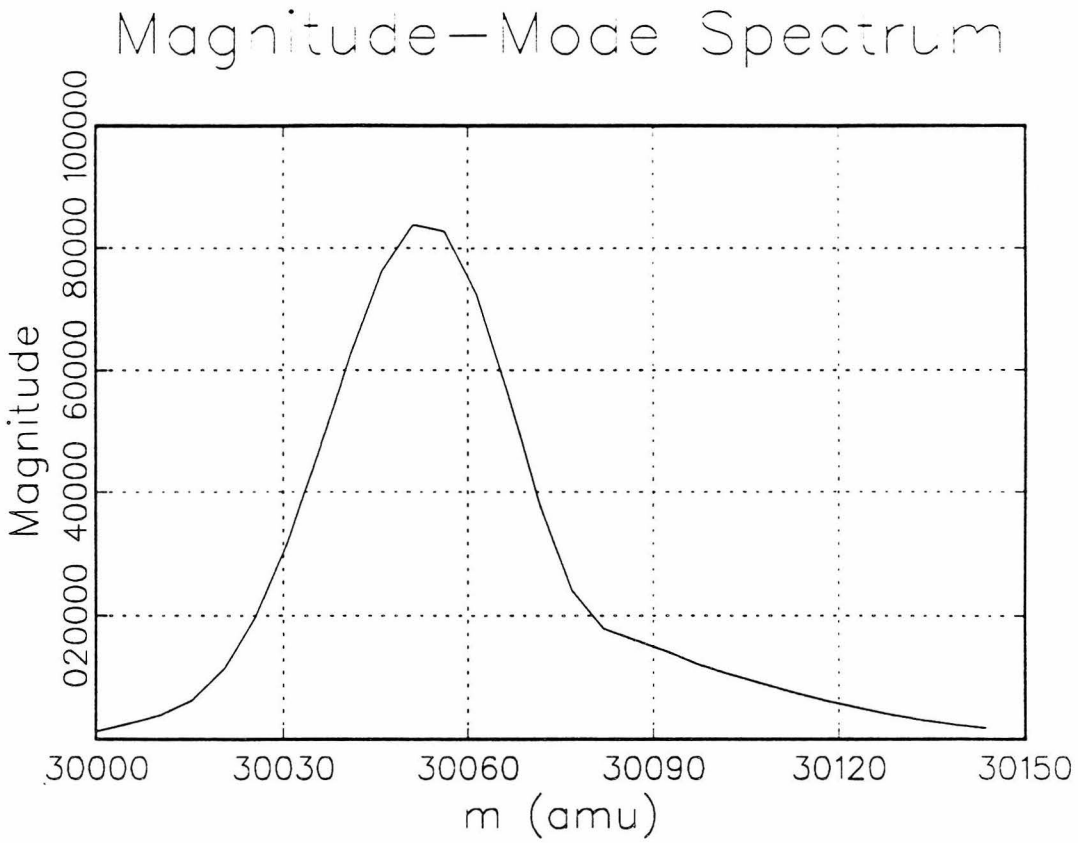
Magnitude–Mode Spectrum
Magnitude
020000 40000 60000 80000 100000
30000 30030 30060 30090 30120 30150
m (amu)

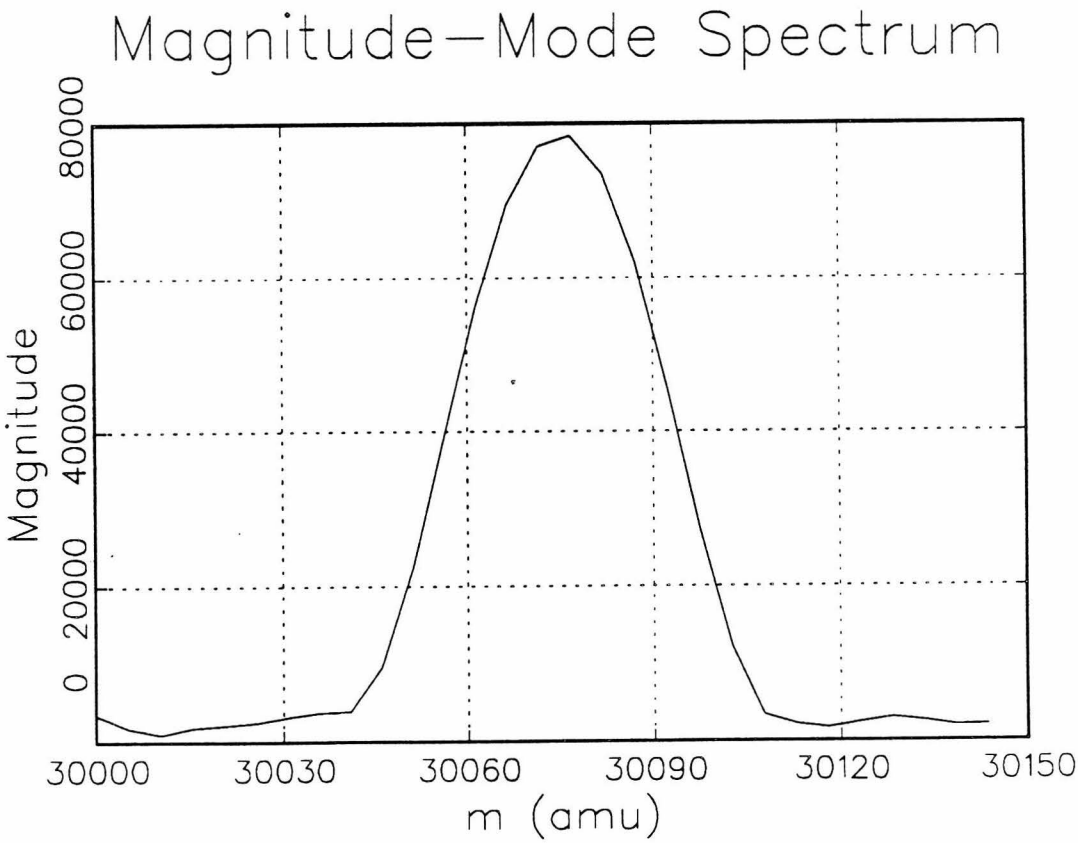
Magnitude–Mode Spectrum
Magnitude
0 20000 40000 60000 80000
30000 30030 30060 30090 30120 30150
m (amu)

7.e

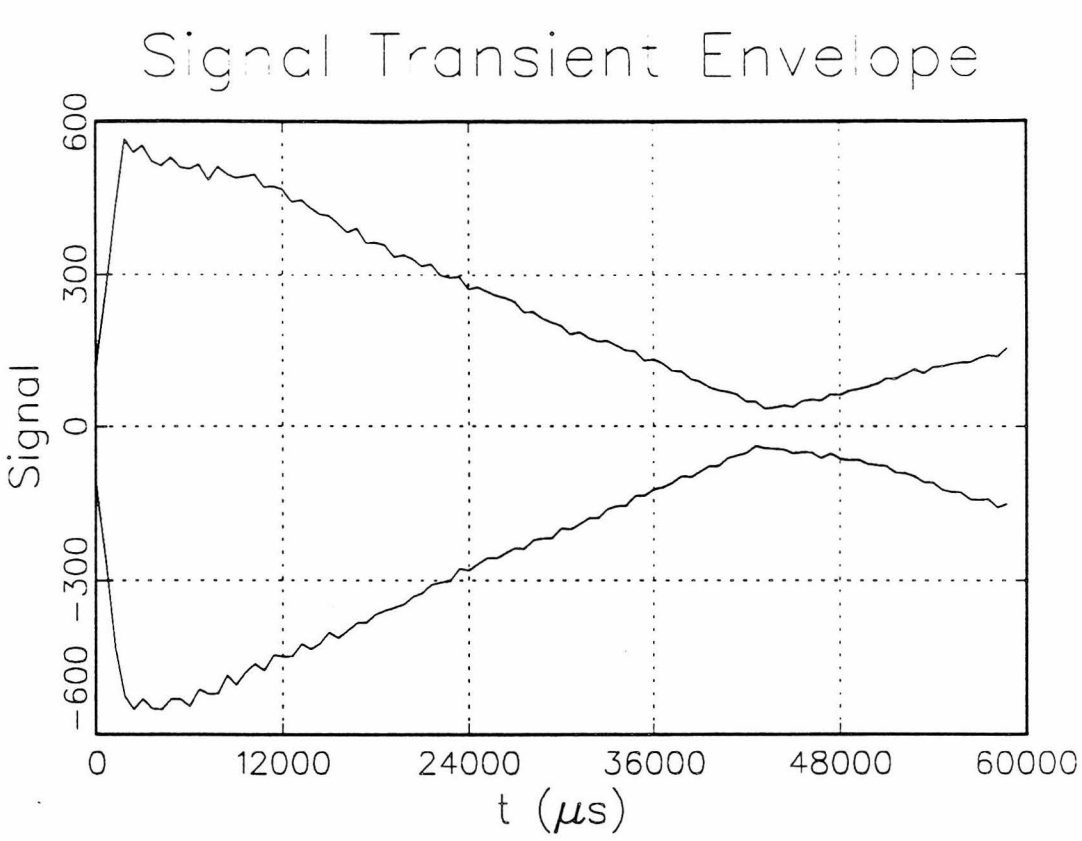
Signal Transient Envelope
Signal
600
300
0
−300
−600
0
12000
24000
36000
48000
60000
t (μs)

7.b

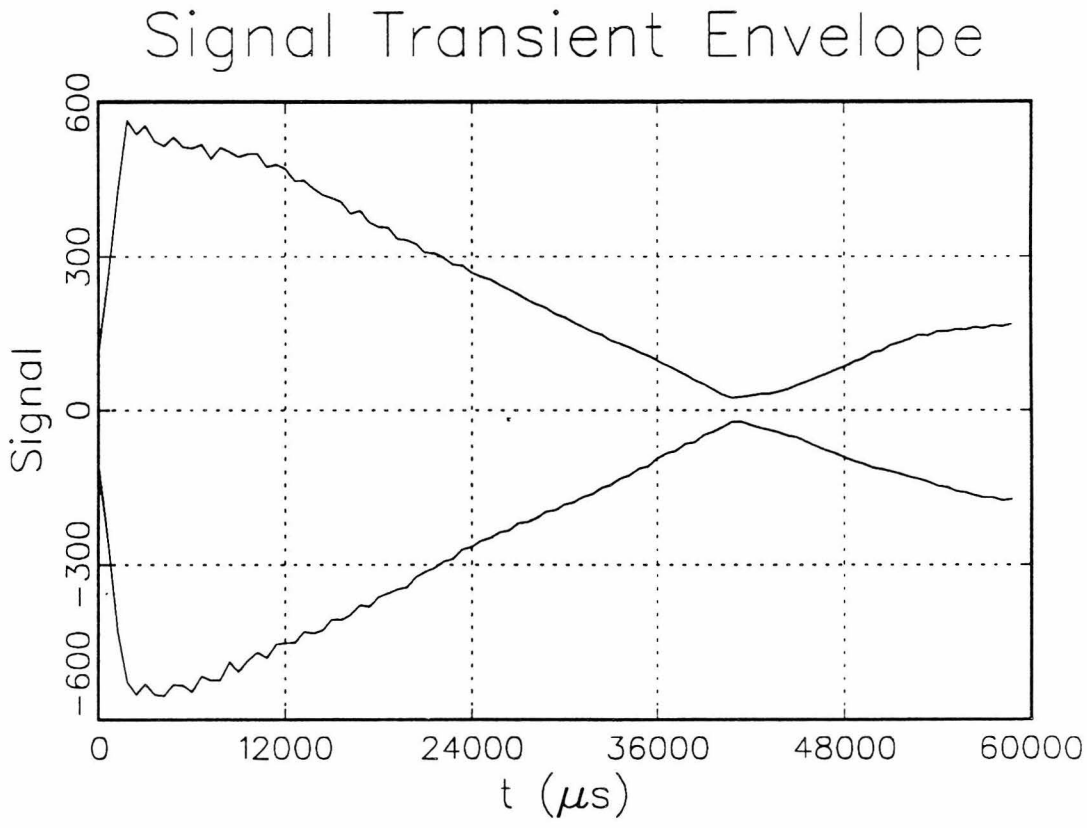
Signal Transient Envelope
Signal
600
300
0
−300
−600
0
12000
24000
36000
48000
60000
t (μs)

7 c

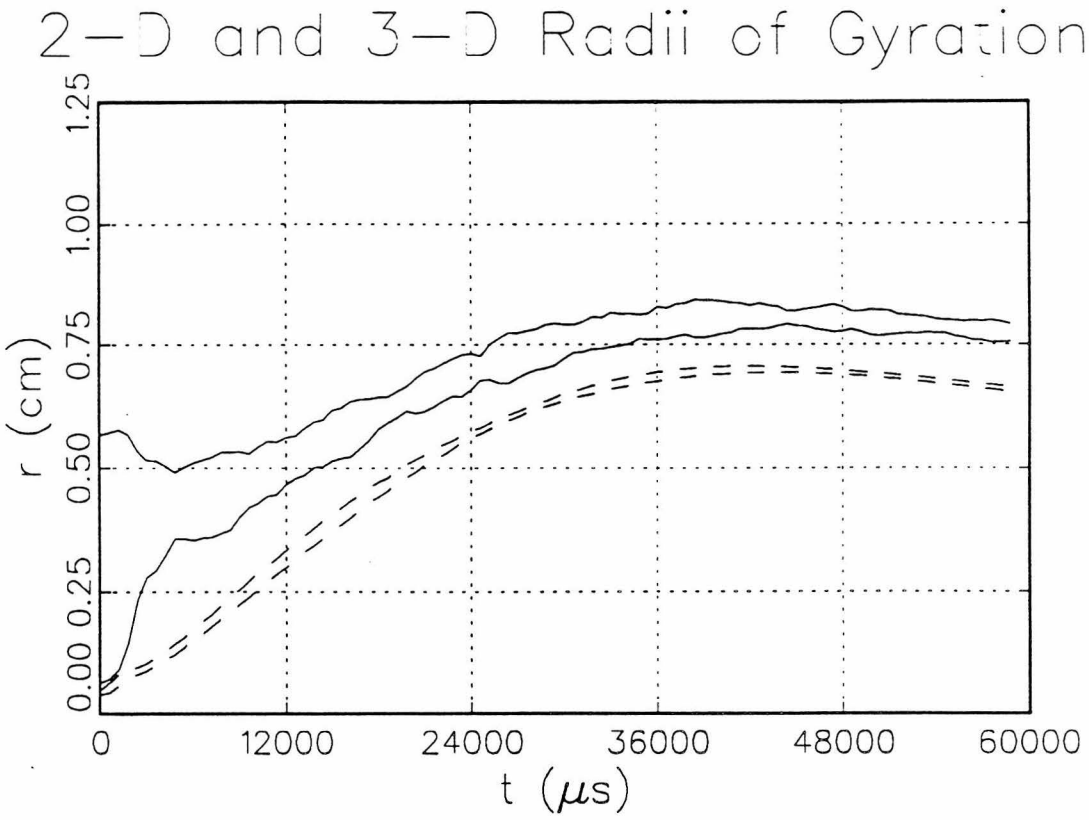
2−D and 3−D Radii of Gyration
r (cm)
0.00
0.25
0.50
0.75
1.00
1.25
0
12000
24000
36000
48000
60000
t (μs)

7 d

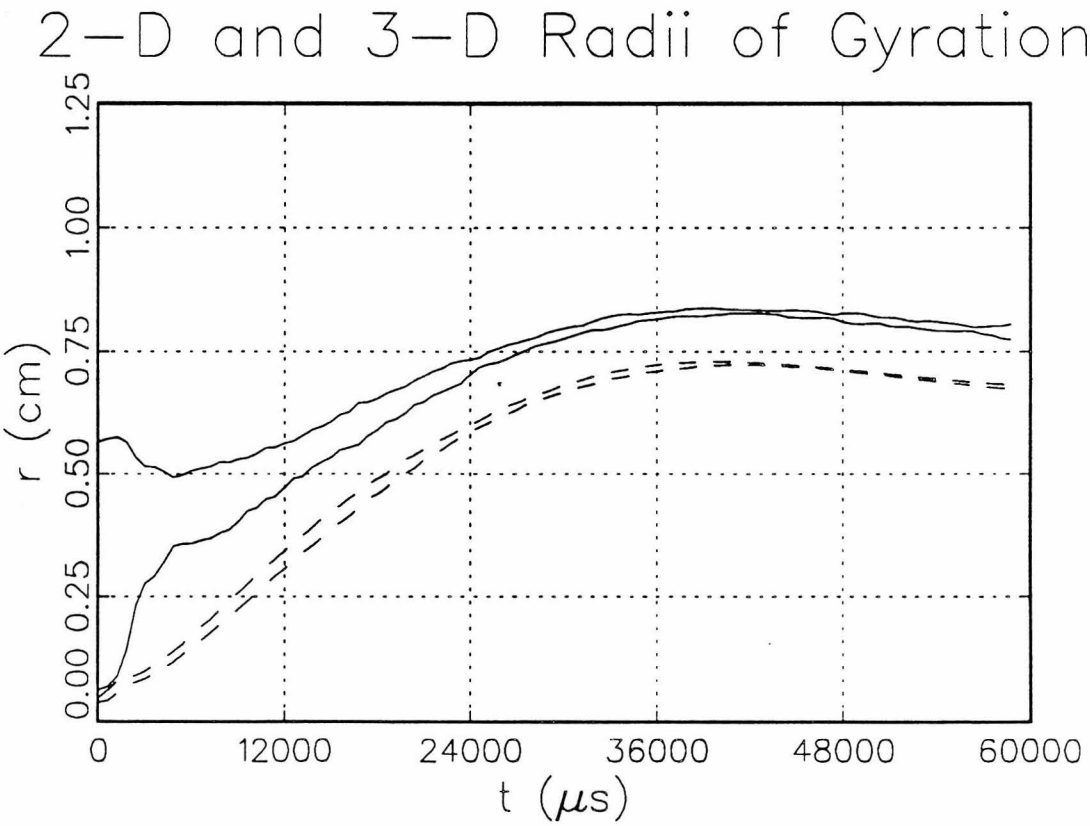
2−D and 3−D Radii of Gyration
r (cm)
0.00
0.25
0.50
0.75
1.00
1.25
0
12000
24000
36000
48000
60000
t (μs)

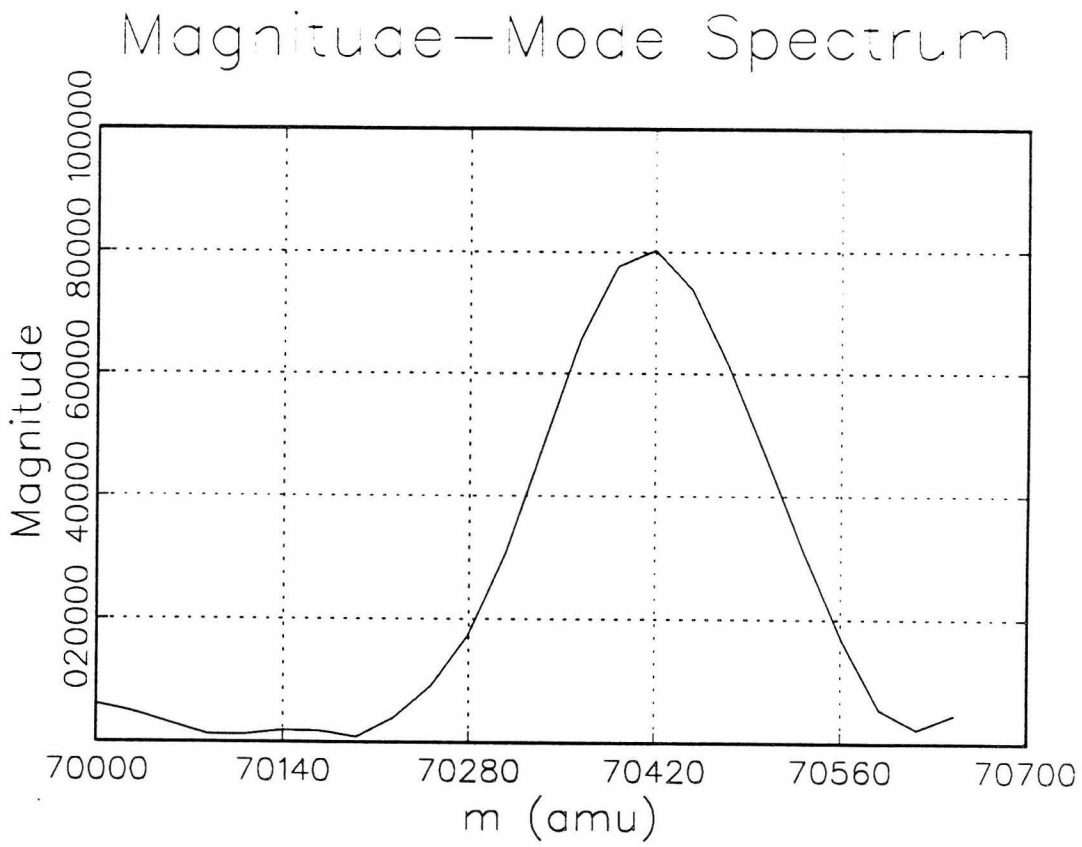
Magnitude–Mode Spectrum
Magnitude
020000 40000 60000 80000 100000
70000 70140 70280 70420 70560 70700
m (amu)

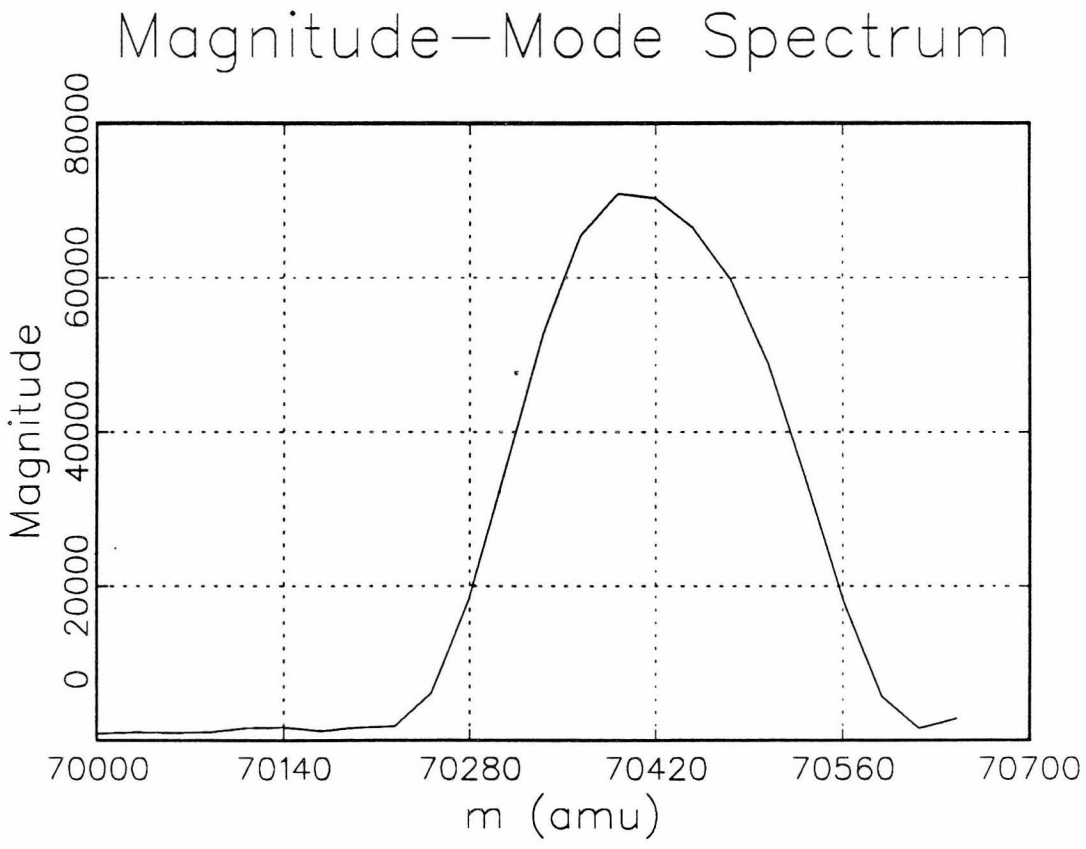
Magnitude–Mode Spectrum
Magnitude
0 20000 40000 60000 80000
70000 70140 70280 70420 70560 70700
m (amu)

8a

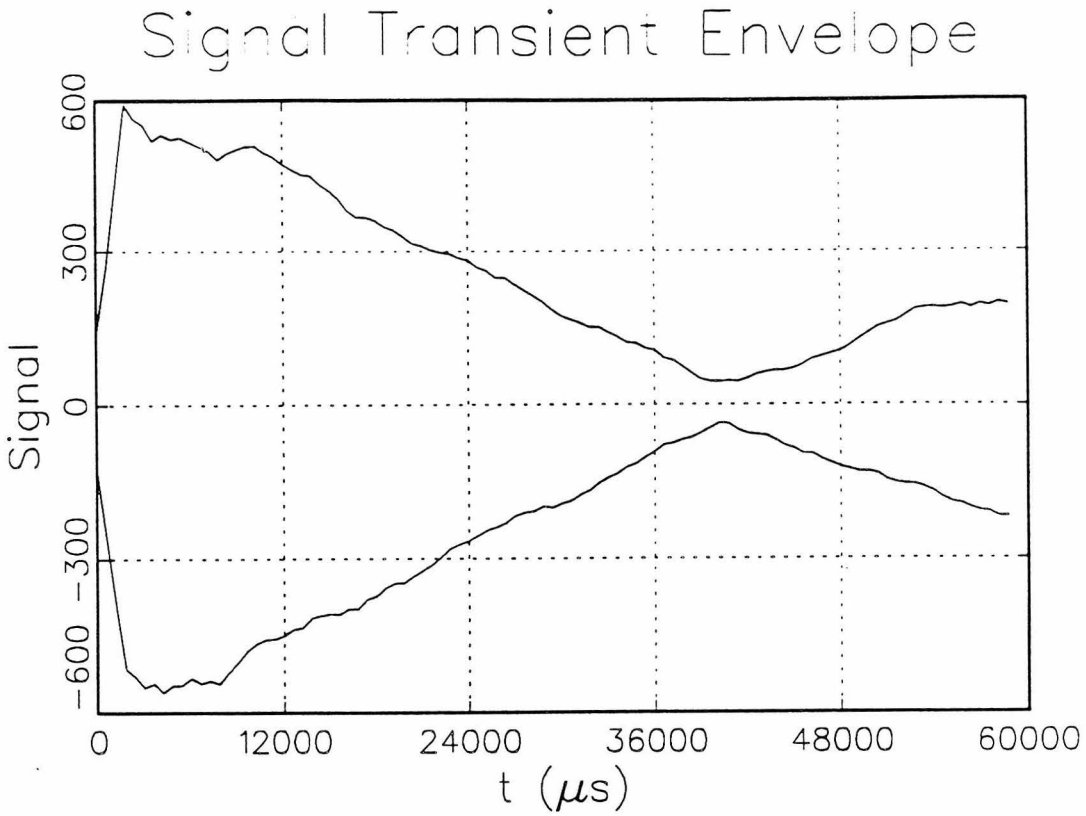
Signal Transient Envelope
Signal
600
300
0
−300
−600
0
12000
24000
36000
48000
60000
t (μs)

8b

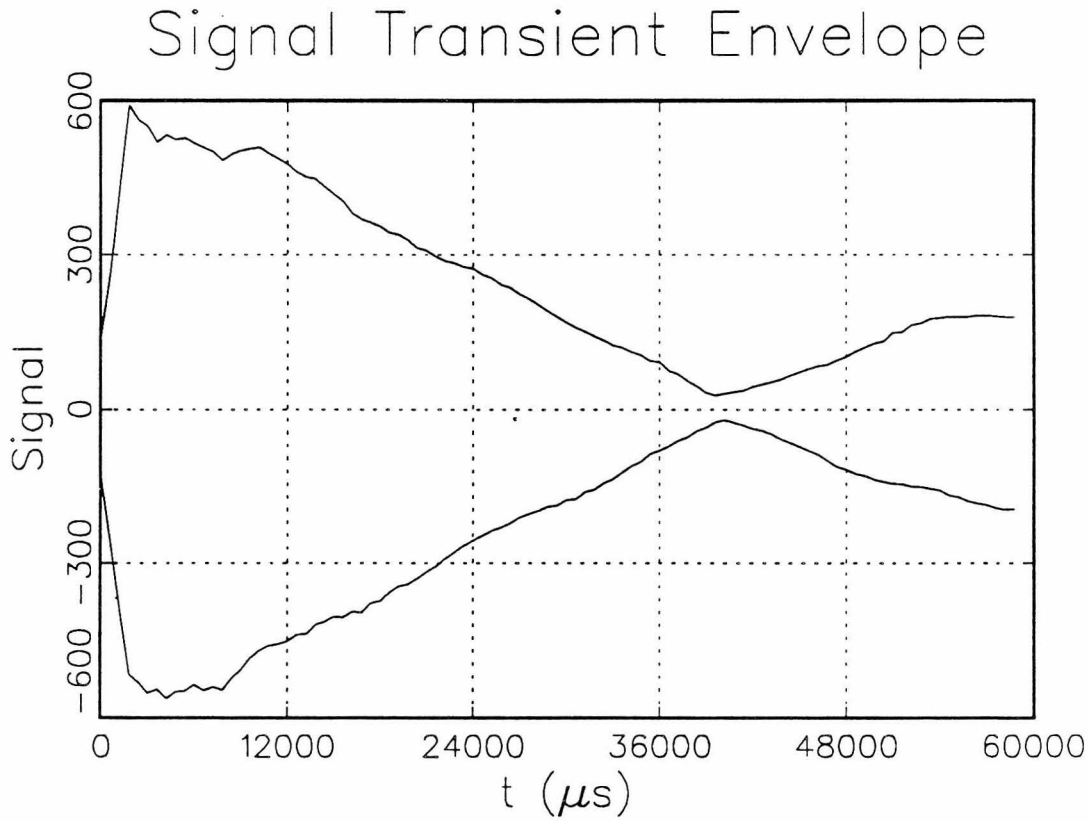
Signal Transient Envelope
Signal
600
300
0
−300
−600
0
12000
24000
36000
48000
60000
t (μs)

8c

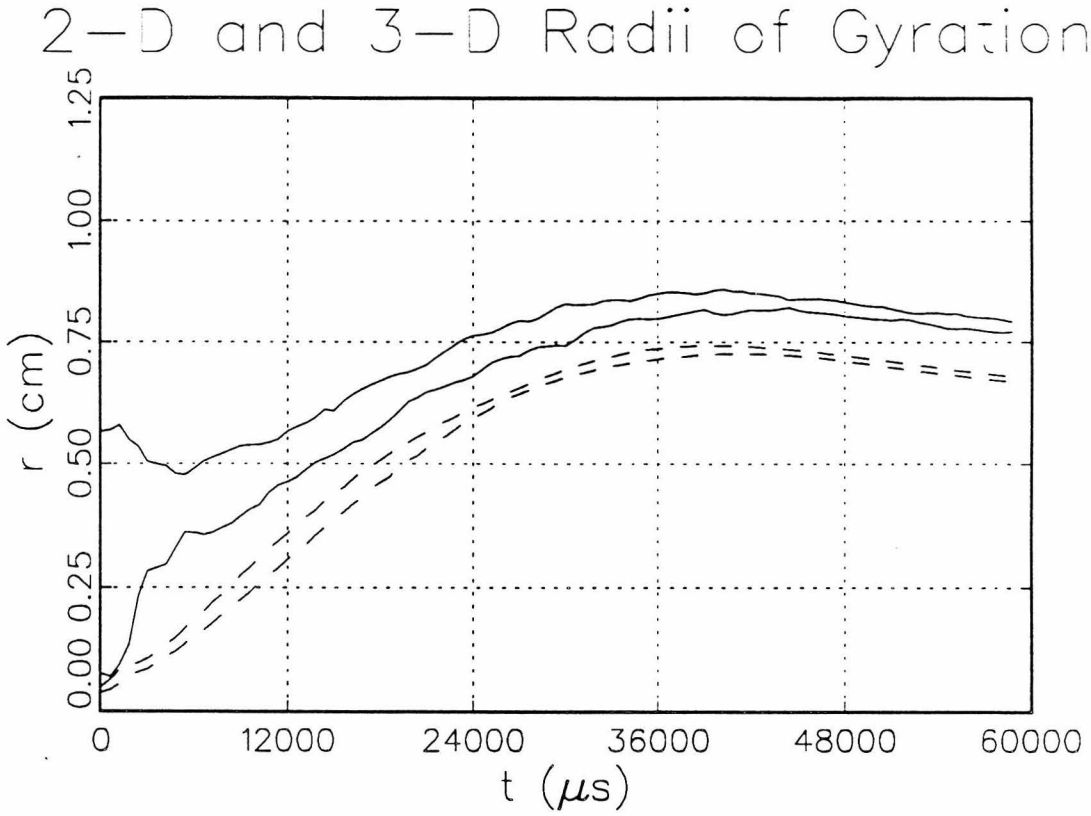
2−D and 3−D Radii of Gyration
r (cm)
0.00
0.25
0.50
0.75
1.00
1.25
0
12000
24000
36000
48000
60000
t (μs)

8d

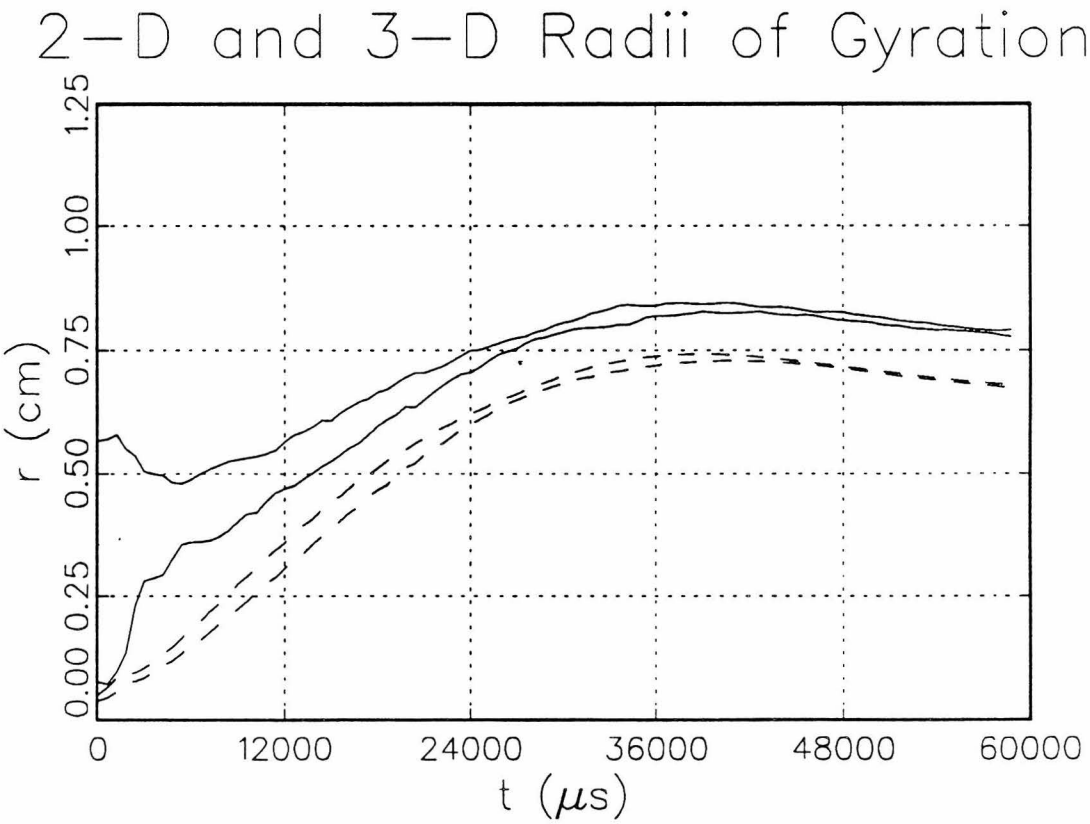
2−D and 3−D Radii of Gyration
r (cm)
0.00
0.25
0.50
0.75
1.00
1.25
0
12000
24000
36000
48000
60000
t (μs)

8e

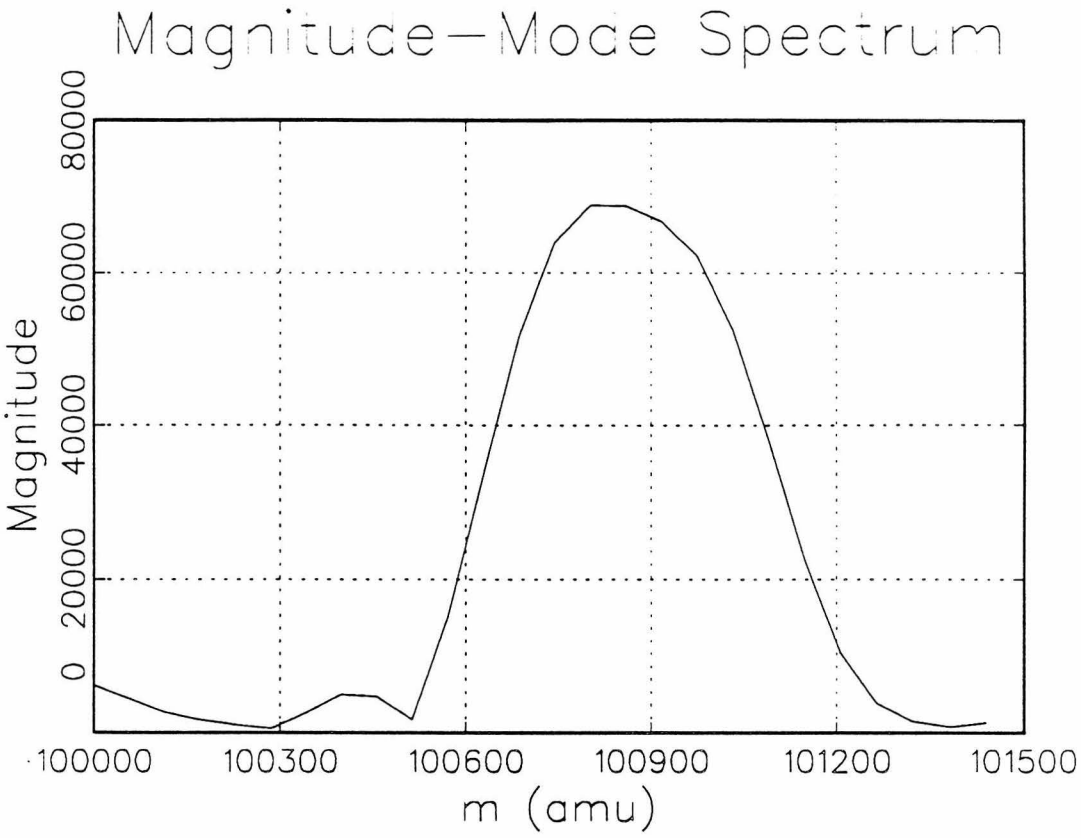
Magnitude–Mode Spectrum
Magnitude
0
20000
40000
60000
80000
100000
100300
100600
100900
101200
101500
m (amu)

8f

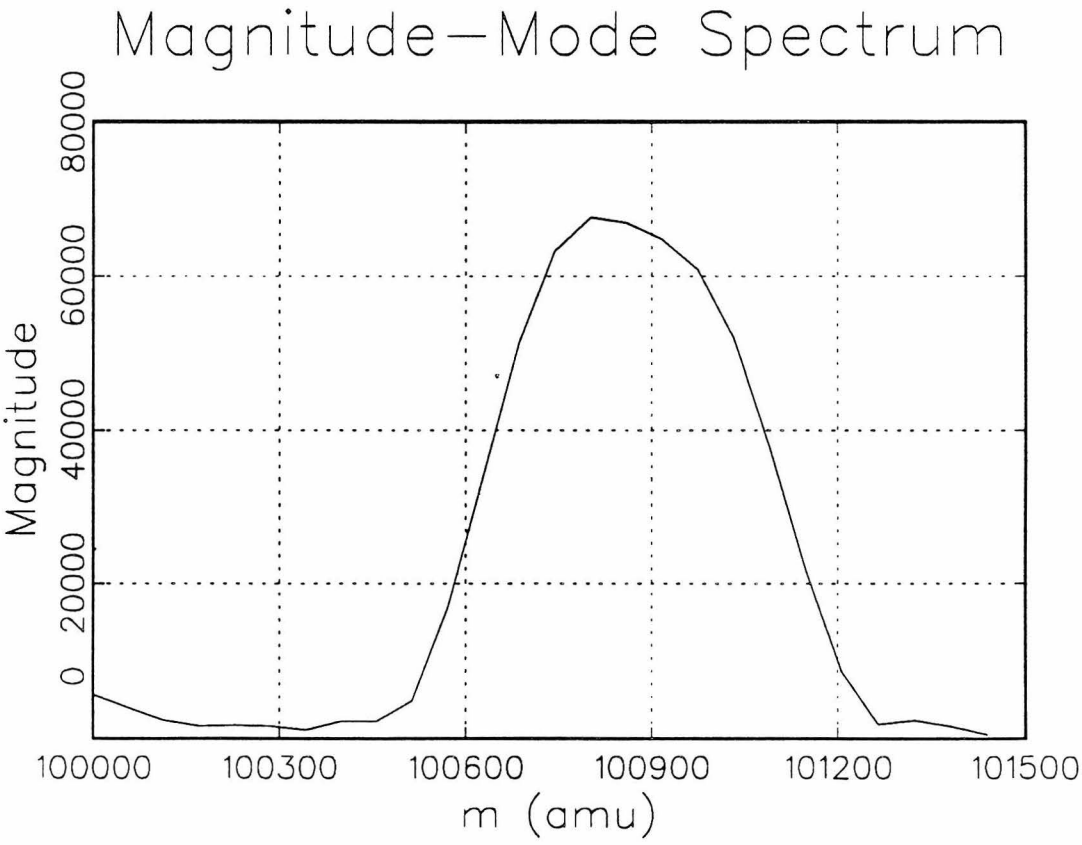
Magnitude–Mode Spectrum
Magnitude
0
20000
40000
60000
80000
100000
100300
100600
100900
101200
101500
m (amu)

9a

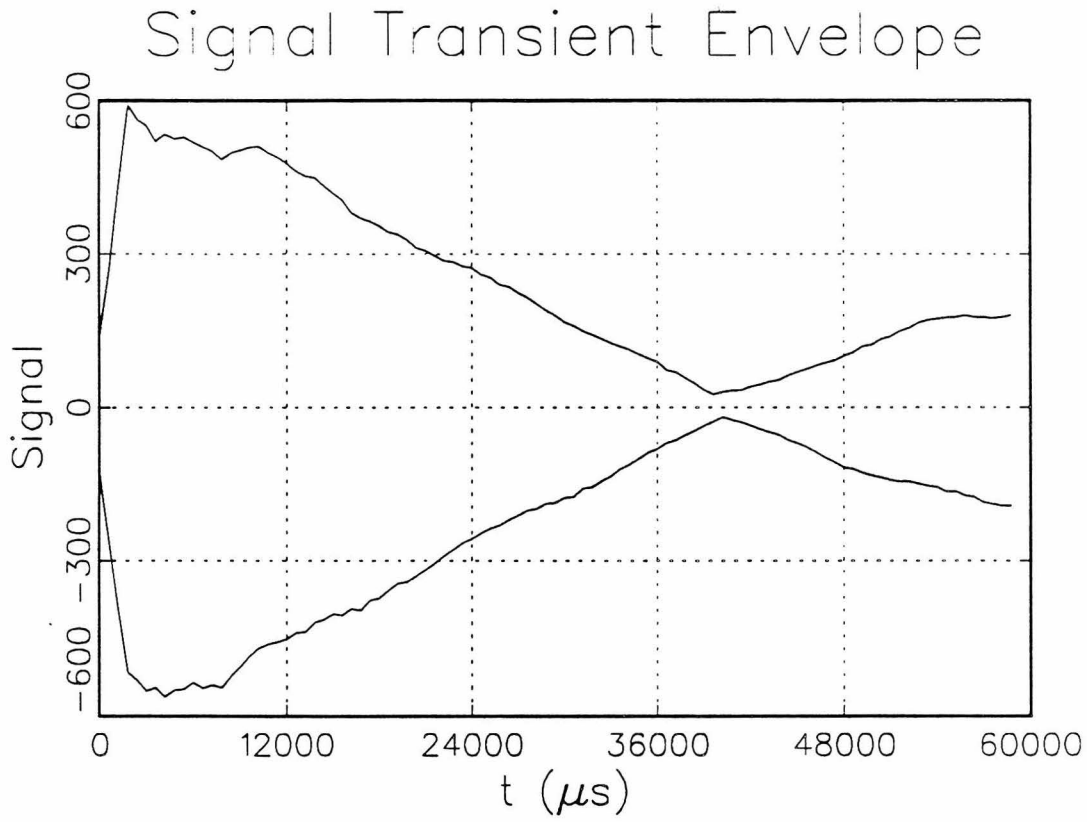
Signal Transient Envelope
Signal
600
300
0
−300
−600
0
12000
24000
36000
48000
60000
t (μs)

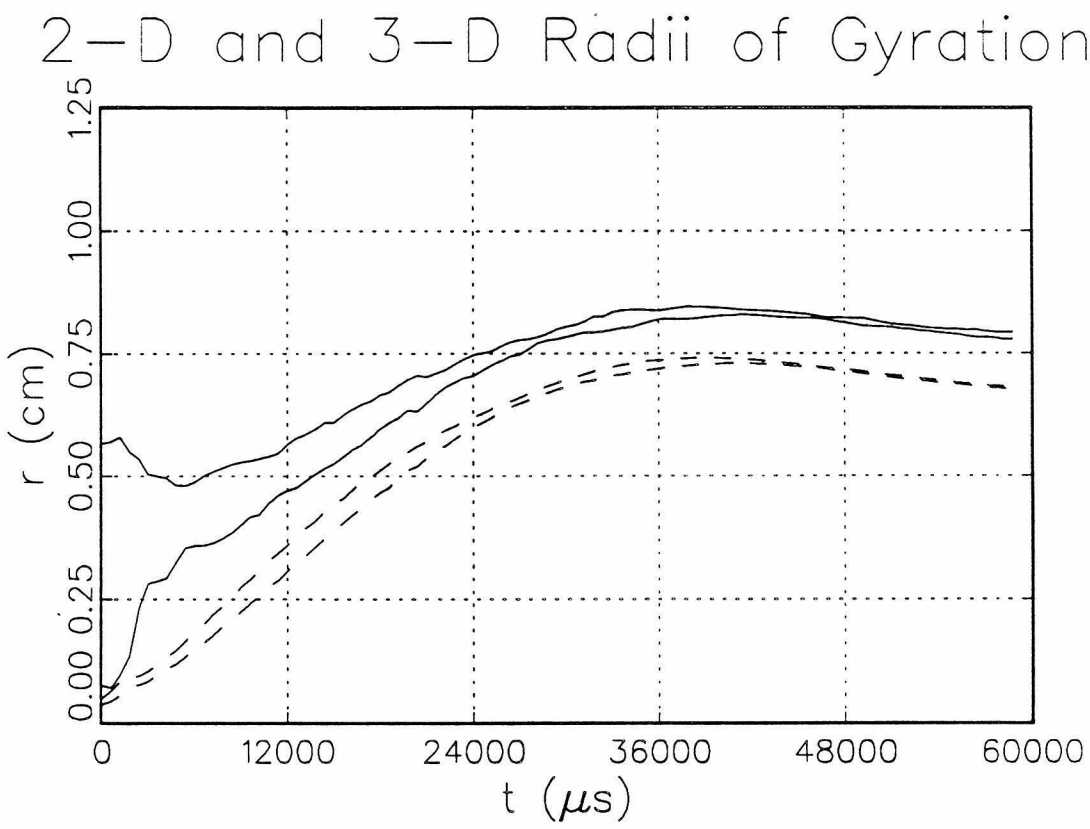
2−D and 3−D Radii of Gyration
r (cm)
0.00
0.25
0.50
0.75
1.00
1.25
0
12000
24000
36000
48000
60000
t (μs)

9c

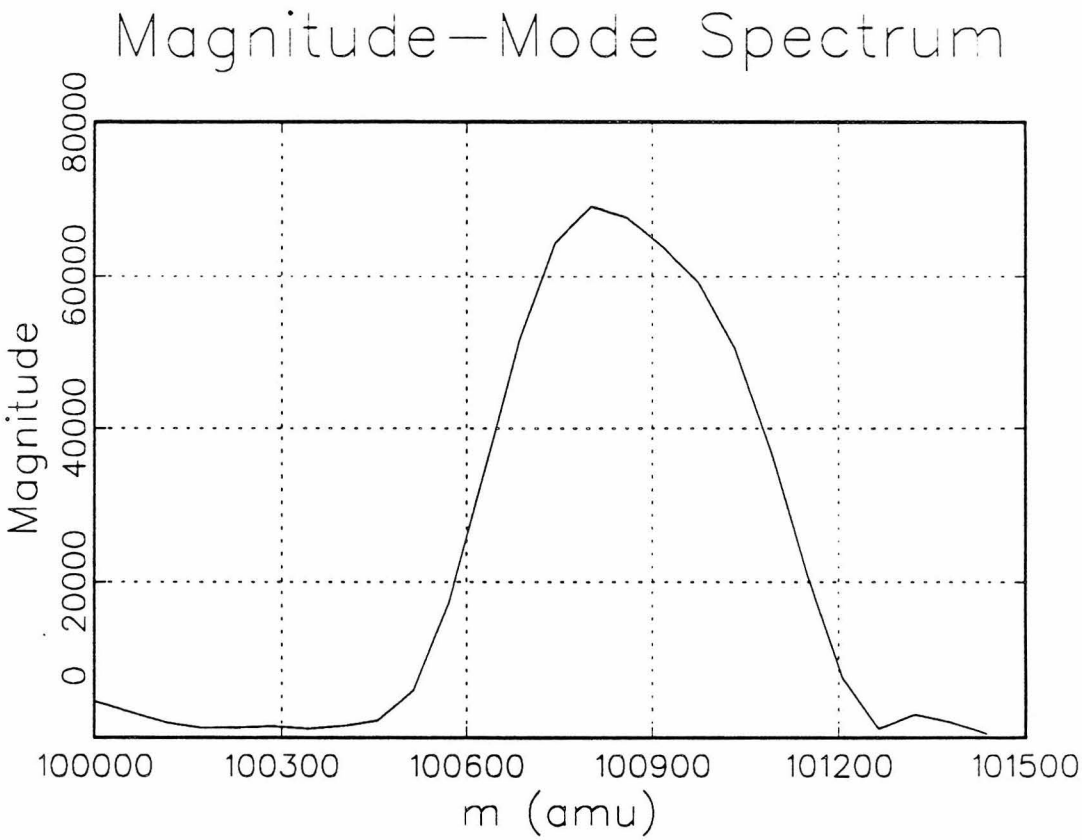
Magnitude–Mode Spectrum
Magnitude
0
20000
40000
60000
80000
100000
100300
100600
100900
101200
101500
m (amu)

10a

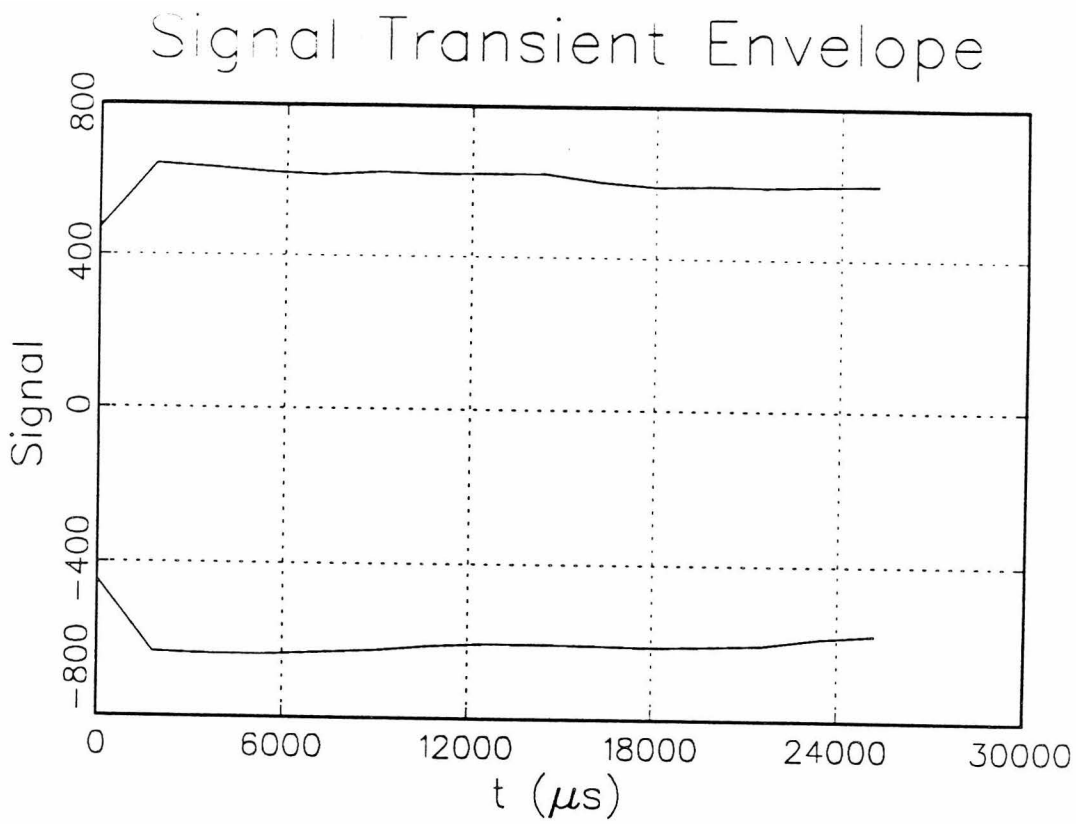
Signal Transient Envelope
Signal
800
400
0
−400
−800
0
6000
12000
18000
24000
30000
t (μs)

10b

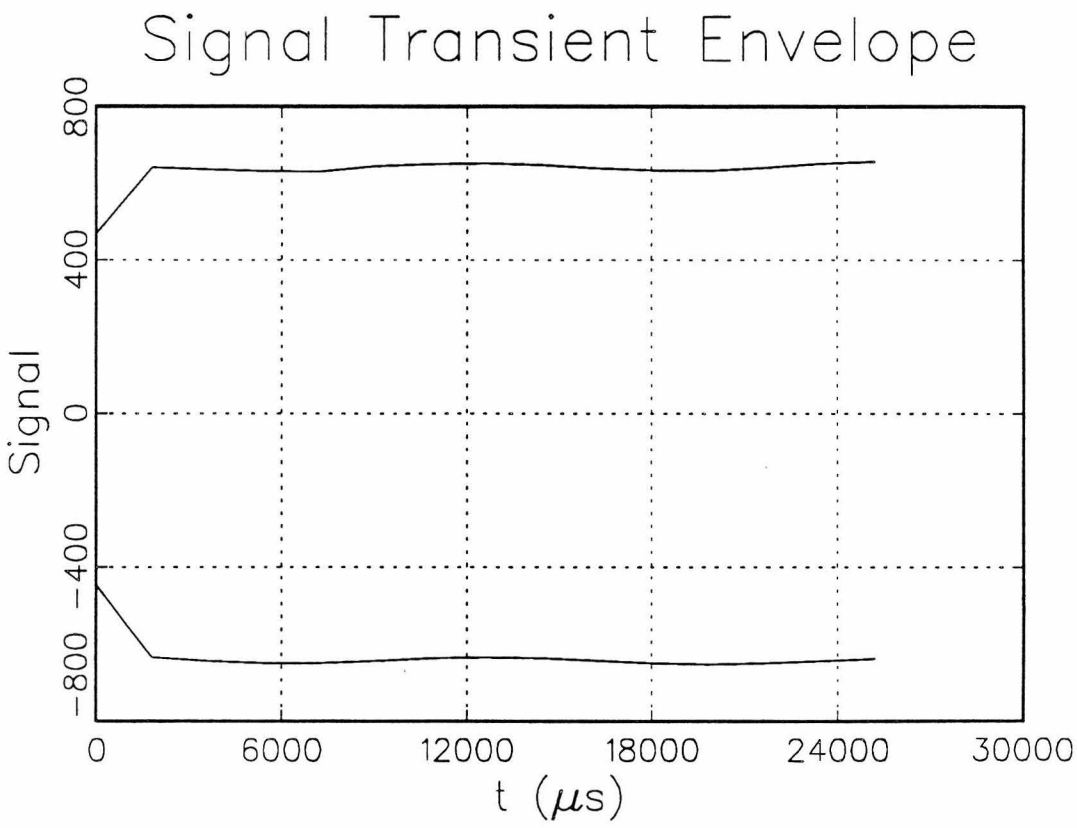
Signal Transient Envelope
Signal
800
400
0
−400
−800
0
6000
12000
18000
24000
30000
t (μs)

10c

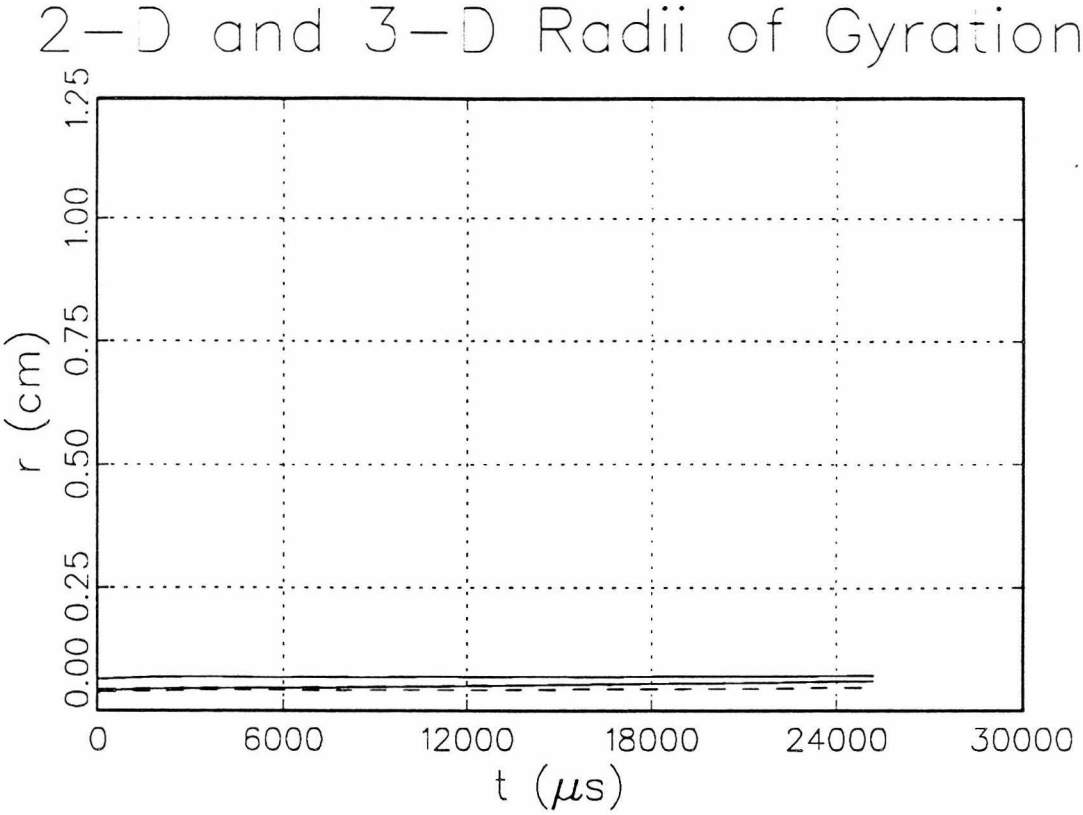
2−D and 3−D Radii of Gyration
r (cm)
0.00
0.25
0.50
0.75
1.00
1.25
0
6000
12000
18000
24000
30000
t (μs)

10f

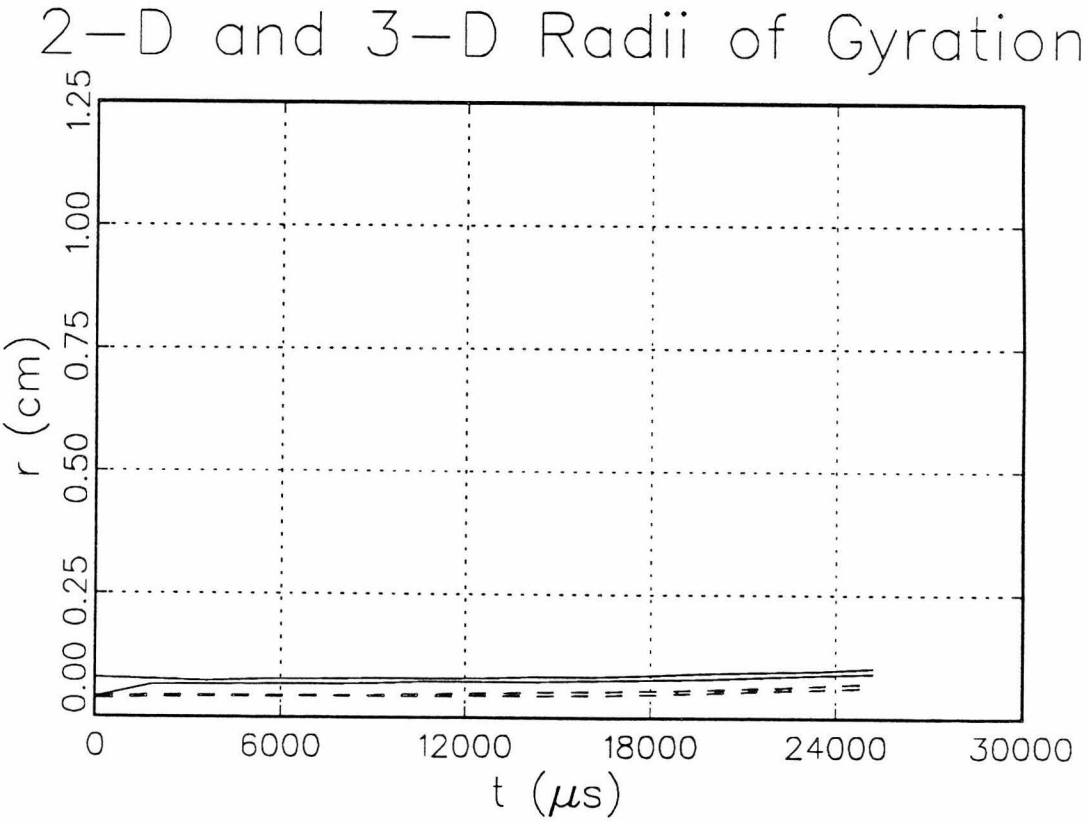
2−D and 3−D Radii of Gyration
r (cm)
0.00
0.25
0.50
0.75
1.00
1.25
0
6000
12000
18000
24000
30000
t (μs)

10e

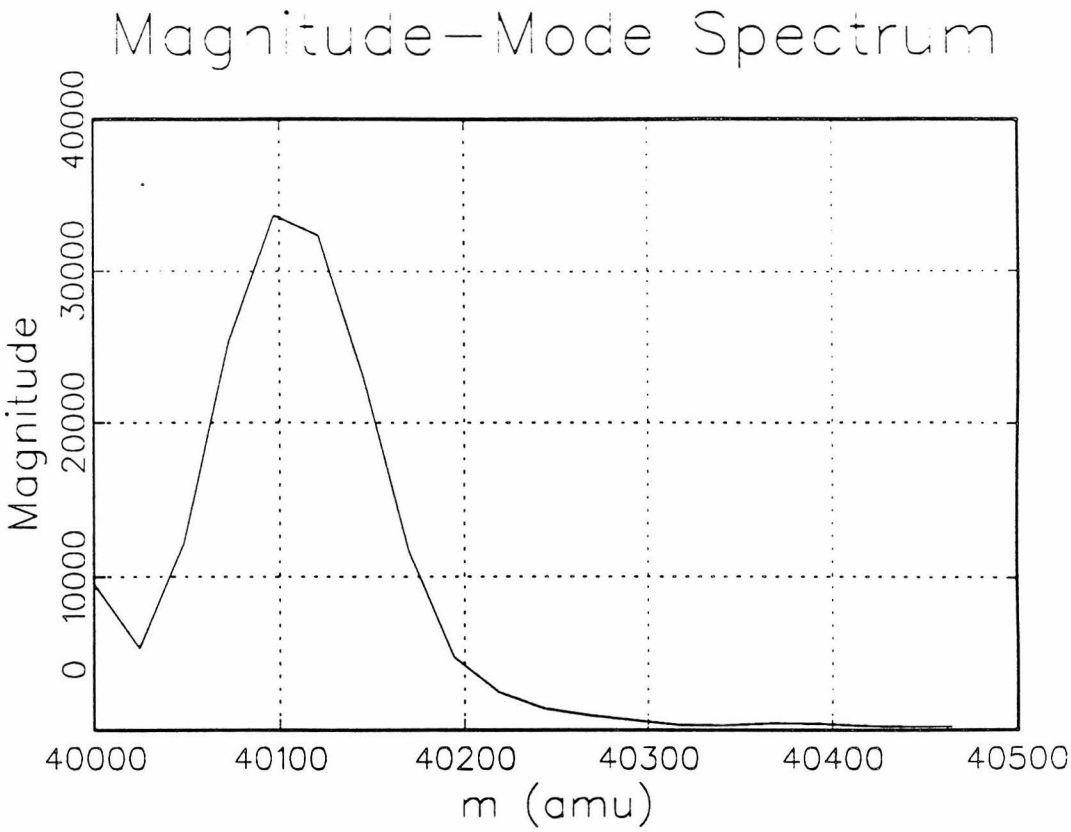
Magnitude–Mode Spectrum
Magnitude
0
10000
20000
30000
40000
40000
40100
40200
40300
40400
40500
m (amu)

10f

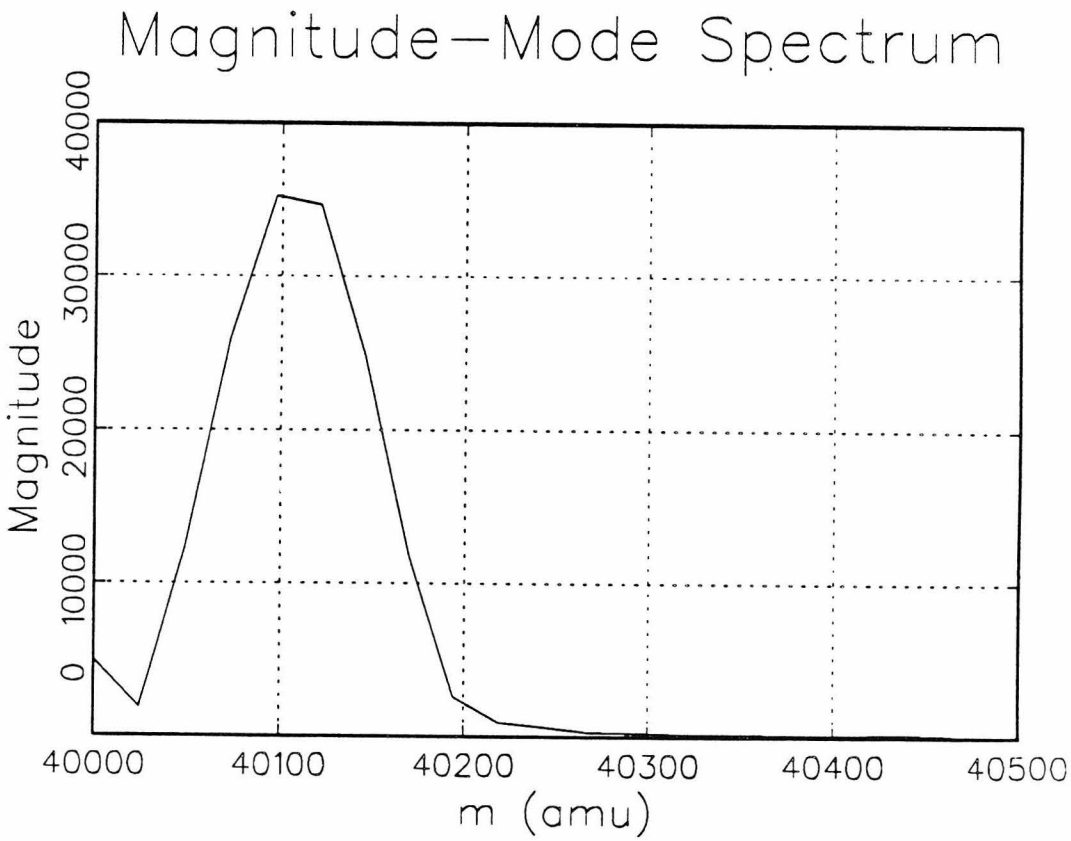
Magnitude–Mode Spectrum
Magnitude
0
10000
20000
30000
40000
40000
40100
40200
40300
40400
40500
m (amu)

11a

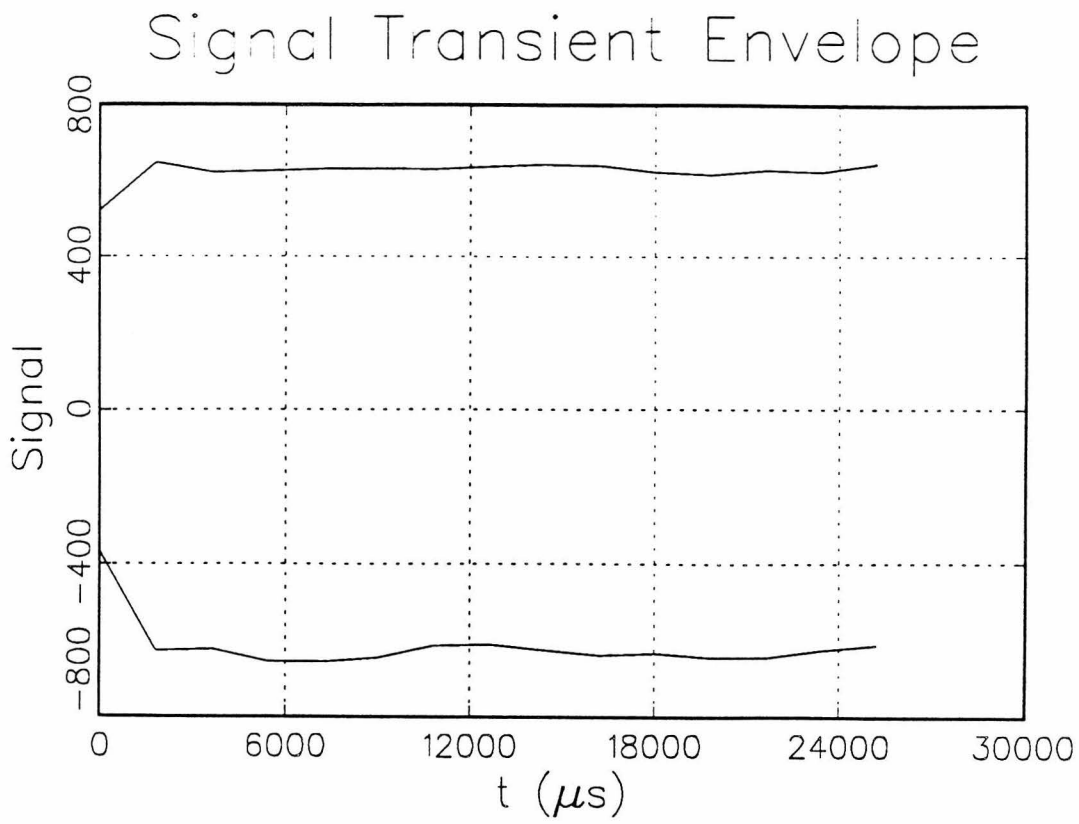
Signal Transient Envelope
Signal
800
400
0
−400
−800
0
6000
12000
18000
24000
30000
t (μs)

11b

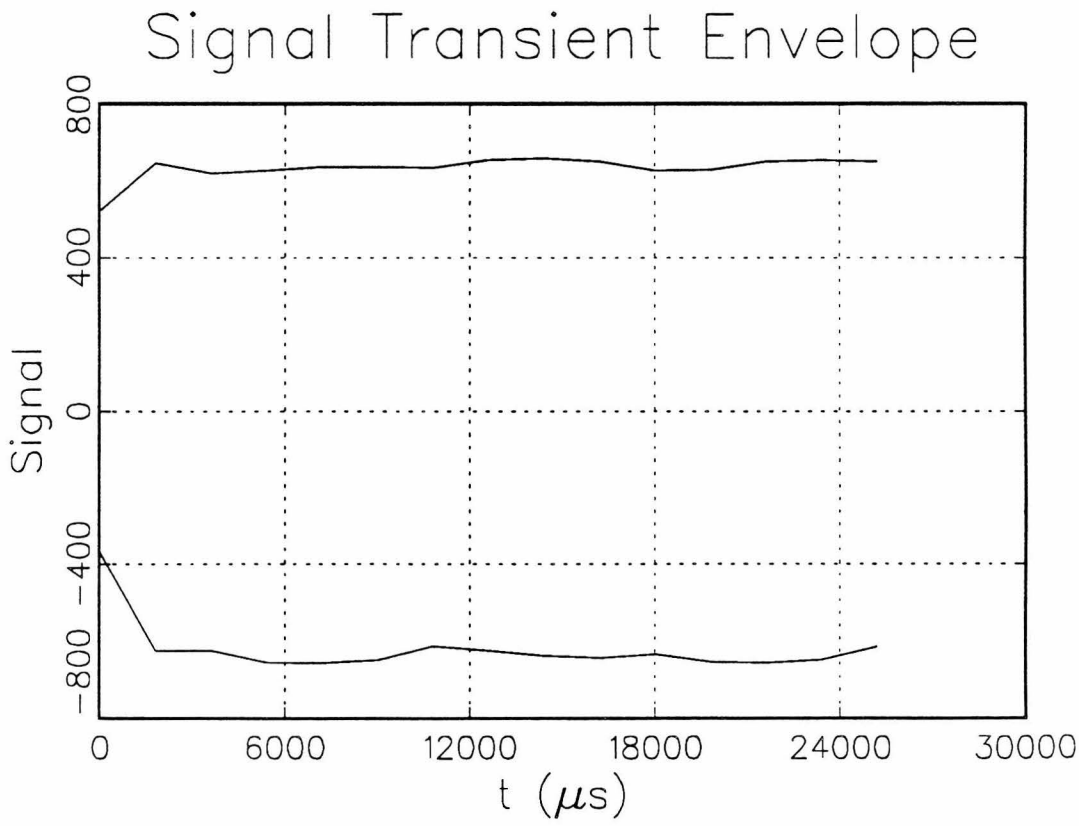
Signal Transient Envelope
Signal
800
400
0
−400
−800
0
6000
12000
18000
24000
30000
t (μs)

11c

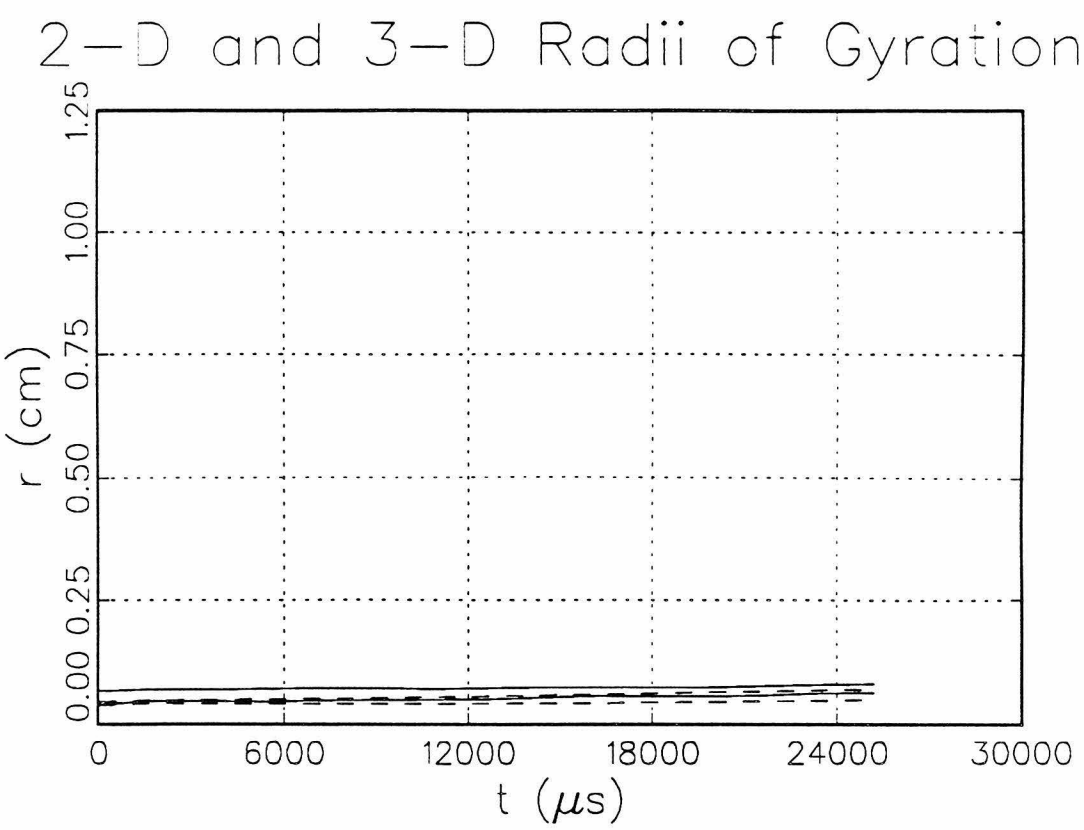
2-D and 3-D Radii of Gyration
r (cm)
0.00
0.25
0.50
0.75
1.00
1.25
0
6000
12000
18000
24000
30000
t (μs)

11d

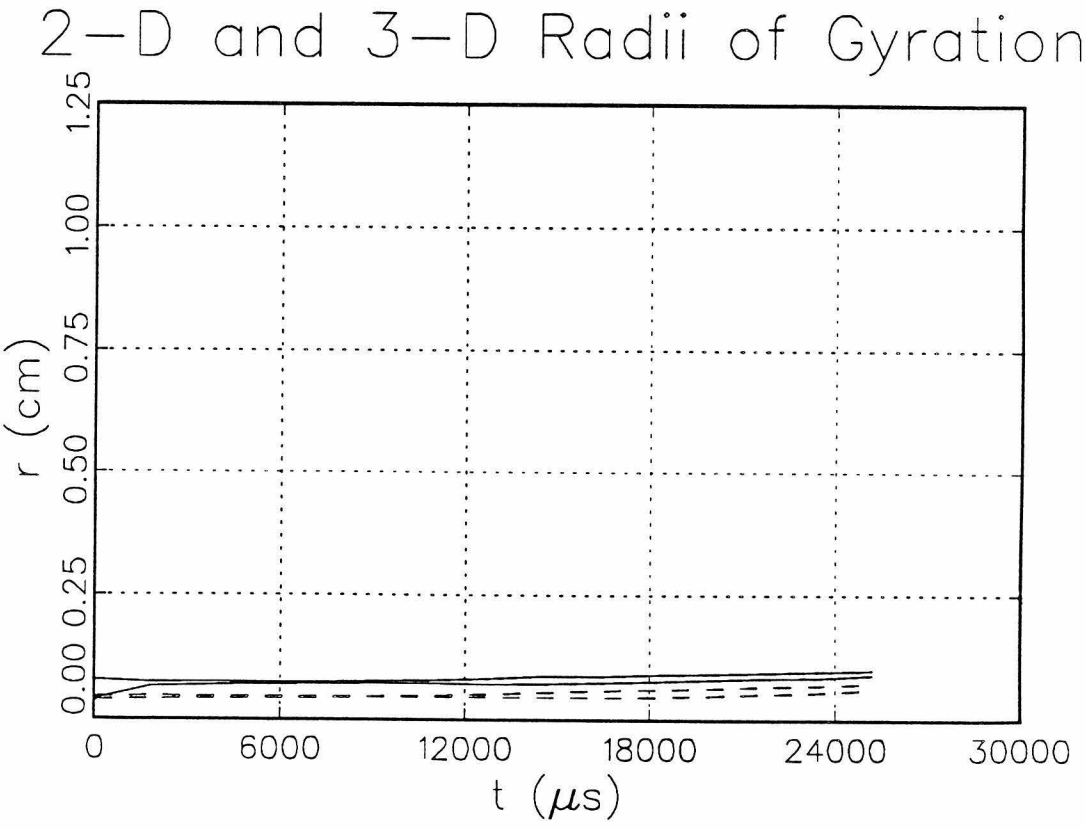
2-D and 3-D Radii of Gyration
r (cm)
0.00
0.25
0.50
0.75
1.00
1.25
0
6000
12000
18000
24000
30000
t (μs)

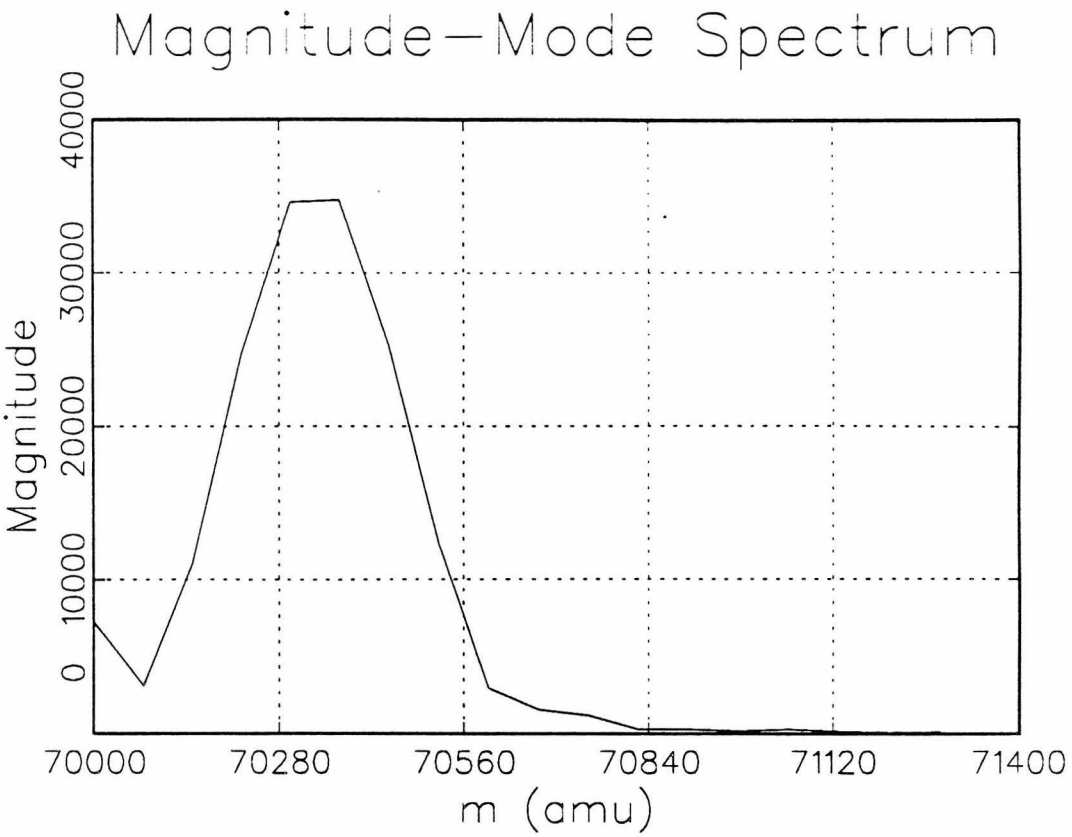
Magnitude–Mode Spectrum
Magnitude
0
10000
20000
30000
40000
70000
70280
70560
70840
71120
71400
m (amu)

11e

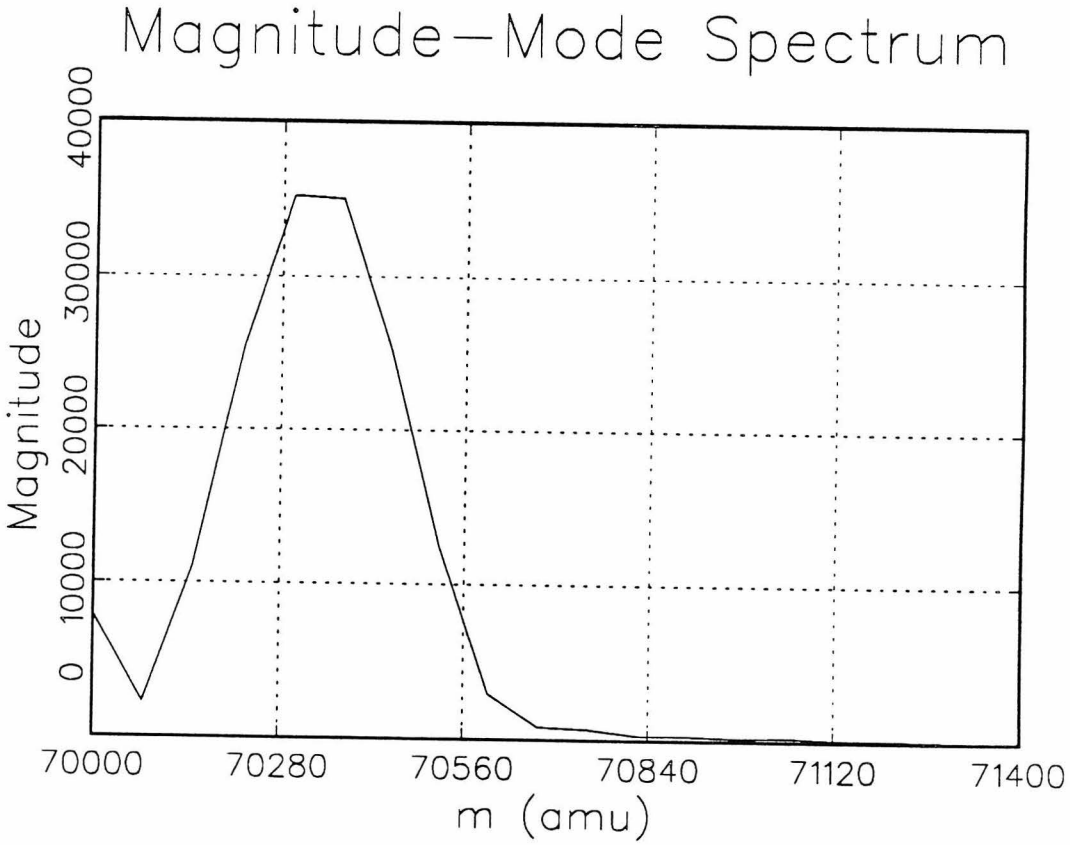
Magnitude–Mode Spectrum
Magnitude
0
10000
20000
30000
40000
70000
70280
70560
70840
71120
71400
m (amu)

11f

12a

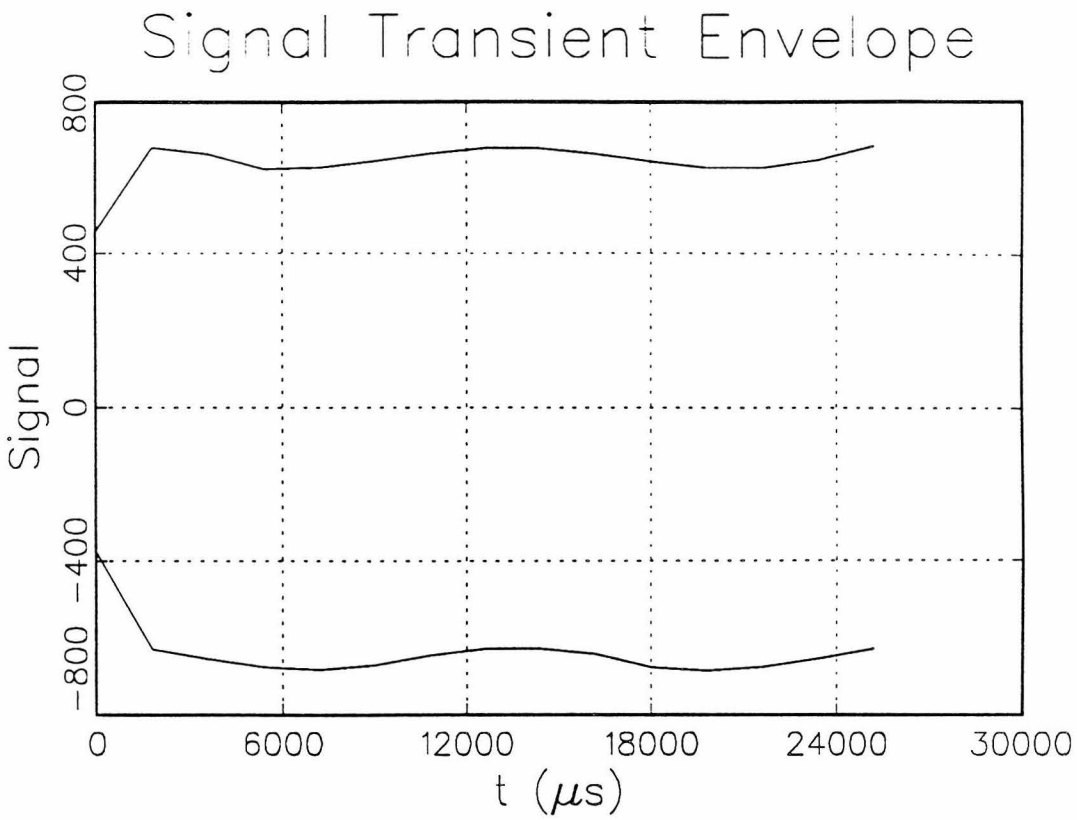
Signal Transient Envelope
Signal
800
400
0
−400
−800
0
6000
12000
18000
24000
30000
t (μs)

12b

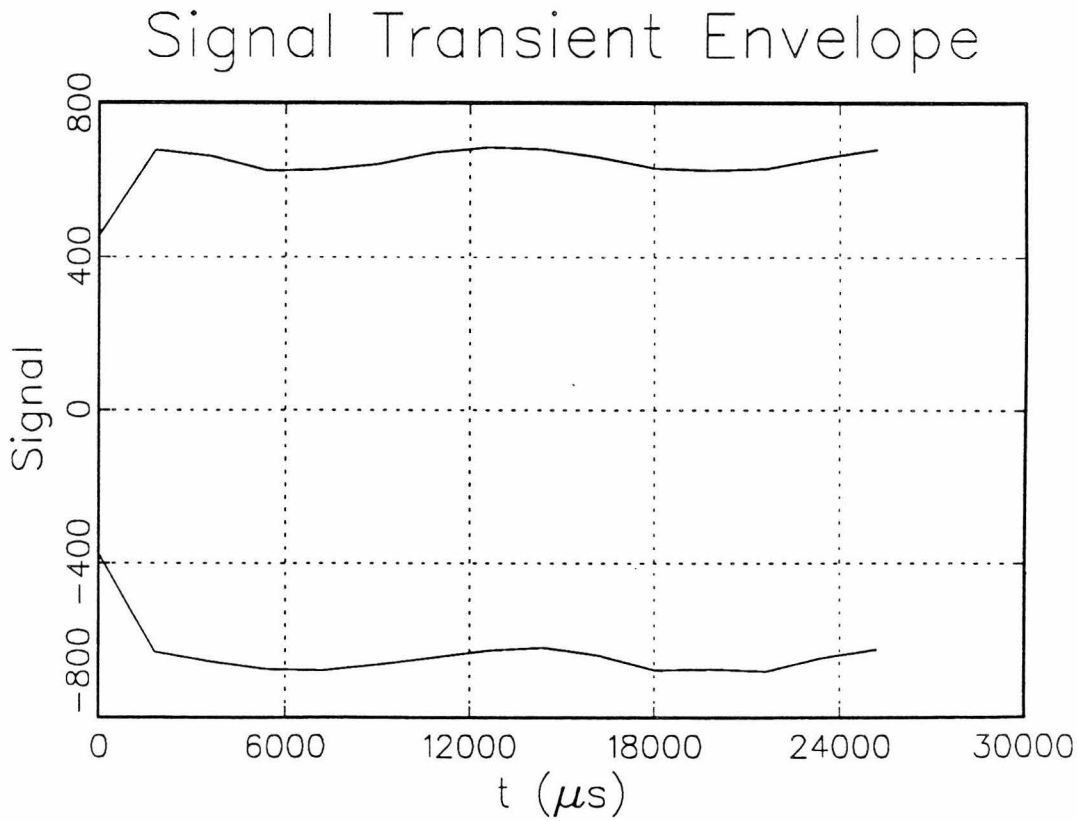
Signal Transient Envelope
Signal
800
400
0
−400
−800
0
6000
12000
18000
24000
30000
t (μs)

12c

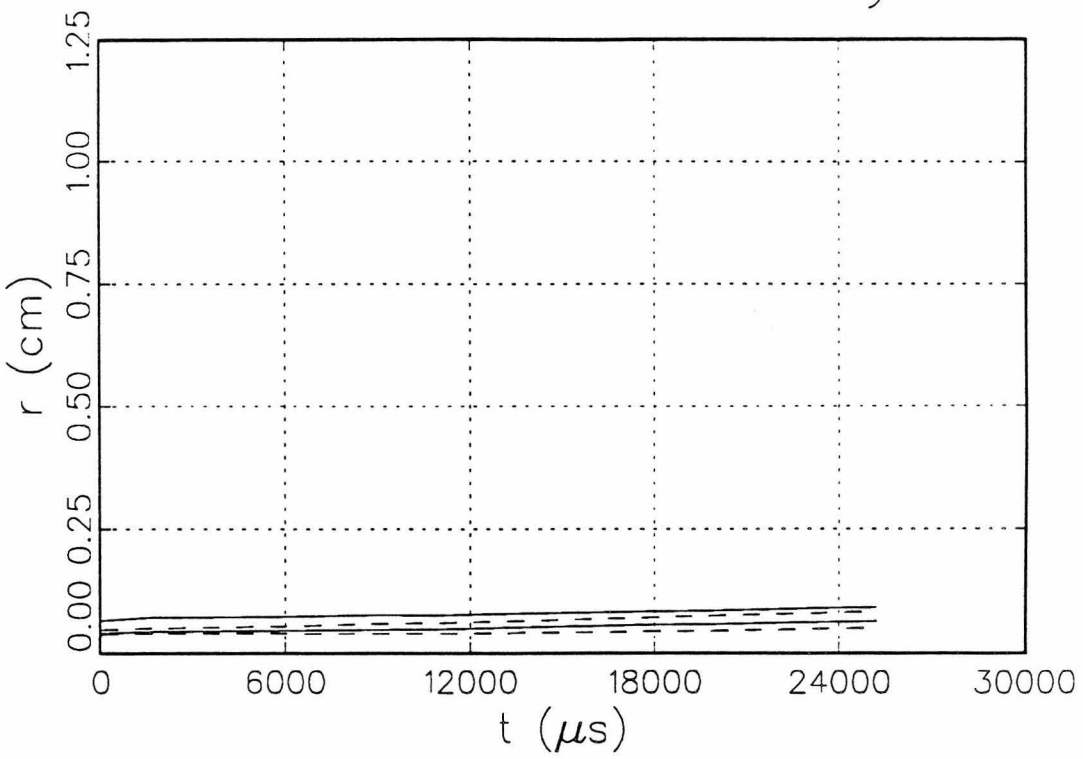
2−D and 3−D Radii of Gyration
r (cm)
0.00
0.25
0.50
0.75
1.00
1.25
0
6000
12000
18000
24000
30000
t (μs)

12d

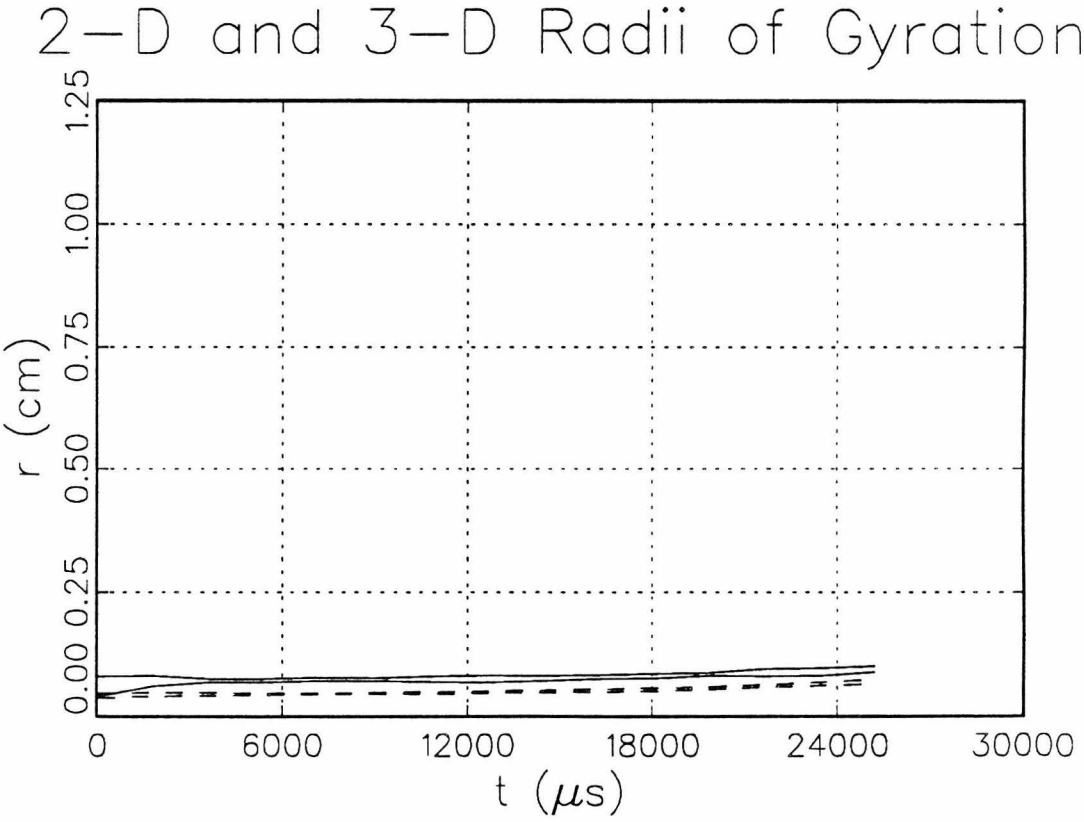
2−D and 3−D Radii of Gyration
r (cm)
0.00
0.25
0.50
0.75
1.00
1.25
0
6000
12000
18000
24000
30000
t (μs)

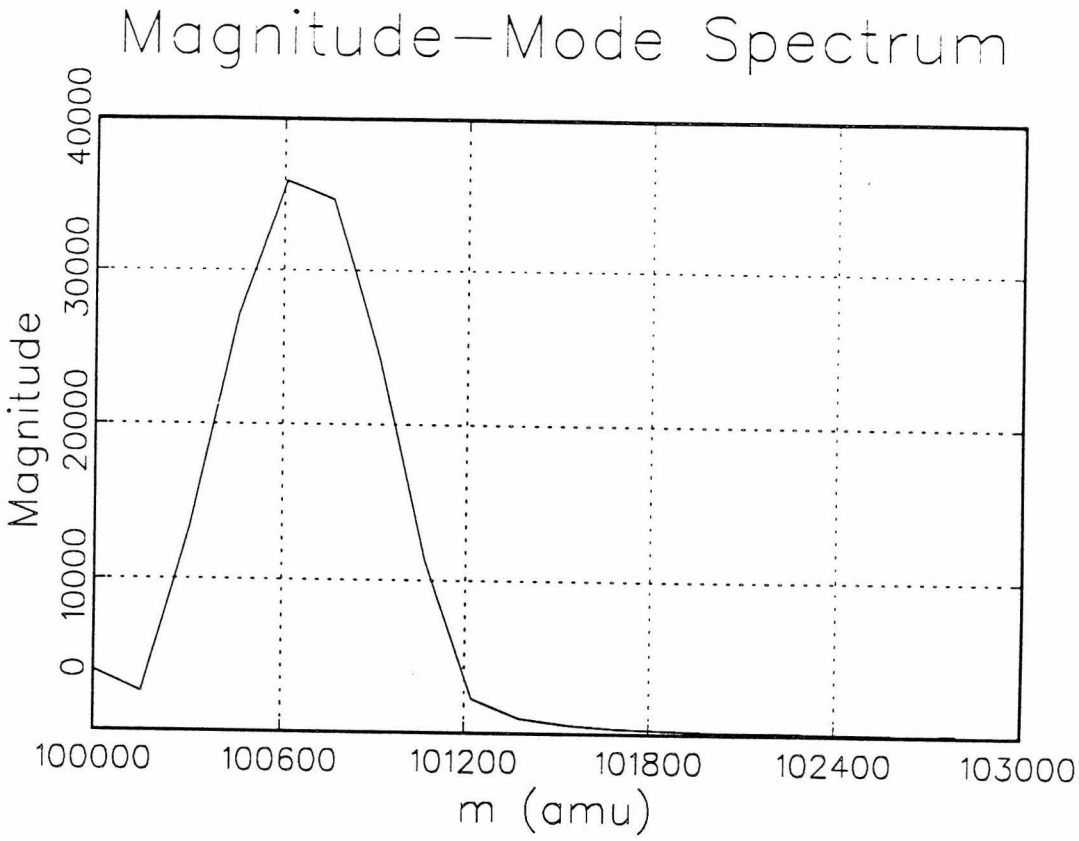
Magnitude–Mode Spectrum
Magnitude
0
10000
20000
30000
40000
100000
100600
101200
101800
102400
103000
m (amu)

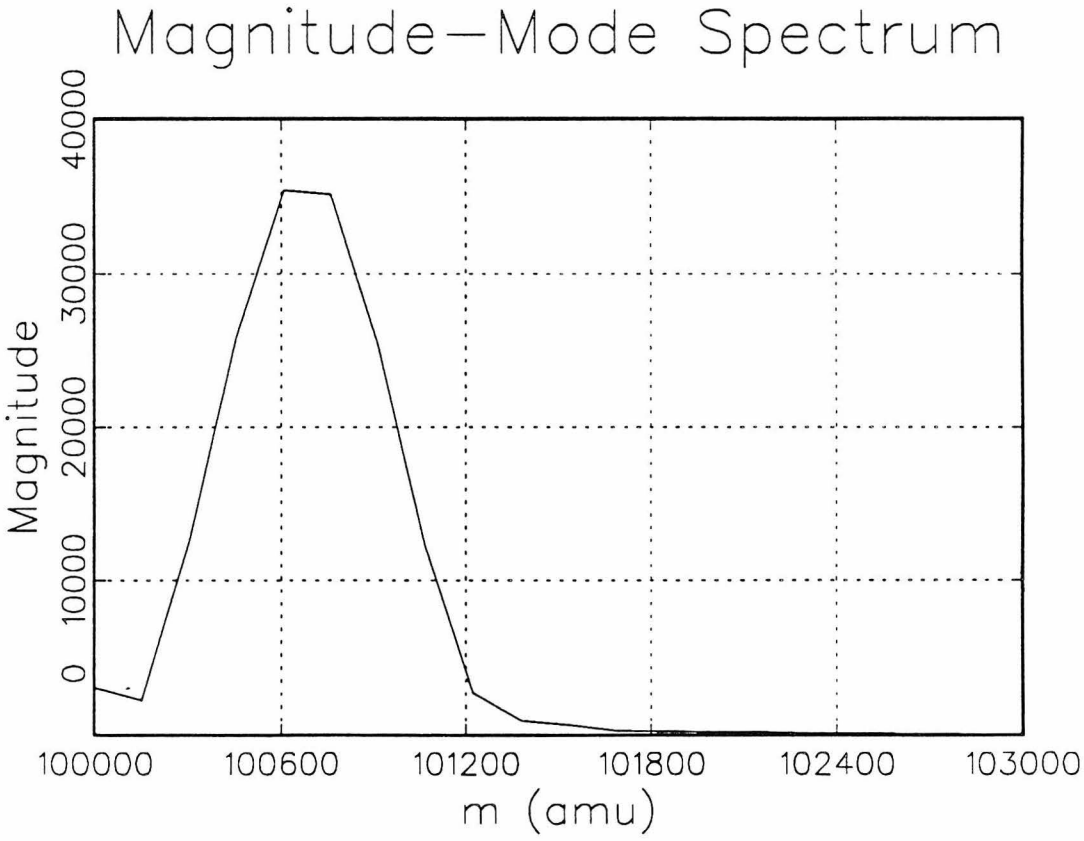
Magnitude–Mode Spectrum
Magnitude
0
10000
20000
30000
40000
100000
100600
101200
101800
102400
103000
m (amu)

13a

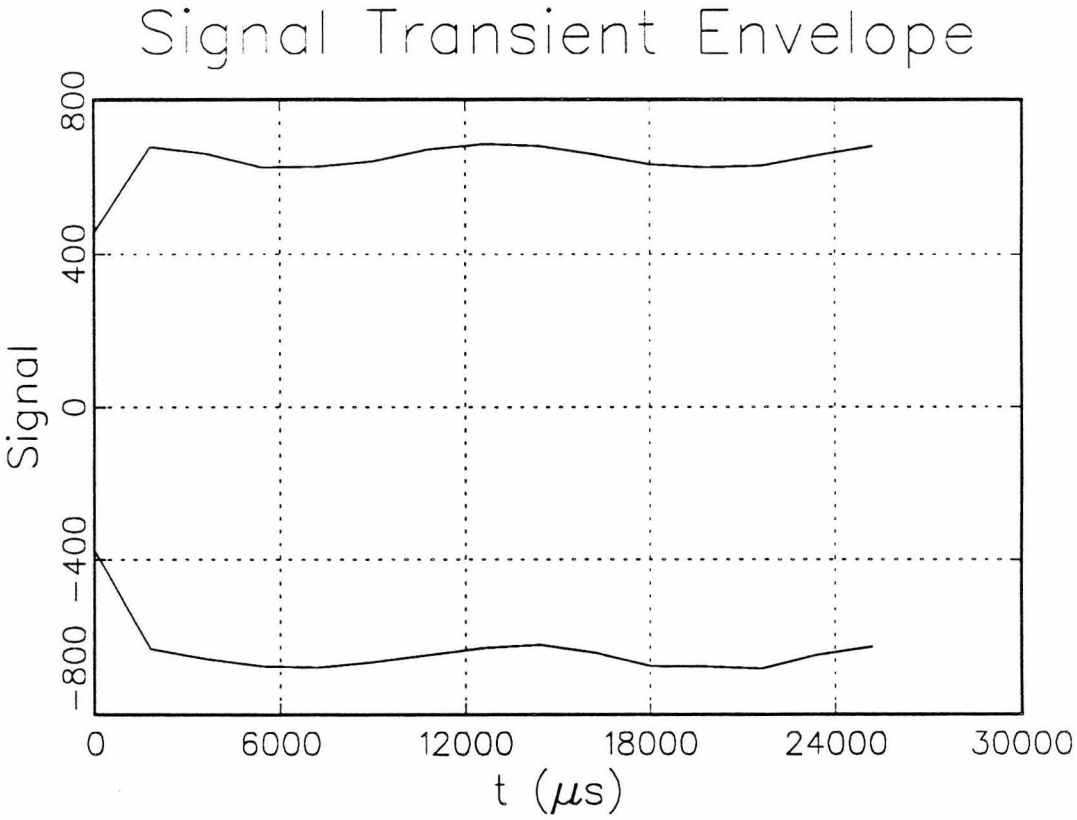
Signal Transient Envelope
Signal
800
400
0
−400
−800
0
6000
12000
18000
24000
30000
t (μs)

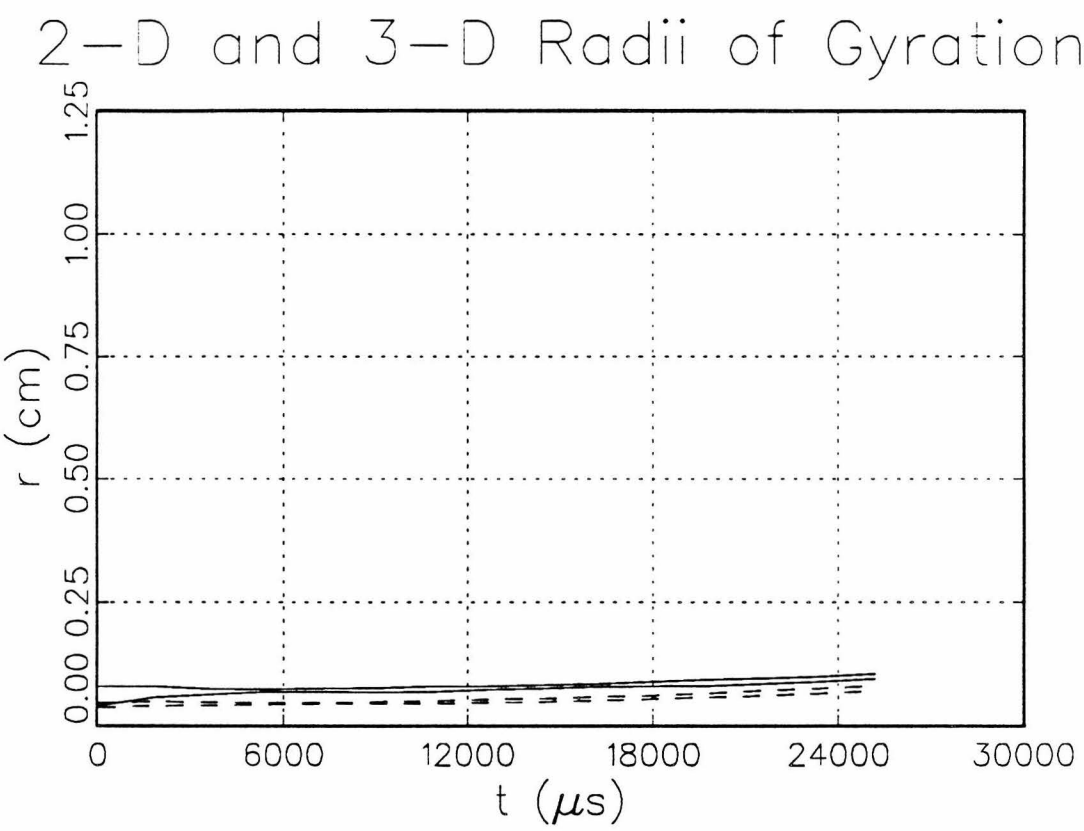
2−D and 3−D Radii of Gyration
r (cm)
0.00
0.25
0.50
0.75
1.00
1.25
0
6000
12000
18000
24000
30000
t (μs)

13c

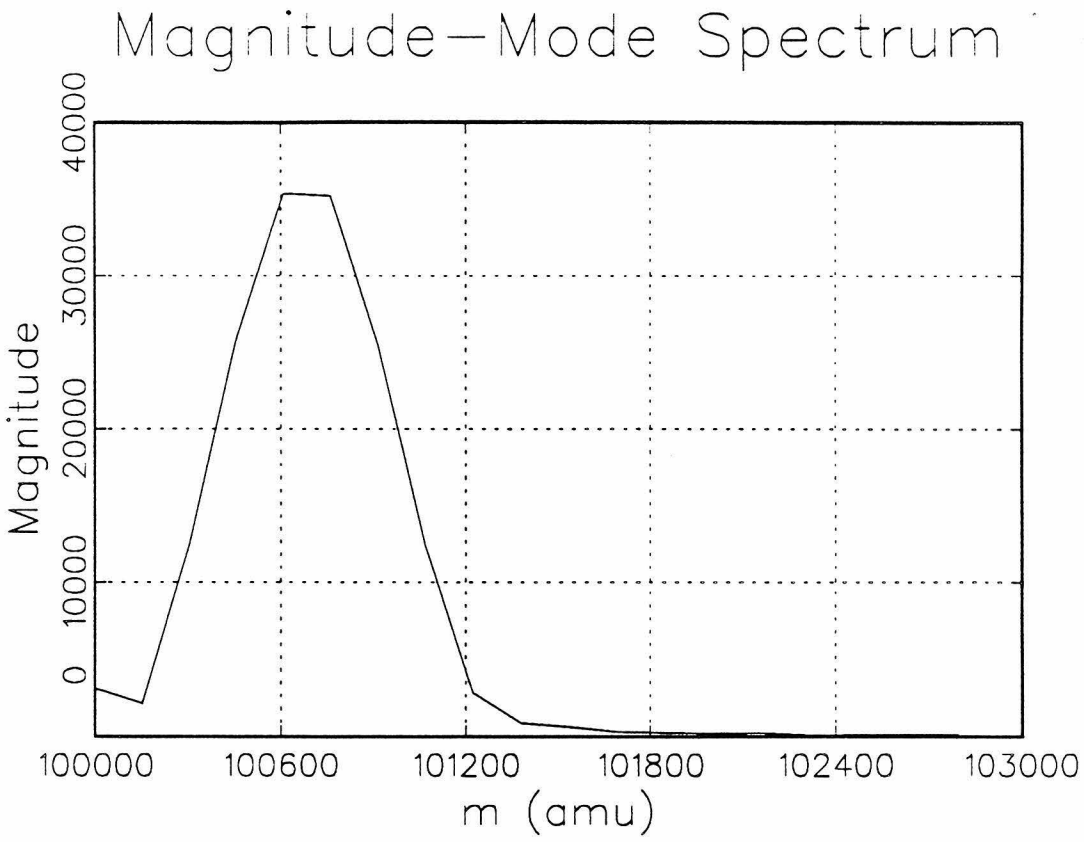
Magnitude–Mode Spectrum
Magnitude
0
10000
20000
30000
40000
100000
100600
101200
101800
102400
103000
m (amu)

CHAPTER IV

A Numerical Study of the Application Of Magnetic Excitation to FT-ICR

M. W. Deem and J. L. Beauchamp

California Institute of Technology, Pasadena, CA 91125

ABSTRACT

A numerical study of the application of magnetic excitation to FT-ICR is presented. It is concluded that magnetic excitation, which would permit nonstandard cell designs, might be practical for excitation to small final cyclotron radii. For greater degrees of excitation, this technique results in excessive magnetron motion and consequent loss of phase coherence and loss of signal. Unlike conventional rf excitation, the time required for magnetic excitation to a given final radius scales linearly with the mass to charge ratio. The technique is thus most applicable to low mass to charge ratio species.

INTRODUCTION

The phenomenon of magnetic excitation of gas-phase ion species has long been known.[1] Although the deleterious effects of spatially varying magnetic fields on ion cyclotron resonance (ICR) resolution have been studied[23], the possibility of using a time-varying axial magnetic field to create an electric field that in turn excites ions seems not to have been examined. This mode of excitation might be imagined to solve several of the problems inherent to conventional rf electric excitation. That is, it is now realized that inhomogeneous electric excitation fields can cause resolution degradation by dephasing an ion packet[4,5,6] or simply by ejecting ions along the z-axis[7,8,9,10,11]. The small time-varying component to the axial magnetic field required for magnetic excitation of ions in an ICR could be created by a solenoidal coil. The axial symmetry of such a coil, to be compared with the traditional cubic differential excitation/detection FT-ICR cell[12], suggests a possible freedom from inhomogeneous excitation fields. Without the requirement of excitation capability, more nearly ideal ("quadrupolar") ion cells, such as a Penning trap[13], could be used, with detection accomplished by very much smaller, and less perturbing to the field, antennas (perhaps wires) than plates. We present here a numerical simulation of the merits of the application of magnetic excitation to FT-ICR.

FT-ICR EM FIELD EQUATIONS.

Despite the possibility of using a different ion cell, our study will focus on the use of the conventional FT-ICR cell. Figure 1 illustrates such a cell. By allowing for the possibility of dephasing, we are presenting a very severe test to the use of magnetic

excitation. The reader should keep in mind that if a hyperbolic trap (Penning trap) were used, any dephasing that magnetic excitation might cause in the cubic cell would not occur.

The geometry of this cubic ICR cell allows Laplace's equation to be separated, and an analytical form for the trapping field can be obtained. The Green function for the cube can be used to derive the difference between the total charges induced on opposite, parallel cube faces, which will be assumed proportional to the experimentally measured signal. Given the fundamental solution[1]

$$\phi(x,y,z) = \frac{16}{\pi^2} \sum_{\substack{m=1 \\ m\ odd}}^{\infty} \sum_{\substack{n=1 \\ n\ odd}}^{\infty} \frac{1}{mn} \sin\left(\frac{m\pi x}{L_x}\right) \sin\left(\frac{n\pi y}{L_y}\right) c_{mn}(z)$$

$$c_{mn}(z) = \left[\frac{\phi_0 e^{-\lambda(L_z - z)} - \phi_1 e^{\lambda z}}{e^{-\lambda L_z} - e^{\lambda L_z}} + \frac{\phi_1 e^{-\lambda z} - \phi_0 e^{\lambda(L_z - z)}}{e^{-\lambda L_z} - e^{\lambda L_z}} \right]$$

$$\lambda^2 = \frac{m^2\pi^2}{L_x^2} + \frac{n^2\pi^2}{L_y^2} \qquad (1)$$

the trapping field is defined by

$$\phi_0 = \phi_1 = V_{trap}$$

$$and$$

$$U_{trap}(x,y,z,t) = \phi(x,y,z) \qquad (2)$$

While the total induced charge difference is given by

$$Q_{obs} = Q_{ind}(0) - Q_{ind}(L_x) =$$

$$\frac{16}{\pi^2} \sum_{\substack{m=1 \\ m\ odd}}^{\infty} \sum_{\substack{n=1 \\ n\ odd}}^{\infty} \frac{1}{mn} \sin\left(\frac{m\pi y'}{L_y}\right) \sin\left(\frac{n\pi z'}{L_z}\right) \times$$

$$\frac{\sinh[\lambda x'] - \sinh[\lambda (L_x - x')]}{\sinh[\lambda L_x]}$$

(3)

These series, which are exponentially converging in m and n but nonuniformly converging at the walls with nonzero boundary conditions, will be used in the numerical integration of the equation of motion.

A small time-varying component to the axial field causes the electric field that will be used for excitation. Recall Maxwell's equations (in MKS units)[14]

$$\nabla \times \boldsymbol{E} = -\frac{\partial \boldsymbol{B}}{\partial t}$$

$$\nabla \times \boldsymbol{B} = \mu_0 \epsilon_0 \frac{\partial \boldsymbol{E}}{\partial t} + \mu_0 \boldsymbol{J}$$

$$\nabla \cdot \boldsymbol{E} = \epsilon_0 \rho$$

$$\nabla \cdot \boldsymbol{B} = 0$$

(4)

Let the imposed axial field be

$$\boldsymbol{B}^{(0)} = B_0[1 + \epsilon \sin(\omega t)]\hat{\boldsymbol{z}}$$

(5)

Then a regular perturbation series expansion gives

$$\boldsymbol{E}^{(1)} = \frac{e B_0 \omega}{2} \cos(\omega t) \; \langle y, -x, 0 \rangle \tag{6}$$

with the further correction

$$d\boldsymbol{B}^{(1)} = -\frac{e B_0 \omega^2}{4c^2} \sin(\omega t) \; (x^2 + y^2) \, \hat{\boldsymbol{z}} \tag{7}$$

so that Eq. (6) is the only significant term created by the perturbation in Eq. (5).

MECHANISM OF MAGNETIC EXCITATION

It is not immediately obvious why the induced electric field, Eq. (6), can cause ion excitation. If an ion were undergoing cyclotron motion about the axis of symmetry, it would appear that there would be no net power adsorbed, for the field given by Eq. (6) reverses direction with time. An ion spinning off-axis is excited, however, by the imposed field if the frequency of the axial magnetic field variation is the cyclotron frequency of the ion. Considering an ion whose cyclotron orbit is entirely to one side of the axis, one can see that the reversal in the field direction is just what is needed to continually impart energy to the ion. Thus it is likely that magnetic excitation will lead to ions with a final cyclotron center that is off-axis, inducing magnetron motion.

The equation of motion, for excitation at the cyclotron frequency, in the x-y plane, ignoring any x-y component to the trapping field, is

$$\ddot{r} + i\omega_c\dot{r} + \frac{i\omega_c^2}{2}\epsilon\cos(\omega_c t)\, r = 0$$

(8)

Where r = x + iy. And where the small axial perturbation has been neglected already. Recall that without a radial component to the trapping field, magnetron motion does not occur. Eq. (8), therefore, precludes the occurrence of magnetron motion.

Postulating a form (also suggested by a multiple scales analysis)

$$r(t) = \alpha(t)\, e^{-i\omega_c t} + \beta(t)$$

(9)

Then

$$\dot{r} = (\dot{\alpha} - i\omega_c\alpha)e^{-i\omega_c t} + \dot{\beta}$$
$$\ddot{r} = (\ddot{\alpha} - 2i\omega_c\dot{\alpha} - \omega_c^2\alpha)e^{-i\omega_c t} + \ddot{\beta}$$

(10)

Assuming

$$\ddot{\beta} \ll \omega_c\dot{\beta}$$

(11)

Eq. (8) becomes

$$(\ddot{\alpha} - i\omega_c\dot{\alpha})e^{-i\omega_c t} + i\omega_c\dot{\beta} + \frac{i\omega_c^2}{2}\epsilon\cos(\omega_c t)(\alpha e^{-i\omega_c t} + \beta) = 0$$

(12)

Averaging Eq. (12) over one cyclotron period[15] leads to

$$i\omega_c\dot{\beta} + \frac{i\omega_c^2}{4}\epsilon\alpha = 0$$

$$or$$

$$\alpha = -\frac{4}{\omega_c\epsilon}\dot{\beta} = -a\dot{\beta}$$

(13)

Now consider the power adsorbed by the form (9) under the field (6).

$$P = \frac{\omega_c}{2\pi}\int_0^{\frac{2\pi}{\omega_c}} q\boldsymbol{E}\cdot\boldsymbol{v}dt = \frac{qB_0\epsilon\alpha^2\omega_c^2\beta}{4}$$

(14)

Assuming the dominance of the magnetic force, the energy can also be expressed in the standard form

$$U = \frac{q^2B_0^2}{2m}\alpha^2$$

(15)

Combining the independent Eqs. (14) and (15) results in

$$\alpha\dot{\beta} = \frac{4}{\epsilon\omega_c}\dot{\alpha} = a\dot{\alpha}$$

(16)

Using Eq. (13),

$$\dot{\beta}\beta = a\dot{\beta}$$

(17)

which has the energy integral

$$\frac{1}{2}\beta^2 = a\beta - C \tag{18}$$

The solution of which is

$$\beta(t) = K\tan\left(\frac{K(t+\delta)}{2a}\right) \tag{19}$$

with, for example, $\delta = 0$ if $\beta(0) = 0$. An approximate solution to Eq. (8) is, then,

$$\beta(t) = K\tan\left(\frac{K\epsilon\omega_c(t+\delta)}{8}\right)$$

and

$$\alpha(t) = -\frac{K^2}{2}\frac{1}{\cos^2\left(\frac{K\epsilon\omega_c(t+\delta)}{8}\right)} \tag{20}$$

The negative sign on $\alpha(t)$ is consistent with the phase of excitation stipulated by Eq. (6). Assumption (11) is satisfied for sufficiently small ϵ and sufficiently small time.

A significant feature of Eq. (20) is that the motion is characterized by $\tau = \epsilon\omega_c t$. Thus, for example, doubling the mass would cause the excitation to be the same if the imposed perturbing field were doubled. Similarly, halving the imposed field requires doubling the excitation time to achieve the same cyclotron radius. The scaling with mass is evident in Eq. (8). The scaling with field strength is not, however.

EXACT EQUATION OF MOTION

The equation of motion for an ion excited at the expected (nonshifted) cyclotron frequency for a time τ is, then,

$$m\ddot{\boldsymbol{x}} = -q\nabla U_{trap} + qE_{excite}(\boldsymbol{x}, t) + q\dot{\boldsymbol{x}}\times\boldsymbol{B}(t)$$
$$\boldsymbol{x}(0) = \boldsymbol{x}_0, \qquad \dot{\boldsymbol{x}}(0) = \boldsymbol{v}_0 \tag{21}$$

Where the $\mathbf{E}_{excite}$ is given by Eq. (6) and the time varying $\mathbf{B}$ is given by Eq. (5). The time variation is active only for $0 \le t \le T_{excite}$. That is

$$\epsilon(t) = \begin{cases} \epsilon, & 0 < t < T_{excite} \\ 0, & T_{excite} < t < \infty \end{cases} \tag{22}$$

The dominant magnetic field will be set to $B_0 = 7$ T. For all our simulations, the trapping voltage is $V_{trap} = 1$ V. For comparison with previous calculations,[6] the initial phase space distribution placed upon Eq. (21) is Maxwellian velocities and positions uniformly distributed in a cylinder centered at the middle of the cell with radius 0.05 cm, the axis of rotation the z-axis, and a length that is 80% of the trapping electrode spacing. The equation of motion, Eq. (21), is integrated numerically by VODE, a variable order, variable step size ODE integration package designed to deal with difficult to integrate, nonlinear equations.[16,17,18,19,20,21] The stable, backward differentiation formula algorithm (MF = 20) is used. For the trajectory calculations we specify a relative error (rtol) of 10^{-6} and an absolute error (atol) of 10^{-8}, which denotes six significant figure accuracy for integration over a reasonable time range. For consistency, Eq. (1) is evaluated to a relative accuracy of

six significant figures.

RESULTS

An important issue is whether the motion of an initially incoherent ion cloud under Eq. (21) results in a coherent ion packet. Consideration of Eq. (20) with initial conditions slightly off-axis suggests it should be, but numerical confirmation is certainly needed. Figure 2 illustrates the first 10 μs of ions undergoing excitation with ϵ = 0.2 / 7.0. It is clear that the ions remain clustered together as they undergo excitation. This extremely high time-varying field would not be experimentally feasible, however. Figure 3 illustrates the trajectory of 1000 amu ions excited to a fairly small final cyclotron radius by an imposed field with ϵ = 0.001 / 7.0. Note that almost no dephasing occurs during the 60 ms observation period.

Figures 4-8 test the parameterization $\tau = \epsilon\omega t$ by varying the amplitude of the imposed field and the excitation time so as to keep ϵT_{excite} constant for mass 100 amu species. It is clear the final radii are the same in all cases. It is also unfortunately clear that the excitation causes an great amount of magnetron motion. This results in the poor signals, with dephasing occurring very rapidly.

Figures 9 and 10 test the parameterization $\tau = \epsilon\omega t$ by varying the mass and the excitation time so as to keep $\epsilon\omega$ for constant T_{excite}. It is clear that the final cyclotron radii are the same in all cases. Again, the magnetic excitation has caused excessive

dephasing.

Figures 11-12 illustrate the effect of the magnetron motion of excitation of higher mass to charge ratio species caused by the exact Eq. (21), which is not taken into account in arriving at the analytical result of Eq. (20). Comparison with Figures 9 and 10 shows that increased excitation time reduces the dephasing caused by magnetron motion, since the signal transients last longer with smaller ϵ. There is a limit to the excitation time, however, for as ϵ is decreased, excitation eventually does not occur. Inhibition of excitation is first evident in Figure 11 d) and Figure 12 c). Consideration of the period of the failed excitation suggests magnetron motion is inhibiting excitation. Indeed, if the calculations are repeated for a hyperbolic trapping field[6], the excitation is still inhibited. Use of a quadratic trapping field,[6] which does not support the magnetron motion a hyperbolic field does, results in excitation. It can be concluded, then, that magnetron motion inhibits the actual excitation event in the magnetic excitation of high mass to charge ratio species.

EXPERIMENTAL IMPLICATIONS

Magnetic excitation seems to work well for excitation to small cyclotron radii. This is because the trapping fields near the axis are hyperbolic and do not cause dephasing when magnetron motion occurs. Excitation to larger radii results in excessive magnetron motion and consequent loss of coherent signal. One solution to this problem would be to use an ion cell that has a hyperbolic trapping potential.[11] A more esoteric solution would be to move the imposed magnetic field (i.e. move the

solenoid) itself as excitation occurs, so as to keep the center of the cyclotron motion near the center of the cube. For the lengthy excitation times necessary for excitation of high mass to charge species, the magnetron motion actually inhibits excitation. An experimental remedy in this case is to use a cell that does not support magnetron motion.[22,23,24,25]

CONCLUSIONS

Magnetic excitation is feasible in FT-ICR applications. The trajectory during excitation is parameterized by the quantity $\tau = \epsilon\omega t$, and thus, for example, higher mass to charge ratios require longer excitation times. Within the confines of the traditional cubic ion cell, however, magnetic excitation appears to be limited to excitation to rather small cyclotron radii. Excitation to moderate radii results in severe magnetron motion and consequent loss of ion packet coherence. Magnetron motion also inhibits excitation if the excitation event is lengthy, which is a further reason for the restriction of the technique to studies of low mass to charge ratio species.

ACKNOWLEDGEMENTS

We would like to thank Paul Messina, the Director of the Caltech Concurrent Supercomputing Facilities, for generous grants of computer time.

REFERENCES

1) J. M. Berger, W. A. Newcomb, J. M. Dawson, E. A. Friedman, R. M. Kulsrud, and A. Lenard, Phys. Fluids 1 (1958) 301.

2) D. Schuch, H, -M. Chung, and H. Hartmann, Int. J. Mass Spectrom. Ion Proc. 54 (1984) 109.

3) Frank H. Laukien, Int. J. Mass Spectrom. Ion Proc. 73 (1986) 81.

4) Mingda Wang and Alan G. Marshall, Anal. Chem. 61 (1989) 1288.

5) Curtiss D. Hanson, Mauro E. Castro, Eric L. Kerley, and David H. Russell, Anal. Chem. 62 (1990) 520.

6) M. W. Deem and J. L. Beauchamp, A Fundamental Mass Resolution Limit of the Conventional FT-ICR Cubic Cell, to appear in Int. J. Mass Spectrom. Ion Proc. 1991.

7) S. K. Huang, D. L. Rempel, and M. L. Gross, Int. J. Mass Spectrom. Ion Proc. 72 (1986) 15.

8) P. Kofel, M. Allemann, HP. Kellerhals, and K. P. Wanczek, Int. J. Mass Spectrom. Ion Proc. 74 (1986) 1.

9) M. Allemann, P. Kopfel, Hp. Kellerhals, and K. -P. Wanczek, Int. J. Mass Spectrom. Ion Proc. 75 (1987) 47.

10) W. J. an der Hart and W. J. van de Guchte, Int. J. Mass Spectrom. Ion Proc. 82 (1988) 17.

11) Mingda Wang and Alan G. Marshall, Anal. Chem. 62 (1990) 515.

12) Melvin B. Comisarow, Int. J. Mass Spec. Ion Phys. 37 (1981) 251-257.

13) D. J. Wineland and Wayne M. Itano, Adv. At. Mol. Phys. 19 (1983) 135.

14) J. D. Jackson, Classical Electrodynamics, 2nd ed., John Wiley & Sons: New York, 1975.

15) Daniel Zwillinger, Handbook of Differential Equations, Academic Press: New York, 1989.

(16) P. N. Brown, G. D. Byrne, and A. C. Hindmarsh, "VODE, a Variable Coefficient ODE Solver," LLNL Report UCRL-98412, June 1988. Also, SIAM J. Sci. Stat. Comput., to appear.

(17) G. D. Byrne and A. C. Hindmarsh, ACM Trans. Math. Software 1 (1975) 71.

(18) A. C. Hindmarsh and G. D. Byrne, "EPISODE: An Effective Package for the Integration of Systems of Ordinary Differential Equations," LLNL Report UCID-30112, Rev. 1, April 1977.

(19) G. D. Byrne and A. C. Hindmarsh, "EPISODEB: An Experimental Package for the Integration of Systems of Ordinary Differential Equations with Banded Jacobians," LLNL Report UCID-30132, April 1976.

(20) A. C. Hindmarsh, Scientific Computing, R. S. Stepleman et al., eds., North-Holland, Amsterdam, 1983, pp. 55-64.

(21) K. R. Jackson and R. Sacks-Davis, ACM Trans. Math. Software 6 (1980) 295.

(22) M. Wang and A. G. Marshal, Anal. Chem. 61 (1989) 1288-1293.

(23) M. Wang and A. G. Marshal, Anal. Chem. 62 (1990) 515-520.

(24) C. D. Hanson, M. E. Castro, E. L. Kerley, and D. H. Russell, Anal. Chem. 62 (1990) 520-526.

(25) D. L. Rempel, R. P. Grese, and M. L.Gross, "A Scaling Technique for Studying the Dynamics of High Mass Ions in FTMS: A Preliminary Report," to appear in Int. J. Mass Spectrom. Ion Proc. 100 (1990).

FIGURES

Figure 1. Depicted is the FT-ICR cell and coordinate system for which our calculations are appropriate. The direction of **B** is along the z-axis as indicated. Also indicated are the trapping, excitation, and detection plates.

Figure 2. Depicted is the motion of five ions during the first 10 μs of excitation with ϵ = 0.2 / 7.0 with m = 100 amu, z = 1 $|e^-|$. Note that the excitation is clearly coherent.

Figure 3. Depicted is the motion of five ions with m = 1000 amu, z = 1 $|e^-|$. In this case, T_{excite} = 2 ms, and ϵ = 0.001 / 7.0. Note that there is almost no dephasing of the ions for this small cyclotron radius. a) depicts the x-y ion motion during the last 200 μs of the motion, b and c) attempt to depict the magnetron motion by plotting the ion positions averaged over 500 μs intervals, d) depicts the induced charged predicted by Eq. (3), and e) depicts the Fourier transform of the signal defined by Eq. (3).[6]

Figure 4. Depicted is the motion of five ions with m = 100 amu, z = 1 $|e^-|$, with T_{excite} = 20 μs, and ϵ = 0.1 / 7.0. For the m = 100 amu plots (only) the final ion motion a) is plotted undersampled at 1 MHz (the cyclotron frequency is 1.075 Hz)

Figure 5. Depicted is the motion of five ions with m = 100 amu, z = 1 $|e^-|$, with

T_{excite} = 40 μs, and ϵ = 0.05 / 7.0.

Figure 6. Depicted is the motion of five ions with m = 100 amu, z = 1 $|e^-|$, with T_{excite} = 200 μs, and ϵ = 0.01 / 7.0.

Figure 7. Depicted is the motion of five ions with m = 100 amu, z = 1 $|e^-|$, with T_{excite} = 400 μs, and ϵ = 0.005 / 7.0.

Figure 8. Depicted is the motion of five ions with m = 100 amu, z = 1 $|e^-|$, with T_{excite} = 2 ms, and ϵ = 0.001 / 7.0.

Figure 9. Depicted is the motion of five ions with m = 1000 amu, z = 1 $|e^-|$, with T_{excite} = 4 ms, and ϵ = 0.005 / 7.0.

Figure 10. Depicted is the motion of five ions with m = 2000 amu, z = 1 $|e^-|$, with T_{excite} = 4 ms, and ϵ = 0.01 / 7.0.

Figure 11. Depicted are the signal envelopes for other values of ϵ for the excitation of the ions of Figure 9. a) is ϵ = 0.1, b) ϵ = 0.05, c) ϵ = 0.01, and d) ϵ = 0.001. In all cases, ϵ T_{excite} = 0.02 / 7.0.

Figure 12. Depicted are the signal envelopes for other values of ϵ for the excitation of the ions of Figure 10. a) is ϵ = 0.1, b) ϵ = 0.05, c) ϵ = 0.005, and d) ϵ = 0.001. In all

cases, ϵ T_{excite} = 0.04 / 7.0.

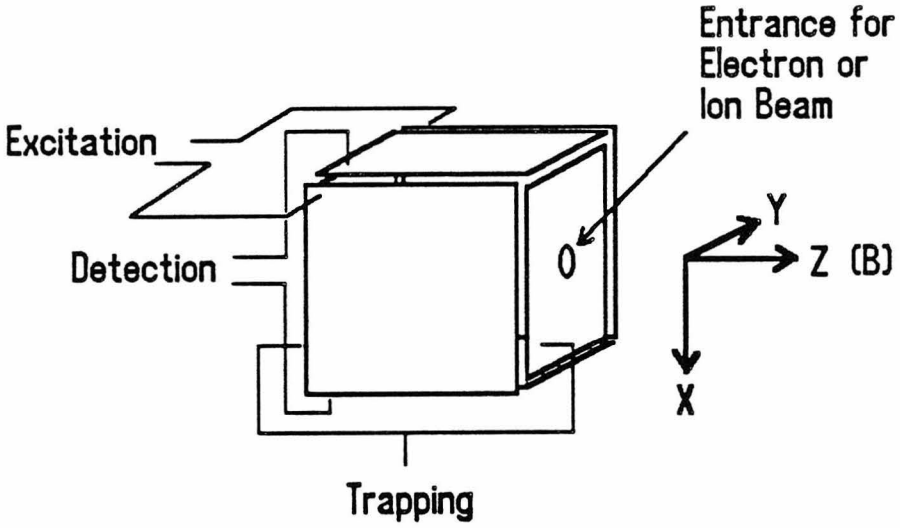
Entrance for
Electron or
Ion Beam
Excitation
Detection
O
Y
Z (B)
X
Trapping

2a

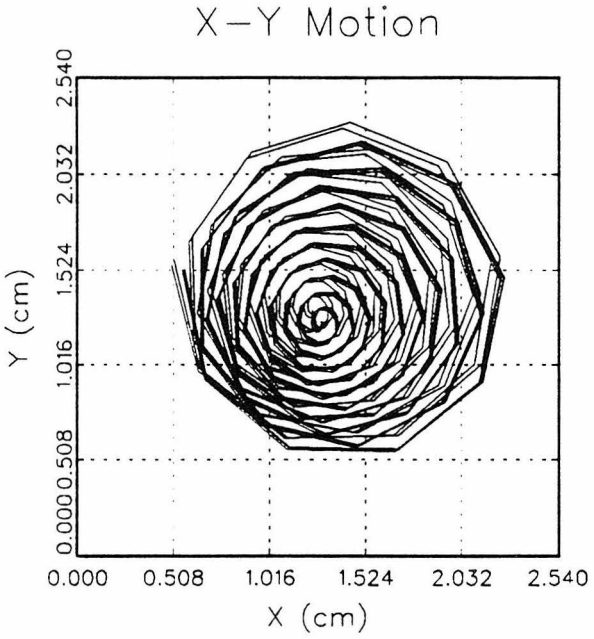
X-Y Motion
Y (cm)
0.000
0.508
1.016
1.524
2.032
2.540
X (cm)

2b

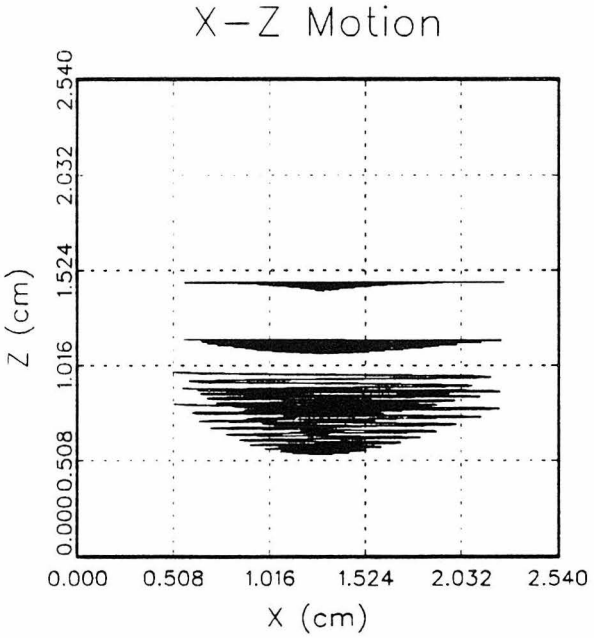
X-Z Motion
Z (cm)
0.000
0.508
1.016
1.524
2.032
2.540
X (cm)

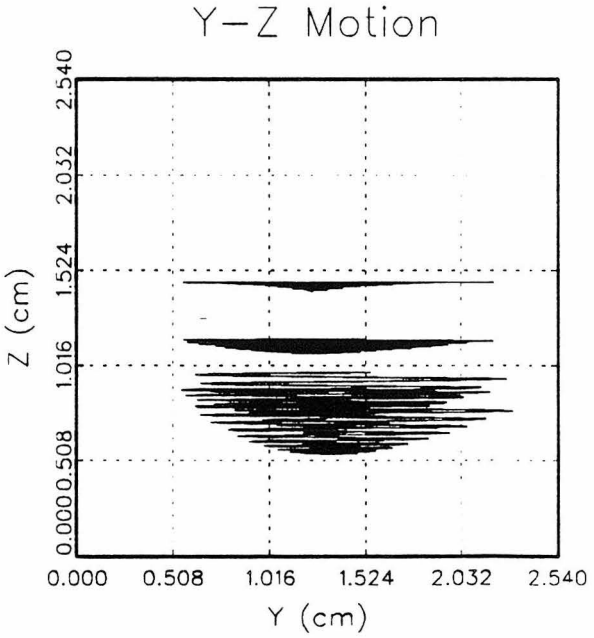
Y-Z Motion
Z (cm)
0.000
0.508
1.016
1.524
2.032
2.540
Y (cm)

2c

3a

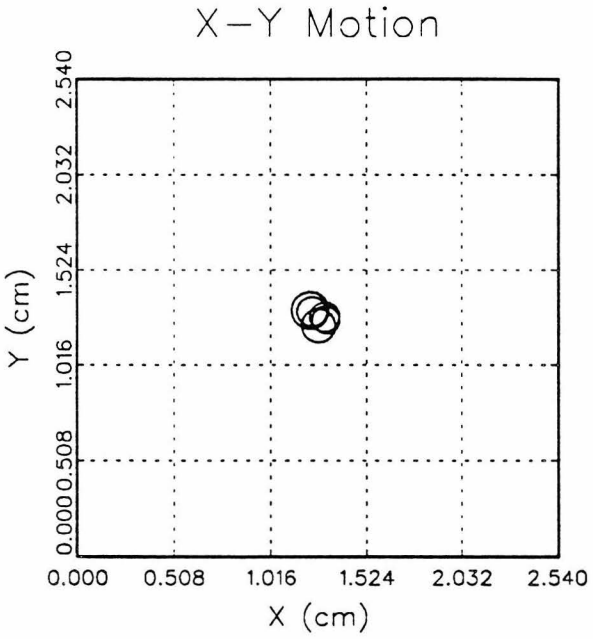
X–Y Motion
Y (cm)
0.000
0.508
1.016
1.524
2.032
2.540
X (cm)

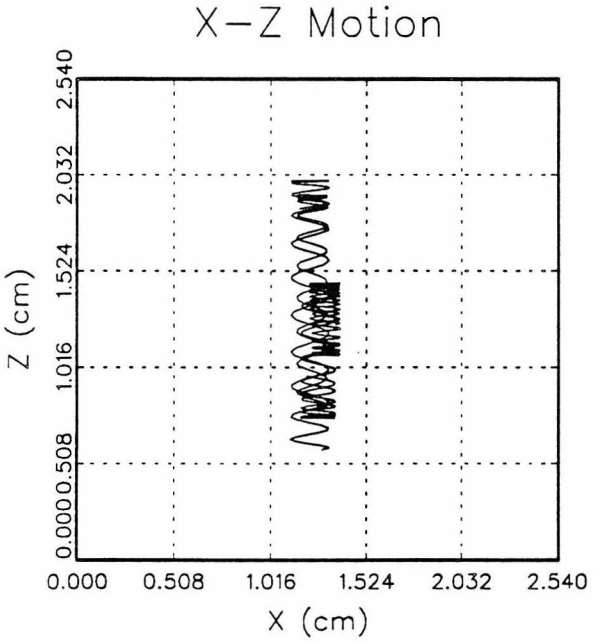
X–Z Motion
Z (cm)
0.000
0.508
1.016
1.524
2.032
2.540
X (cm)

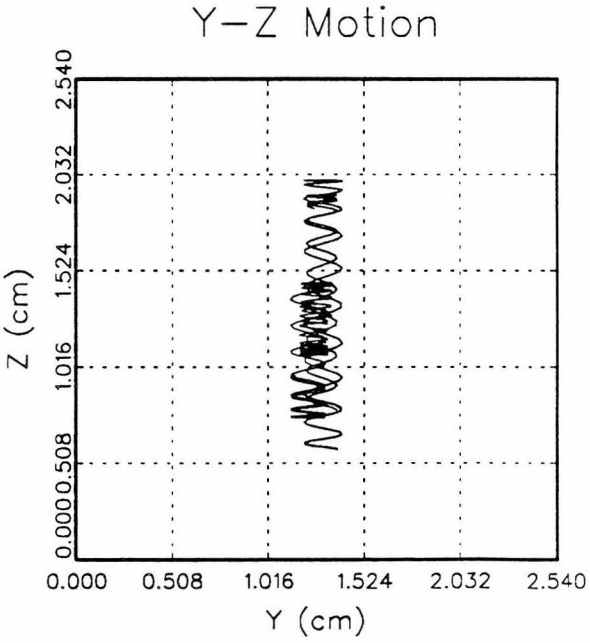
Y–Z Motion
Z (cm)
0.000
0.508
1.016
1.524
2.032
2.540
Y (cm)

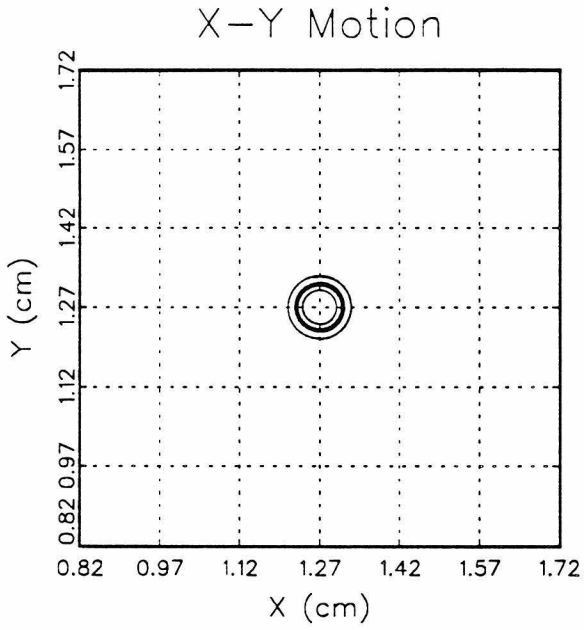
X–Y Motion
Y (cm)
X (cm)
0.82
0.97
1.12
1.27
1.42
1.57
1.72

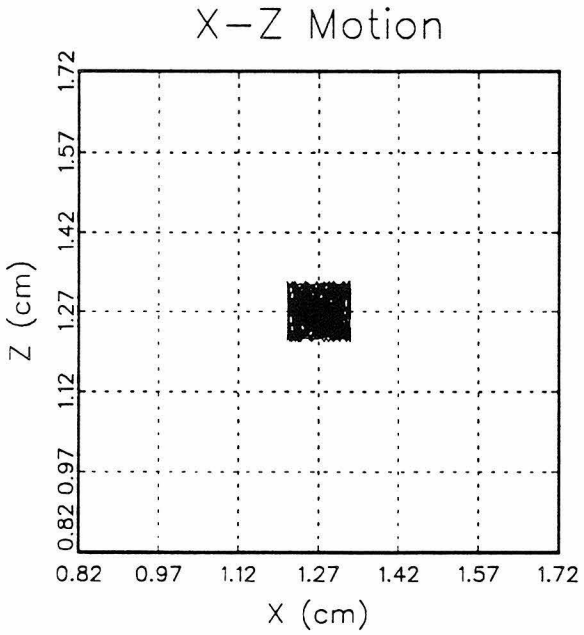
X–Z Motion
Z (cm)
X (cm)
0.82
0.97
1.12
1.27
1.42
1.57
1.72

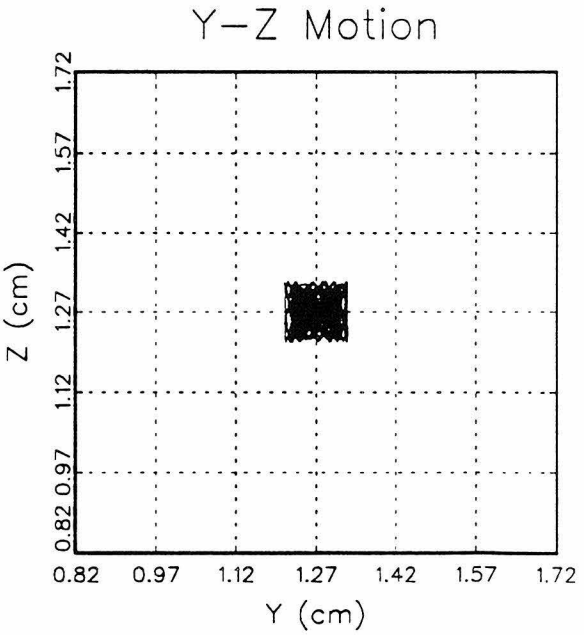
Y–Z Motion
Z (cm)
Y (cm)
0.82
0.97
1.12
1.27
1.42
1.57
1.72

3d

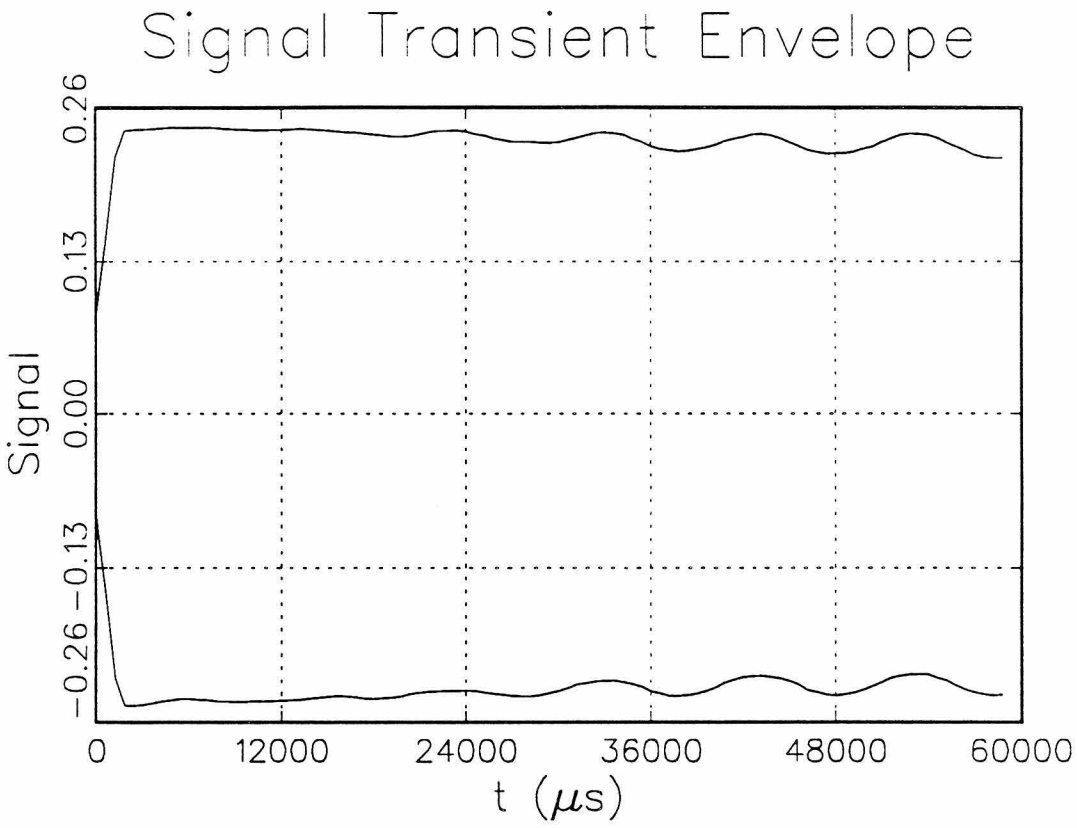
Signal Transient Envelope
Signal
0.26
0.13
0.00
−0.13
−0.26
0
12000
24000
36000
48000
60000
t (μs)

3e

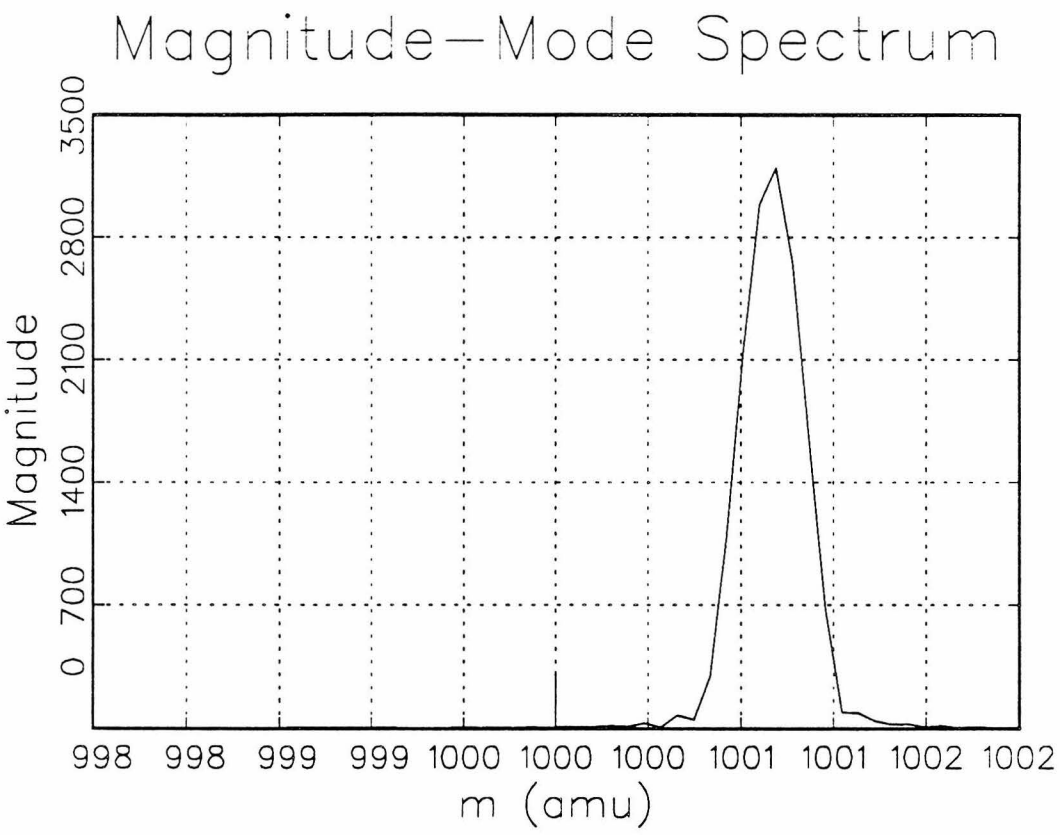
Magnitude–Mode Spectrum
Magnitude
0 700 1400 2100 2800 3500
998 998 999 999 1000 1000 1000 1001 1001 1002 1002
m (amu)

4a

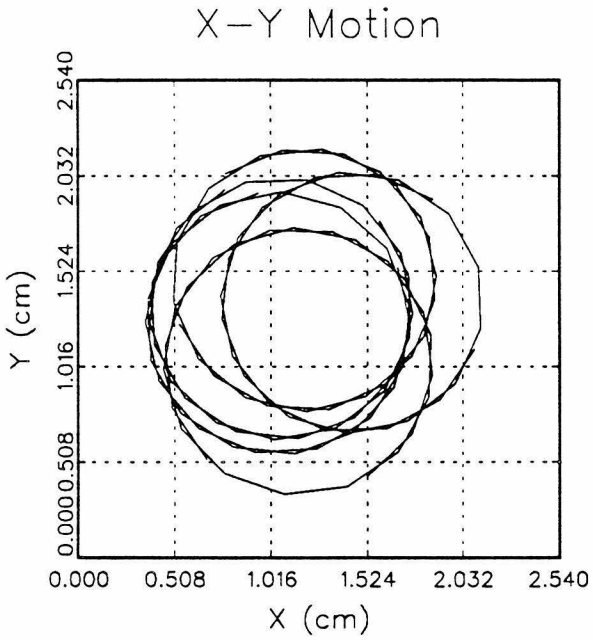
X–Y Motion
Y (cm)
0.000
0.508
1.016
1.524
2.032
2.540
X (cm)

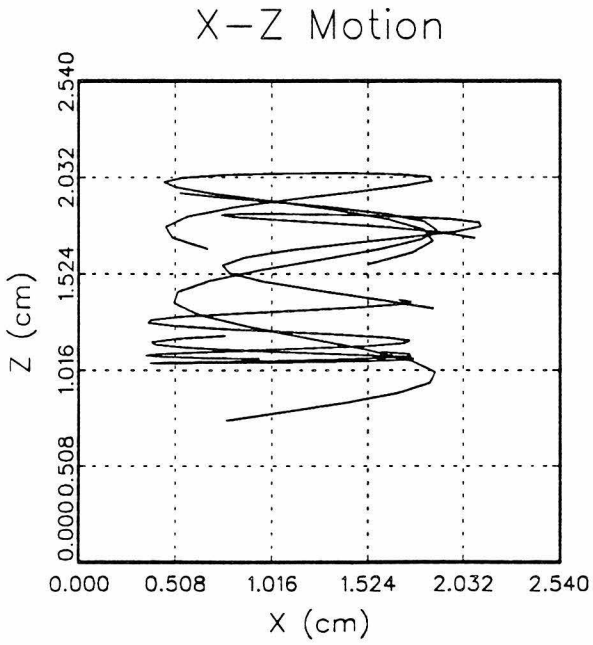
X–Z Motion
Z (cm)
0.000
0.508
1.016
1.524
2.032
2.540
X (cm)

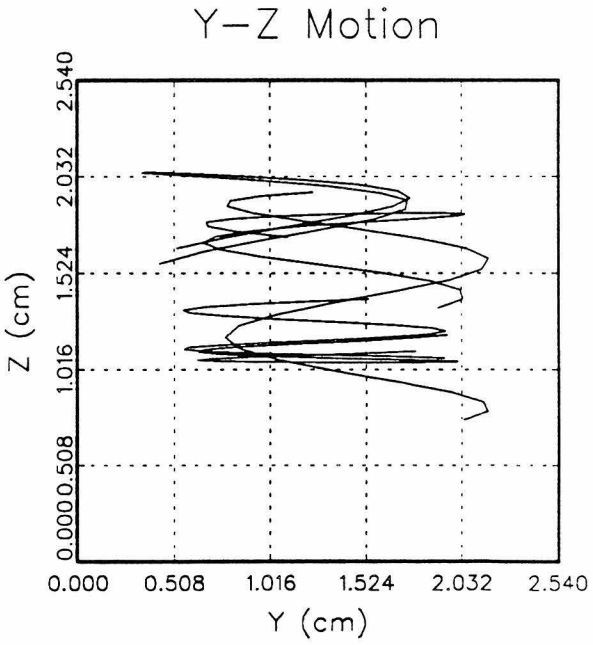
Y–Z Motion
Z (cm)
0.000
0.508
1.016
1.524
2.032
2.540
Y (cm)

4b

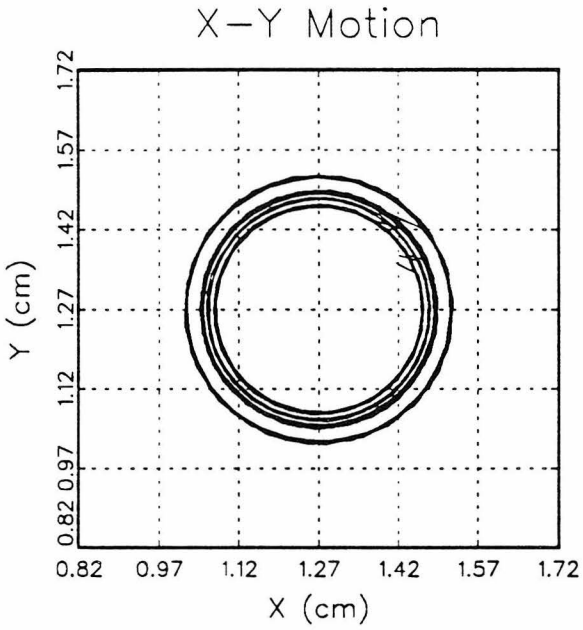
X−Y Motion
Y (cm)
X (cm)
0.82
0.97
1.12
1.27
1.42
1.57
1.72

4c

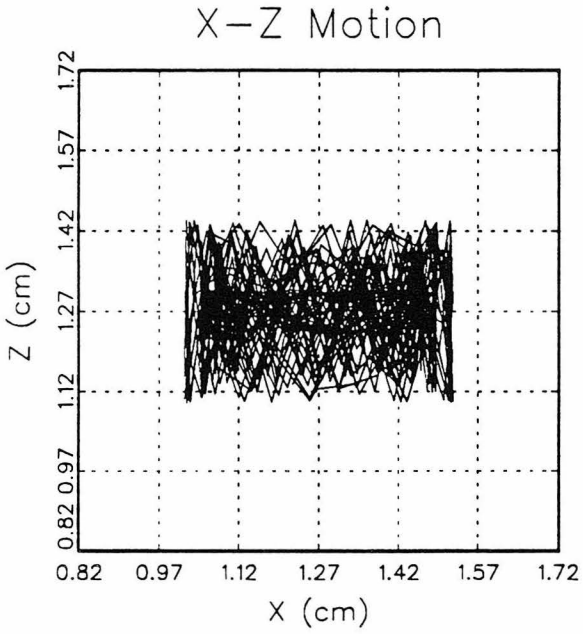
X−Z Motion
Z (cm)
X (cm)
0.82
0.97
1.12
1.27
1.42
1.57
1.72

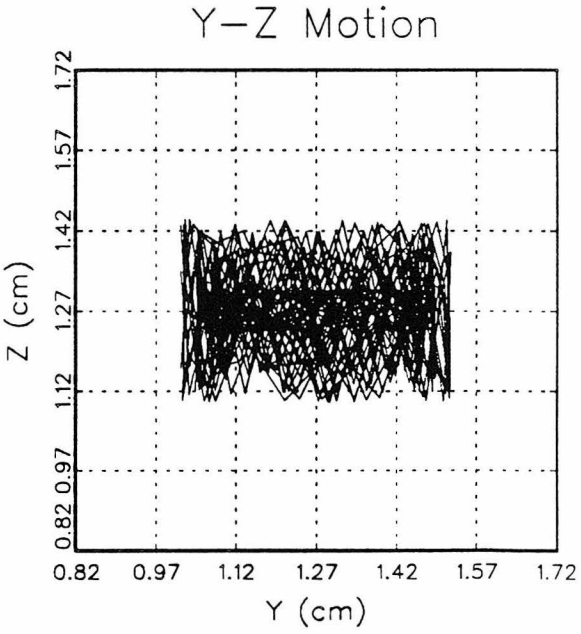
Y−Z Motion
Z (cm)
Y (cm)
0.82
0.97
1.12
1.27
1.42
1.57
1.72

ud

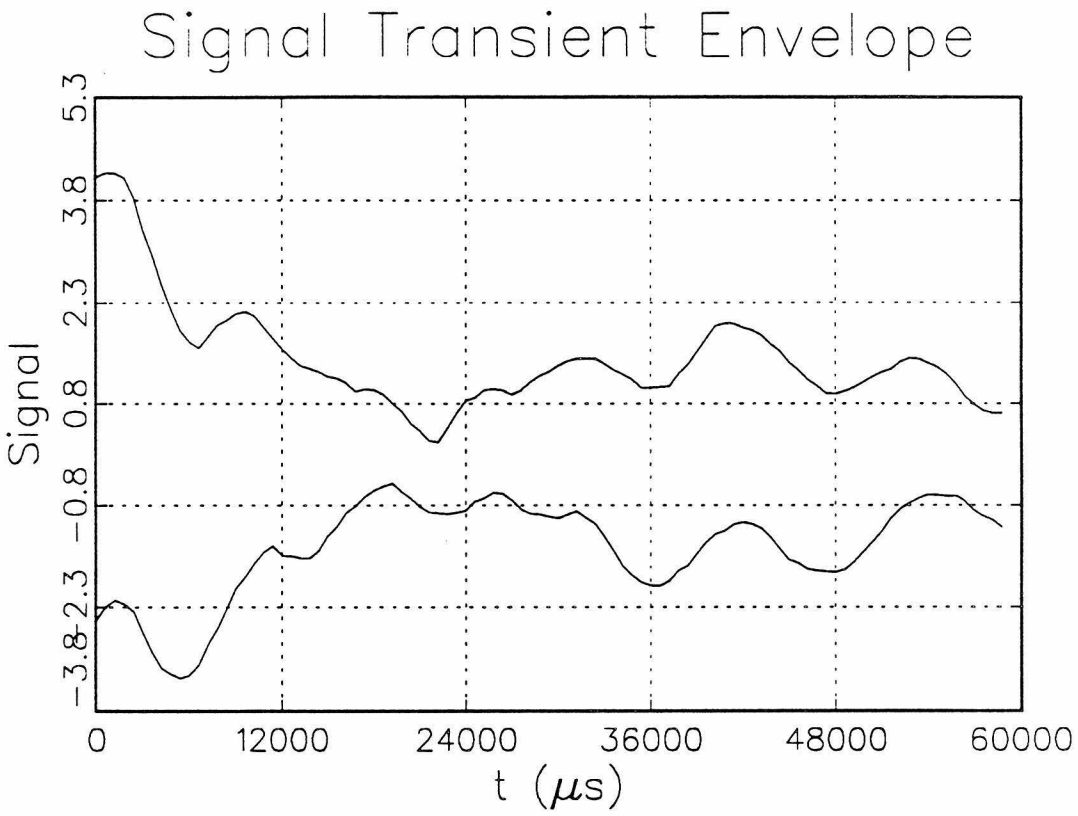
Signal Transient Envelope
Signal
5.3
3.8
2.3
0.8
−0.8
−2.3
−3.8
0
12000
24000
36000
48000
60000
t (μs)

4e

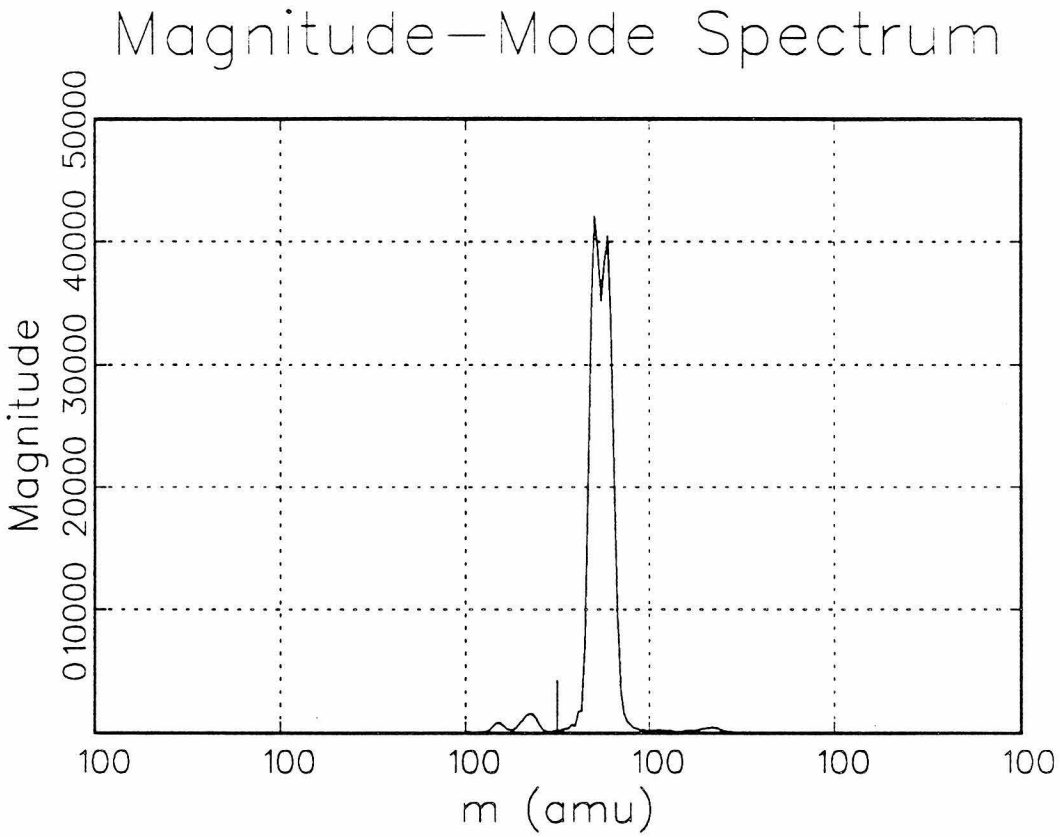
Magnitude–Mode Spectrum
Magnitude
010000 20000 30000 40000 50000
100 100 100 100 100 100
m (amu)

5a

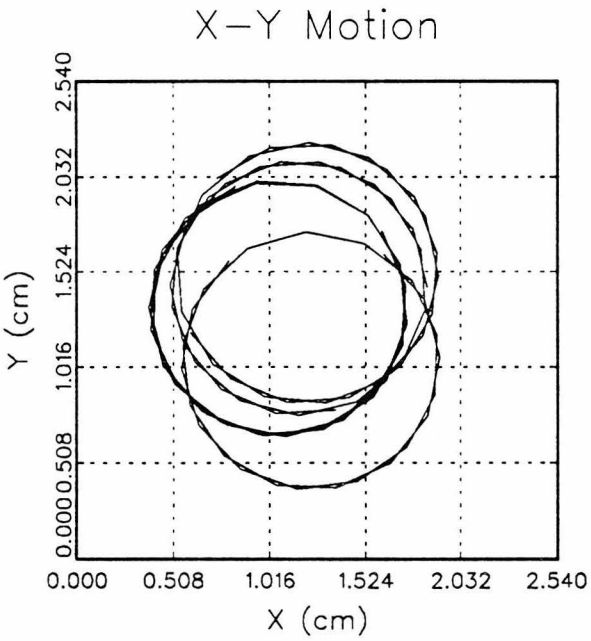
X–Y Motion
Y (cm)
X (cm)
0.000
0.508
1.016
1.524
2.032
2.540

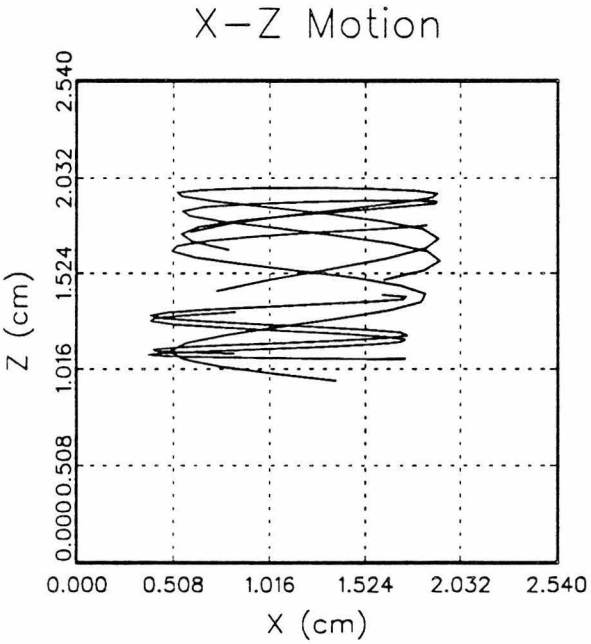
X–Z Motion
Z (cm)
X (cm)
0.000
0.508
1.016
1.524
2.032
2.540

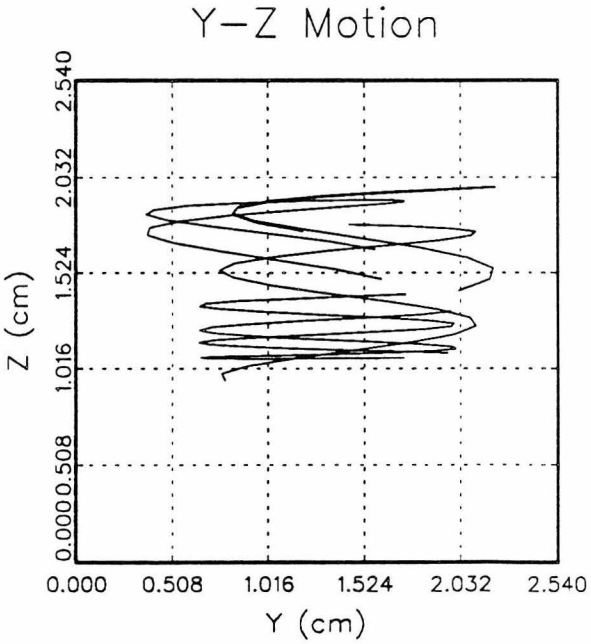
Y–Z Motion
Z (cm)
Y (cm)
0.000
0.508
1.016
1.524
2.032
2.540

5b

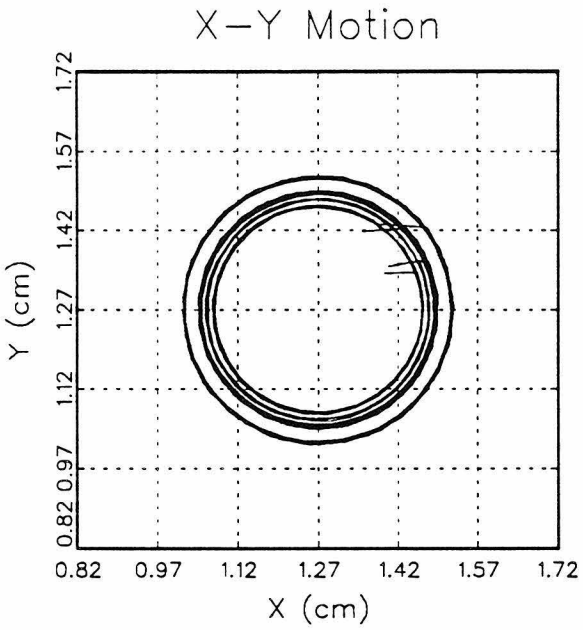
X–Y Motion
Y (cm)
X (cm)
0.82
0.97
1.12
1.27
1.42
1.57
1.72

5c

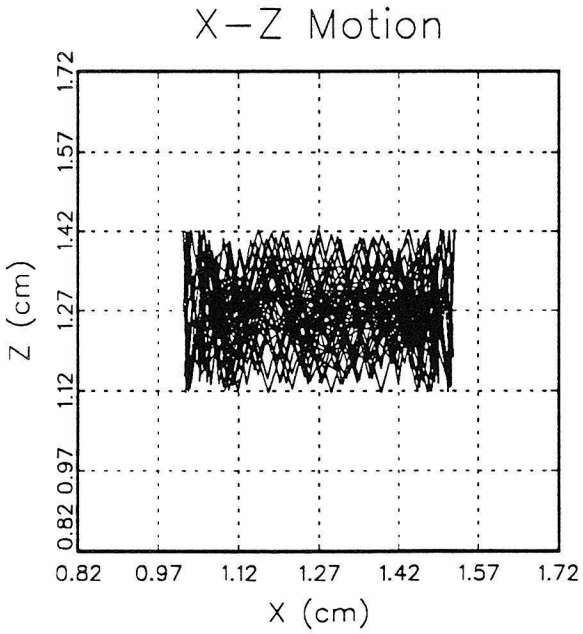
X–Z Motion
Z (cm)
X (cm)
0.82
0.97
1.12
1.27
1.42
1.57
1.72

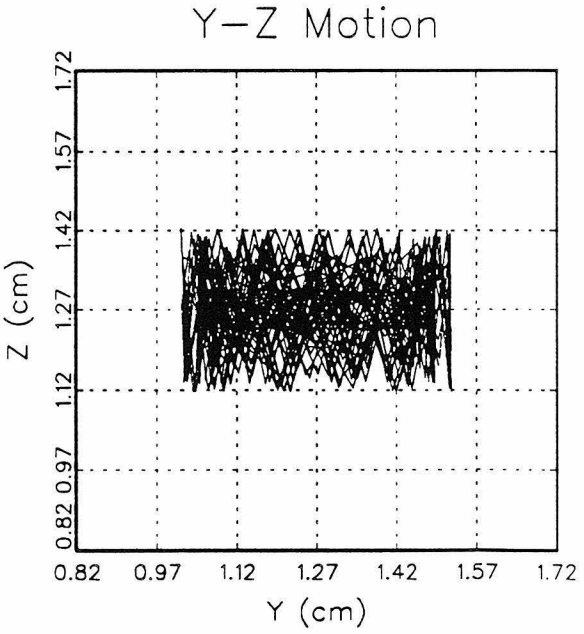
Y–Z Motion
Z (cm)
Y (cm)
0.82
0.97
1.12
1.27
1.42
1.57
1.72

5d

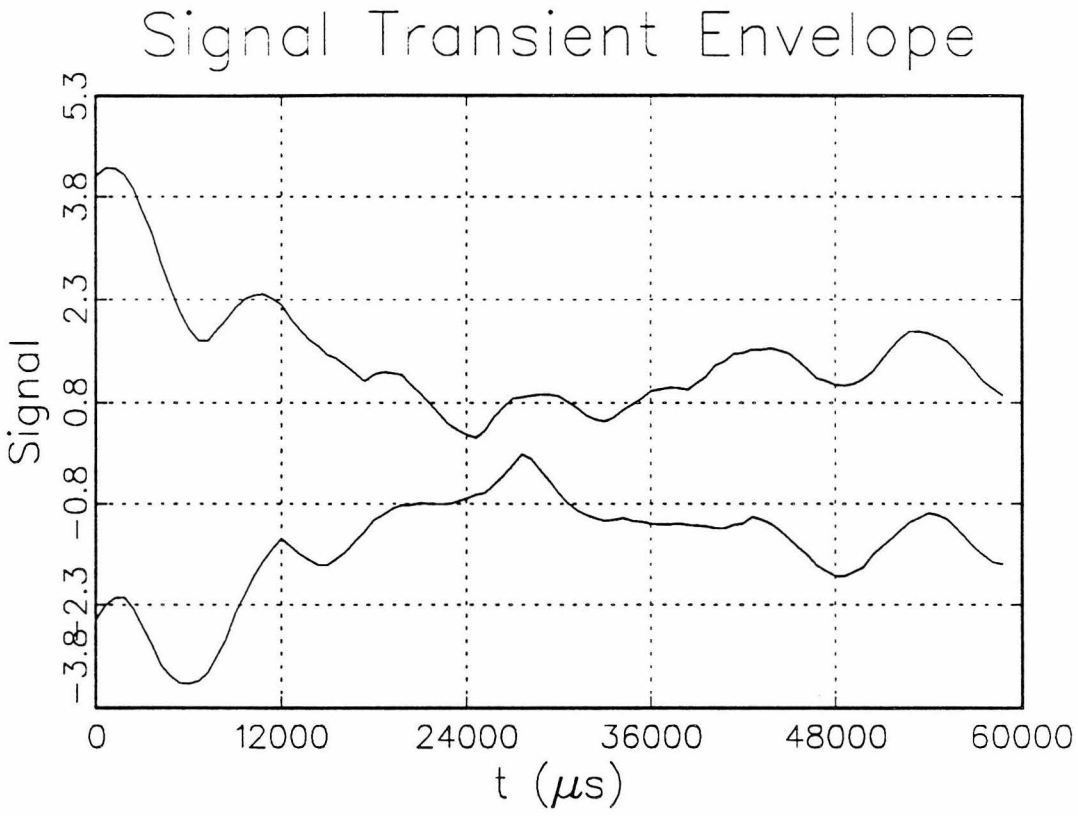
Signal Transient Envelope
Signal
5.3
3.8
2.3
0.8
-0.8
-2.3
-3.8
0
12000
24000
36000
48000
60000
t (μs)

5e

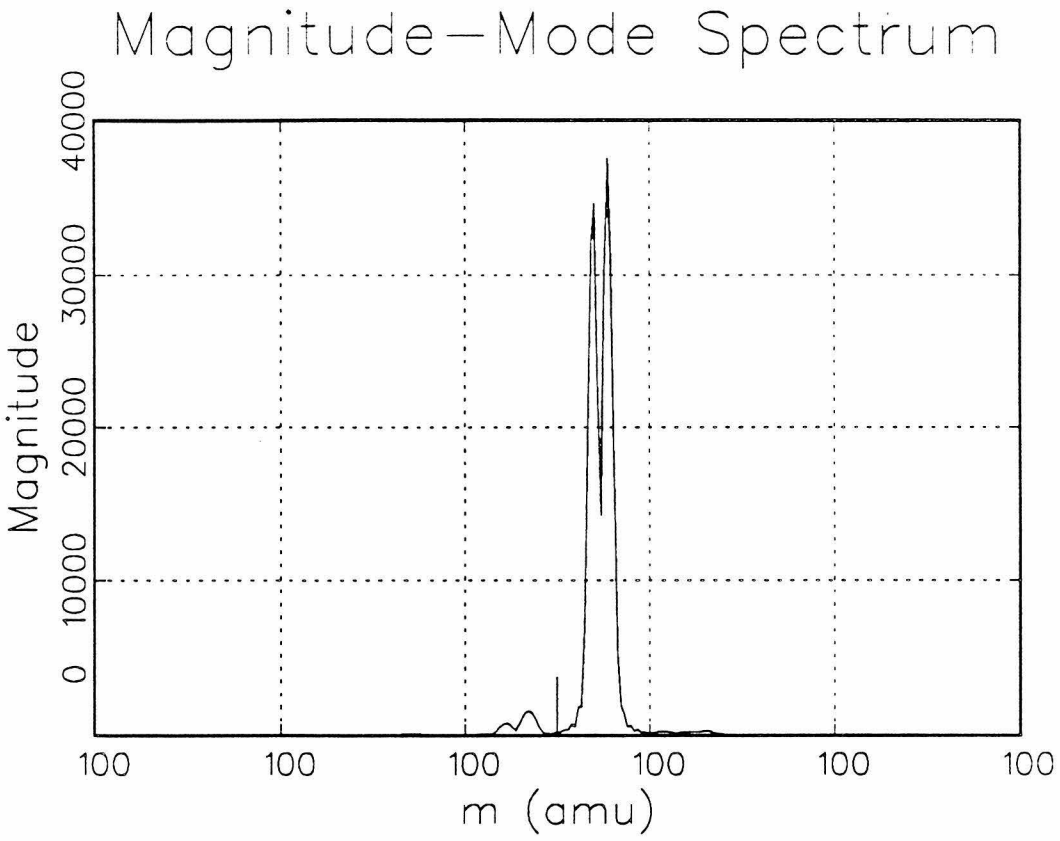
Magnitude–Mode Spectrum
Magnitude
0
10000
20000
30000
40000
100
100
100
100
100
100
m (amu)

6a

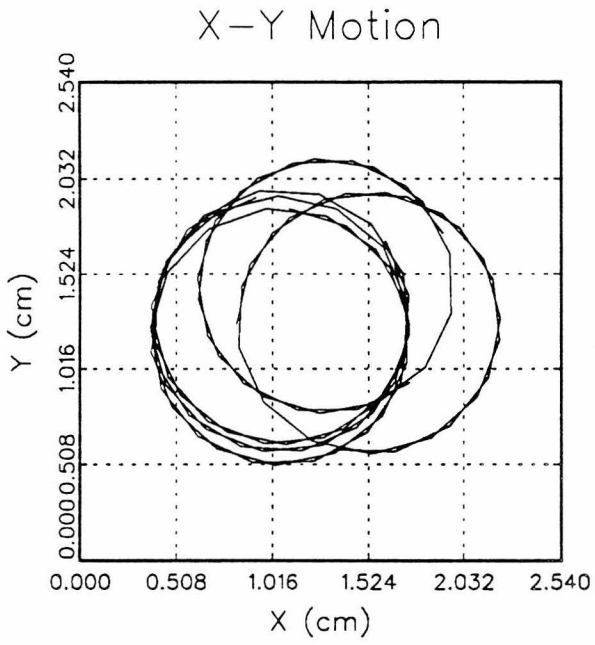
X–Y Motion
Y (cm)
0.000
0.508
1.016
1.524
2.032
2.540
X (cm)

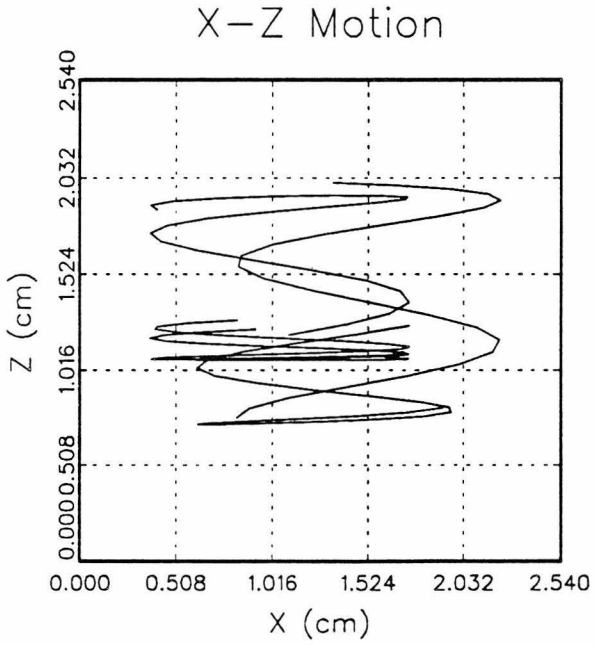
X–Z Motion
Z (cm)
0.000
0.508
1.016
1.524
2.032
2.540
X (cm)

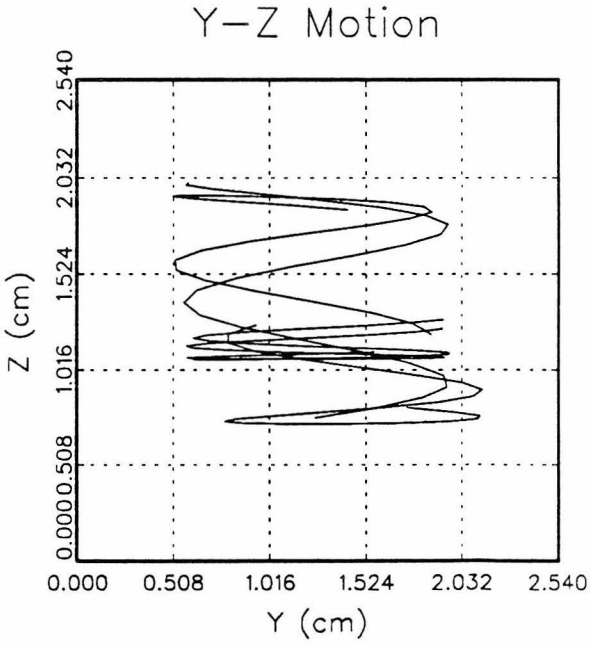
Y–Z Motion
Z (cm)
0.000
0.508
1.016
1.524
2.032
2.540
Y (cm)

6b

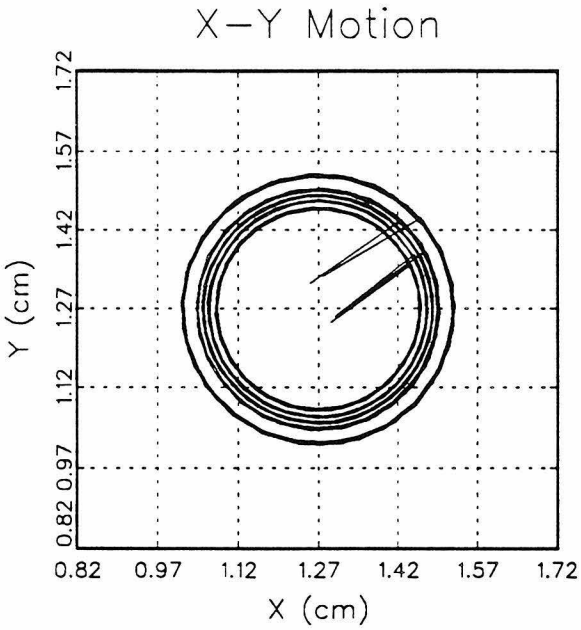
X–Y Motion
Y (cm)
X (cm)
0.82
0.97
1.12
1.27
1.42
1.57
1.72

6c

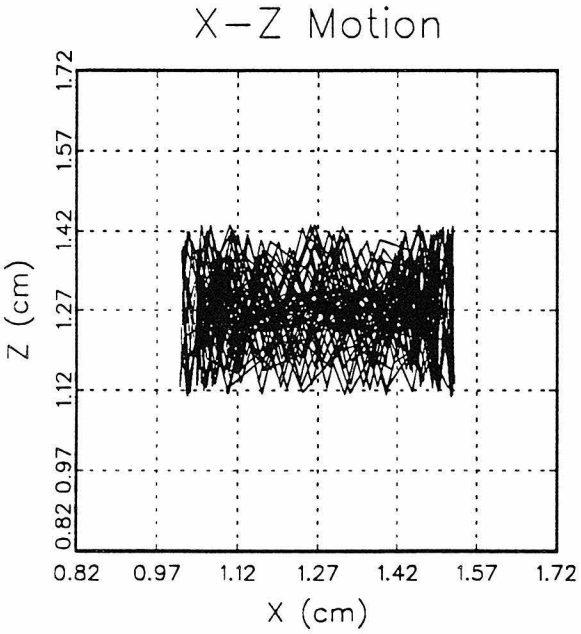
X–Z Motion
Z (cm)
X (cm)
0.82
0.97
1.12
1.27
1.42
1.57
1.72

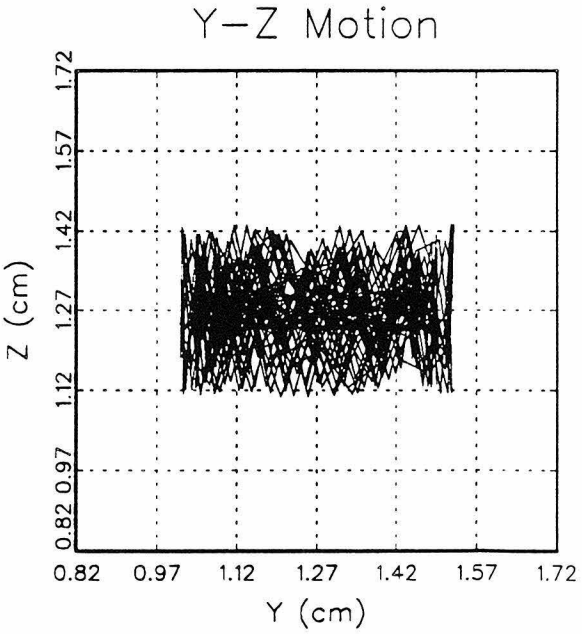
Y–Z Motion
Z (cm)
Y (cm)
0.82
0.97
1.12
1.27
1.42
1.57
1.72

6d

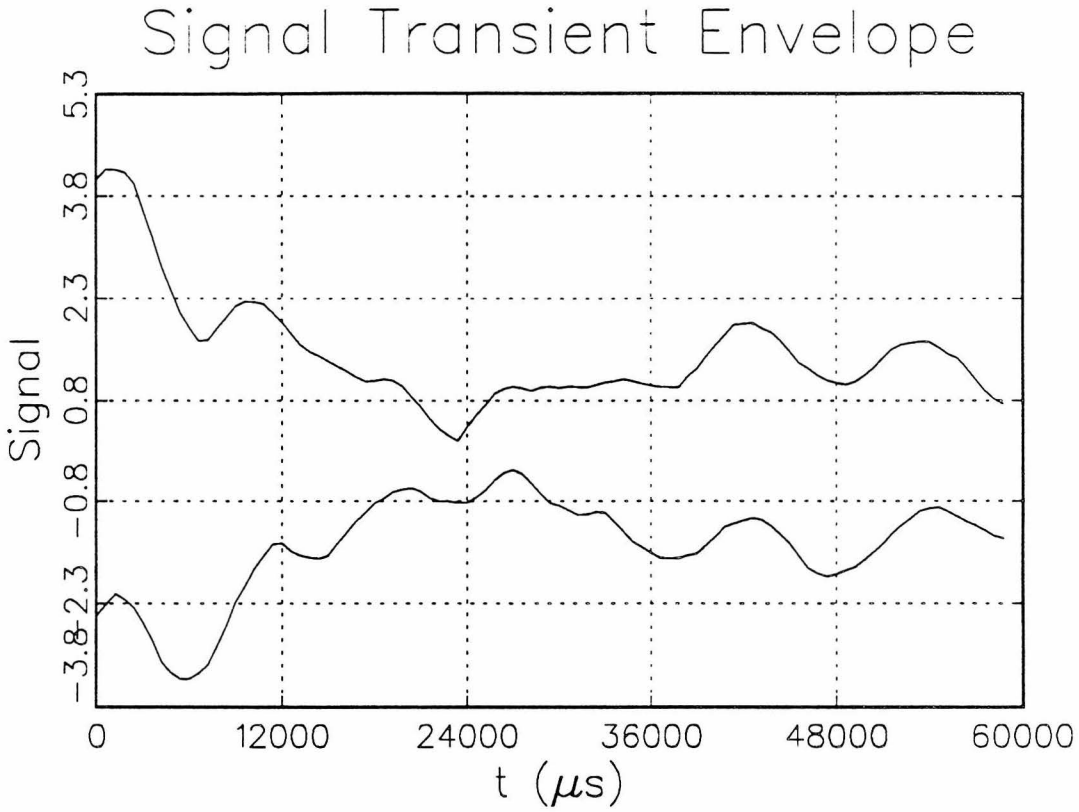
Signal Transient Envelope
Signal
5.3
3.8
2.3
0.8
−0.8
−2.3
−3.8
0
12000
24000
36000
48000
60000
t (μs)

6e

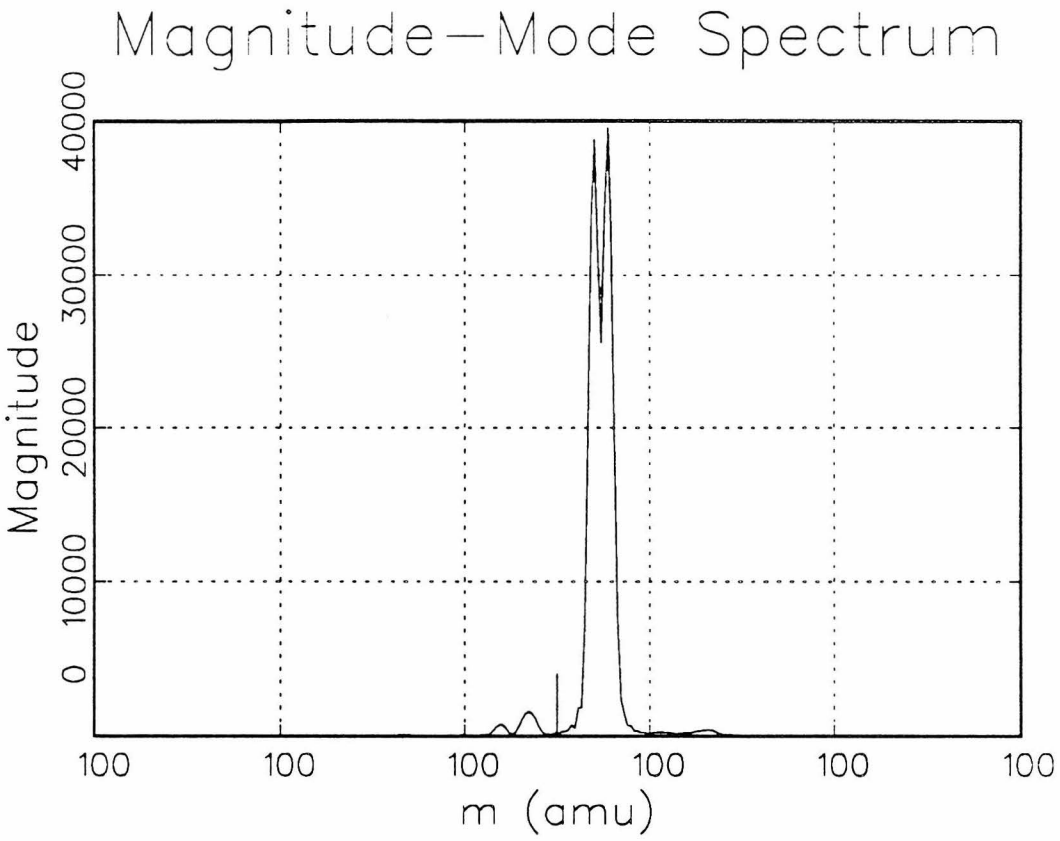
Magnitude–Mode Spectrum
Magnitude
0
10000
20000
30000
40000
100
100
100
100
100
100
m (amu)

7a

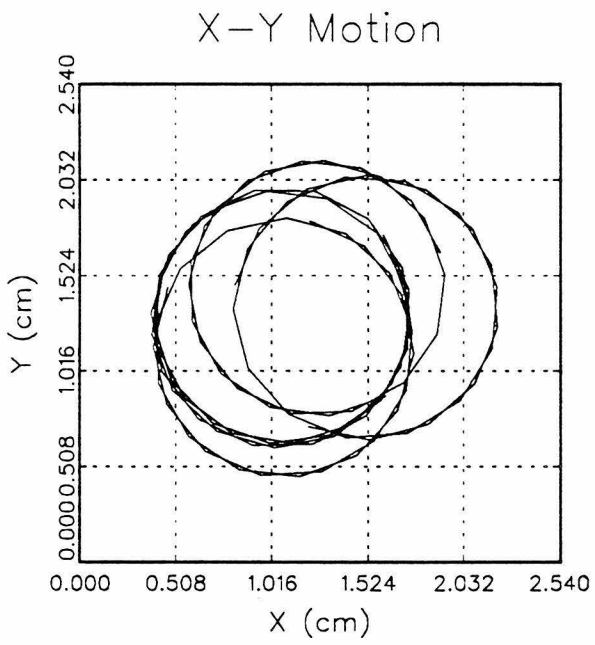
X–Y Motion
Y (cm)
0.000
0.508
1.016
1.524
2.032
2.540
X (cm)

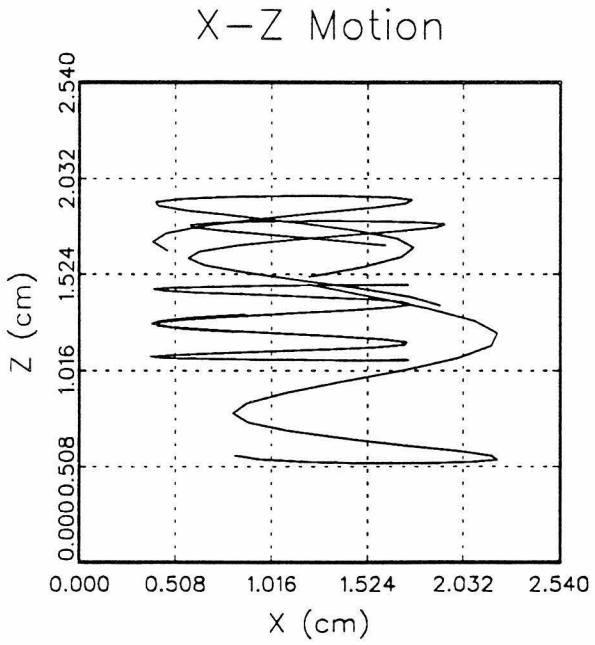
X–Z Motion
Z (cm)
0.000
0.508
1.016
1.524
2.032
2.540
X (cm)

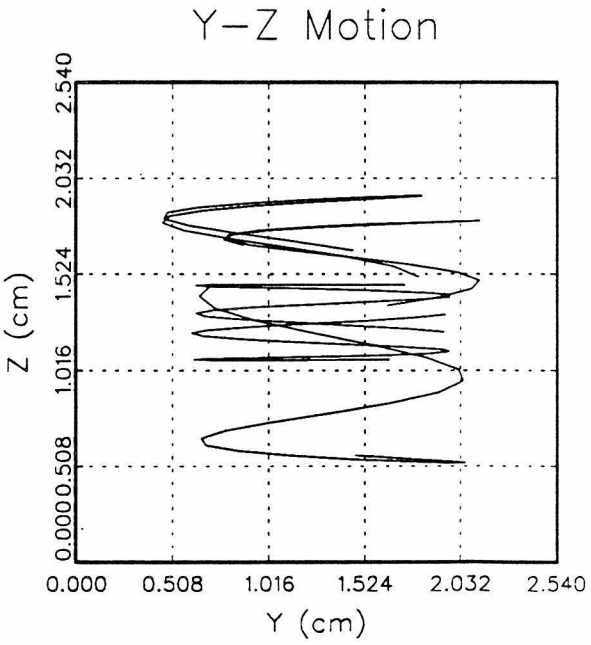
Y–Z Motion
Z (cm)
0.000
0.508
1.016
1.524
2.032
2.540
Y (cm)

7b

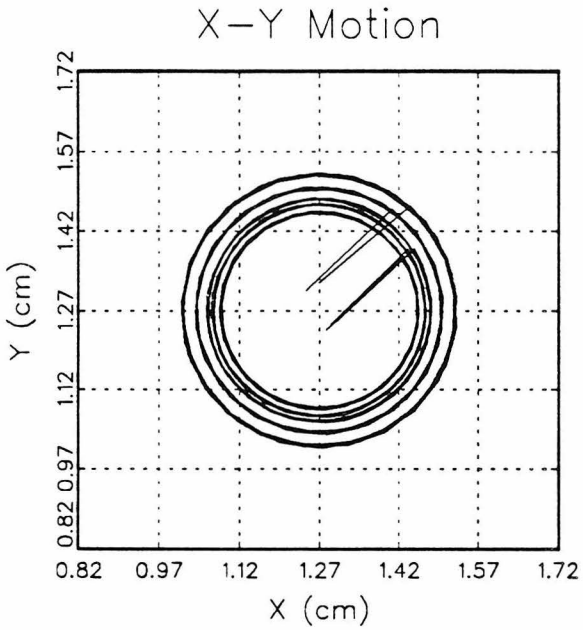
X–Y Motion
Y (cm)
X (cm)
0.82
0.97
1.12
1.27
1.42
1.57
1.72

7c

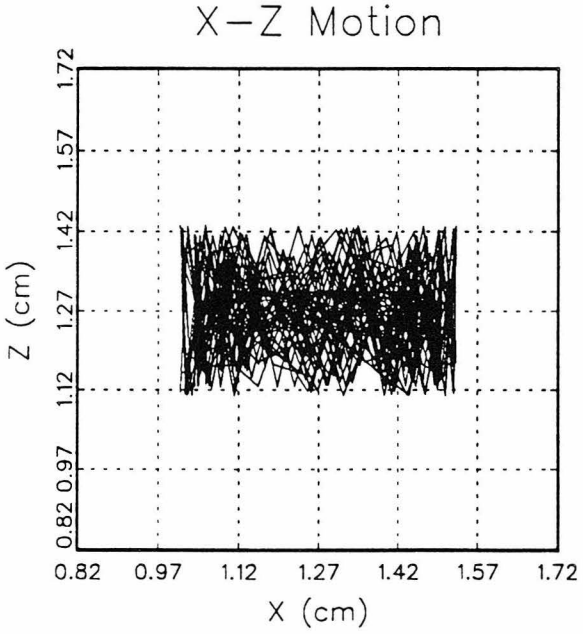
X–Z Motion
Z (cm)
X (cm)
0.82
0.97
1.12
1.27
1.42
1.57
1.72

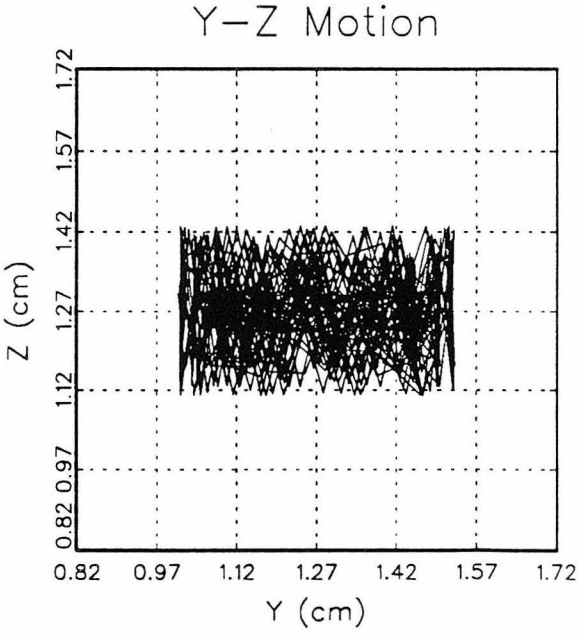
Y–Z Motion
Z (cm)
Y (cm)
0.82
0.97
1.12
1.27
1.42
1.57
1.72

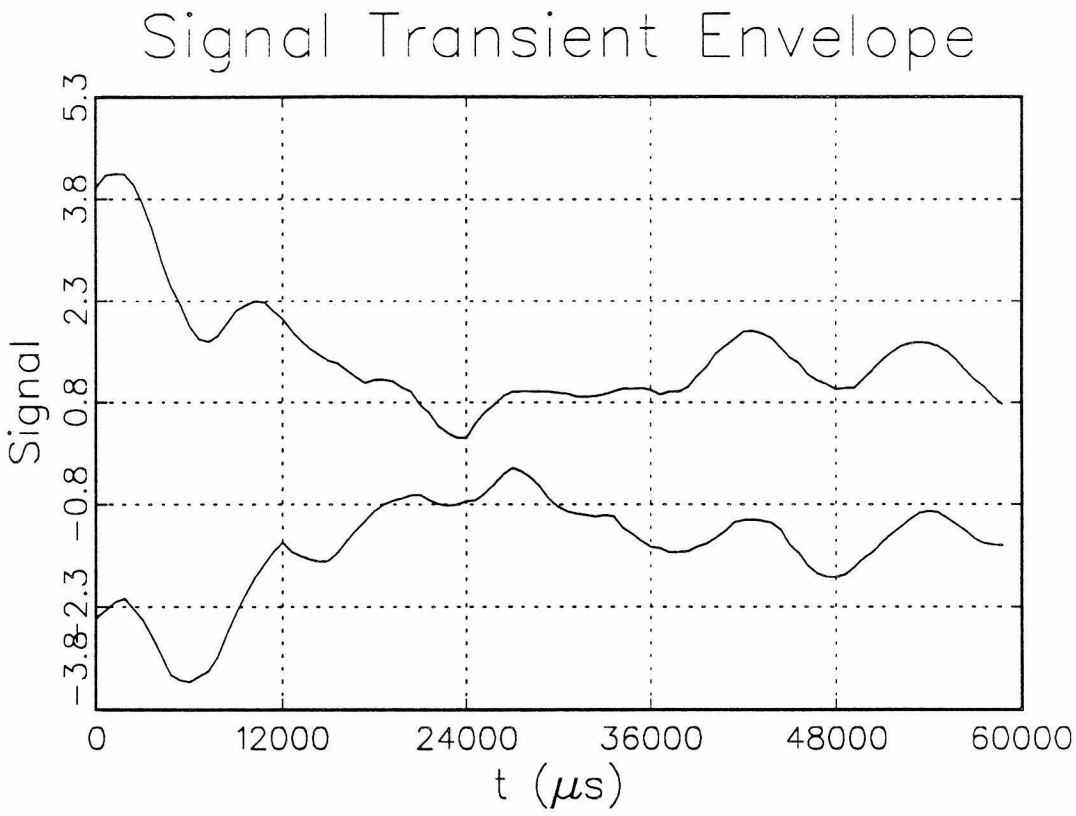
Signal Transient Envelope
Signal
5.3
3.8
2.3
0.8
−0.8
−2.3
−3.8
0
12000
24000
36000
48000
60000
t (μs)

7e

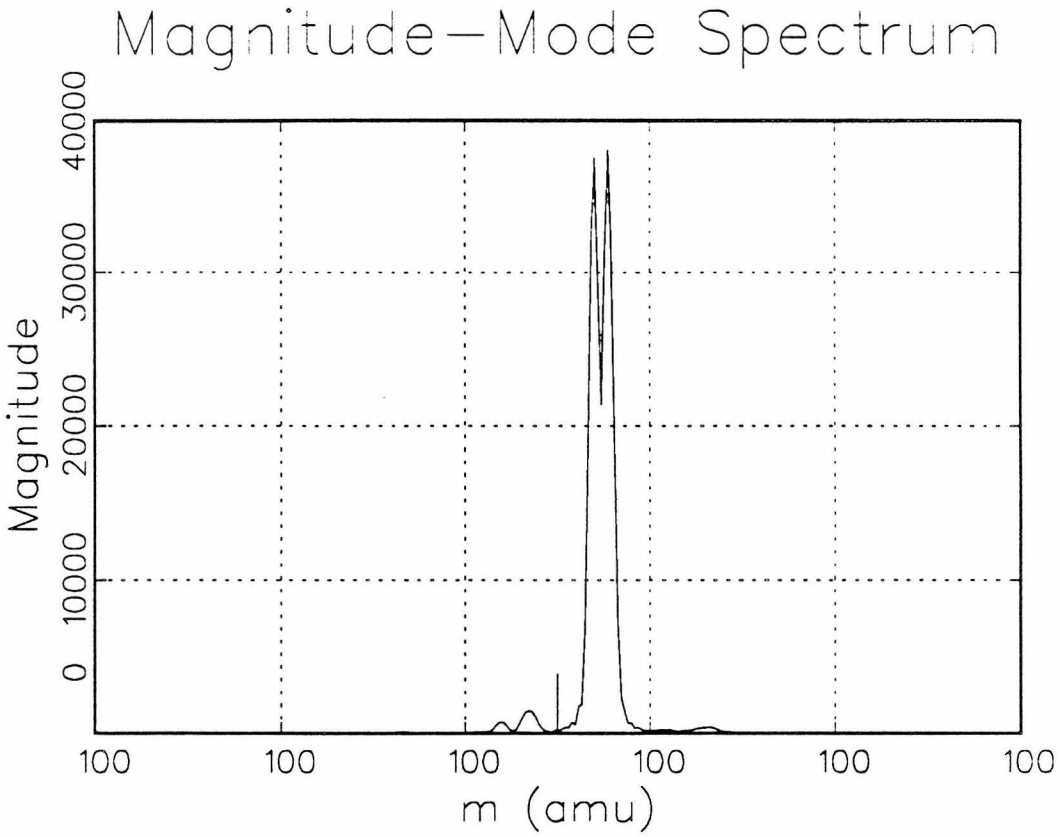
Magnitude–Mode Spectrum
Magnitude
0
10000
20000
30000
40000
100
100
100
100
100
100
m (amu)

8a

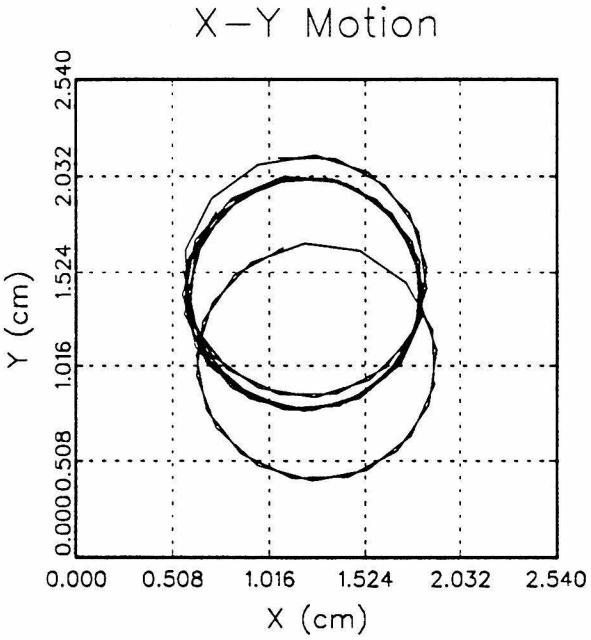
X–Y Motion
Y (cm)
0.000
0.508
1.016
1.524
2.032
2.540
X (cm)

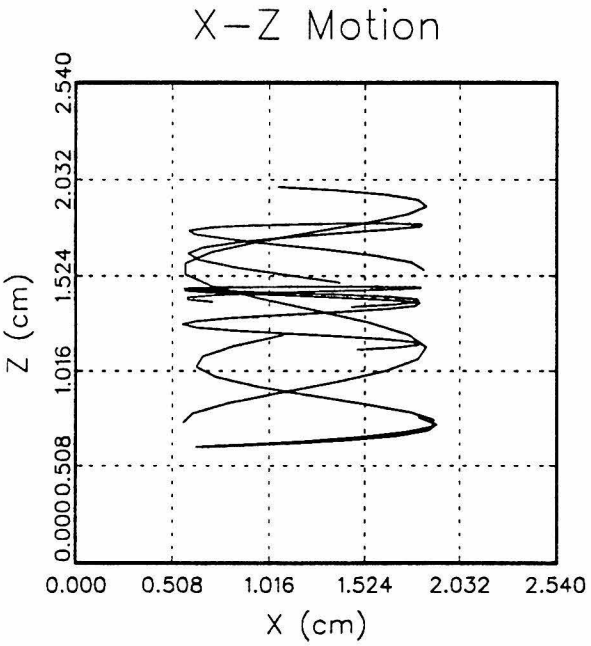
X–Z Motion
Z (cm)
0.000
0.508
1.016
1.524
2.032
2.540
X (cm)

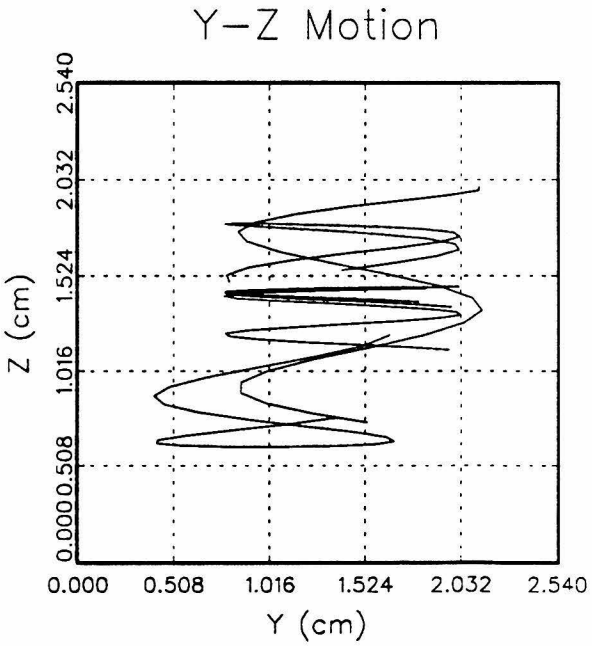
Y–Z Motion
Z (cm)
0.000
0.508
1.016
1.524
2.032
2.540
Y (cm)

8b

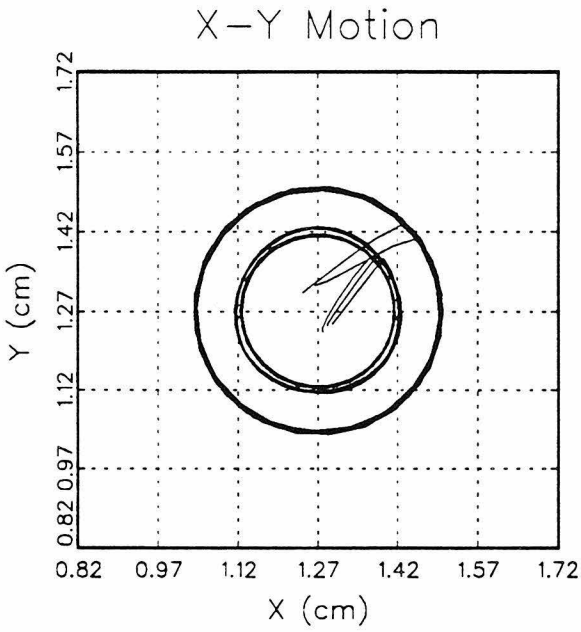
X–Y Motion
Y (cm)
X (cm)
0.82
0.97
1.12
1.27
1.42
1.57
1.72

8c

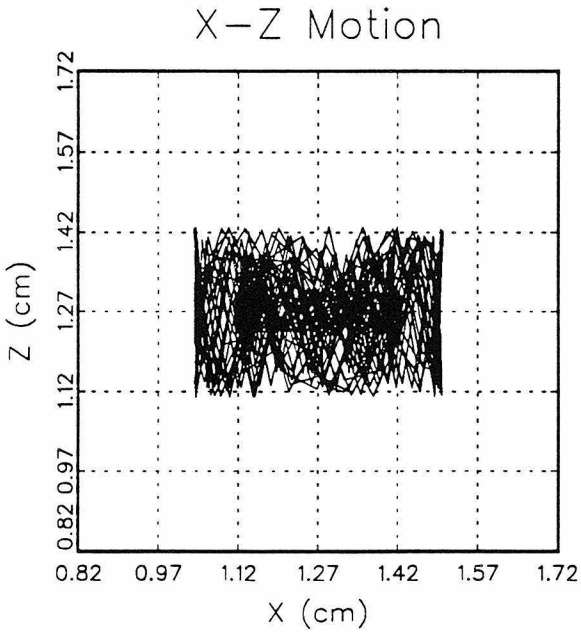
X–Z Motion
Z (cm)
X (cm)
0.82
0.97
1.12
1.27
1.42
1.57
1.72

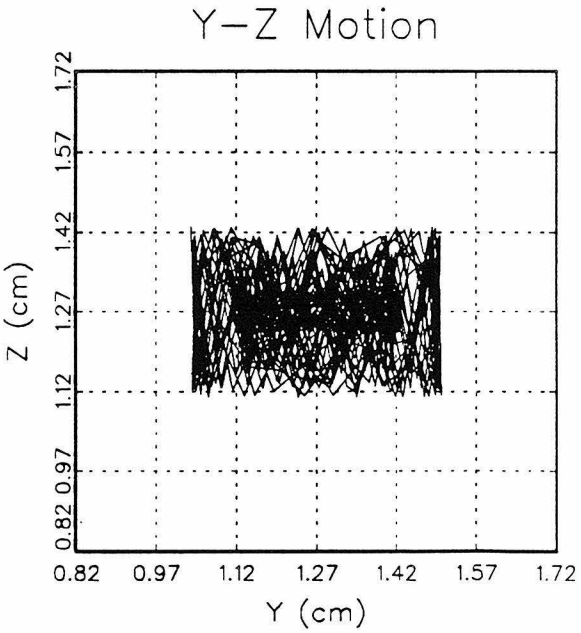
Y–Z Motion
Z (cm)
Y (cm)
0.82
0.97
1.12
1.27
1.42
1.57
1.72

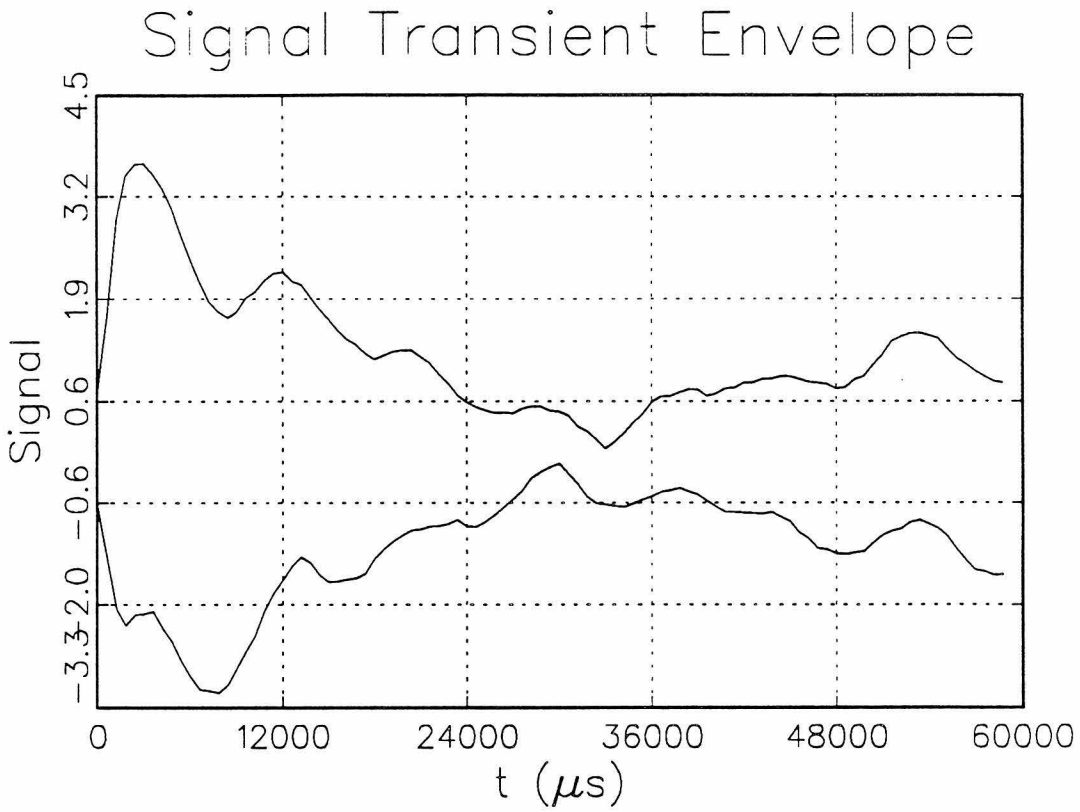
Signal Transient Envelope
Signal
4.5
3.2
1.9
0.6
−0.6
−2.0
−3.3
0
12000
24000
36000
48000
60000
t (μs)

8e

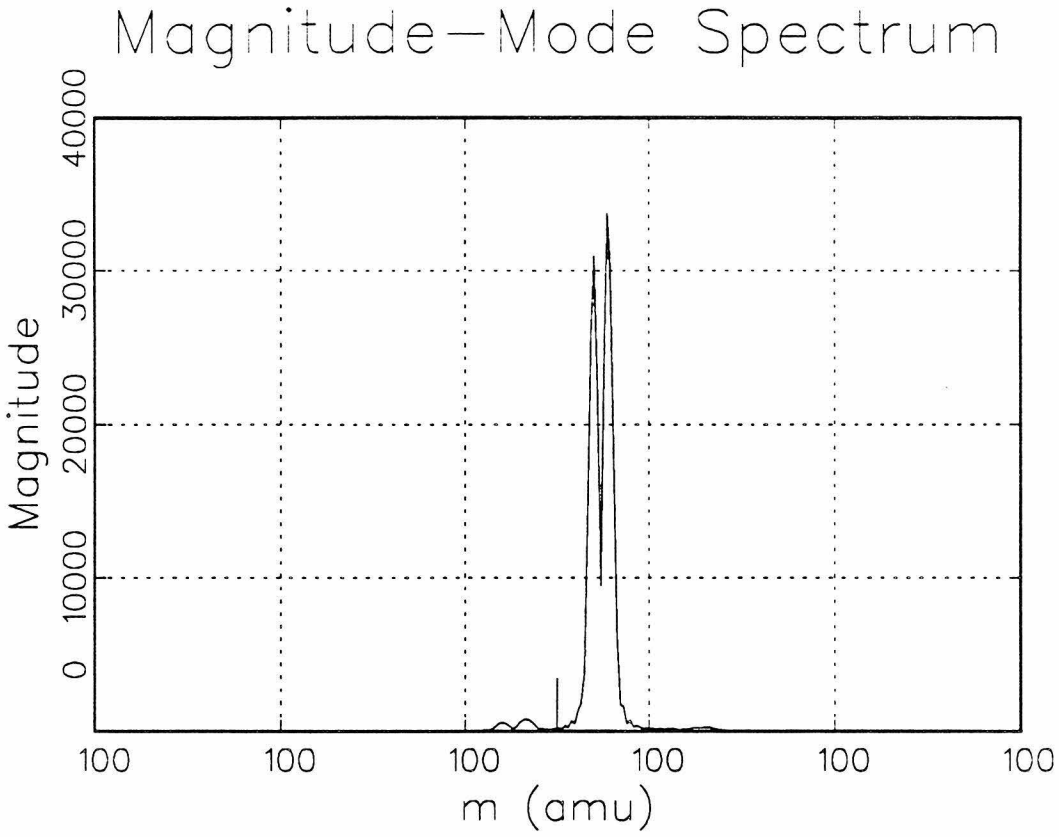
Magnitude–Mode Spectrum
Magnitude
0
10000
20000
30000
40000
100
100
100
100
100
100
m (amu)

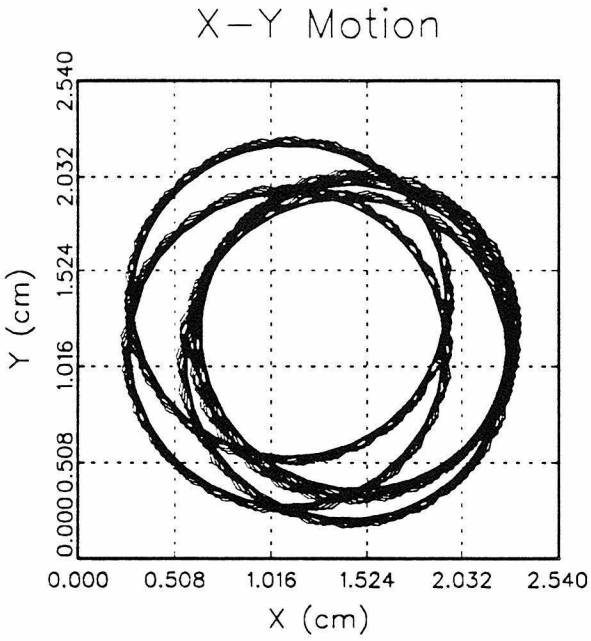
X-Y Motion
Y (cm)
X (cm)
0.000
0.508
1.016
1.524
2.032
2.540

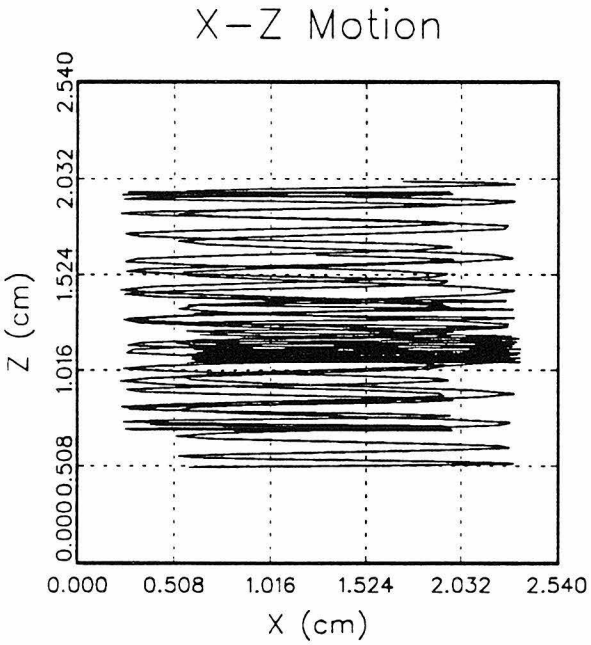
X-Z Motion
Z (cm)
X (cm)
0.000
0.508
1.016
1.524
2.032
2.540

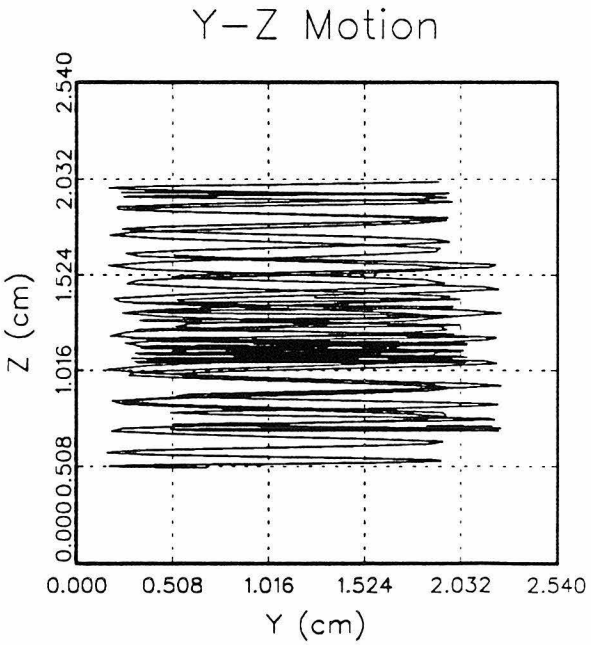
Y-Z Motion
Z (cm)
Y (cm)
0.000
0.508
1.016
1.524
2.032
2.540

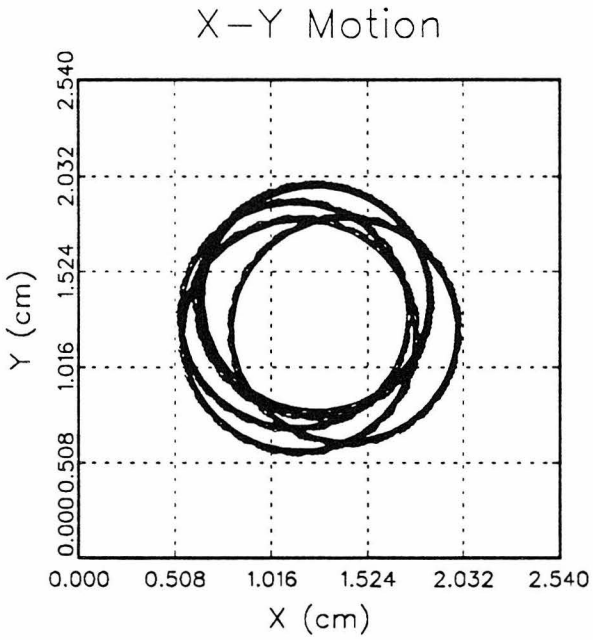
X−Y Motion
Y (cm)
0.000
0.508
1.016
1.524
2.032
2.540
X (cm)

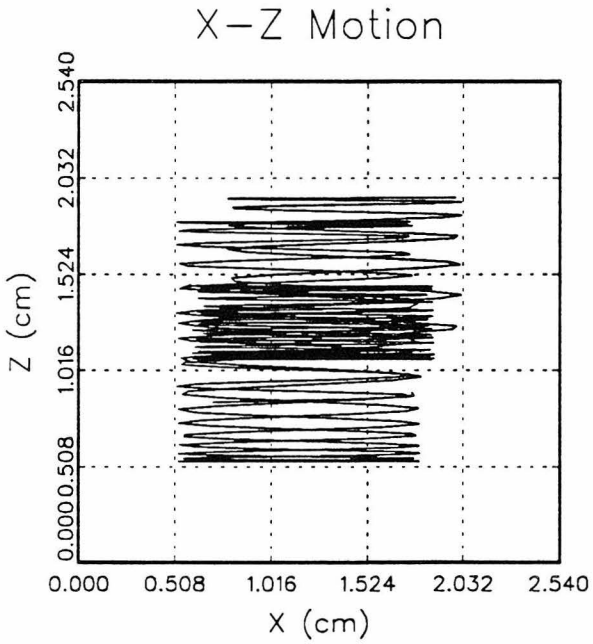
X−Z Motion
Z (cm)
0.000
0.508
1.016
1.524
2.032
2.540
X (cm)

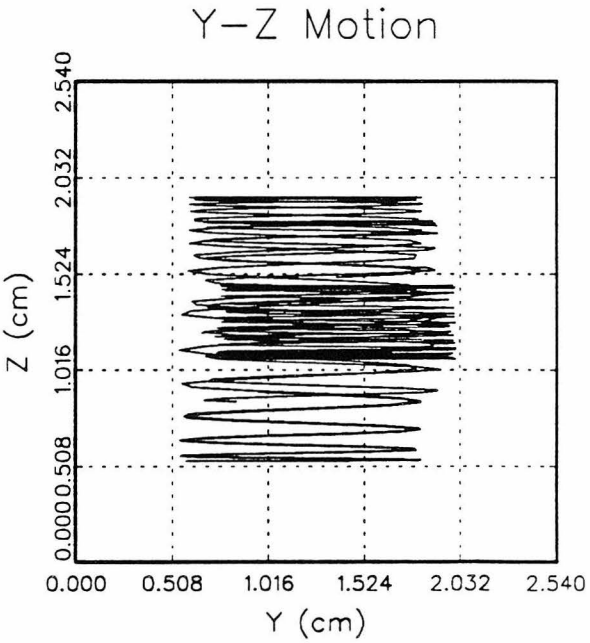
Y−Z Motion
Z (cm)
0.000
0.508
1.016
1.524
2.032
2.540
Y (cm)

9b

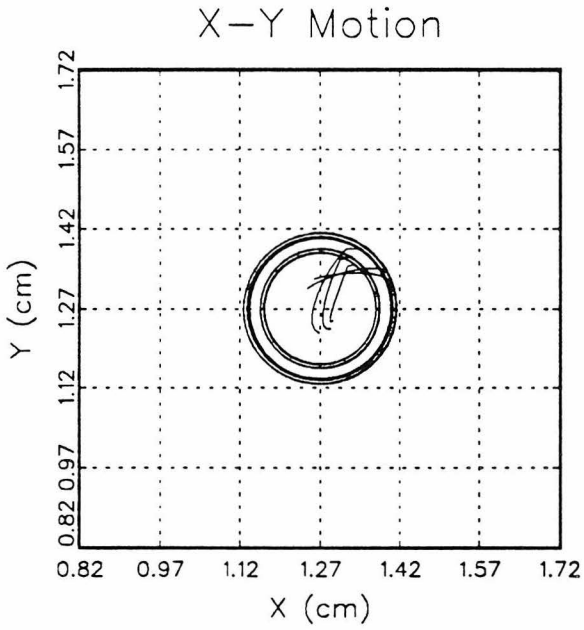
X–Y Motion
Y (cm)
X (cm)
0.82
0.97
1.12
1.27
1.42
1.57
1.72

9c

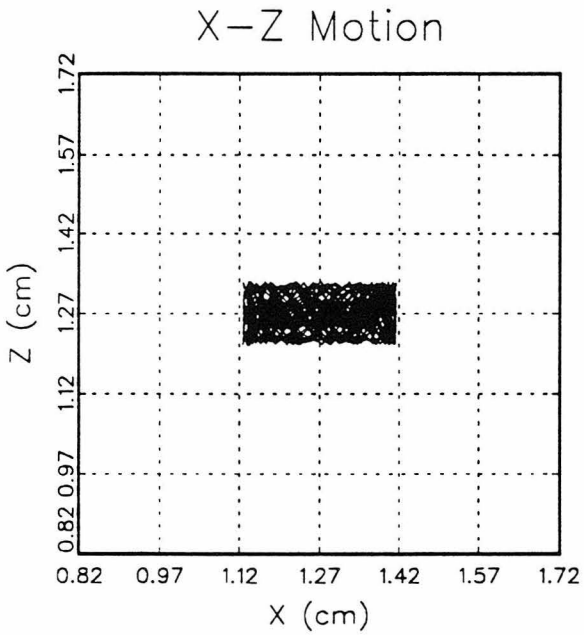
X–Z Motion
Z (cm)
X (cm)
0.82
0.97
1.12
1.27
1.42
1.57
1.72

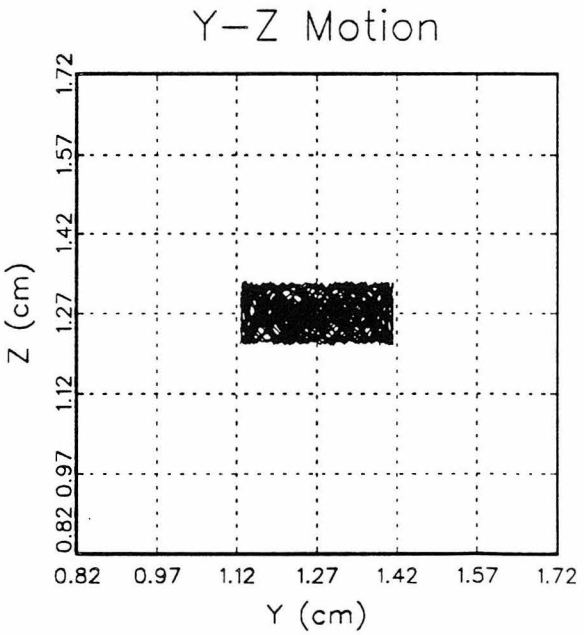
Y–Z Motion
Z (cm)
Y (cm)
0.82
0.97
1.12
1.27
1.42
1.57
1.72

9d

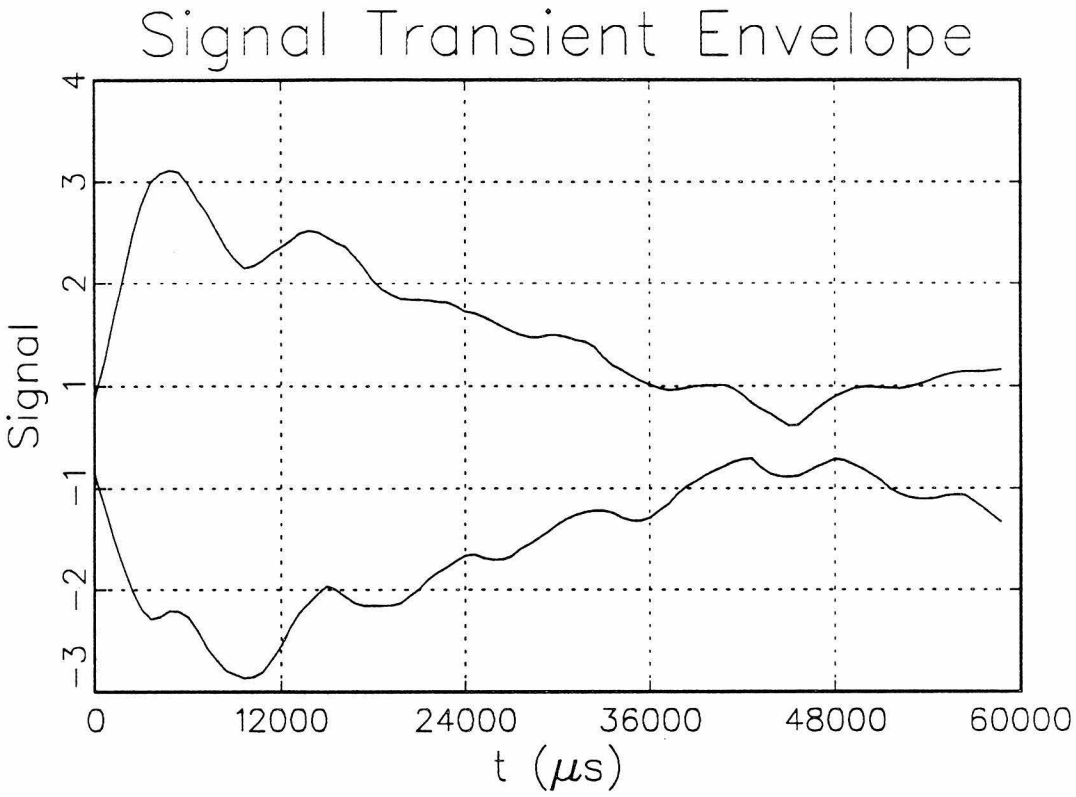
Signal Transient Envelope
Signal
4
3
2
1
−1
−2
−3
0
12000
24000
36000
48000
60000
t (μs)

9e

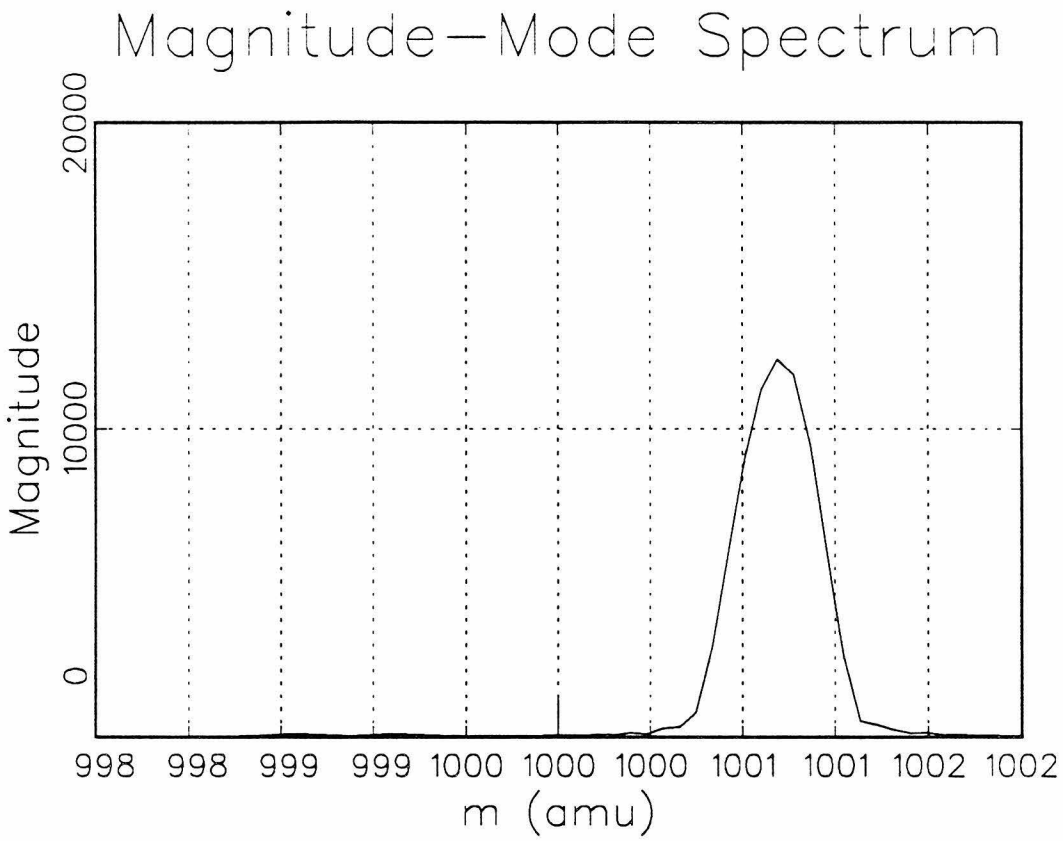
Magnitude—Mode Spectrum
Magnitude
0
10000
20000
998 998 999 999 1000 1000 1000 1001 1001 1002 1002
m (amu)

10a

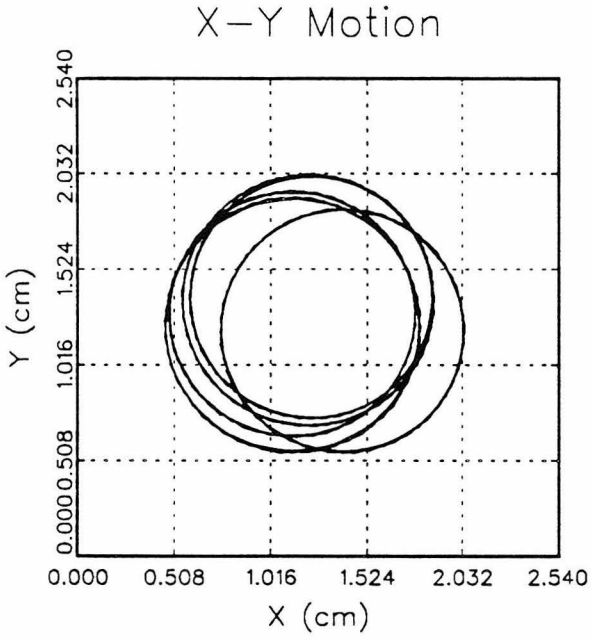
X–Y Motion
Y (cm)
0.000
0.508
1.016
1.524
2.032
2.540
X (cm)

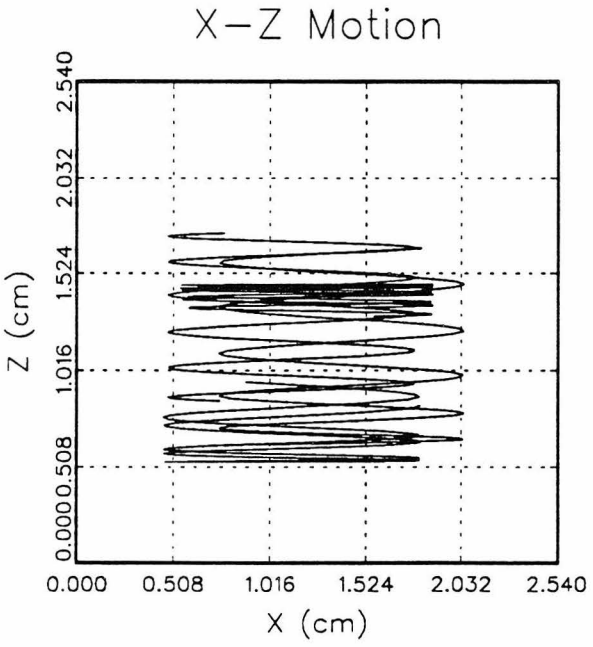
X–Z Motion
Z (cm)
0.000
0.508
1.016
1.524
2.032
2.540
X (cm)

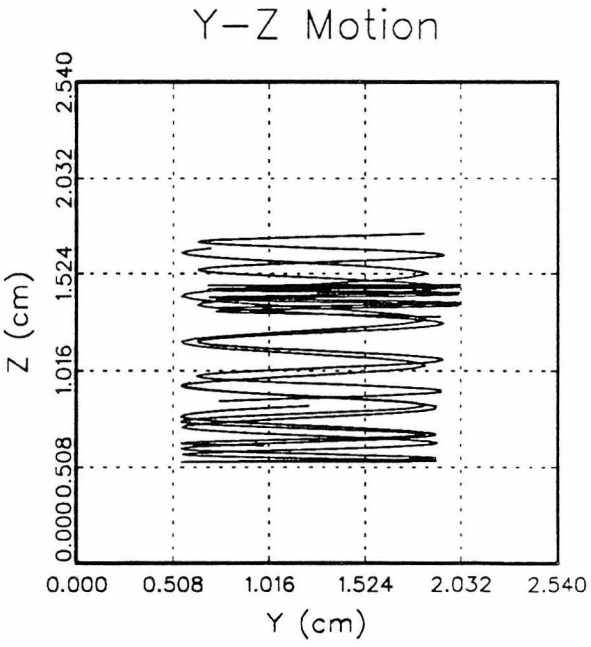
Y–Z Motion
Z (cm)
0.000
0.508
1.016
1.524
2.032
2.540
Y (cm)

10b

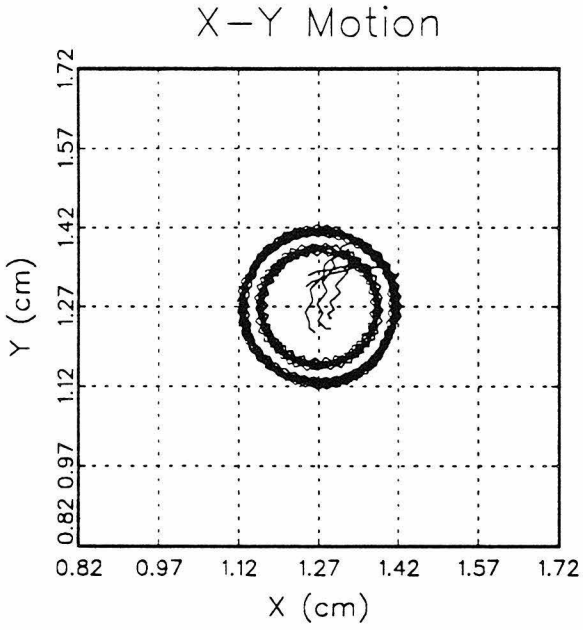
X–Y Motion
Y (cm)
X (cm)
0.82
0.97
1.12
1.27
1.42
1.57
1.72

10c

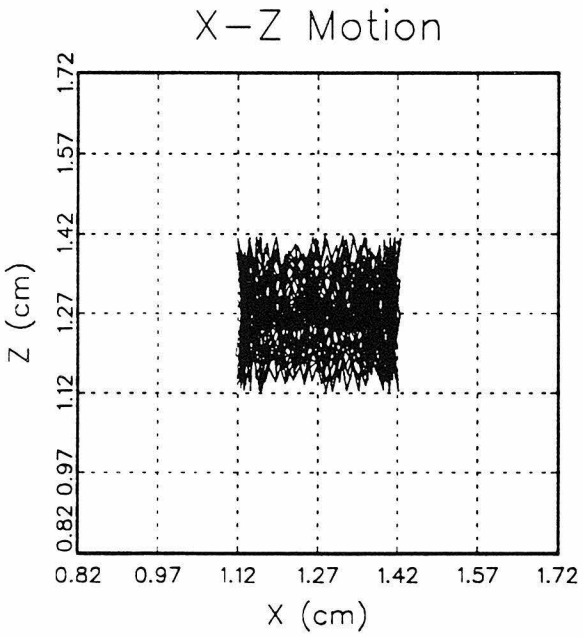
X–Z Motion
Z (cm)
X (cm)
0.82
0.97
1.12
1.27
1.42
1.57
1.72

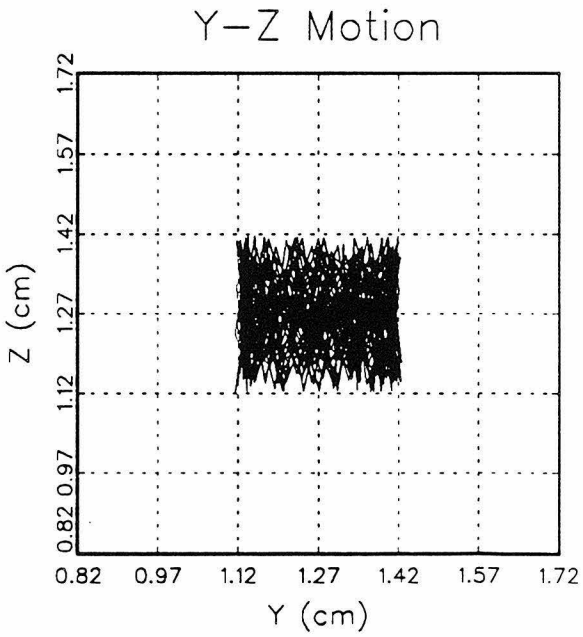
Y–Z Motion
Z (cm)
Y (cm)
0.82
0.97
1.12
1.27
1.42
1.57
1.72

10d

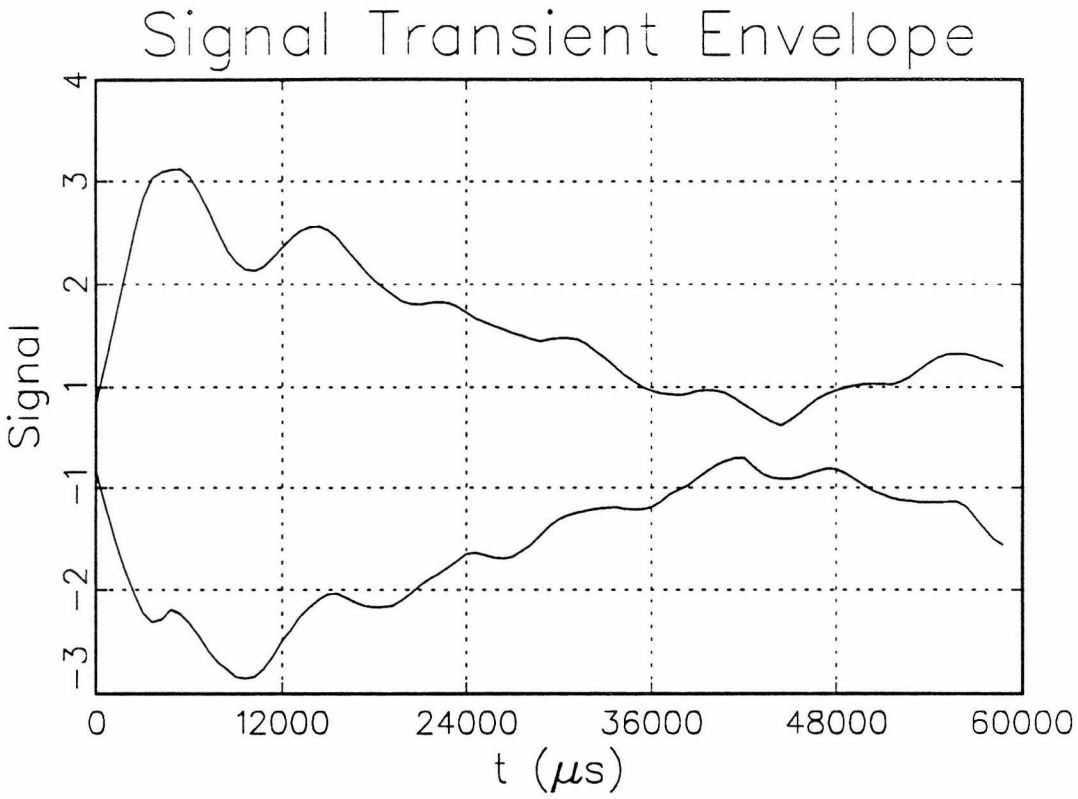
Signal Transient Envelope
Signal
4
3
2
1
−1
−2
−3
0
12000
24000
36000
48000
60000
t (μs)

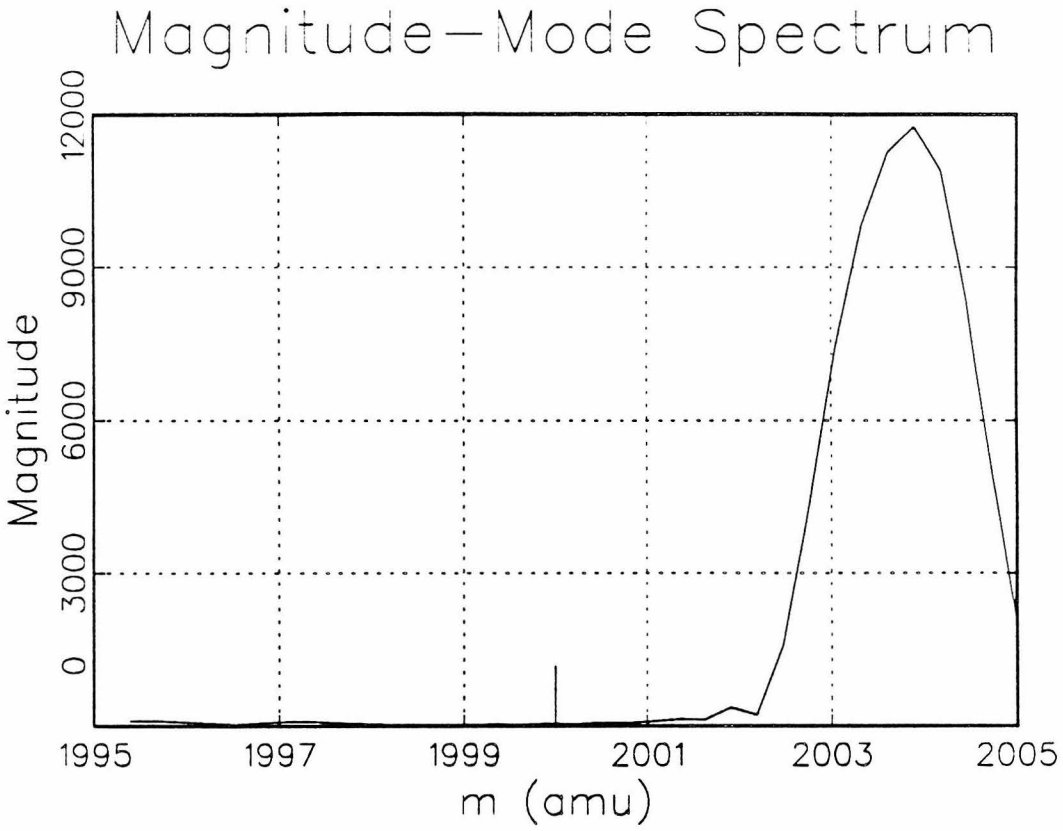
Magnitude–Mode Spectrum
Magnitude
0
3000
6000
9000
12000
1995
1997
1999
2001
2003
2005
m (amu)

10_e

11a

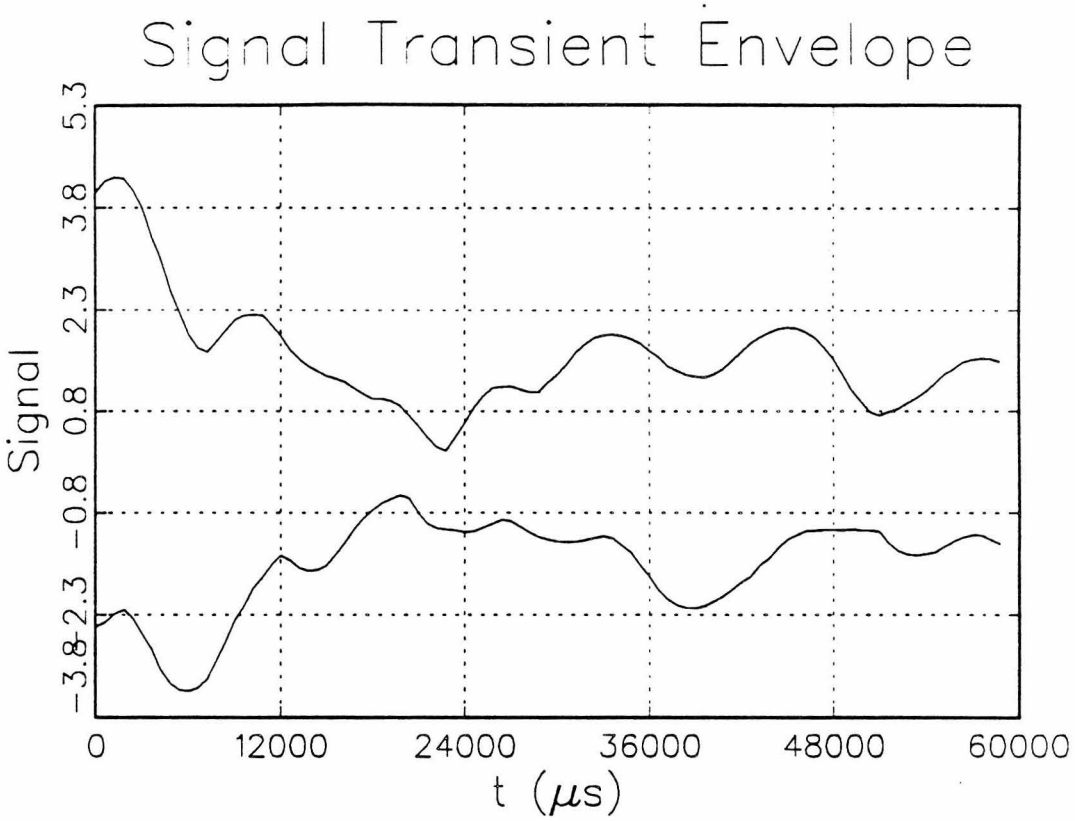
Signal Transient Envelope
Signal
5.3
3.8
2.3
0.8
−0.8
−2.3
−3.8
0
12000
24000
36000
48000
60000
t (μs)

11b

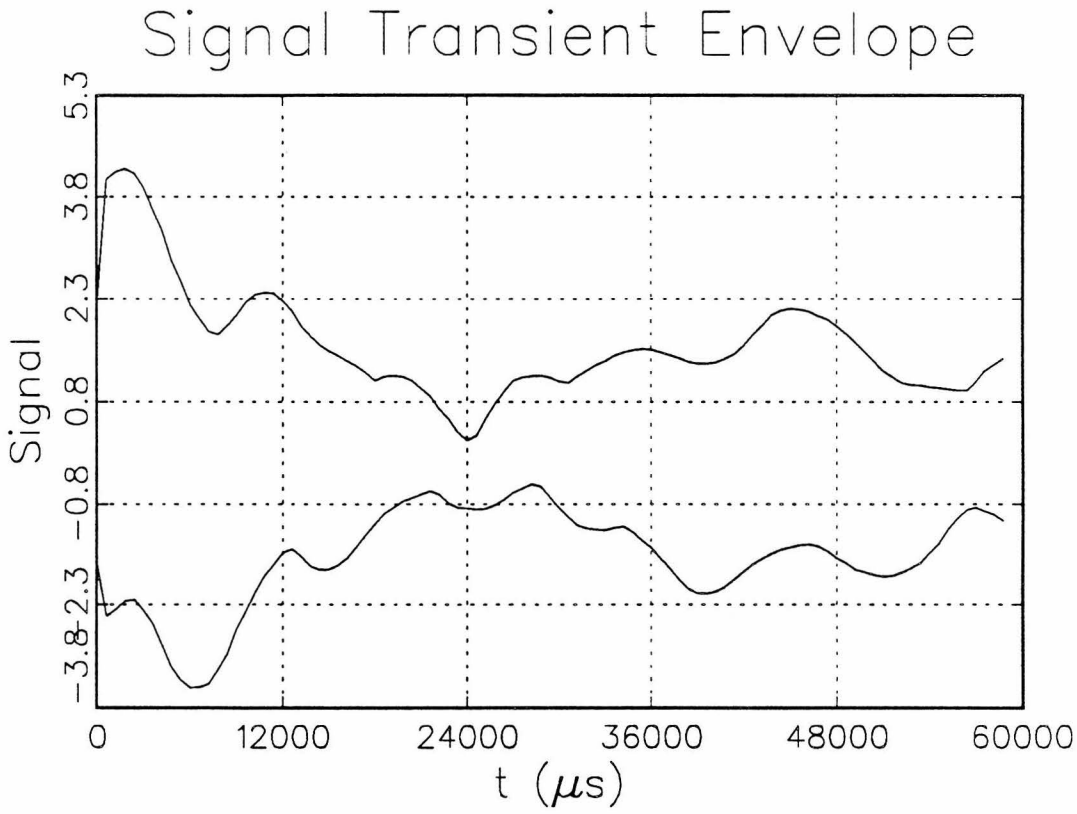
Signal Transient Envelope
Signal
5.3
3.8
2.3
0.8
-0.8
-2.3
-3.8
0
12000
24000
36000
48000
60000
t (μs)

11c

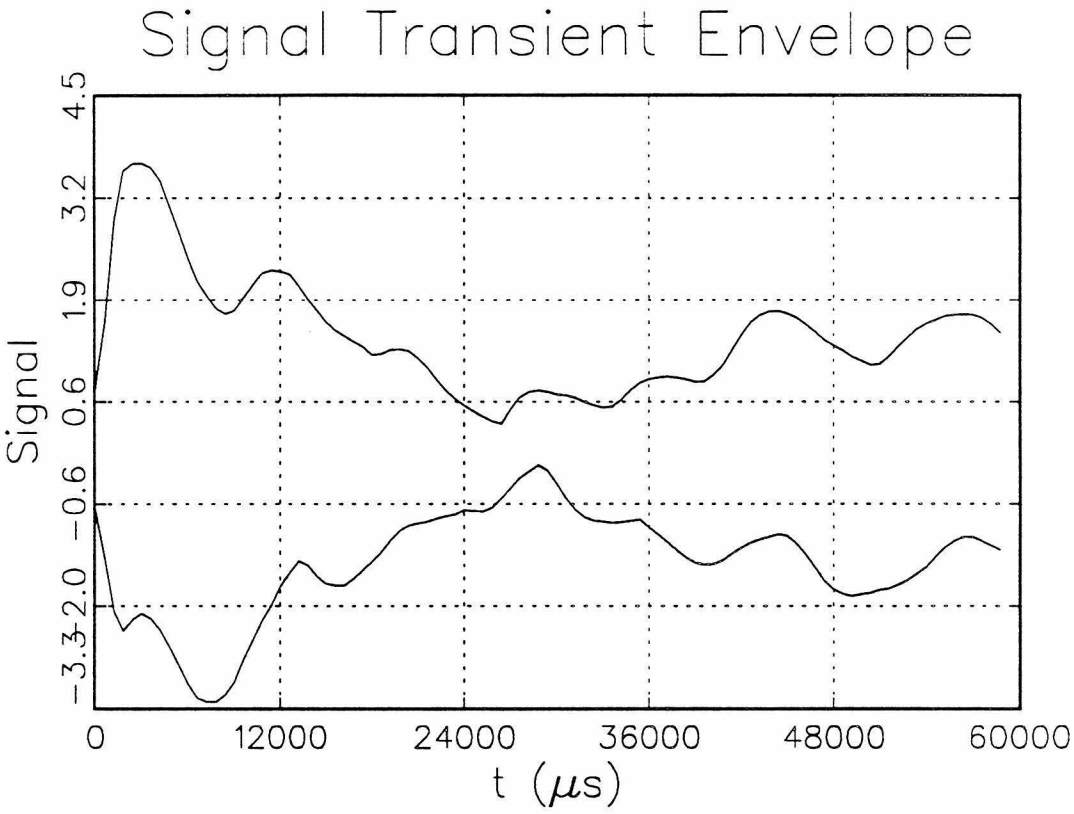
Signal Transient Envelope
Signal
4.5
3.2
1.9
0.6
−0.6
−2.0
−3.3
0
12000
24000
36000
48000
60000
t (μs)

11d

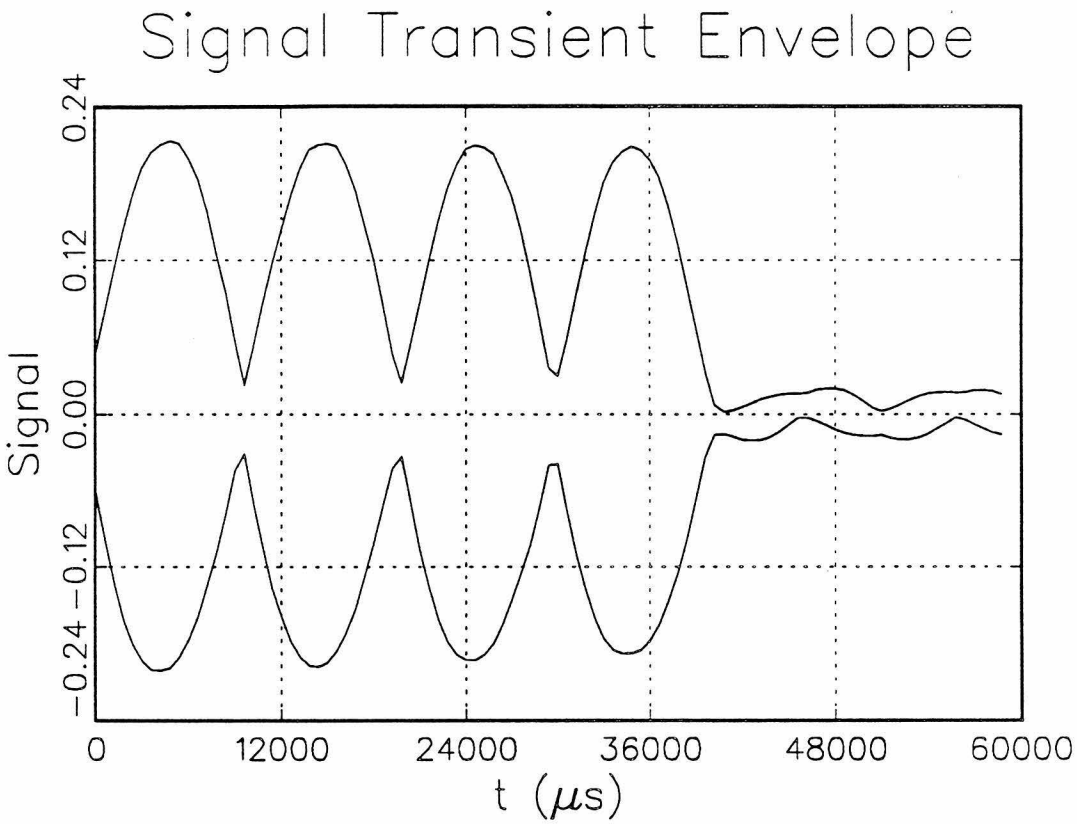
Signal Transient Envelope
Signal
0.24
0.12
0.00
−0.12
−0.24
0
12000
24000
36000
48000
60000
t (μs)

12a

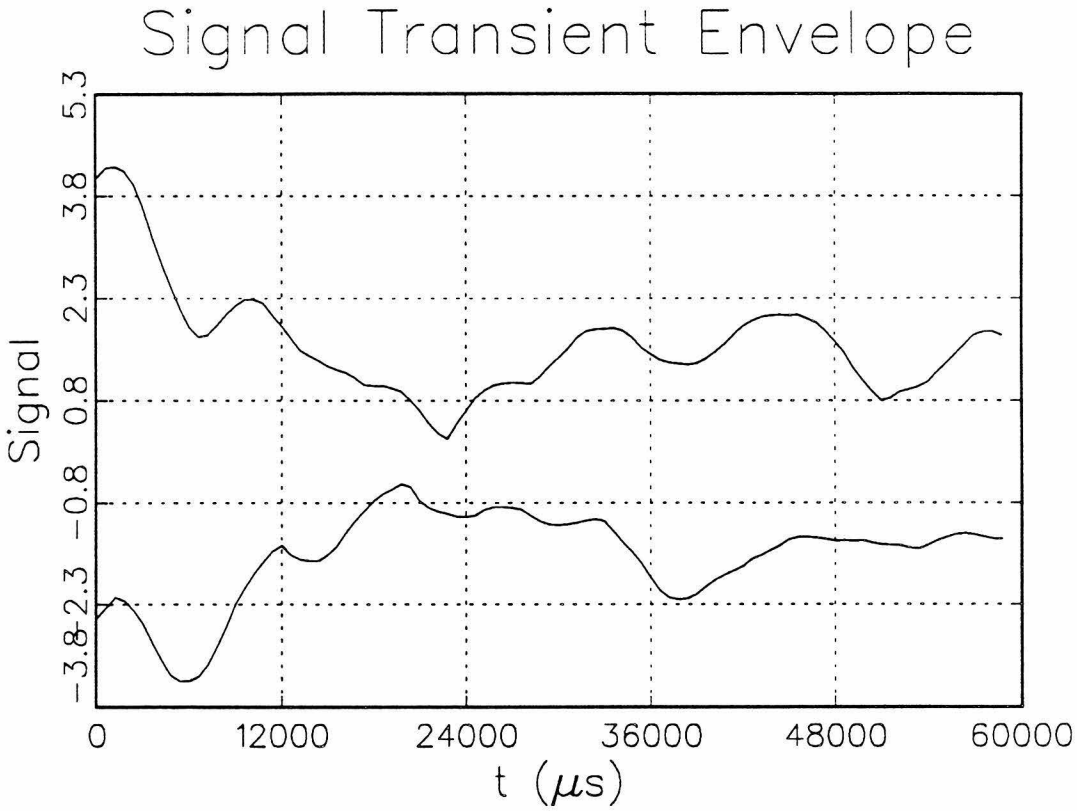
Signal Transient Envelope
Signal
5.3
3.8
2.3
0.8
−0.8
−2.3
−3.8
0
12000
24000
36000
48000
60000
t (μs)

12b

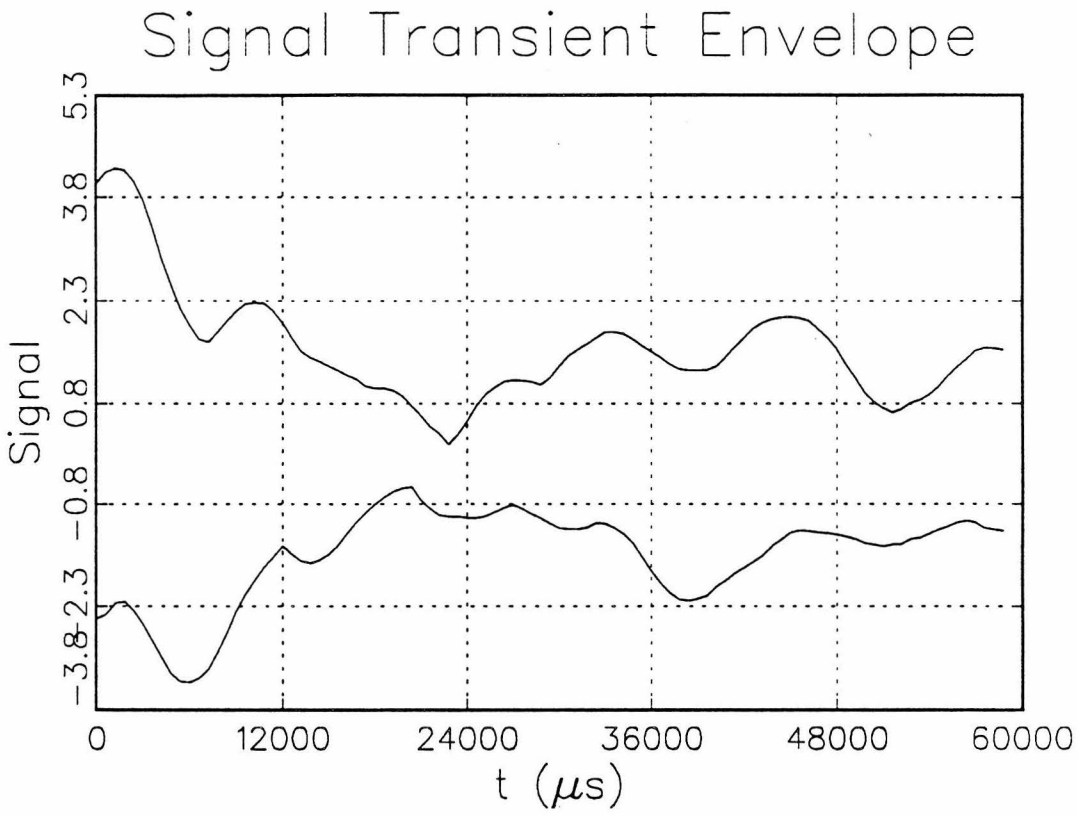
Signal Transient Envelope
Signal
5.3
3.8
2.3
0.8
-0.8
-2.3
-3.8
0
12000
24000
36000
48000
60000
t (μs)

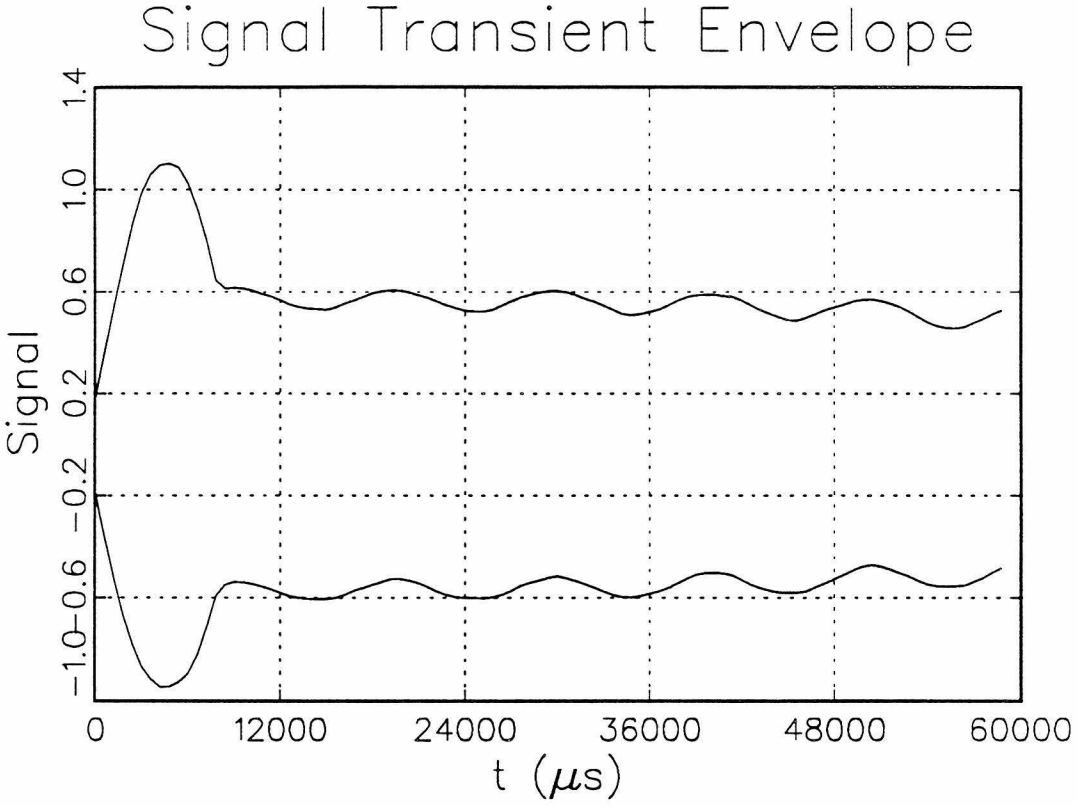
Signal Transient Envelope
Signal
1.4
1.0
0.6
0.2
−0.2
−0.6
−1.0
0
12000
24000
36000
48000
60000
t (μs)

12d

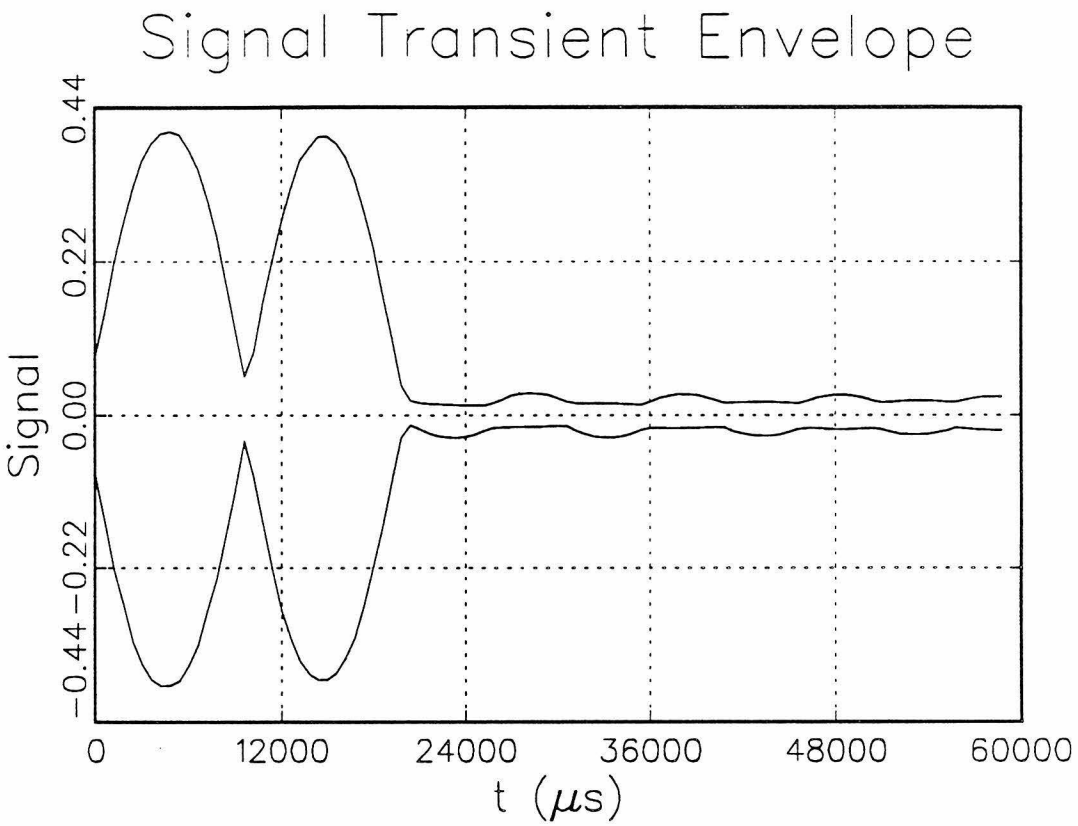
Signal Transient Envelope
Signal
0.44
0.22
0.00
−0.22
−0.44
0
12000
24000
36000
48000
60000
t (μs)

CHAPTER V

A Monte Carlo Study of Thermal Cross Sections and Collision Rates of Multiply-Charged, Linear, Gas-phase Proteins

M. W. Deem and J. L. Beauchamp

California Institute of Technology, Pasadena, CA 91125

ABSTRACT

We present here computational results for the collision cross section and rate constant for proton transfer reactions of a multiply-charged, linear, gas-phase protein. The protein is intended to resemble cytochrome c, with a length of 400 Å, a mass of 12 400 amu. The model protein is studied with proton charges of between 9 and 15 $|e^-|$. The computational reactant is intended to model dimethyl amine, with a mass of 45 amu, a polarizability of 5.0 $Å^3$ (dimethyl amine has a polarizability estimated by the Le Fevre method of 5.86 A^3[1]), and a dipole moment of 1.03 Debye[2]. Results for low linear charge densities on the protein are interpretable in terms of a geometric model that accounts for the overlap of adjacent spheres of capture of each charge on the protein.

INTRODUCTION

The feasibility of forming multiply charged, high-mass ions in the gas phase via electrospray ionization has recently been shown.[3,4,5] This technique should be applicable to a wide range of molecules that are currently of much experimental interest, such as clusters, polymers, and biomolecules. Several studies of multiply-charged, gas-phase biomolecules have, in fact, recently been done. One study of ubiquitin (relative molecular mass 8586 amu) suggests correlations between solution phase structure, charging level, and three-dimensional structure.[6] That is, ubiquitin samples prepared in denaturing solutions are left in a more highly charged state by electrospray ionization than are those prepared in solutions that do not denature the protein. A potentially more quantitative study recently reported reaction rates of horse heart cytochrome c (relative molecular mass of 12 360 amu) with charge levels of 9 to 15 $|e^-|$ with dimethyl amine in a quadrupole ion trap.[7] Application of Fourier transform ion cyclotron resonance (FT-ICR) spectroscopy, rather than quadrupole ion trap spectroscopy, to such high mass species should be possible and could conceivably result in the most accurate reaction rates reported to date for such proton transfer reactions.[8,9]

In anticipation of experimental work that is to be done on these systems, we present here a theoretical analysis of the thermal collision cross sections and rate constants for the proton transfer reaction of a multiply-charged, linear, gas-phase protein. The protein is intended to model a linear (completely denatured) cytochrome c, while the base is modeled after dimethyl amine. Essentially this work is a computational

extension of the Langevine analysis[10] to multiply charged systems. Monte carlo methods are used to evaluate the cross sections and rate constants.

ANALYTIC THEORY OF RATE CONSTANTS: THE SHADOW EFFECT

Classical collision rate theory predicts the cross section for collision between an ion of charge e and a molecule of polarizability α approaching with a collision energy E_c to be (in cgs units)[10]

$$\sigma(E_c) = \pi\left(\frac{2\alpha e^2}{E_c}\right)^{1/2} \tag{1}$$

while the collision rate constant in predicted to be[10]

$$k = \left(\frac{4\pi^2\alpha e^2}{\mu}\right)^{1/2} \tag{2}$$

Averaging the cross section (1) over the Maxwell-Boltzman distribution results in

$$\sigma(T) = \left(\frac{8\pi\alpha e^2}{k_B T}\right)^{1/2} \tag{3}$$

No similar theory exists for an array of point charges. In particular we are interested in the geometry of Figure 1. Taking a geometric (rather than dynamic) view of Figure 1, one can imagine the total cross section to be the average over all orientations of the

biomolecule of the projected area of the spheres of capture on the plane of incidence. Note that at small incident angles relative to the biomolecules axis, more near spheres of capture prevent an incident molecule from reaching more distant spheres. This shadow effect is, then, what causes the cross section of a biomolecule with n charges to be less than n times that of the Langevine cross section (1).

In order to compute the reduction in cross section caused by the shadow effect, we first compute the area of overlap of two circles of radius r separated by a distance x_0. (See Figure 2.) The area is, for $x_0 < 2$ r,

$$A(x_0, R) = 4 \int_0^{\theta_0} \left(R\cos(\theta) - \frac{x_0}{2} \right) R\cos(\theta)\, d\theta \tag{4}$$

where θ_0 is the angle at which the two circles intersect,

$$\tan(\theta_0) = \sqrt{4 \frac{R^2}{x_0^2} - 1} \tag{5}$$

Performing the integral in Eq. (4) leads to the expression

$$A(x_0, R) = \begin{cases} 2R^2 \tan^{-1} \sqrt{4 \frac{R^2}{x_0^2} - 1} - x_0 \sqrt{R^2 - \frac{x_0^2}{4}}, & x_0 < 2r \\ 0, & x_0 \geq 2r \end{cases} \tag{6}$$

For the linear biomolecule of Figure 1,

$$x_0 = \frac{L}{n - 1} \sin(\theta)$$

(7)

where L is the length of the biomolecule with n equally spaced charges, and θ_0 is the angle of incidence. Note that in Figure 2, R is defined by $\sigma_{Langevine}(v) = \pi R(v)^2$, and is, thus, velocity dependent. Averaging the incident-angle-dependent overlap area, Eq. (7), over all incident angles as well as over a Maxwell-Boltzman velocity distribution results in

$$\langle A(T) \rangle = \frac{4}{\sqrt{\pi}} \left(\frac{m}{2k_B t} \right)^{3/2} \int_0^{\infty} \int_0^{\frac{\pi}{2}} A(\theta, v) \sin(\theta) \, d\theta \; v^2 \, e^{\frac{-mv^2}{2k_B T}} \, dv$$

(8)

The double integral appearing in Eq. (8) can be performed numerically when quantitative results are needed.[11]

The numerical consequence of the geometrical shadow effect is constructed from Eq. (8). The cross section is decreased from n times the single-charge, Langevine value by the number of adjacent overlapping spheres times the average overlapping area. That is

$$\sigma_{shadow}(T) = n\sigma_{Langevine}(T) - (n - 1) \langle A(T) \rangle$$

(9)

The rate constant computed analogously is

$$k_{shadow}(T) = nk_{Langevine}(T) - (n-1)\langle v\,A(T)\rangle \tag{10}$$

where

$$\langle v\,A(T)\rangle = \frac{4}{\sqrt{\pi}}\left(\frac{m}{2k_B t}\right)^{3/2}\int_0^{\infty}\int_0^{\frac{\pi}{2}} A(\theta,v)\,\sin(\theta)\,d\theta\;\; v^3\, e^{\frac{-mv^2}{2k_B T}}\,dv \tag{11}$$

The double integral in Eq. (8) can be removed if the approximation of using a thermally averaged radius defined by Eq. (3) is used in the determination of the overlap area, rather than thermally averaging Eq. (7). That is

$$\langle A(T)\rangle = \int_0^{\frac{\pi}{2}} A(\theta,T)\,\sin(\theta)\,d\theta \tag{12}$$

Note that Eq. (9), (10), and (12) are clearly dilute limit expansions, for in the opposite limit of n charges at a single point, Eqs. (2) and (3) show the proper values to be n times that for a single charge, while Eq. (9), (10), and (12) predict the single-charge value. This suggests that, at least in the high density limit, the geometrical Eq. (9), (10), and (12) will predict collision cross sections and rate constants that are lower than the correct, dynamical values.

SIMULATION

Monte Carlo Approach

We are interested in calculating thermal collision cross sections and rate constants for a multiply-charged, linear, gas-phase biomolecule. We perform the necessary integrals by a monte carlo approach.[12] That is we numerically follow the trajectories of polar, polarizable molecules approaching the biomolecule. We randomly orient the biomolecule, with its center of mass at the origin. The protons on the biomolecule are equally spaced a distance L/(n-1) along the axis. We initially define the x-coordinate of the basic molecule some distance beyond the projection of the biomolecule on the x-axis (100 Å when no dipole moment is included and 200 Å when the molecule is polar). The random y-z coordinates of the basic molecule are generated uniformly in a rectangle (a "halo") around the projection of the axis of the biomolecule on the y-z plane. (See Figure 1.) The rectangle is defined to be a distance r_{halo} from the biomolecule's axis in projection (r_{halo} is 30 Å for nonpolar basic molecule and 35 Å for a polar one). The basic molecule is defined to have a Maxwell-Boltzman velocity in the **-x** direction. The procedure for determining the collision cross sections and rate constants, then, is to generate random initial conditions as above, then to use

$$\sigma = \frac{1}{N} \sum area_i \ (Trajectory\ i\ hit\ charge) = \langle \sigma \rangle_{Boltz} \qquad (13)$$

$$k = \frac{1}{N} \sum v_i \, area_i \, (Trajectory \; i \; hit \; charge) = \langle v \, \sigma \rangle_{Boltz} \tag{14}$$

where the Iverson convention (S) stands for 1 if S is true, and 0 otherwise.[13] The number of different trajectories attempted, N, is 20 000 in all of our calculations. The halo area depends on the initial conditions through the orientation of the biomolecule, and the velocity is, of course, also a random variable. A trajectory is defined to "hit" the biomolecule if it comes within 1 Å of one of the n charges on the axis.

Error bars on the estimates provided by Eqs. (13) and (14) can be computed. That is the standard deviation of the estimate is given by the standard deviation of the data divided by the square root of N. This definition of error bar will be used below.

We anticipate that the approximation of not following the rotational motion of the biomolecule will be an adequate one. A typical velocity of our basic molecule at room temperature is $v \approx 4$ Å/ps, and a typical rotational velocity is $\omega_x \approx \omega_y \approx \omega_z \approx 2$ rad/ps. This values are both very much larger than the typical rotational velocity of $\omega_x \approx \omega_y \approx 10^{-3}$ rad/ps of the biomolecule. While the biomolecule would not be stationary during the 100 Å flight of the basic molecule, it would be substantially so. We will make the computation expedient of ignoring this motion.

Since the forces that lead to collisions are relatively long range, we suspect the

approximation of a rigid basic molecule is a fairly good one. For the model of dimethyl amine, we treated the methyl groups as 15 amu atoms, and ignored the hydrogen bonded to the nitrogen. The dipole moment of this molecule was assumed to be perpendicular to the plane containing the methyl groups and the nitrogen. We also suspect that the assumption of a smoothly varying electric field, which leads to expression of the interaction energy by a dipole moment and a polarizability[14], is valid because whether a molecule will collide with the biomolecule is determined at a relatively long range.

Integration of Equation of Motion

Numerically following the trajectory of the basic molecule entails integrating Newton's equation, as well as Euler's equations of rotation if the molecule is polar.[15] Specifically,

$$\begin{aligned} \boldsymbol{a}_{CM} &= \frac{\boldsymbol{F}}{m} \\ I\dot{\omega}_1 - \omega_2\omega_3(I_2 - I_3) &= N_1 \\ I\dot{\omega}_2 - \omega_3\omega_1(I_3 - I_1) &= N_2 \\ I\dot{\omega}_3 - \omega_1\omega_2(I_1 - I_2) &= N_3 \end{aligned} \tag{15}$$

Where Newton's equation applies to the center of mass position of the basic molecule, and Euler's equations apply to the orientation of the basic molecule in its principal axes coordinate system. Actually, since Euler's equations are singular when integrated in terms of Euler's angles, the much more numerically stable quaternion parameter method is used in the integration.[16] The force on the basic molecule

is defined by[14]

$$\boldsymbol{F} = \alpha \boldsymbol{E}(\boldsymbol{r}) \cdot \nabla \boldsymbol{E}(\boldsymbol{r}) + \boldsymbol{d} \cdot \nabla \boldsymbol{E}(\boldsymbol{r}) \tag{16}$$

and the torque on the basic molecule is given by[14]

$$\boldsymbol{N} = \boldsymbol{d} \times \boldsymbol{E}(\boldsymbol{r}) \tag{17}$$

where the electric field at the position of the basic molecule, **E**(**r**), is given by the sum of the Coulomb fields due to the point charges on the biomolecule

$$\boldsymbol{E}(\boldsymbol{r}) = \sum_{i=1}^{N} \frac{q_i}{|\boldsymbol{r} - \boldsymbol{r}_i|^3} (\boldsymbol{r} - \boldsymbol{r}_i) \tag{18}$$

where q_i is the value of the i^{th} charge on the biomolecule, and $\mathbf{r}_i$ is the position of the i^{th} charge. In all our calculations, q_i is assumed to be one unit charge, $|e^-|$.

The equation of motion, Eq. (12), is integrated numerically by VODE, a variable order, variable step size ODE integration package designed to deal with difficult to integrate, nonlinear equations. [17,18,19,20,21,22] The stable, backward differentiation formula algorithm (MF = 20) is used in the eight-byte-real version of this code. For the trajectory calculations we specify rtol = 10^{-4} and atol = 10^{-6}, which means essentially four significant figure accuracy for integration over a reasonable time range. This accuracy is more than adequate for the relatively short range trajectories we perform.

RESULTS

Figure 3 depicts the results of the numerical monte carlo calculations for the model cyctochrome c / dimethyl amine system. In addition, various levels of geometric approximations are used to determine in a more computationally expedient fashion an approximate cross section and rate constant. As a check on the code, note that the calculated monte carlo cross section for a single charge is $(2.67 \pm 0.06) \times 10^{-14}$ cm^2, while that calculated from Eq. (3) is 2.64×10^{-14} cm^2. The calculated monte carlo rate constant is $(7.91 \pm 0.22) \times 10^{-10}$ cm^3/molecule/s, while that calculated from Eq. (2) is 7.80×10^{-10} cm^3/molecule/s. The monte carlo approach seems, thus, to be producing valid results.

Figure 4 depicts the monte carlo results for a biomolecule of higher charge density. Again plotted are various geometric approximations to the dynamic cross sections and rate constants. As is apparent, the dilute expansions Eqs. (9), (10), and (12) are less valid here than in Figure 3.

In order to gauge the importance of the interaction between the electric fields of the individual charges on the biomolecule, rather than seeing the effect of averaging over all orientations, Figure 5 depicts the monte carlo results for the basic molecule normally incident upon biomolecule of varying length but with a fixed charge of 13 $|e^-|$. The biomolecule is, thus, constrained to be in the y-z plane. Various charge densities are shown, with a clear transition away from a constant cross section as the

spheres of capture begin to overlap.

Figure 6 complements Figure 5 by varying the charge density on a biomolecule of fixed length 200 Å. The basic molecule is again normally incident upon the biomolecule. A transition away from the cross section predicted by n $\sigma_{Langevine}(T)$ is seen, although it is less striking that the one in Figure 5.

Finally, Figure 7 evaluates the importance of the permanent dipole moment of dimethyl amine on its collision cross section and rate constant. Both are increased by no more than a factor of 1.5. Not shown in the Figure are the calculated monte carlo cross section of $(3.67 \pm 0.08) \times 10^{-14}$ cm^2 and the calculated monte carlo rate constant of $(10.8 \pm 0.29) \times 10^{-10}$ cm^3/molecule/s for the polar basic molecule incident upon a single charge. The thermally averaged radius used in Eq. (12) is calculated from this monte carlo estimate for the single-charge cross section. And $k_{Langevine}(T)$ is defined to be the monte carlo estimate.

DISCUSSION

The major point to be gleaned from Figures 3-7 is that interactions of the electric fields of the protons on the axis of the biomolecule never reduce the collision cross section or rate constant by even a factor of two over the simple n $\sigma_{Langevine}(T)$ or n $k_{Langevine}$ value. At higher proton densities than are currently experimentally observed[6,7], it appears that linear scaling with number of charges is not followed, although in the limit

of n charges at a point, the simple linear scaling is rigorously true. Perhaps the most marked deviation from linear scaling is offered by Figure 5, where the length of the biomolecule is decreased while the number of charges is kept constant.

Note, however, that in all cases the monte carlo collision cross section and rate constant estimates are below those calculated from Eqs. (9) and (10). These equations, rather than Eq. (12), should be expected to be a rigorous evaluation of the effects of the geometrical shadow effect. As discussed above, it is clear that in the high density limit, the accurate monte carlo estimates should be greater than those provided by Eqs. (9) and (10). It is also intuitively plausible that at moderate densities, the electric fields of adjacent protons add coherently at long range to produce, for example, a dynamical cross section that is greater than that predicted by the geometrical overlap argument.

CONCLUSIONS

Monte carlo calculations for a model system that is intended to resemble multiply protonated, linear, gas-phase cytochrome c attacked by polarizable dimethyl amine show deviations from linear scaling of the cross section with number of charges that are explainable in terms of a geometrical shadow effect. That is, for low linear charge density systems, an incident basic molecule simply cannot reach some of the charges on the biomolecule when the biomolecule is in certain orientations. At higher densities, densities higher than have been experimentally observed, the collision cross

sections and rate constants tend to fall between linear scaling and the correct evaluation of the geometrical shadow effect.

ACKNOWLEDGEMENTS

We would like to thank Paul Messina, the Director of the Caltech Concurrent Supercomputing Facilities, for generous grants of computer time. We also wish to acknowledge the Advanced Computing Laboratory of the Los Alamos National Laboratory, Los Alamos, NM 87545, for generous grants of IBM RS6000 time. The computer time required for this research was obtained through the Caltech Concurrent Supercomputer Facility and is supported by the NSF under Cooperative Agreement No. CCR-8809615. The government has certain rights in this material.

REFERENCES

1) R. J. W. Le Fevre, Advan. Phys. Org. Chem., 3 (1965) 1.

2) R. D. Nelson, Jr., D. R. Linde, Jr., and A. A. Maryott, Selected Values of Electric Dipole Moments for Molecules in the Gas Phase, National Standard Reference Data Series-National Bureau of Standards 10, 1967, p. 23.

3) J. B. Fenn, M. Mann, C. K. Meng, S. F. Wong, and C. M. Whitehouse, Science, 246 (1989) 64.

4) J. A. Loo, H. R. Udseth, and R. D. Smith, Anal. Biochem. 179 (1989) 404.

5) T. R. Covey, R. F. Bonner, B. I. Shushan, and J. D. Henion, Rapid Commun. Mass Spectrom. 2 (1988) 249.

6) J. A. Loo, R. R. O. Loo, H. R. Udseth, C. G. Edmonds, and R. D. Smith, Rapid Commun. Mass Spectrom. 5 (1991) 101.

7) S. A. McLuckey, G J. Van Berkel, and G. L. Glish, J. Am. Chem. Soc. 112 (1990) 5668.

8) T. B. McMahon and J. L. Beauchamp, Rev. Sci. Instrum. 43 (1972) 509.

9) P. R. Kemper and M. T. Bowers, "Ion Cyclotron Resonance Spectroscopy," in Techniques for the Study of Ion-Molecule Reactions, J. M. Farrar and W. H Saunders, Jr., eds., Vol. XX of Techniques in Chemistry, John Wiley & Sons, 1988, pp. 1-59.

10) J. I. Steinfeld, J. S. Francisco, and W. L. Hase, Chemical Kinetics and Dynamics, Prentice Hall, 1989, pp. 272-274.

11) W. H. Press, B. P. Flannery, S. A. Teukolsky, and W. T. Vetterling, Numerical Recipes: The Art of Scientific Computing, Cambridge University Press, 1987.

12) M. H. Kalos and P. A. Whitlock, Monte Carlo Methods, Volume I: Basics, John Wiley & Sons, 1986.

13) R. L. Graham, D. E. Knuth, O. Patashnik, Concrete Mathematics, Addison-Wesley, 1989, p. 23.

14) J. D. Jackson, Classical Electrodynamics, John Wiley & Sons, 1975.

15) H. Goldstein, Classical Mechanics, Addison-Wesley. 1981, p. 205.

16) R. Sonnenschein, J. Comput. Phys. 59 (1985) 347. Note that the torques appearing in Eq. (5) in this reference are principal axes torques.

(17) P. N. Brown, G. D. Byrne, and A. C. Hindmarsh, "VODE, a Variable Coefficient ODE Solver," LLNL Report UCRL-98412, June 1988. Also, SIAM J. Sci. Stat. Comput., to appear.

(18) G. D. Byrne and A. C. Hindmarsh, ACM Trans. Math. Software 1 (1975) 71.

(19) A. C. Hindmarsh and G. D. Byrne, "EPISODE: An Effective Package for the Integration of Systems of Ordinary Differential Equations," LLNL Report UCID-30112, Rev. 1, April 1977.

(20) G. D. Byrne and A. C. Hindmarsh, "EPISODEB: An Experimental Package for the Integration of Systems of Ordinary Differential Equations with Banded Jacobians," LLNL Report UCID-30132, April 1976.

(21) A. C. Hindmarsh, Scientific Computing, R. S. Stepleman et al., eds., North-Holland, Amsterdam, 1983, pp. 55-64.

(22) K. R. Jackson and R. Sacks-Davis, ACM Trans. Math. Software 6 (1980) 295.

FIGURES

Figure 1. Depicted is a typical multiply-charged, linear, gas-phase biomolecule. Indicated are the individual spheres of capture around each charge. Note that at a viewing angle more nearly along the axis, spheres more distant from the viewpoint would be blocked from view by nearer spheres. This is the shadow effect. The dashed box indicates the "halo" used in the monte carlo evaluation of the cross sections and rate constants.

Figure 2. Depicted in a) is the geometry leading to the numerical evaluation of the value of the shadow effect, Eq. (8). The angle of incidence relative to the axis of the biomolecule, θ, is depicted. Also indicated is the projected distance, x_0, of the separation of the spheres of capture. Depicted in b) is the geometry leading to Eq. (6). Also displayed is the θ_0 defined by Eq. (5).

Figure 3. Depicted are data for a biomolecule of length 400 Å with charge 9 to 15 $|e^-|$ and a nonpolar molecule with polarizability 5 $Å^3$, mass 45 amu, and temperature 300 K. a) Illustrated are the monte carlo cross sections with error bars (circles), the cross section computed by Eq. (9) (solid line), the cross section computed as n $\sigma_{Langevine}(T)$ (long dashed line), and the cross section computed by Eq. (12) (short dashed line). The cross section units are 10^{-16} cm^2. b) Illustrated are the monte carlo rate constants at 300 K (circles), one set of monte carlo rate constants at 2000 K (squares), the rate constants predicted by Eq. (10) (solid line), and the rate constants

computed as n $k_{Langevine}$ (long dashed line). The rate constant units are 10^{-10} cm^3/molecule/s.

Figure 4. Depicted are data for a biomolecule of length 200 Å with charge 9 to 15 $|e^-|$ and a nonpolar molecule with polarizability 5 $Å^3$, mass 45 amu, and temperature 300 K. a) Illustrated are the monte carlo cross sections with error bars (circles), the cross section computed by Eq. (9) (solid line), the cross section computed as n $\sigma_{Langevine}(T)$ (long dashed line), and the cross section computed by Eq. (12) (short dashed line). The cross section units are 10^{-16} cm^2. b) Illustrated are the monte carlo rate constants at 300 K (circles), the rate constants predicted by Eq. (10) (solid line), and the rate constants computed as n $k_{Langevine}$ (long dashed line). The rate constant units are 10^{-10} cm^3/molecule/s.

Figure 5. Depicted are data for a biomolecule of length L = 100 to 600 Å with charge 13 $|e^-|$ and a nonpolar molecule with polarizability 5 $Å^3$, mass 45 amu, and temperature 300 K. The basic molecule is normally incident upon the biomolecule in this case. a) Illustrated are the monte carlo cross section with error bars (circles), the cross section computed by Eq. (9) (solid line), the cross section computed as n $\sigma_{Langevine}(T)$ (long dashed line), and the cross section computed by Eq. (12) (short dashed line). The cross section units are 10^{-16} cm^2. b) Illustrated are the monte carlo rate constants at 300 K (circles), the rate constants predicted by Eq. (10) (solid line), and the rate constants computed as n $k_{Langevine}$ (long dashed line). The rate constant

units are 10^{-10} cm^3/molecule/s.

Figure 6. Depicted are data for a biomolecule of length 200 Å with charge 9 to 15 $|e^-|$ and a nonpolar molecule with polarizability 5 $Å^3$, mass 45 amu, and temperature 300 K. The basic molecule is normally incident upon the biomolecule in this case. a) Illustrated are the monte carlo cross section with error bars (circles), the cross section computed by Eq. (9) (solid line), the cross section computed as n $\sigma_{Langevine}(T)$ (long dashed line), and the cross section computed by Eq. (12) (short dashed line). The cross section units are 10^{-16} cm^2. b) Illustrated are the monte carlo rate constants at 300 K (circles), the rate constants predicted by Eq. (10) (solid line), and the rate constant computed as n $k_{Langevine}$ (long dashed line). The rate constant units are 10^{-10} cm^3/molecule/s.

Figure 7. Depicted are data for a biomolecule of length 400 Å with charge 9 to 15 $|e^-|$ and a polar molecule with polarizability 5 $Å^3$; principal dipole moment <1.03, 0, 0> Debye; principal moments of inertia I_{xx} 7.61, I_{yy} 15.25, and I_{zz} = 43.63 amu $Å^2$; mass 45 amu; and temperature 300 K. a) Illustrated are the monte carlo cross sections with error bars (circles), the cross section computed as n $\sigma_{Langevine}(T)$ (long dashed line), and the cross section computed by Eq. (12) (short dashed line). The cross section units are 10^{-16} cm^2. b) Illustrated are the monte carlo rate constants at 300 K (circles) and the rate constants computed as n $k_{Langevine}$ (long dashed line). The rate constant units are 10^{-10} cm^3/molecule/s.

Figure 1

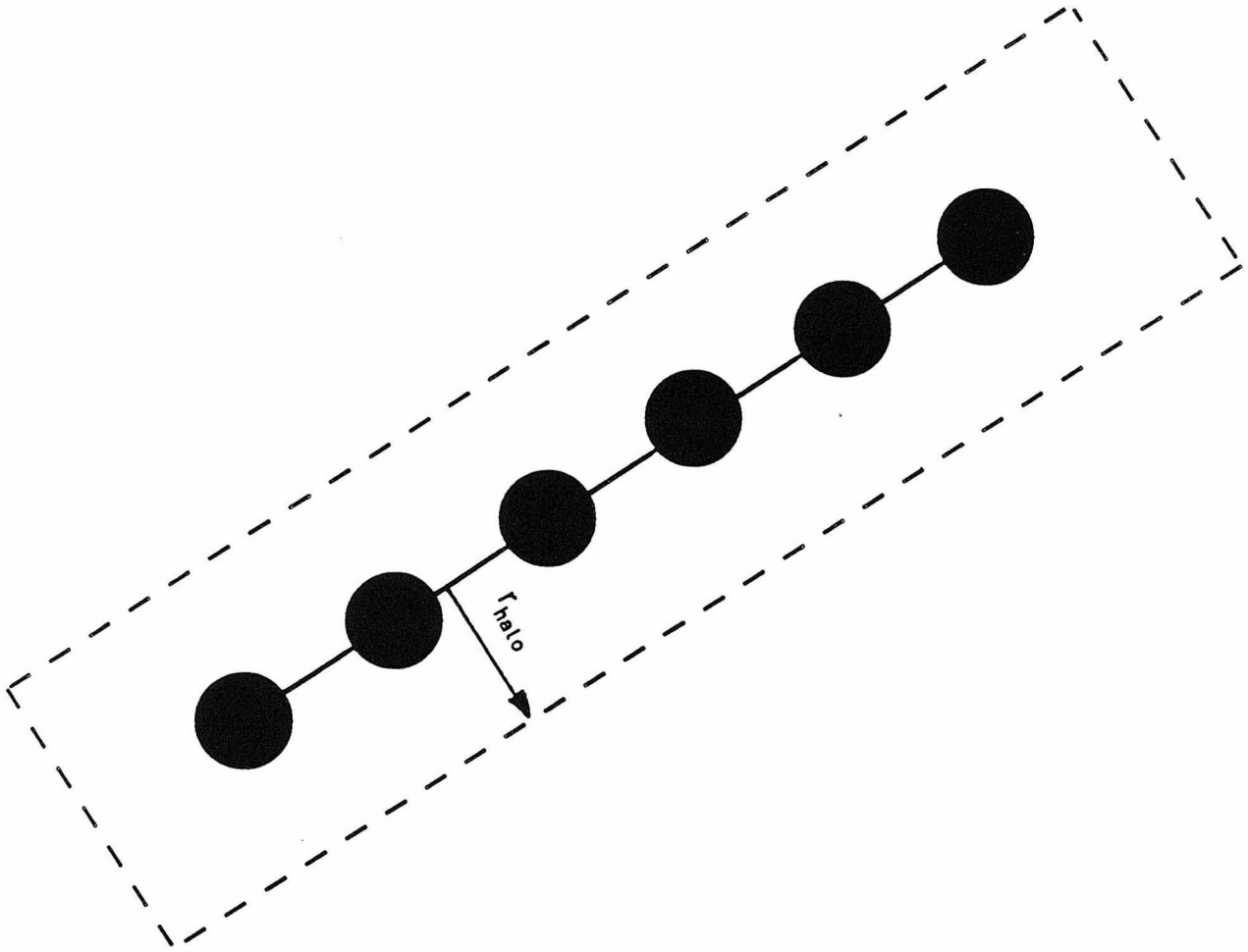

Figure 2

a)

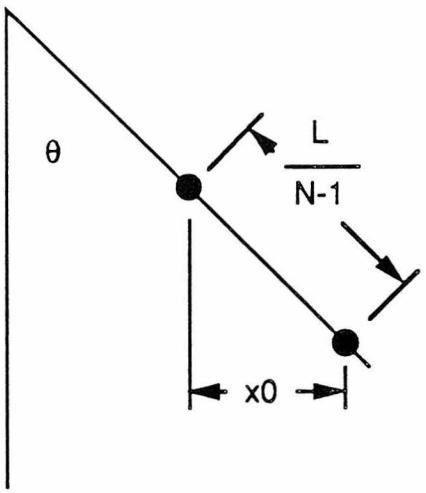

b)

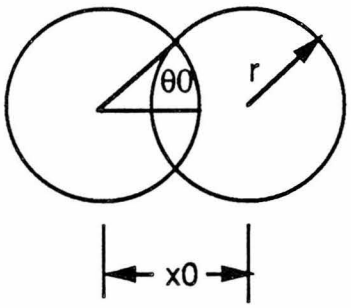

Figure 3a

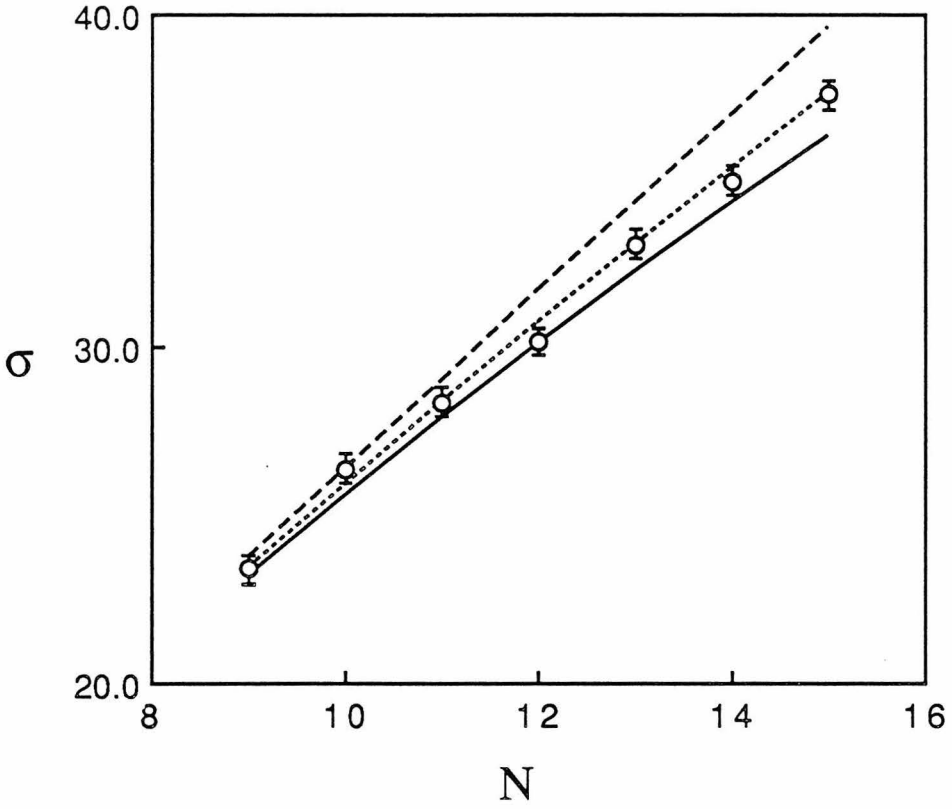

Figure 3b

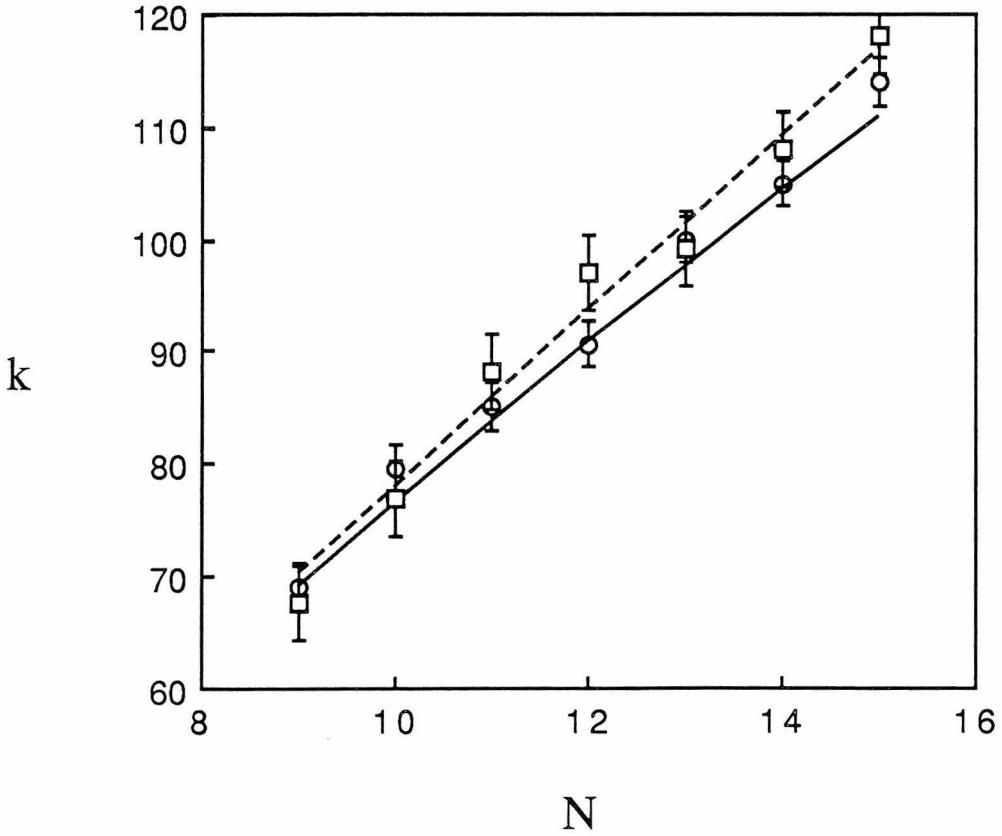

Figure 4a

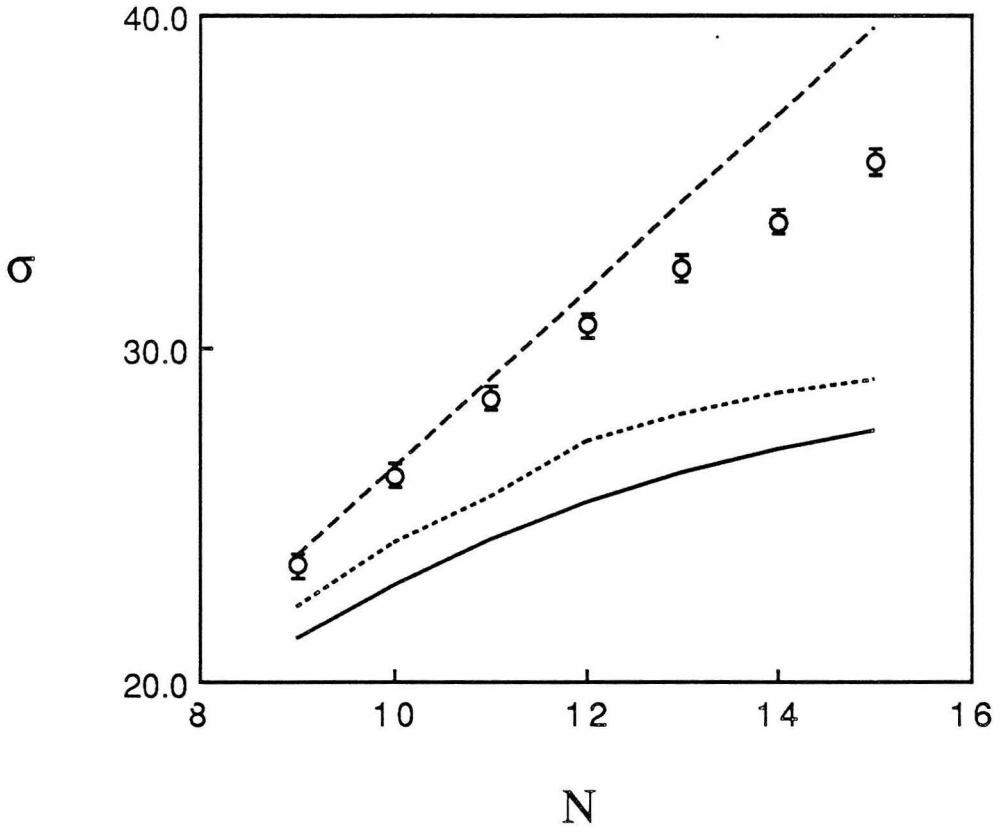

Figure 4b

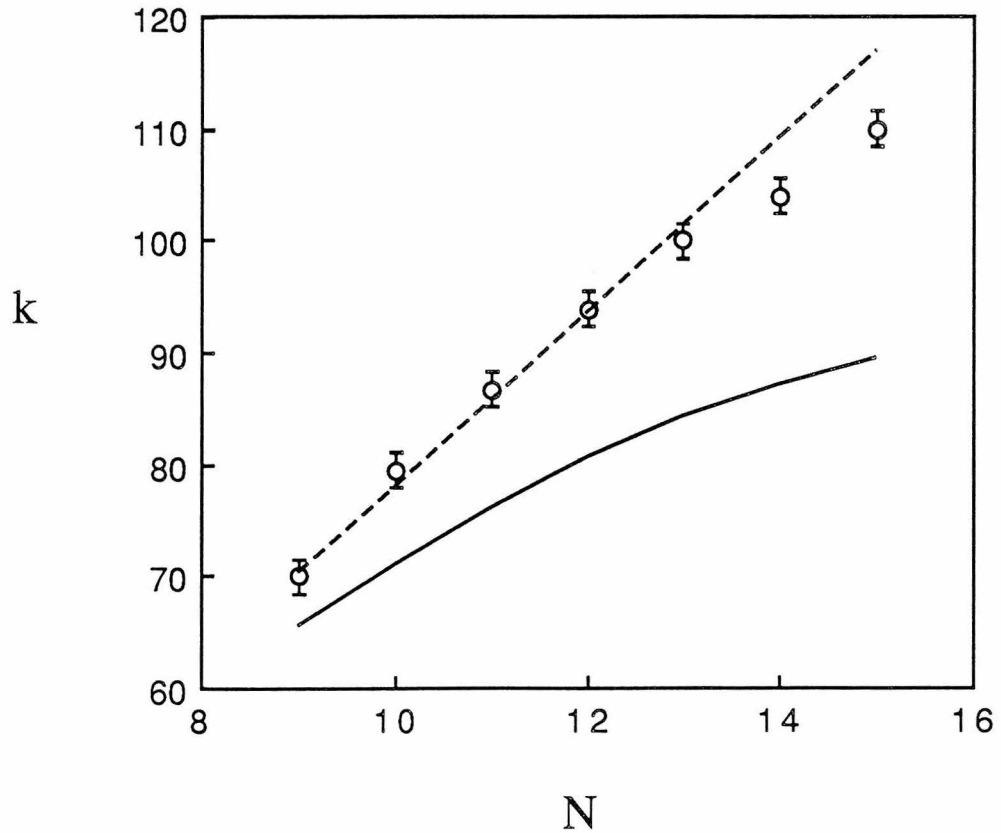

Figure 5a

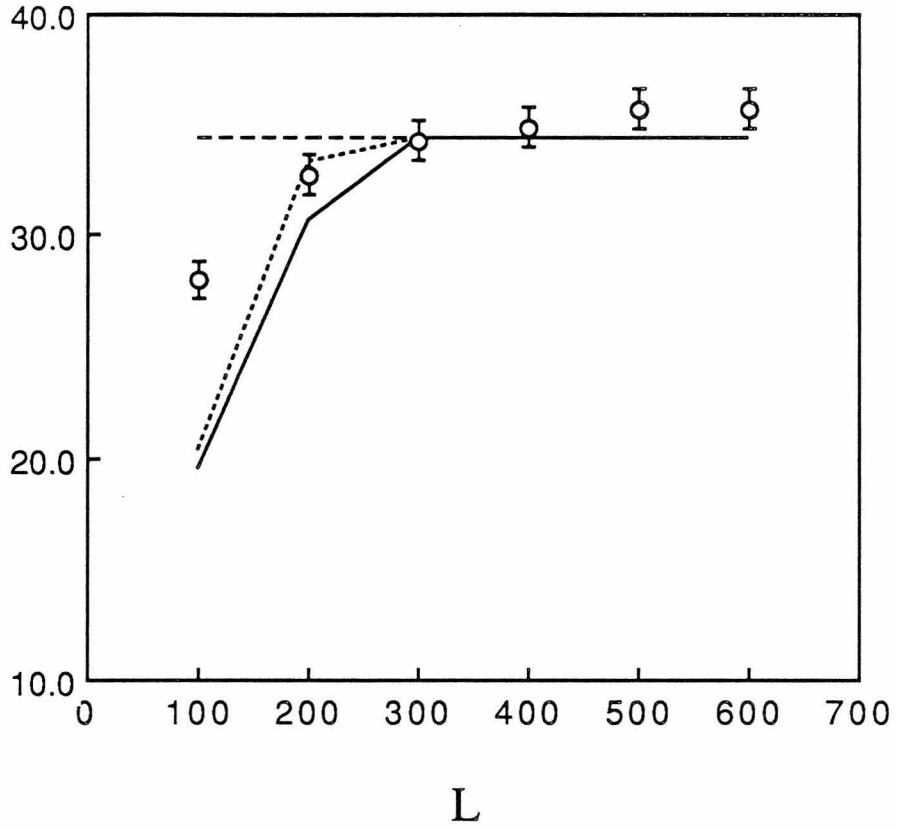

Figure 5b

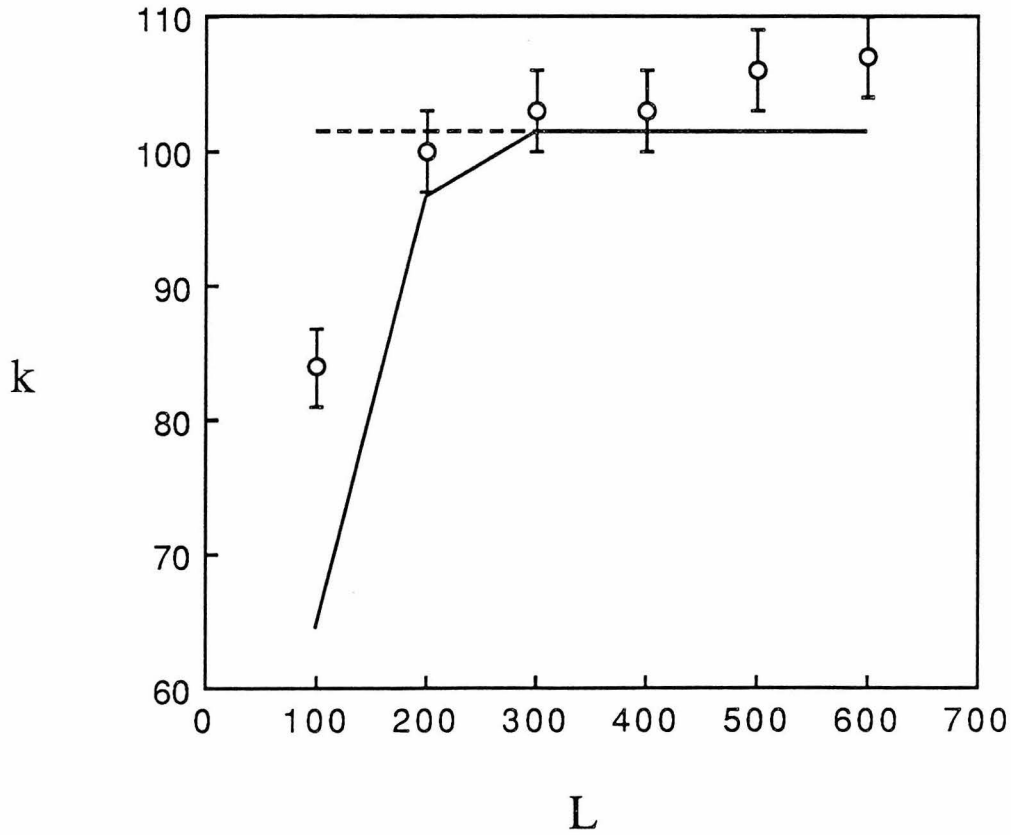

Figure 6a

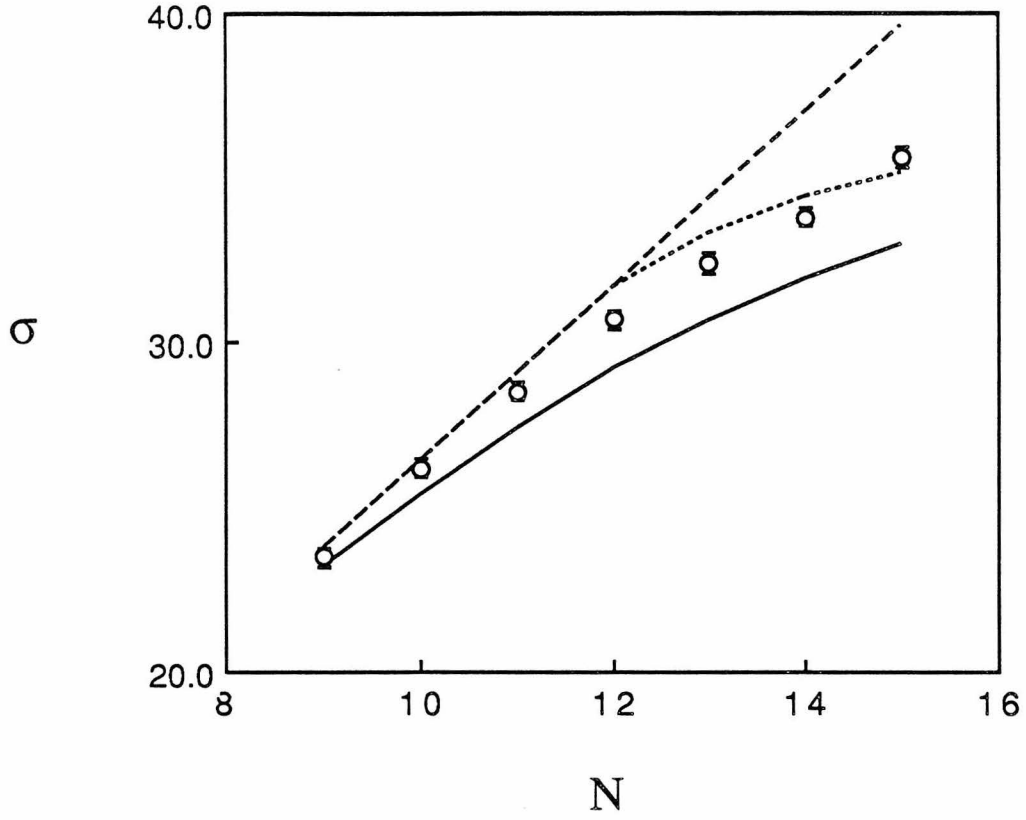

Figure 6b

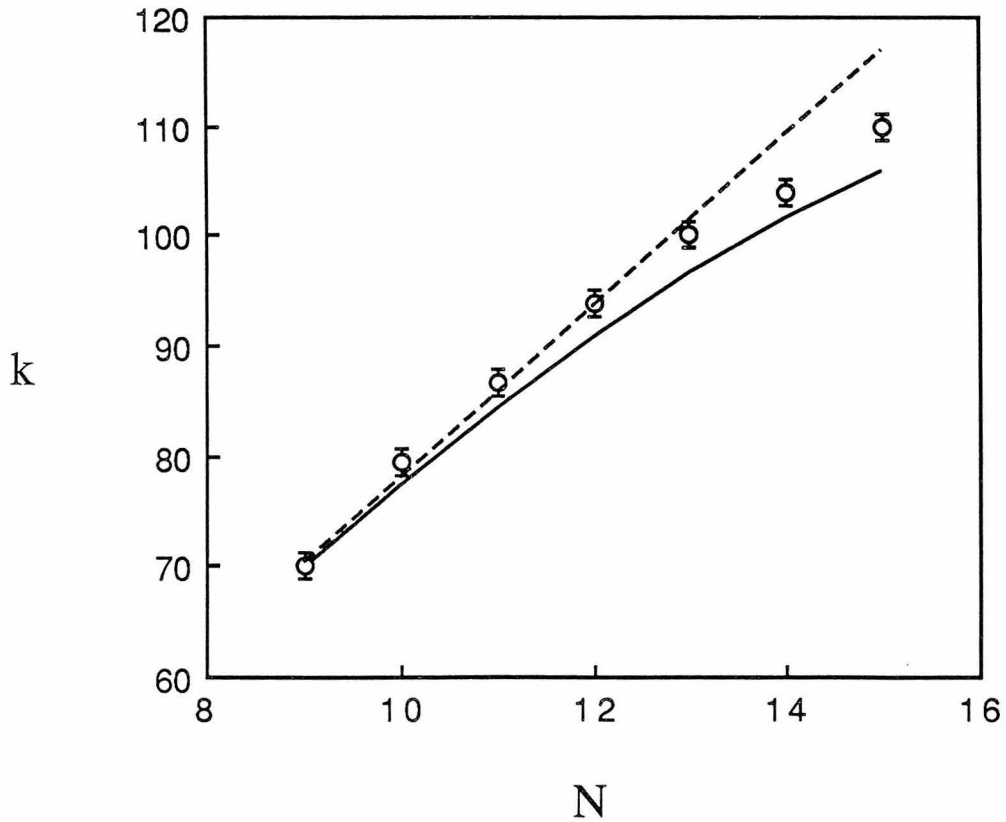

Figure 7a

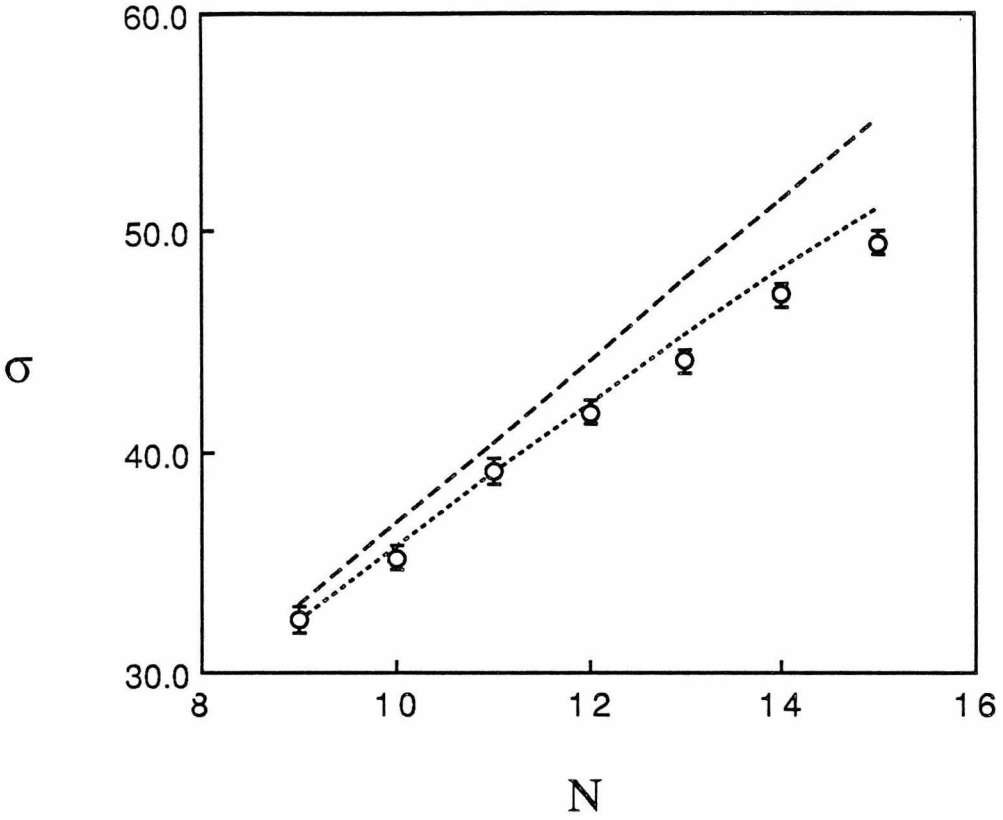

Figure 7b